The Dissertation Committee for Drit Sokoli Certifies that this is the approved version of the following dissertation:

Fracture of High-Strength Bars in Concrete Frame Members under Earthquake Loads

Committee:

Michael D. Engelhardt, Supervisor

Wassim M. Ghannoum, Co-Supervisor

Trevor D. Hrynyk

James O. Jirsa

Eric B. Williamson

Fracture of High-Strength Bars in Concrete Frame Members under Earthquake Loads

by

Drit Sokoli

Dissertation

Presented to the Faculty of the Graduate School of

The University of Texas at Austin

in Partial Fulfillment

of the Requirements

for the Degree of

Doctor of Philosophy

The University of Texas at Austin

August 2018

To my family.

Acknowledgements

First of all, I would like to express my gratitude to my academic advisor and life mentor, Dr. Wassim Ghannoum. His knowledge and dedication guided my research and shaped this dissertation. I feel indebted to Dr. Engelhardt for serving as the official supervisor, but above all, for always taking the time to discuss the material, even though reinforced concrete is not his favorite topic. I am honored and thankful that Dr. Jirsa read my work and provided invaluable feedback in a short amount of time. Dr. Hrynyk and Dr. Williamson are wonderful professors both inside and outside the classroom. It has been a privilege to be their student.

I would like to thank my research partner Albert Limantono for his friendship, and commitment to the work we carried together. Also, Chase Slavin, Graham Hogsett, and Stephen Zhao have been instrumental in the successful completion of the research, and I will always be thankful. I am grateful to Nawaf Alotaibi, Gloriana Arrieta, Kostas Belivanis, Sepehr Dara, Paul Biju-Duval, Michalis Hadjioannou, Kerry Kreitman, Ali Morovat, Colter Roskos, William Shekarchi and Ali Abu Yousef for their friendship, help and support. Many other friends and colleagues helped at one point or another in the laboratory, too, and I am thankful to each and every one of them. I hope to have returned at least partly the assistance they offered me.

I would like to thank the personnel of Ferguson Structural Engineering Laboratory. Particularly, I would like to extend my gratitude to Blake Staseny for helping me with the laboratory work in a daily basis.

This study wouldn't have been possible without the generous financial support of the Charles Pankow Foundation, the Concrete Reinforcing Steel Institute, and the American Concrete Institute Foundation Strategic Development Council. The steel and fabrication donations of member mills of the Concrete Reinforcing Steel Institute are appreciated, as is their financial and technical commitment to developing new high-strength reinforcing bars.

Last, but not least, I would like to thank my family for their unconditional love and support since day one, and more so during these years of graduate studies.

Fracture of High-Strength Bars in Concrete Frame Members under Earthquake Loads

Drit Sokoli, Ph.D.

The University of Texas at Austin, 2018

Supervisor: Michael D. Engelhardt

Co-Supervisor: Wassim M. Ghannoum

Fracture of longitudinal bars due to high-strain low-cycle fatigue is a critical failure mode in seismically detailed reinforced concrete frame members because it can lead to rapid strength loss and structural instability. The issue has recently attracted attention due to a national effort aimed at introducing high-strength reinforcing bars (HSRB) with yield strengths of 80 and 100 ksi in concrete construction. The HSRB being produced in the United States possess varying post-yield mechanical properties, such as the tensile-to-yield strength ratio, uniform or fracture elongations, as well as low-cycle fatigue life. The behavior of Special Moment Frame (SMF) members with different types of HSRB subjected to large inelastic demands up to bar fracture is investigated through laboratory testing and analytical examination.

Laboratory tests were performed to identify any major issues in the performance of HSRB in concrete members. More specifically, the work aimed to assess the influence of the tensile-to-yield strength (*T/Y*) ratio, fracture elongation, and shape of stress strain curve of HSRB on the behavior of seismically detailed concrete columns. Four specimens were

tested under constant axial load and reverse cyclic lateral loading of increasing amplitudes until fracture of longitudinal bars. Three columns were reinforced with grade 100 bars sourced from different manufacturers and therefore having different post-yield mechanical properties. The fourth column was reinforced with conventional grade 60 ASTM A706 (2016) bars. Concrete columns reinforced with HSRB reached similar lateral drift levels as the specimen reinforced with grade 60 bars before significant loss in lateral strength.

A computational framework based on fiber-section elements and mechanics-based behavioral models is proposed to accurately estimate both member-level deformations and strain demands in longitudinal bars and the concrete surrounding them within the plastic hinge regions of frame members. Particularly, the effects of the mechanical properties and steel grade of reinforcing bars on their strain demands are quantified experimentally and estimated by the proposed framework.

The strain demands derived through the proposed analytical framework were used to track the damage progress in longitudinal bars that lead to buckling and fracture. A buckling initiation model is proposed that accounts for the mechanical properties of the reinforcing bars, as well as the loading history the bars and the surrounding concrete experience prior to buckling. Material specific bar fatigue relations calibrated through material test results are used to predict the number of half-cycle to bar fracture based on accumulation of strain demands prior and after buckling if it occurs.

Table of Contents

List of Figures xiii

List of Tables xxi

List of Equations xxiii

1. Preface 1

1.1 Motivation 1

1.2 Research Topic 4

1.3 Paper 1 6

1.4 Paper 2 7

1.5 Paper 3 8

1.6 Intellectual contributions 8

2. Paper 1: Special Moment frame Columns with High-strength Reinforcement[1] 9

2.1 Introduction 10

2.2 Research Significance 12

2.3 Laboratory Test Program 13

2.3.1 Specimen Design and Detailing 13

2.3.2 Material Properties 17

2.3.3 Test Setup and Instrumentation 20

2.4 Test Results 23

2.4.1 General Behavior 23

2.4.2 Lateral Drift Components 30

2.4.3 Dissipated Energy 31

2.4.4 Strain Demands 33

2.4.5 Plasticity Spread 35

2.5 Comparison with Analytical Models 39

2.5.1 Moment Strength 39

2.5.2 Shear Demands 42

2.5.3 Effective Stiffness 43

2.5.4 ASCE/SEI 41 Drift Capacity 45

2.6 Conclusions 47

3. Paper 2: From Global to Local Deformations of Concrete Special Moment Frame Members[1] 51

3.1 Introduction 52
3.2 Experimental Data 55
3.2.1 Behavioral Milestones 59
3.2.2 Measured Strains in Longitudinal Bars 61
3.2.3 Measured Surface Strains in Plastic Hinge Regions 66
3.2 Fiber-Section Computational Model 70
3.2.1 Fiber-Section Distributed Plasticity Element 70
3.2.2 Fiber Discretization 71
3.2.3 Material Models 72
3.2.4 Shear Deformations 79
3.2.5 Bar Slip Deformations 80
3.2.6 Flexural Deformations 82
3.2.7 Simulated Member-Level Behavior 86
3.3 Estimating Strains in Reinforcing bars 93
3.3.1 Tensile Strains 93
3.3.2 Compressive Strains 98
3.3.3 Cyclic Strain Demands 100
3.4 Concrete Surface Strains 102
3.4.1 Tensile Strains 102
3.4.2 Compressive Strains 107
3.4.3 Cyclic Strain Demands 110
3.5 Summary and Conclusions 112
3.6 Limitations and recommendation for future work 113

4. Paper 3: Buckling and Fracture of HSRB in Special Moment Frame Members [1] 114

4.1 Introduction 115
4.2 Experimental Data 120
4.3 From Fiber-Section Strains To Representative strains 125
4.3.1 Representative strain histories in longitudinal bars at member ends 126
4.3.2 Representative smeared longitudinal strain histories over buckling length 128
4.3.3 Representative strain histories in longitudinal bars at hoop-spacing distance from member ends 131
4.4 Buckling initiation model 135
4.4.1 Prior Buckling Initiation Models 135
4.4.2 Proposed Buckling Initiation Model 137
4.4.3 Reinforcing Bar Tangent Modulus of Elasticity 140
4.4.4 Alpha and Beta Factors 146

4.5 Damage Accumulation Index and Fracture 150
4.5.1 Fatigue Fracture Models 150
4.5.2 Predicting Fracture 152
4.6 Summary and Conclusions 157
4.7 Limitations and recommendation for future work 159

5. Summary, Conclusions, and Discussion 160
5.1 Paper 1 161
5.2 Paper 2 165
5.3 Paper 3 167

6. Appendix A: Experimental Program Information 169
6.1 Design Calculations and Checks per ACI 318-14 169
6.2 Detailed Drawings of the Specimens 179
6.3 Pictures from Specimen Construction and Test Setup 184
6.4 Concrete Mix Properties and Compressive Strength 189
6.5 Reinforcing Steel Tensile Test Results 191
6.6 Test Setup and Instrumentation – Additional Information 195

7. Appendix B: Additional Experimental Results 197
7.1 Data Processing 197
7.1.1 Large Deformation Equilibrium 198
7.1.2 Deformation Measurements 200
7.1.3 Strain Measurements 202
7.1.4 Damage Evaluation 202
7.1.5 Behavioral Milestones 204
7.2 Test Results for CH100 206
7.2.1 General Behavior 207
7.2.2 Deformation Components 214
7.2.3 Strain History 215
7.2.4 Crack Widths 218
7.2.5 Buckling History 220
7.2.6 Energy Dissipation 221
7.3 Test Results for CL100 223
7.3.1 General Behavior 224
7.3.2 Deformation Components 231
7.3.3 Strain History 233
7.3.4 Strain Profile 235

7.3.5 Crack Widths 236
7.3.6 Buckling History 238
7.3.7 Energy Dissipation 240
7.4 Test Results for CM100 241
7.4.1 General Behavior 242
7.4.2 Deformation Components 250
7.4.3 Strain History 252
7.4.4 Strain Profile 254
7.4.5 Buckling History 257
7.4.6 Energy Dissipation 259
7.5 Test Results for CH60 260
7.5.1 General Behavior 261
7.5.2 Deformation Components 268
7.5.3 Strain History 270
7.5.4 Strain Profile 272
7.5.5 Crack Widths 272
7.5.6 Buckling History 275
7.5.7 Energy Dissipation 278

8. Appendix C: Supporting Information for Chapter 3 279

8.1 Experimental Tests 279
8.2 Matched tensile Strains in longitudinal bars 289
8.3 Matched tensile Strains in The Concrete Surface 291

List of References 292

List of Figures

Figure 2-1: Cross-sectional layout of the reinforcement in tested specimens 14

Figure 2-2: Elevation layout of the reinforcement in tested specimens.....15

Figure 2-3: Typical stress-strain curves for the a) #6 longitudinal bars and b) #4 transverse bars used in each column. 20

Figure 2-4: State of damage for the four specimens at the last cycles of loading 22

Figure 2-5: Lateral response with behavioral milestones of the four tested specimens 25

Figure 2-6: Pictures of columns at first bar fracture (red circle showing location) and respective fractured bars 25

Figure 2-7: Lateral response of CH100 and CL100 with respective milestones (filled markers for CH100, hollow markers for CL100) 26

Figure 2-8: Crack pattern (up) and largest principal strains (down) for each specimen at the first excursion to +2% and +4% drift ratios 28

Figure 2-9: Deformation components for each specimen at target drift ratio as percentage of total lateral displacements 31

Figure 2-10: a) Cumulative dissipated energy (CDE) in the first cycles to each drift target; b) CDE in the second cycles to each drift target; c) Total CDE normalized to M_{nm} 32

Figure 2-11: Average strain demands as measured at the column ends 34

Figure 2-12: Spread of inelastic strains on the longitudinal bars for each specimen: a) strain at the end of linear response in CM100 calculated using the 0.2% offset rule; b) strain at the end of linear response in CM100 taken as the strain at 100 ksi 36

Figure 2-13: Displacement capacity envelope as predicted from ASCE/SEI 41-13 and ASCE/SEI 41-17 vs. response envelopes of tested columns (X – drift at which 20% lateral strength was lost) 46

Figure 3-1: Example of surface strain tracking locations and damage states 60

Figure 3-2: Sample strain gauge recording for four of the members (positive strain values indicate tensile strains) 62

Figure 3-3: Mean Largest tensile strain demands (ε_M) versus drift ratios (up), and ε_M normalized to section depth versus drift ratios (down) for all specimens 65

Figure 3-4: Mean measured strains in compression for all members (left) and columns only (right) 66

Figure 3-5: Schematics of monitored strains on concrete surface 67

Figure 3-6: Sample longitudinal surface strains in member plastic hinge regions 67

Figure 3-7: Mean concrete surface strain demands (up) and normalized to section depth (down) for six of the specimens 69

Figure 3-8: Distributed plasticity fiber-section Model 71

Figure 3-9: Fiber section configuration for all modeled member 72

Figure 3-10: Stress-strain model with fracture energy in compression as highlighted area (adapted from Kent-Park 1971) 74

Figure 3-11: Lateral response sensitivity to Gfc for CS80 74

Figure 3-12: Comparison between cylinder test and regularized model for CL100 75

Figure 3-13: Cover and core concrete model 76

Figure 3-14: Comparison of measured and modeled stress-strain curves for bars in CH100 and CM100 78

Figure 3-15: Tension strain comparison for Steel02 and Reinforcing steel material models 79

Figure 3-16: Deformation components at drift targets for columns of series 3 80

Figure 3-17: Measured and modeled flexural deformation component of CS80 84

Figure 3-18: CH100 - Influence of number of integration points on the tensile strains in longitudinal bars 85

Figure 3-19: Global behavior prediction – CS80, CH100, BH100 87

Figure 3-20: Comparison of a typical cyclic strain gauge reading and corresponding result from analyses 88

Figure 3-21: Tensile strains from analysis and measured for all members 92

Figure 3-22: Extracted *TSF* at drift ratios of 2%, 3% and 4% 94

Figure 3-23: Influential parameters on *TSF* 96

Figure 3-24: Matched vs. estimated TSF 97

Figure 3-25: Mean measured strain in compression at 3% drift ratio vs. axial load ratio (left) all members, (right) columns only 98

Figure 3-26: Comparison of unscaled vs. scaled strain demands from analysis for a cycle of loading in CS80 101

Figure 3-27: Comparison of a typical cyclic strain gauge reading and corresponding scaled result from fiber-section analyses 101

Figure 3-28: Mean measured tensile surface strains vs. estimated strains from analysis 103

Figure 3-29: Extracted *STSF* at drift ratios of 2%, 3% and 4% 105

Figure 3-30: Influential parameter on *STSF* 105

Figure 3-31: Mean measured compression surface strains vs. estimated strains from analysis 108

Figure 3-32: Extracted *STSF* at drift ratios of 2%, 3% and 4% 109

Figure 3-33: Comparison of unscaled vs. scaled strain demands from analysis for a cycle of loading in CH100 111

Figure 3-34: Comparison of a typical measured cyclic strain in the concrete surface of CH100 vs. corresponding unscaled and scaled results from fiber-section 111

Figure 4-1: Types of representative strains and bar fracture locations 116

Figure 4-2: Flow-chart for predicting bar fracture in SMF members 118

Figure 4-3: Low cycle fatigue tests of bars gripped at spans of 4 and 6 bar diameter: a) pictures of grade 100 bars during testing b) measured longitudinal strains in grade 80 bars during testing (adopted from Ghannoum and Slavin 2016) 119

Figure 4-4: Representative strain history in longitudinal bars at member ends scaled from strain from analysis 127

Figure 4-5: Representative strain history in concrete surface vs. strain from analysis 129

Figure 4-6: Measured surface strains from experiment in column CH100 with and without bar-slip deformation 131

Figure 4-7: Schematic of calculating strain at a distance spacing from base 132

Figure 4-8: SSF – strain spacing factor at various target drift ratios 133

Figure 4-9: Effective length of buckled bar 139

Figure 4-10: Stress-strain curve of bars in the second loading cycle 142

Figure 4-11: Tangent modulus vs. strain increment from load reversal 143

Figure 4-12: Tangent modulus vs. normalized strain increment from load reversal to yield strain 144

Figure 4-13: Tangent modulus from material testing compared to prediction from Equation 4-5 145

Figure 4-14: Variation of factor α and β with strain demand (negative values represent compression strains) 148

Figure 4-15: Representative strain demands in the longitudinal bars of member CH100 through the loading history 154

Figure 4-16: Accumulation of Damage index in the longitudinal bars of CH100 as the column is cycled laterally 155

Figure 6-1: Steel cage assembly and strain gauge installation 185

Figure 6-2: Slump test and concrete cylinder preparation for a typical cast 186

Figure 6-3: Column casting process 187

Figure 6-4: Test setup 188

Figure 6-5: stress-strain curves of all longitudinal and transverse reinforcing bars under monotonic tension loading 193

Figure 6-6: Strain gage locations 196

Figure 6-7: Strain gauge installation process (Sokoli, 2014).....196

Figure 7-1: Free-body diagram of the test setup 199

Figure 7-2: Deformation components in a concrete member (Sokoli et al. 2014) 200

Figure 7-3: Behavioral milestones naming and corresponding marker 204

Figure 7-4: CH100 – measured lateral displacement at every captured frame.....206

Figure 7-5: CH100 – applied axial load ratio at every captured frame 207

Figure 7-6: CH100 – lateral response 208

Figure 7-7: CH100 – cracking pattern (up) and measured largest principal strains (down) at several drift ratio targets 210

Figure 7-8: CH100 – base and top moment vs. drift ratio 211

Figure 7-9: CH100 – last cycles response.....213

Figure 7-10: CH100 – pictures of fractured and buckled bars.....213

Figure 7-11: CH100 – deformation components 215

Figure 7-12: CH100 – strain gauge L17NW (top north-western corner) recording at the interface between the column and top footing.....216

Figure 7-13: CH100 – column-end bar strain gauge recordings at each drift target and calculated average.....216

Figure 7-14: CH100 – longitudinal reinforcement strain demands over height at drift targets.....217

Figure 7-15: CH100 – average values of largest flexural crack widths at drift targets.....219

Figure 7-16: CH100 – width of one of the two largest flexural cracks 219

Figure 7-17: CH100 – longitudinal bar buckling.....220

Figure 7-18: CH100 – rotation at a distance 9 inches from the base.....221

Figure 7-19: CH100 – dissipated energy at drift targets for each cycle 222

Figure 7-20: L100 – measured lateral displacement at every captured frame.....223

Figure 7-21: CL100 – applied axial load ratio at every captured frame.....224

Figure 7-22: CL100 – lateral response.....225

Figure 7-23: CL100 - cracking pattern (up) and measured largest principal strains (down) at several drift ratio targets 227

Figure 7-24: CL100 - base and top moment vs. drift ratio 228

Figure 7-25: CL100 – last cycles response.....230

Figure 7-26: CL100 – pictures of fractured and buckled bars at the end of the test..230

Figure 7-27: CL100 – deformation components.....232

Figure 7-28: CL100 – strain gauge L4NE (bottom north-eastern corner) recording at the interface between the column and bottom footing.....234

Figure 7-29: CL100 –column-end bar strain gauge recordings at each drift target and calculated average.....234

Figure 7-30: CL100 – longitudinal reinforcement strain demands over height at drift targets.....235

Figure 7-31: CL100 - average values of largest flexural crack widths at drift targets.....237

Figure 7-32: CL100 – width of one of the two largest flexural cracks.....237

Figure 7-33: CL100 – longitudinal bar buckling 239

Figure 7-34: CL100 – rotation at a distance 9 inches from the base 239

Figure 7-35: CL100 – dissipated energy at drift targets for each cycle.....240

Figure 7-36: CM100 – measured lateral displacement at every captured frame 241

Figure 7-37: CM100 – applied axial load ratio at every captured frame.....242

Figure 7-38: CM100 – lateral response 243

Figure 7-39: CM100 - cracking pattern (up) and measured principal strains (down) at drift targets....245

Figure 7-40: CM100 - base and top moment vs. drift ratio....247

Figure 7-41: CM100 – last cycles response....249

Figure 7-42: CM100 – pictures of fractured and buckled bars at the end of the test.249

Figure 7-43: CM100 – deformation components....251

Figure 7-44: CM100 – strain gauge L4SW (top south-western corner) recording at the interface between the column and top footing....253

Figure 7-45: CM100 – column-end bar strain gauge recordings at each drift target and calculated average....253

Figure 7-46: CM100 – longitudinal reinforcement strain demands over height at drift targets....254

Figure 7-47: CM100 - average values of largest flexural crack widths at drift targets....256

Figure 7-48: CM100 – width of one of the two largest flexural cracks....256

Figure 7-49: CM100 – longitudinal bar buckling....258

Figure 7-50: CM100 – rotation at a distance 9 inches from the base....258

Figure 7-51: CM100 – dissipated energy at drift targets for each cycle....259

Figure 7-52: CH60 – measured lateral displacement at every captured frame....260

Figure 7-53: CH60 – applied axial load ratio at every captured frame....261

Figure 7-54: CH60 – lateral response....262

Figure 7-55: CH60 - cracking pattern (up) and measured principal strains (down) at drift targets....264

Figure 7-56: CH60 - base and top moment vs. drift ratio....265

Figure 7-57: CH60 – last cycles response....267

Figure 7-58: CH60 – picture of fractured and buckled bars....267

Figure 7-59: CH60 – deformation components 269

Figure 7-60: CH60 – strain gauge L4NW (bottom north-western corner) recording at the interface between the column and top footing 271

Figure 7-61: CH60 – column-end bar strain gauge recordings and calculated average 271

Figure 7-62: CH60 – longitudinal reinforcement strain demands over height at drift targets 272

Figure 7-63: CH60 – average values of largest flexural crack widths at drift targets 274

Figure 7-64: CH60 – width of one of the two largest flexural cracks 274

Figure 7-65: CH60 – rotation at a distance 9 inches from the base 276

Figure 7-66: CH60 – longitudinal bar buckling 277

Figure 7-67: CH60 – dissipated energy at drift targets for each cycle 278

Figure 8-1: Estimated vs measured tensile strains in the bars 290

Figure 8-2: Estimated vs measured surface tensile strains 291

List of Tables

Table 2-1: mechanical properties of reinforcing bars used in test specimens* 19

Table 2-2: Summary of behavioral milestones for each specimen 24

Table 2-3: Experimental and calculated moment strengths of columns 40

Table 2-4: Experimental peak shear demands and calculated shear strengths of columns 42

Table 2-5: Experimental and standard effective lateral stiffnesses 44

Table 3-1: Structural parameters for each specimen.....58

Table 3-2: Drift ratios at behavioral milestones 61

Table 3-3: Strain hardening ratio 78

Table 4-1: Structural parameters for each specimen.....122

Table 4-2: Drift ratios at behavioral milestones for members that sustained bar buckling/fracture.....124

Table 4-3: Drift ratios at behavioral milestones for members which did not sustain bar buckling/fracture.....124

Table 4-4: Properties of bars tested in low cycle fatigue.....141

Table 4-5: Buckling initiation prediction calculations for all members 149

Table 4-6: Summary of material coefficients for fatigue life equation 151

Table 4-7: Summary of experimentally observed and predicted buckling and fracture.....156

Table 6-1: Concrete mix design quantities 189

Table 6-2: Concrete cylinders' compressive strength.....190

Table 6-3: Mechanical properties of longitudinal and transverse reinforcing bars ...194

Table 7-1: CH100 - behavioral milestones 208

Table 7-2: CH100 – deformation components as percentage of total 214

Table 7-3: CL100 - behavioral milestones.....225
Table 7-4: CL100 - deformation components as percentage of total.....231
Table 7-5: CM100 - behavioral milestones 243
Table 7-6: CM100 - deformation components as percentage of total 251
Table 7-7: CH60 - behavioral milestones 262
Table 7-8: CH60 - deformation components as percentage of total 268
Table 8-1: Cross-sectional details.....283
Table 8-2: Reinforcement details.....284
Table 8-3: concrete compressive strength.....285
Table 8-4: Mechanical Properties of Reinforcing Bars 286
Table 8-5: Applied axial load ratio 287
Table 8-6: Lateral loading protocol 288

List of Equations

Equation 2-1: Effective lateral stiffness....43

Equation 3-1: Strain at constant energy initiation....73

Equation 3-2: Calculating strain hardening ratio....77

Equation 3-3: Shear spring stiffness....79

Equation 3-4: Bar-slip spring stiffness....81

Equation 3-5: Tensile strain scaling procedure....93

Equation 3-6: Tensile strain factor....96

Equation 3-7: Strain in compression at a drift ratio of 3%....99

Equation 3-8: Compression strain scaling procedure....99

Equation 3-9: Compression strain scaling factor....99

Equation 3-10: Summary of scaling procedure for strains in longitudinal bars....100

Equation 3-11: Tensile strain scaling procedure....104

Equation 3-12: Tensile strain factor....106

Equation 3-13: Tensile strain scaling procedure....107

Equation 3-14: Compression strain factor....109

Equation 3-15: Summary of scaling procedure for surface concrete strains....110

Equation 4-1: Estimating strain at a distance spacing from base....132

Equation 4-2: Tensile strains at a distance spacing from base....134

Equation 4-3: Critical strength of the bar at buckling initiation....138

Equation 4-4: Assumed stress in the bar at buckling initiation....139

Equation 4-5: Tangent modulus at inelastic strains....144

Equation 4-6: Relation of strain range to the number of half-cycles to failure....151

Equation 4-7: Coffin-Manson cumulative damage index.....152

1. PREFACE

1.1 MOTIVATION

There is an increased demand for higher strength reinforcing bars (HSRB) in concrete construction in the United States and worldwide. This demand is fueled by the need to build larger and more complex structures to address population and societal demands. Congestion in construction is another motivation for seeking HSRB. Additionally, economic and environmental considerations contribute to the demand for HSRB. Introducing HSRB in concrete construction has the potential to reduce the overall volumes of steel installed by the construction industry. A reduction in steel volumes would translate into reductions in reinforcement congestion, with associated reductions in labor costs and construction time. A reduction in overall volumes could also translate into reductions in energy consumption related to manufacturing, fabricating, and shipping the steel, with associated reductions in cost. Moreover, as the world population increases, so does the demand for primary materials, and steel is not an exception. Reductions in the volume of steel bars installed in concrete construction can therefore reduce the environmental impact of the construction industry significantly, both in terms of demands on primary resources as well as demands on energy.

Nevertheless, current code limits on the strength of reinforcing steel, combined with a lack of understanding of the effects of HSRB on the performance of concrete members, are hindering progress in structural designs. Many of today's limits on strength of concrete

reinforcing steel have been enforced since the 1950s. The 1956 version of the ACI 318 building code (ACI 318, 1956) set the yield-strength limit on reinforcement at 60 ksi, increasing it from 40 ksi. In the 1971 version of the ACI 318 code, an 80 ksi limit was placed for gravity systems (ACI 318, 1971). To this date, the limit remains at 80 ksi for non-seismic systems except for shear, which has to be designed using a maximum yield strength of transverse reinforcement of 60 ksi. For seismic design, the limit currently remains at 60 ksi (ACI 318, 2014). Grade 100 steel was recently allowed in the ACI building code but only for designing confinement reinforcement.

Performance concerns that have maintained the code limits on the strength of reinforcing steel span a wide range of behavioral aspects. An increase in steel strength in reinforcing bars is associated with an increase in the strain at yield, and often with a reduction in the fracture elongation, the tensile-to-yield strength ratio, and the length of the yield plateau. For a given bar size, higher strength steel implies larger tensile and compressive forces. Larger tensile forces for the same bar size result in an increase in bond demands and the forces at bar hooks or heads. On the other hand, larger compressive forces for the same bar size can increase bar buckling susceptibility given the same lateral bracing. The larger strain at yielding in higher-strength steel can cause larger strains at service loads and therefore increase crack widths and deflections. Larger crack widths in turn can lead to the weakening of the concrete shear-transfer mechanisms and lower shear strengths. Additionally, the lower ductility of high-strength steel may affect seismic design, member deformation capacity, as well as bar-bend performance. There is also evidence that the

tensile-to-yield strength ratio affects the spread of plasticity in reinforced concrete members and a low value of the ratio can concentrate strains in bars at cracks. Strain concentrations in the longitudinal reinforcement in turn can reduce member ductility and cause premature bar fracture.

Limited test data exists on the behavior of high-strength reinforcing steel in concrete structures. New experimental data is needed to assess the implication of using high-strength reinforcements in concrete structures and allow the alleviation of code restrictions on the strength of reinforcing bars.

1.2 RESEARCH TOPIC

The research presented in this dissertation aimed to investigate the behavior of Special Moment Frame (SMF) members with different types of high-strength reinforcing bars (HSRB) subjected to large inelastic demands, up to longitudinal bar fracture. Fracture of longitudinal bars due to high-strain low-cycle fatigue is a critical failure mode in seismically detailed reinforced concrete frame members because it can lead to rapid strength loss and structural instability. The issue has recently attracted increased attention due to a national effort aimed at introducing HSRB with yield strengths of 80 and 100 ksi in concrete construction. The HSRB being produced in the United States possess varying post-yield mechanical properties, such as the tensile-to-yield strength ratio, and uniform or fracture elongations. These mechanical properties have typically lower values than those of grade 60 reinforcing bars, which have been traditionally used in construction practice for over five decades. Conversely, tests on concrete members with HSRB have indicated that high-strength bars can experience significantly larger strain demands than their lower strength counterparts (Macchi et al. 1996, Aoyama 2001, Sokoli 2014, Sokoli and Ghannoum 2016, Sokoli et al. 2018). Moreover, recent low-cycle fatigue studies (Ghannoum and Slavin 2016 and Hogsett 2017) have indicated that HSRB can have significantly different fatigue lives than grade 60 bars, with some variants having significantly higher fatigue lives and others significantly lower fatigue lives, on the order of only 30% of those of grade 60 counterparts. Such findings have raised concerns about

possible premature fractures of HSRB in concrete members designed to resist seismic loads.

The research work is presented in the form of three collated technical papers. The behavior of SMF members with HSRB subjected to large inelastic demands is investigated through laboratory testing and analytical examination. The experimental program consisted of four SMF concrete columns reinforced with HSRB tested under constant axial load and reverse cyclic lateral loading of increasing amplitudes until fracture of longitudinal bars. A computational framework based on fiber-section elements and mechanics-based behavioral models is proposed to accurately estimate both member-level deformations and strain demands in longitudinal bars, as well as in the surrounding concrete. Strain demands derived through the proposed analytical framework were used to track the damage progress on longitudinal bars that lead to buckling and fracture.

The strain prediction computational framework together with a methodology to predict longitudinal bar buckling and fracture provide the means to calculating the overall collapse risk due to bar fracture in reinforced concrete frames subjected to earthquake loads. Quantifying and comparing the collapse risk associated with the use of different types of grade 100 bars can lead to an objective decision in determining the minimum acceptable mechanical properties of HSRB to be specified in ASTM standards.

1.3 PAPER 1

In the first paper (Sokoli et. al., submitted for peer-review in July 2018), results from a laboratory testing carried out to determine any major issues in the performance of HSRB in concrete members are presented. Of particular interest was identifying the influence of the tensile-to-yield strength (*T/Y*) ratio, fracture elongation, and shape of stress strain curve of HSRB on the behavior of seismically detailed concrete columns. Four specimens were tested under constant axial load and reversed cyclic lateral loading of increasing amplitudes until fracture of longitudinal bars. Three columns were reinforced with grade 100 bars sourced from different manufacturers and therefore having different post-yield mechanical properties. The fourth column was reinforced with conventional grade 60 ASTM A706 (2016) bars. Concrete columns reinforced with HSRB reached similar lateral drift levels as the specimen reinforced with grade 60 bars before losing 20% of their lateral strength. Longitudinal bars with higher *T/Y* ratios exhibited greater plasticity spread and lower strain concentrations compared with those having lower *T/Y* ratios.

1.4 PAPER 2

In the second paper (Sokoli et. al., to be submitted for peer-review), a computational framework based on fiber-section elements and mechanics-based behavioral models is proposed to accurately estimate both member-level deformations and strain demands in longitudinal bars and the concrete surrounding them within the plastic hinge regions of frame members. Particularly, the effects of the mechanical properties and steel grade of reinforcing bars on strain demands are quantified experimentally and estimated by the proposed framework.

The framework is calibrated using 12 tests conducted on concrete columns and beams that were cycled laterally to large damage states and in some cases bar fracture. The experimental beam and column dataset contained members reinforced with regular strength, or grade 60 reinforcing bars, as well as higher strength bars of grades 80 and 100.

This work was part of the larger study investigating the fatigue fracture potential of newly introduced high-strength reinforcing bars in seismic applications, for which accurate estimates of strain demands related to bar fracture were required. However, the proposed framework is intended to be applicable beyond fracture fatigue problems and aid in the development of the next generation of performance-based standards.

1.5 PAPER 3

In the third paper (Sokoli et. al., to be submitted for peer-review), the strain demands derived through the proposed analytical framework were used to track the damage progress on longitudinal bars that lead to buckling and fracture. A buckling initiation model is proposed that accounts for the mechanical properties of the reinforcing bars, as well as the loading history the bars and surrounding concrete experience prior to buckling. Material specific bar fatigue relations calibrated through material test results are used to predict the number of half-cycle to bar fracture for buckled and un-buckled bars based on accumulation of strain demands prior and after buckling if it occurs. The framework is tested on 12 column and beam tests and accurately predicted in most cases if and at what points in a loading history buckling of longitudinal bars and fracture occurred.

1.6 INTELLECTUAL CONTRIBUTIONS

The author of this dissertation was the primary investigator responsible for the research project, with the guidance of his supervisors. The author organized the laboratory activities, planned and carried of the experimental testing, and the analysis of experimental and numerical results presented in this dissertation. Credit to journal-paper co-authors is given accordingly though references and footnotes at the beginning of each chapter.

2. PAPER 1: SPECIAL MOMENT FRAME COLUMNS WITH HIGH-STRENGTH REINFORCEMENT[1]

High-strength reinforcing bars (HSRB) with a yield strength of at least 80 ksi are currently under development in the United States. Laboratory tests were conducted to identify any major issues in the performance of HSRB in concrete members, and more specifically to assess the influence of the tensile-to-yield strength (*T/Y*) ratio, fracture elongation, and shape of stress strain curve of HSRB on the behavior of seismically detailed concrete columns. Four specimens were tested under constant axial load and reverse cyclic lateral loading of increasing amplitudes until fracture of longitudinal bars. Three columns were reinforced with grade 100 bars sourced from different manufacturers and therefore having different post-yield mechanical properties. The fourth column was reinforced with conventional grade 60 ASTM A706 (2016) bars. Concrete columns reinforced with HSRB reached similar lateral drift levels as the specimen reinforced with grade 60 bars before losing 20% of their lateral strength. Longitudinal bars with higher *T/Y* ratios achieved greater plasticity spread and lower strain concentrations compared with those having lower *T/Y* ratios.

[1] *Part of the material presented in this chapter and corresponding appendices have been submitted to the sponsor of the project: Sokoli, D. Limantono, A., and Ghannoum, W. M., "Defining Structurally Acceptable Properties of High-Strength Steel Bars through Material and Column Testing, Part II: Column testing report," (05-14), Charles Pankow Foundation, August 2017, pp. 219. http://www.pankowfoundation.org . Additionally, information in this chapter has been submitted for peer-review to the ACI Structural Journal in June 2018. D. Sokoli was the lead student investigator of the project, responsible for organizing, planning, and executing the laboratory testing, analyzing the gathered data, and writing the manuscript with the corresponding figures and tables. A. A. Limantono assisted in the building and testing of the specimens' part of the experimental investigations. W. M. Ghannoum supervised the research, and reviewed/edited the manuscript.*

2.1 INTRODUCTION

Economic, constructability, and environmental incentives are fueling the demand for higher strength reinforcing steel in concrete construction, and more particularly in highly congested seismic designs. In response, steel mills in the United States are developing high-strength reinforcing bars (HSRB) that could potentially be used in seismic applications. However, different manufacturers achieve higher strengths using different techniques (i.e., micro-alloying, quenching and tempering, etc.), leading to HSRB having varying mechanical properties. Moreover, none of the currently available HSRB are able to match the benchmark mechanical properties of the most commonly used reinforcing bars in seismic designs, grade 60 bars having a specified yield strength of 60 ksi and satisfying the ASTM A706 requirements.

An increase in steel strength in reinforcing bars is typically associated with a reduction in the fracture elongation, the tensile-to-yield (*T/Y*) strength ratio, and the length of the yield plateau (Slavin 2015, Hoggsett 2017). The above-mentioned properties are all affected by the production technique used to achieve HSRB. Additionally, the *T/Y* strength ratio and the fracture elongation are coupled properties (Slavin 2015, Hoggsett 2017), meaning that achieving higher values for one of those properties can result in sacrificing the other. Certain production techniques can also lead to HSRB that do not exhibit a distinct yielding point. Such differences in the stress-strain relations of HSRB produced using various techniques raise questions about what constitutes acceptable mechanical properties

for HSRB that can ensure satisfactory performance in concrete members subjected to seismic loads.

Past research has indicated that the *T/Y* strength ratio of reinforcing bars may affect the spread of plasticity in reinforced concrete members pushed to inelastic demands (Macchi et al. 1996, Aoyama 2001, ATC-115 2015, NIST GCR-14-917-30 2014, Sokoli 2014, Sokoli and Ghannoum 2016), with a low value of the ratio resulting in higher strain concentrations in bars at cracks. Past research has also indicated that HSRB can exhibit significantly different low-cycle fatigue life than grade 60 A706 bars, with some HSRB variants having lower fatigue lives and others having significantly higher fatigue lives than their grade 60 counterparts (Slavin 2015, Hoggsett 2017, Slavin and Ghannoum 2015, Ghannoum and Slavin 2016). Increased strain concentrations in HSRB due to lower *T/Y* ratios, coupled with lower fracture elongations and possible lower fatigue lives have raised concerns about premature fractures in HSRB in high-strain applications (Sokoli 2014, Sokoli and Ghannoum 2016).

A pilot experimental program was undertaken to determine any major issues in the performance of grade 100 HSRB in high-strain applications in concrete members. Of particular interest was to identify the influence of the *T/Y* strength ratio, fracture elongation, and shape of stress-strain curves of HSRB on the behavior of concrete columns subjected to cyclic lateral loading. Four columns were tested as part of this study, which was part of a broader research effort aimed at setting the minimum acceptable *T/Y* strength ratios and elongations in future ASTM specifications for seismic grade 80 and 100 reinforcing bars

(Slavin 2015, Hoggsett 2017, ATC-115 2015, NIST GCR-14-917-30 2014, Sokoli 2014, Sokoli and Ghannoum, Slavin and Ghannoum 2015, Ghannoum and Slavin 2016, Zhao and Ghannoum 2016, Sokoli et al. 2017, To and Moehle 2017, Huq et al. 2017, Puranam et al. 2017).

Salient test results are presented and compared with results of various analysis methods commonly used to estimate stiffness, strength, and deformation capacity of reinforced concrete columns.

2.2 RESEARCH SIGNIFICANCE

The ACI 318 Building Code (2014) only allows the use of 60 ksi as specified reinforcement yield strength in moment, axial force, and shear strength calculations due to earthquake loads, with up to 100 ksi allowed in reinforcement used to confine concrete or provide lateral support for longitudinal reinforcement. The restrictions are mainly due to scarce test data on the effects of the varying mechanical properties of the newly developed grade 80 and 100 bars in special seismic systems. This laboratory test program provides data and recommendations to advance the use of higher-grade reinforcement in reinforced concrete buildings subjected to seismic demands.

2.3 LABORATORY TEST PROGRAM

Four concrete columns were designed, built, and tested as part of this experimental program. The column specimens were:

- CH100: reinforced with grade 100 longitudinal and transverse bars having a relatively high (H) tensile-to-yield (*T/Y*) strength ratio. The steel used in this column was produced using the micro-alloying process and possesses a distinct yield point.
- CL100: reinforced with grade 100 longitudinal bars having a relatively low (L) *T/Y* ratio. The yield strength of transverse bars was targeted to be at least 100 ksi in this column. However, it was measured to be lower than expected, at around 85 ksi. The steel used in this column was produced using the quenching and tempering process and possesses a distinct yield point.
- CM100: reinforced with grade 100 longitudinal and transverse bars satisfying the ASTM A1035 (2016). The steel used in this column was produced using the MMFX proprietary process (MMFX Technologies Corporation 2012) and does not possess a well-defined yield point.
- CH60: reinforced with grade 60 longitudinal and transverse bars satisfying the ASTM A706 standard and having a typical *T/Y* ratio for that grade.

2.3.1 Specimen Design and Detailing

The specimens were designed to impart large tensile-strain and low-cycle fatigue demands in the longitudinal bars. As such, the members did not provide a scenario where the use of HSRB aims to reduce congestion. To that effect, a relatively low compressive

axial load ratio of approximately 15% was applied to the columns. The axial load ratio is defined here as the applied axial load divided by the gross-section area and the measured concrete compressive strength. Relatively low shear stresses were also targeted, below $4\sqrt{f_c'}$, to minimize the beneficial effects of the tension-shift phenomenon on the spread of flexural plasticity (Park and Paulay 1975). By keeping the shear stresses at these levels, the spread of inelastic strains away from flexural cracks is more reliant on the post-yield hardening of the longitudinal reinforcement, thus producing higher strain concentrations in the longitudinal bars (Park and Paulay 1975).

All columns with grade 100 bars were nominally identical in design and reinforcement detailing. All columns had 8 #6 longitudinal bars (Figure 2-1**,** Figure 2-2), which generated similar moment capacities and associated shear demands in the columns with grade 100 bars, and a lower moment strength and associated shear demands in column CH60. The same bar size was maintained in all columns as previous research has shown that longitudinal bar diameter can directly influence strain concentrations in bars at cracks (ATC-115 2015, NIST GCR-14-917-30 2014, Sokoli 2014, Sokoli and Ghannoum 2016).

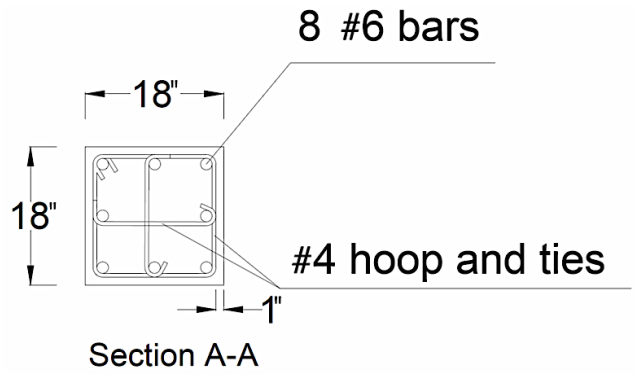

FIGURE 2-1: CROSS-SECTIONAL LAYOUT OF THE REINFORCEMENT IN TESTED SPECIMENS

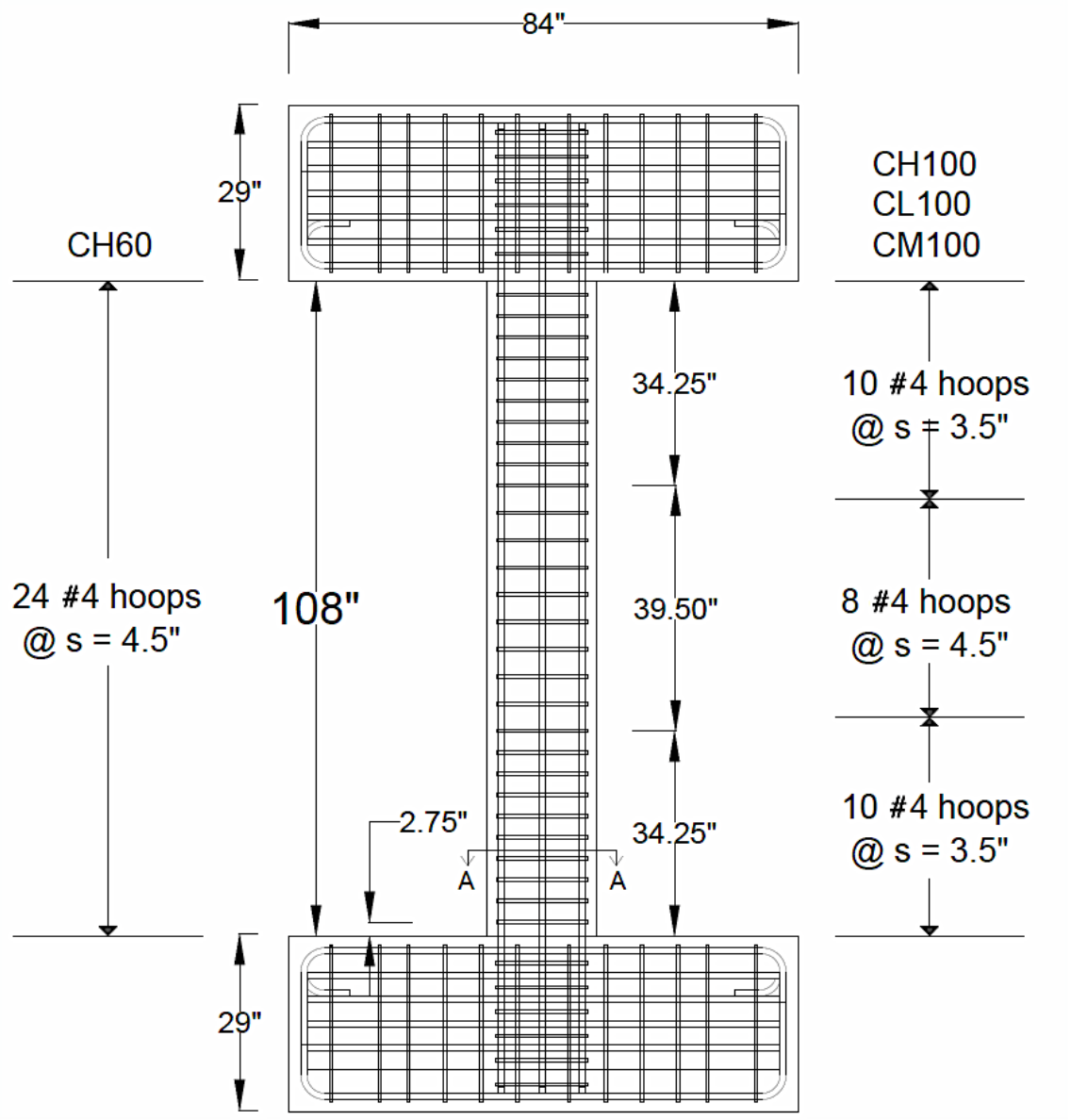

FIGURE 2-2: ELEVATION LAYOUT OF THE REINFORCEMENT IN TESTED SPECIMENS

Column specimens were 108 in. in length. The cross-sectional dimensions were 18x18 in. (Figure 2-1**,** Figure 2-2). Cross-sectional dimensions of the columns were assumed to be 2/3 scale models of prototype columns. As such, the selected clear cover was one inch. The shear span-to-depth ratio (*a/d* ratio) for this geometry was 3.4 for all columns (where a = shear span = half the clear length of the column and d = the effective depth of the section measured from the centroid of the outermost layer of steel to the compression face of the section). The transverse reinforcement at each level consisted of a single #4 seismic hoop and two #4 seismic cross-ties as defined in ACI 318-14. The cross-ties were bent to 90-degrees in one end and 135-degress in the other end. For specimens reinforced with grade 100 longitudinal bars, transverse reinforcement was spaced at 3.5 in. center-to-center, or $4.7d_b$ (with d_b being the diameter of the longitudinal bars). This spacing is lower than the maximum required by ACI 318-14 for Special Moment Frame columns ($6d_b$) and closer to the $5d_b$ spacing recommended in NIST GCR 13-917-30 (2014) when grade 80 and higher longitudinal bars are used. Transverse reinforcement in CH60 was spaced at 4.5 in. center-to-center, which corresponds to a spacing of $6d_b$, satisfying ACI 318-14 Special Moment Frame provisions. All bars met ACI 318-14 bend requirements. Columns did not contain any splices and satisfied all the seismic provisions for Special Moment Frames of ACI 318-14. All columns were designed assuming an expected concrete compressive strength of 5 ksi.

Each column was cast individually using modular steel forms and in three stages using the same concrete mix design. First the bottom footing was cast and the interface with the column was roughened. Then the column was cast and the interface with the top

footing was roughened. Finally, the top footing was cast. Pictures of specimen construction can be found in SECTION 6.3 OF APPENDIX A.

2.3.2 Material Properties

Concrete strength was measured just prior to column testing using three cylinders per ASTM C39 (2018). The three-cylinder average compressive strengths for the concrete in each column were 5.2 ksi for CH100 and CL100, 5.6 ksi for CM100, and 4.6 ksi for CH60. The average measured concrete compressive strengths at the day of testing for all columns were within 12% from the target strength of 5 ksi. Concrete mix design quantities together with measured concrete cylinders' compressive strength at 7, 14, 21, and 28 days are given in SECTION 6.4 OF APPENDIX A.

Sample reinforcing bars from the same heat as the steel used in the columns were tested in tension for both longitudinal and transverse reinforcement. Three samples per bar type were tested monotonically in tension to fracture per ASTM A370 (2017). Bar testing results are summarized in Table 2-1. Stress-strain curves and measured properties for all bars can be found in SECTION 6.5 OF APPENDIX A. The uniform elongations presented in Table 2-1 are defined as the strains corresponding to peak stress and were calculated in accordance with ASTM E8 (2016). The yield strength was calculated using the 0.2% offset method as detailed in ASTM E8. The elastic strain limit for the ASTM A1035 bars was also computed using the 0.2% offset method. For bars having a stress-strain curve that exhibits a distinct yield plateau, the elastic strain limit was taken as the strain at the end of the linear response.

Typical stress-strain curves from the #6 and #4 bars used in each column are plotted in Figure 2-3. The stress-strain curves of grade 100 bars produced using micro-alloying (CH100) and quenching and tempering (CL100) had a similar shape, exhibiting a well-defined yield plateau (Figure 2-3). The fracture elongation in longitudinal bars of column CH100 was 10.4% as opposed to 12.5% for the longitudinal bars of column CL100, whereas uniform elongations were 7.6% and 8.6%, respectively. Bars exhibiting the lower *T/Y* ratio had larger fracture and uniform strain values (Table 2-1). The steel bars used in column CM100 satisfied ASTM A1035 requirements and did not exhibit a distinct yield point. The uniform elongation for the #6 bars in CM100 was on average 35% lower than the uniform elongation of #6 bars in CH100 and 43% lower than for bars in CL100. The conventional grade 60 A706 longitudinal reinforcement in specimen CH60 had a higher *T/Y* ratio compared to grade 100 longitudinal reinforcement: 1.45 for bars in CH60 vs. 1.27, 1.16, for grade 100 bars in CH100, CL100, respectively (Table 2-1). Grade 60 bars had a higher ductility as well when compared to grade 100 bars. Steel bars used as transverse reinforcement were sourced from the same manufacturer as the longitudinal bars in each column.

TABLE 2-1: MECHANICAL PROPERTIES OF REINFORCING BARS USED IN TEST SPECIMENS*

Specimen	Bar Size	Reinforcing Steel Type	Yield Strength † (ksi)	Tensile Strength (ksi)	*T/Y* Ratio	Elastic Strain Limit (%)	Uniform Elongation (%)	Fracture Elongation (%)
CH100	#4	Grade 100 Micro-alloying	101.1	122.7	1.21	0.35	9.0	12.8
	#6		100.0	127.2	1.27	0.32	7.6	10.4
CL100	#4	Grade 100 Quenching and Tempering	84.6	99.6	1.18	0.32	8.0	11.5
	#6		106.4	123.4	1.16	0.45	8.6	12.5
CM100	#4	Grade 100 ASTM A1035	140.5	171.1	1.22!	0.60†	4.7	8.6
	#6		124.2	157.4	1.27!	0.63†	4.9	9.8
CH60	#4	Grade 60 ASTM A706	68.5	95.8	1.40	0.22	9.9	12.4
	#6		64.4	93.3	1.45	0.24	11.8	17.6

* *Average mechanical properties obtained from three tension tests per bar type*

† *Yield strength and elastic strain limit defined with 0.2% offset criterion*

! *T/Y ratio reported for ASTM A1035 bars may not be representative of bar inelastic hardening behavior as for bars with a distinct yield point.*

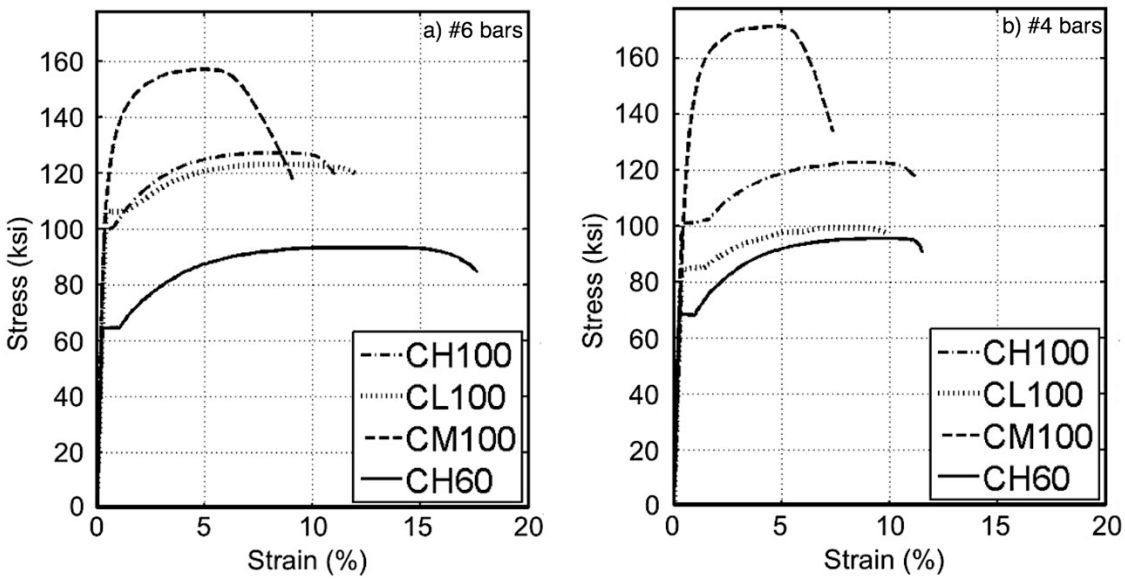

FIGURE 2-3: TYPICAL STRESS-STRAIN CURVES FOR THE A) #6 LONGITUDINAL BARS AND B) #4 TRANSVERSE BARS USED IN EACH COLUMN.

2.3.3 Test Setup and Instrumentation

Specimens were tested under symmetric double curvature with fixed rotation boundary conditions at the top and bottom. Pictures of the test setup can be found in SECTION 6.3 OF APPENDIX A. The I-shaped specimens (Figure 2-4) were connected to the strong floor and steel reaction frame using threaded rods. Two vertical actuators applied a constant compressive axial load that was adjusted for large deformation equilibrium during the tests. The resulting compressive axial load on columns, including the self-weight of the specimens and apparatus, was calculated using same day material testing of concrete in order to achieve the same axial load ratio of 15% for all specimens. The lateral loading protocol on all four columns consisted of two fully reversed lateral drift cycles in the north-south direction at increasing target drifts as per FEMA 461 (2007) recommendations. The

targeted lateral drift ratios (i.e., the ratios of lateral drifts to column clear height) were: 0.2%, 0.3%, 0.4%, 0.6%, 0.8%, 1.0%, 1.5%, 2.0%, 3.0%, 4.0%, 5.5%, and 7.0%. Tests were carried in displacement control under slow loading rates.

The test setup and specimens were instrumented to measure the applied loads, surface deformations, and strains in reinforcing bars. Strain gauges were installed on longitudinal bars over a length that encompasses the expected top and bottom plastic hinge regions. Additional information about instrumentation can be found in SECTION 6.6 OF APPENDIX A. Twelve strain gauges were affixed to longitudinal bars at the interfaces with the top and bottom footings, where bar strain demands were expected to be highest. A Digital Image Correlation (DIC) system developed by the authors (Sokoli et al. 2014 and Sokoli and Ghannoum 2016) was used to measure column surface deformations. The DIC system was able to resolve column deformations on the order of 1/10,000th of an inch over the field of view. Column deformations were obtained at targets placed in a regular 2.75 x 2.75 in. grid over the west surface of each column (Figure 2-4).

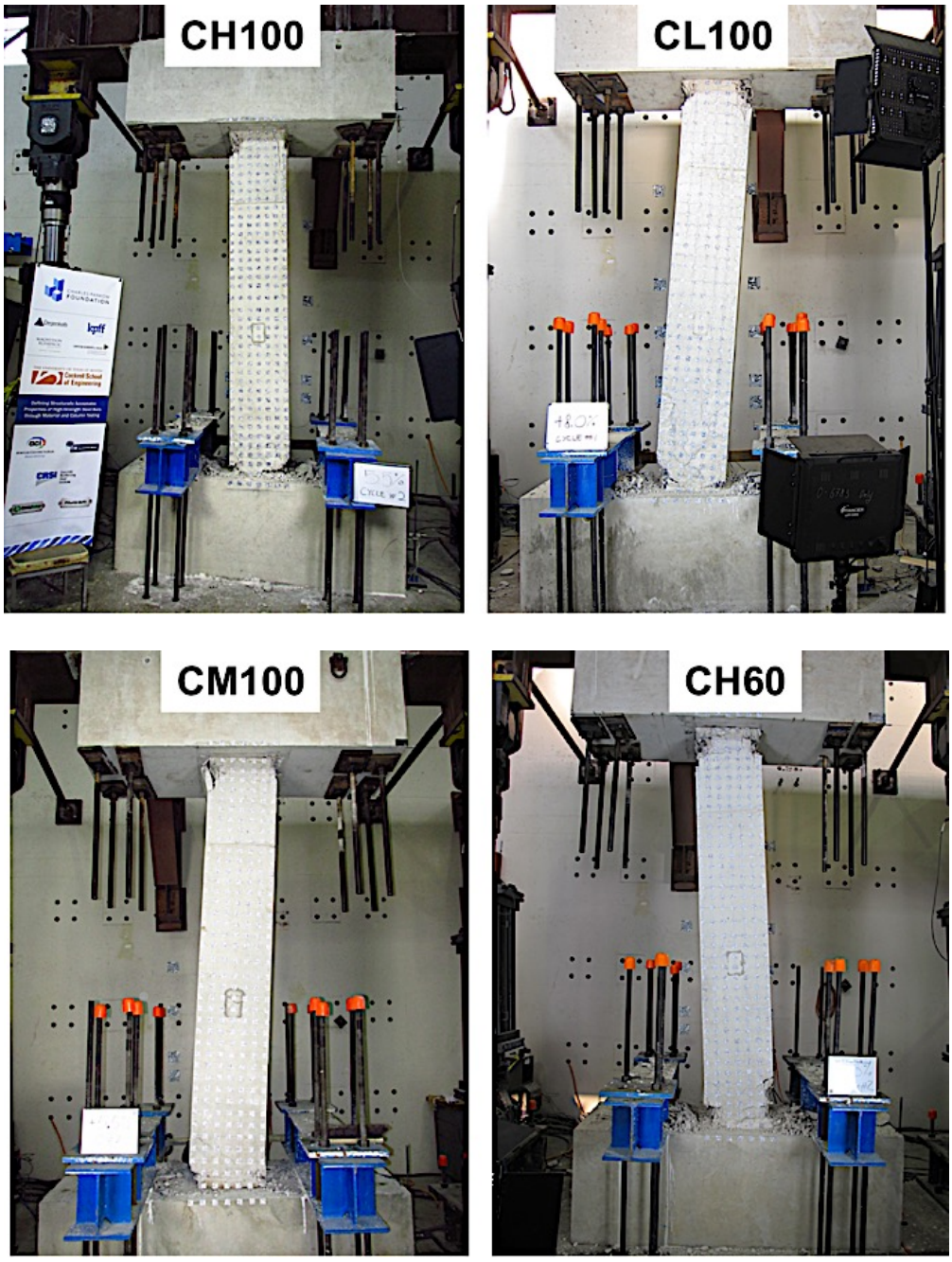

FIGURE 2-4: STATE OF DAMAGE FOR THE FOUR SPECIMENS AT THE LAST CYCLES OF LOADING

2.4 TEST RESULTS

Detailed results for each test can be found in Sokoli et al. (2017) and for completeness are included in Appendix B. A summary and discussion of the experimental data is presented in this section.

2.4.1 General Behavior

Behavioral and damage milestones for all columns are summarized in

Table 2-2 and identified on the column lateral load versus lateral drift-ratio plots in Figure 2-5. It is noted that a positive drift ratio indicates drifts to the south. The different mechanical properties of the reinforcement in each column lead to members reaching major milestones at different drift ratios. However, the overall behavior was similar between all four specimens. All specimens sustained flexural degradation characterized by concrete crushing, in some instances longitudinal bar buckling, and eventually longitudinal bar fracture. The uniform elongations of longitudinal bars, which varied from a minimum of 4.9% in CM100 to a maximum of 11.8% in CH60, did not have a determining role in the drift capacity of the tested columns. In all columns expect CM100, significant bar buckling of the longitudinal bars always preceded their fracture within the buckled region – between the first and second hoops (Figure 2-6). In CM100, longitudinal bars did not exhibit significant buckling and fractured at the column-footing interface.

TABLE 2-2: SUMMARY OF BEHAVIORAL MILESTONES FOR EACH SPECIMEN

	CH100		CL100		CM100		CH60	
	Drift Ratio (%)	Lateral Load (kips)	Drift Ratio (%)	Lateral Load (kips)	Drift Ratio (%)	Lateral Load (kips)	Drift Ratio (%)	Lateral Load (kips)
FFC†	+0.20	+40.2	+0.20	+38.2	0.20	+42.6	+0.20	+37.9
FIC	+0.61	+60.4	+0.61	+57.8	+0.60	+65.2	+0.61	+58.9
FLRY	+1.01	+69.2	+1.00	+78.4	+1.51	+87.5	+0.58	+56.3
CSC	+1.50	+72.8	+1.50	+79.4	+1.50	+87.5	+1.00	+63.7
PSF	-2.03	-81.9	-2.01	-80.8	-2.93	-97.5	+1.51	+64.0
LBB	+5.50	+64.3	+5.50	+64.0	-5.50	-80.6	-5.50	-46.3
FBF	-3.63	-55.6	+4.80	+58.6	+4.28	+74.1	+5.53	+40.0

† *Acronyms refer to the milestones in lateral response plots: FFC – First Flexural Crack; FLRY – First Longitudinal Reinforcement Yield; FIC – First Inclined Crack; CSC – Cover Splitting Crack; PSF – Peak Shear Force; LBB – Longitudinal Bar Buckling; FBF – First Bar Fracture*

All columns showed comparable drift capacities and completed at least one full cycle to a drift ratio of 5.5% prior to bar fracture or 20% loss of lateral strength. A stable response with limited lateral strength loss up to a drift ratio of 4% is generally considered to be an acceptable performance objective for collapse prevention at the Maximum Considered Earthquake (MCE) hazard level. The four tested columns satisfied that performance criteria and can be considered to have acceptable materials for designs in regions of high seismicity.

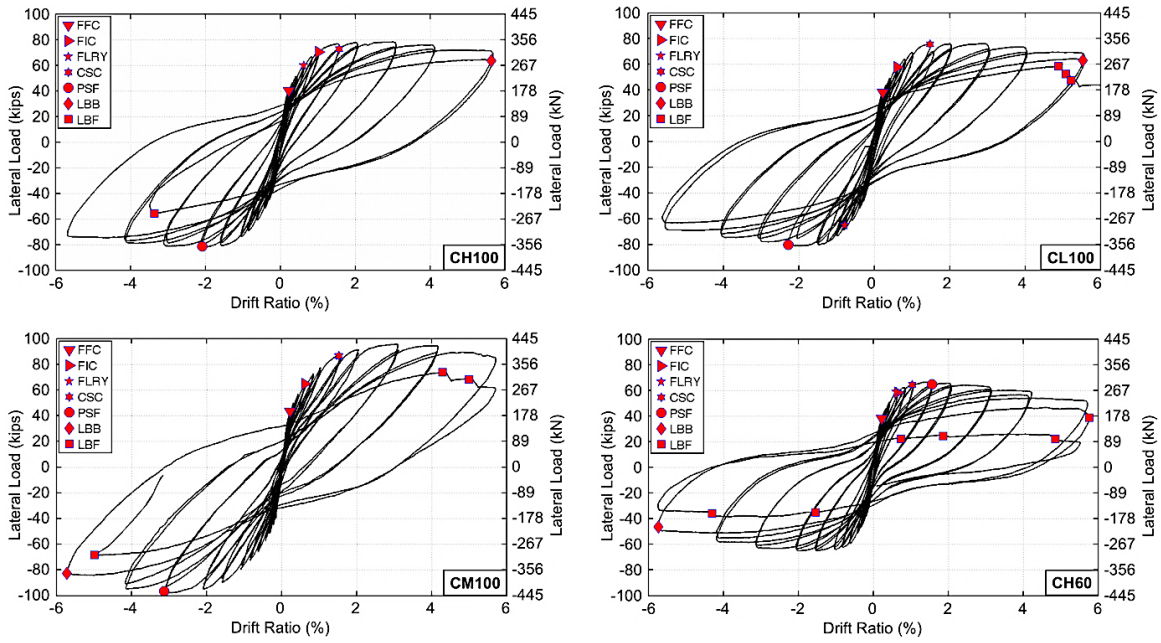

FIGURE 2-5: LATERAL RESPONSE WITH BEHAVIORAL MILESTONES OF THE FOUR TESTED SPECIMENS

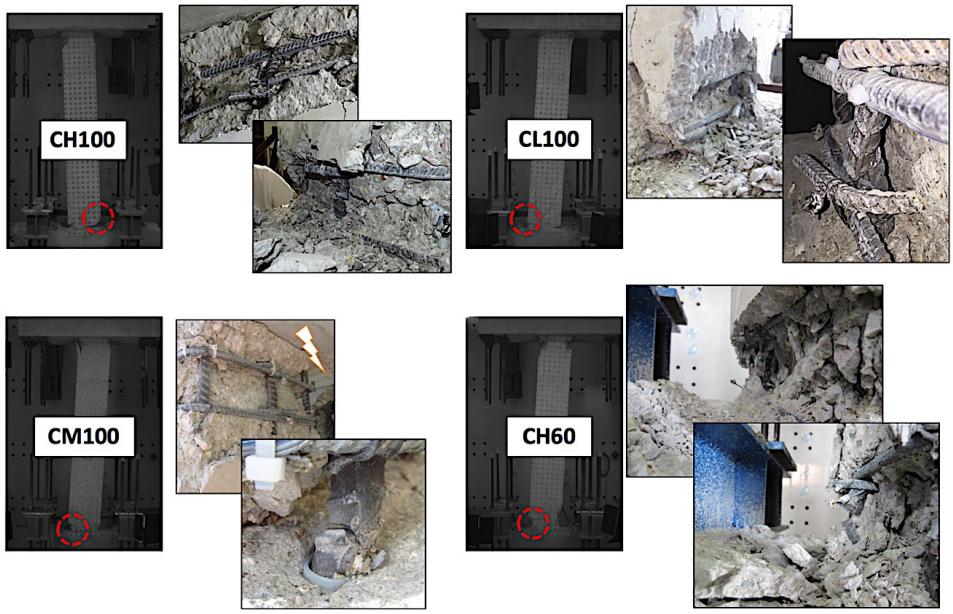

[£] *Pictures show buckled bars in the half-cycle before the one leading to the first bar fracture.*
[¢] *Picture showing the buckling extend of the longitudinal bars in CM100. Picture was taken after unloading and removing the concrete cover.*

FIGURE 2-6: PICTURES OF COLUMNS AT FIRST BAR FRACTURE (RED CIRCLE SHOWING LOCATION) AND RESPECTIVE FRACTURED BARS

Differences in the mechanical properties of the reinforcement in columns CH100 and CL100 did not dictate major differences between the overall lateral force versus lateral drift behaviors of the two specimens. These two columns were identical in design, with the only difference being the inelastic mechanical properties between the two types of grade 100 reinforcing bars used in each. Measured load versus drift ratio responses of columns CH100 and CL100 are overlaid in Figure 2-7, in which filled markers correspond to milestones in CH100 and hollow markers correspond to milestones in CL100. Both columns reached major milestones at similar drifts. All the milestones occurred at nearly identical drifts in the two columns, except those corresponding to first bar fracture and first longitudinal reinforcement yield; thus, markers overlap in Figure 2-7. Column CL100 reached similar drift targets as CH100 before any bar fracture.

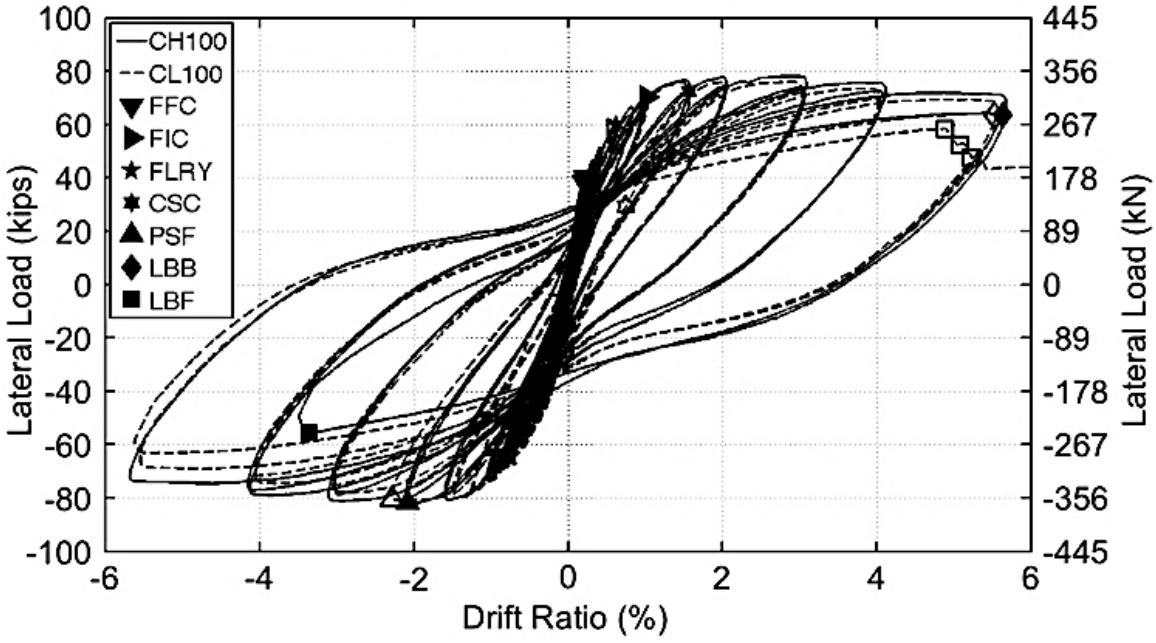

FIGURE 2-7: LATERAL RESPONSE OF CH100 AND CL100 WITH RESPECTIVE MILESTONES (FILLED MARKERS FOR CH100, HOLLOW MARKERS FOR CL100)

Crack pattern is an indicator of the spread of inelastic deformations in a concrete member. The crack patterns and the measured largest principal strains on the surface of each specimen at the first excursion to a drift ratio of +2% and +4% are presented in Figure 2-8. The three specimens reinforced with steel having a distinct yielding point, CH100, CL100, and CH60, showed a similar crack pattern. As targeted shear stresses were relatively low in all columns, specimens only exhibited minor inclined cracking. The higher tensile strength of the steel used in CM100 contributed to higher shear stresses in the section. For this reason, specimen CM100 exhibited inclined cracks that propagated further towards the centerline of the column than in other columns (Figure 2-8). The lower strength of the grade 60 #6 bars compared to the #6 grade 100 bars, led to a lower lateral strength and lower applied shear stress for CH60 than for columns reinforced with grade 100 bars. The same trends were observed in the measured deformation components (Figure 2-9), which are discussed in more details in the following section. In all columns, transverse reinforcement yielded in the plastic hinge regions as lateral drifts increased.

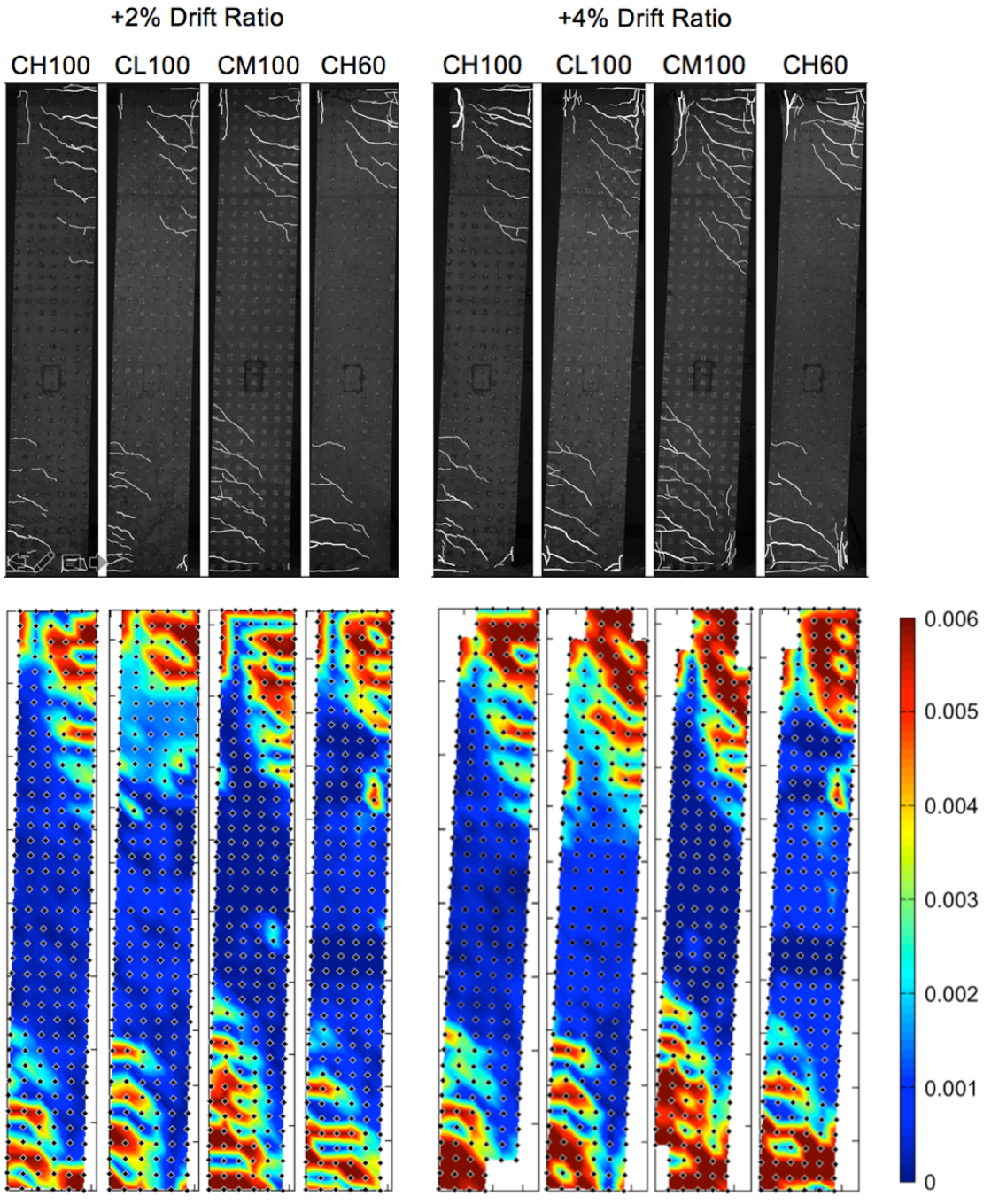

FIGURE 2-8: CRACK PATTERN (UP) AND LARGEST PRINCIPAL STRAINS (DOWN) FOR EACH SPECIMEN AT THE FIRST EXCURSION TO +2% AND +4% DRIFT RATIOS

Discussion on Bar Buckling and Fracture

Buckling and fracture are important milestones in the loading history of seismic concrete columns as each of them may lead to lateral strength loss. Column CH60 reinforced with the conventional grade 60 bars and having hoops and cross-ties spaced at 6.0 longitudinal bar diameters ($6.0d_b$) sustained the most pronounced bar buckling of all columns (Figure 2-6), which initiated earlier in the loading protocol (starting during the first cycle to a drift ratio of +5.5%). Columns with grade 100 bars had hoops and cross-ties spaced at $4.7d_b$, which appears to have restrained the longitudinal reinforcement and confined the core concrete better than observed in CH60. In columns CH100, CL100, and CH60 the first bar fracture occurred in a middle bar, within the buckled region of the bars between the first and second hoops (Figure 2-6). The 90-degree cross-ties appeared to open up at these locations, allowing for larger buckling amplitudes.

Longitudinal bars buckled at about the same drift demands in columns CH100, CL100, and CH60. Therefore, the adjusted hoop spacing in the columns with grade 100 bars offset the detrimental effects of the higher bar strength and associated higher buckling propensity. Based on this observation, using a larger hoop spacing for grade 100 bars up to those currently permitted in ACI 318-14 for grade 60 bars (i.e., $6.0d_b$) is not advised, as that could produce lower drift capacities for columns reinforced with grade 100 bars than for those reinforced with grade 60 bars.

The longitudinal-bar behavior was different in column CM100 which was reinforced with bars satisfying ASTM A1035 standard compared to other columns.

Longitudinal bars in CM100 exhibited only minor bar buckling and fractured due to low-cycle fatigue at the column-footing interface starting in a corner bar (Figure 2-6). The absence of a yield plateau combined with the high tangent modulus during strain hardening in ASTM A1035 bars may have limited the opening of the cross-tie bends. Moreover, the absence of a defined yielding point combined with the higher tangent axial stiffness in the inelastic strain range of longitudinal bars may have enhanced their buckling strength compared with that of bars exhibiting a yield plateau.

2.4.2 Lateral Drift Components

Column lateral drift measured at the interface with the top footing was deconstructed into three components: flexural, bar-slip, and shear. The deconstruction was achieved using surface deformation data recorded by the Digital Image Correlation system developed by the authors (Sokoli et al. 2014, Sokoli and Ghannoum 2016, Sokoli et. al 2017), and are explained in more detail in SECTION 8.1.2 of APPENDIX B. The drift components at the end of the first excursion to a new drift level are shown in Figure 2-9 as a fraction of the total lateral displacement for each specimen. Similar trends were observed in all four specimens. Flexural deformations contributed between 50% and 70% of the lateral drift throughout each test. At higher lateral deformation demands the relative weight of flexural deformations lowered as the bar-slip component increased from about 30% of the total drift at low drift levels, to about 40% in the post-yield drifts. Shear deformations were relatively low in all specimens, not exceeding 5% of total lateral drift for CH100 and CL100, 4% for CH60, and 7% for CM100. The shear deformations were higher for

specimen CM100, as compared to other specimens reinforced with grade 100 due to the higher shear stresses developed in CM100. Results for deformation components were not reliable after cycles to a drift ratio of 4.0%.

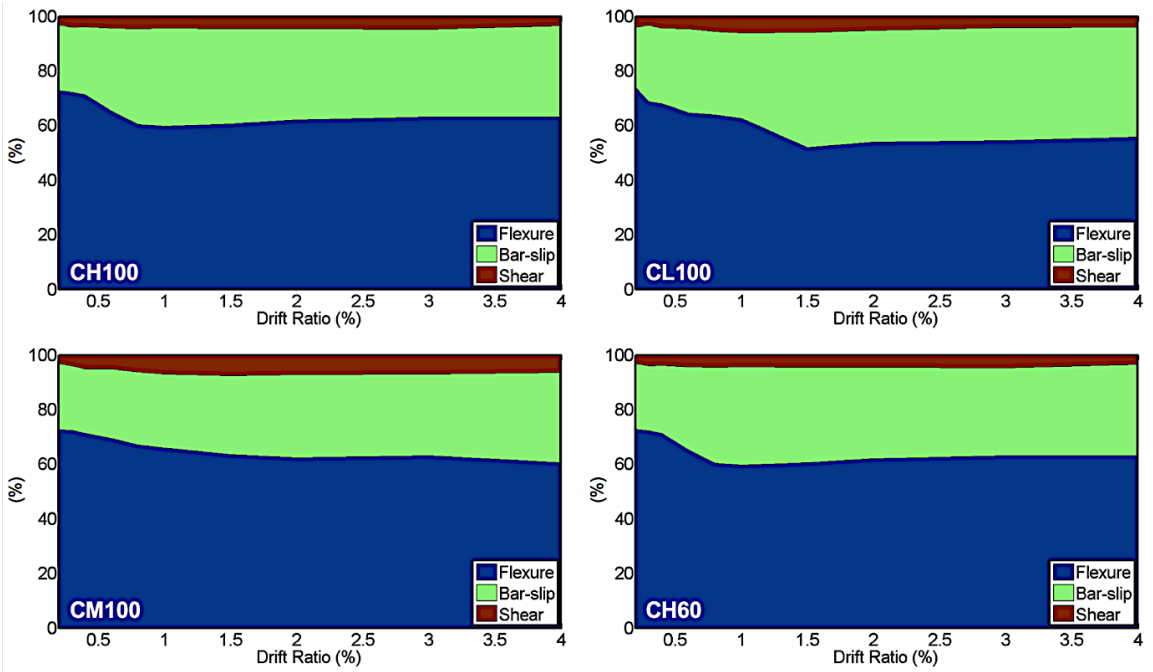

FIGURE 2-9: DEFORMATION COMPONENTS FOR EACH SPECIMEN AT TARGET DRIFT RATIO AS PERCENTAGE OF TOTAL LATERAL DISPLACEMENTS

2.4.3 Dissipated Energy

The cumulative dissipated energy of each member up to a drift ratio of 4.0% is plotted in Figure 2-10. Cumulative energy was evaluated as the cumulative area under the average top and bottom moment versus drift ratio curves. The first and second cycles to the same drift target are treated separately in the figure. The amount of total energy dissipated in the first cycles to the drift targets was similar for CH60, CH100, and CL100, even though there were differences in the moment strengths of the columns. The

cumulative dissipated energy in the second cycles pronounced those differences, with CM100 dissipating 35% less energy during the second cycle to the 4.0% drift target as compared to CH100. When normalized by the nominal moment strength of each member (M_{nm} or M_{ns}, see the Notation section for definitions), CH60 had a larger normalized energy dissipation capacity given a design strength than CH100, CL100 and especially CM100. The lower amount of dissipated energy in CM100 can partly be attributed to the higher peak strength it exhibited given the same elastic stiffness as the other columns, and partly due to a less steep unloading lateral stiffness. Bars with a higher *T/Y* ratio and a distinct yield point resulted in larger energy dissipation.

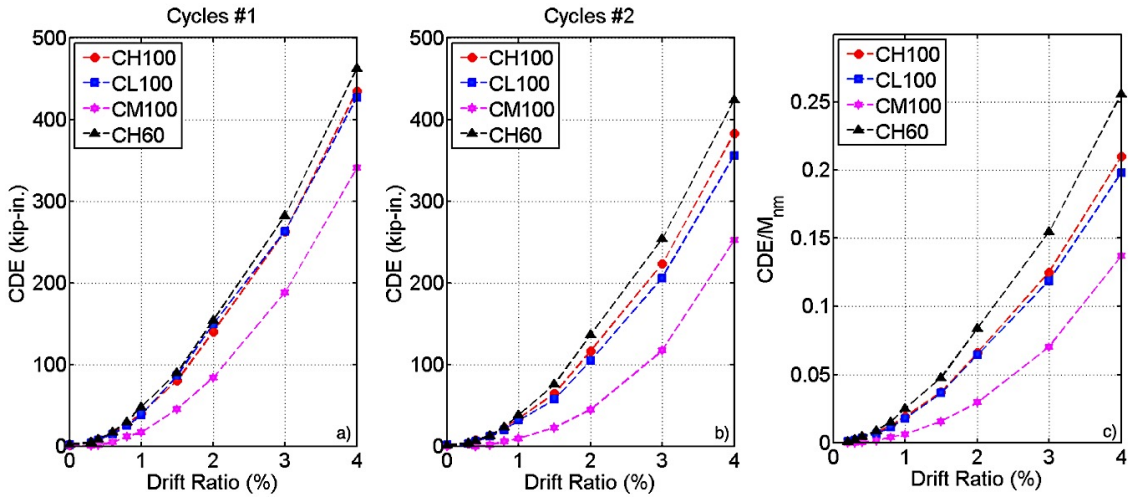

FIGURE 2-10: A) CUMULATIVE DISSIPATED ENERGY (CDE) IN THE FIRST CYCLES TO EACH DRIFT TARGET; B) CDE IN THE SECOND CYCLES TO EACH DRIFT TARGET; C) TOTAL CDE NORMALIZED TO M_{NM}

2.4.4 Strain Demands

In seismically detailed concrete columns, loss of lateral strength can be expected from crushing of the concrete in the core and buckling or fracture of the longitudinal bars. When relatively high levels of confinement are provided, as was the case for the four columns in this study, the deformation capacity associated with loss of lateral strength is often determined by the behavior of the longitudinal bars. In turn, the behavior of the longitudinal bars is governed by their mechanical properties, lateral restraint, and strain demands.

The average measured strains in longitudinal bars of all columns are presented in Figure 2-11. These strains were measured at the top and bottom column interfaces with the adjacent footings. Strain measurements are reported at the peak of each drift excursion up to a drift ratio of 5.5%. After a drift ratio of 4% many strain gages were lost, however available data provided reasonable strain demand values at a drift ratio of 5.5%. As can be seen in Figure 2-11, prior to first yield, peak tension strain demands in longitudinal bars were similar for all columns. Columns CH100, CL100 and CH60 experienced jumps in the tension strain demands of longitudinal bars just after yielding (Figure 2-11). Possibly the increase in strain without an increase in bar strength in the yield plateau phase concentrated strains at the critical crack. The length of the yield plateau accounted for most of the difference in strain demands that bars in columns CH100, CL100 and CH60 experienced just after first yield or at a drift ratios below 2%. Strains were redistributed away from the critical crack and the rate of increase in strain demands with increasing drift reduced, once

bars were pushed to strains in the strain hardening region. No strain jumps were observed in the longitudinal bars of CM100, which did not exhibit a yield plateau. Strain demands in the longitudinal bars of CM100 therefore were lower than those of bars in other columns at moderate drift ratio ranges (1.5% to 3%).

Bar properties such as the existence of a yield plateau, the length of the yield plateau, the tangent modulus during strain hardening, and the *T/Y* ratio were observed to influence strain concentrations at cracks (Figure 2-11). Peak inelastic strain demands in bars of CH60, which had the highest *T/Y* ratio, were observed to increase less rapidly with increasing drifts than those of columns CH100 and CL100, which had lower *T/Y* ratios.

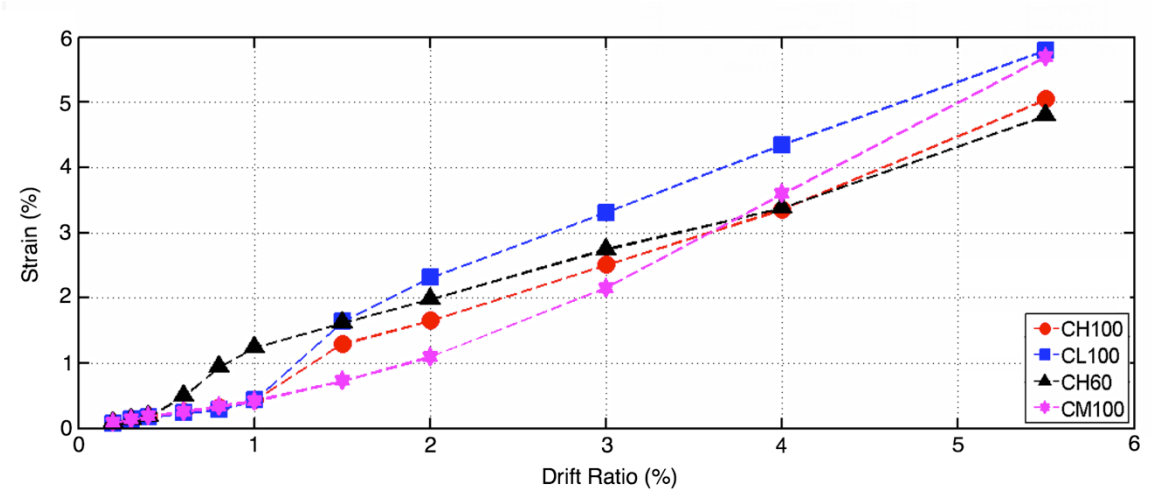

FIGURE 2-11: AVERAGE STRAIN DEMANDS AS MEASURED AT THE COLUMN ENDS

2.4.5 Plasticity Spread

The distance from column end over which inelastic tensile strains spread in the longitudinal bars of the specimens is plotted in Figure 2-12. The height up to which inelastic strains spread in individual longitudinal bars is shown with un-filled markers. The distance up to which inelastic strains spread in a certain bar was calculated by linear interpolation between the farthest strain gauge from column end recording a strain larger than the measured yield strain and the adjacent gauge with a strain recording that remained in the elastic range. The solid lines with filled markers in Figure 2-12 represent the average distance inelastic strains spread from either column end, for all longitudinal bars in a given column with reliable strain gauge readings. In Figure 2-12a the strain at the end of linear response for the longitudinal bars in CM100 was taken from the 0.2% offset method (0.0063, Table 2-1), whereas in Figure 2-12b the strain at the end of linear response was taken as 0.0034, which is the strain corresponding to a stress of 100 ksi in the bar.

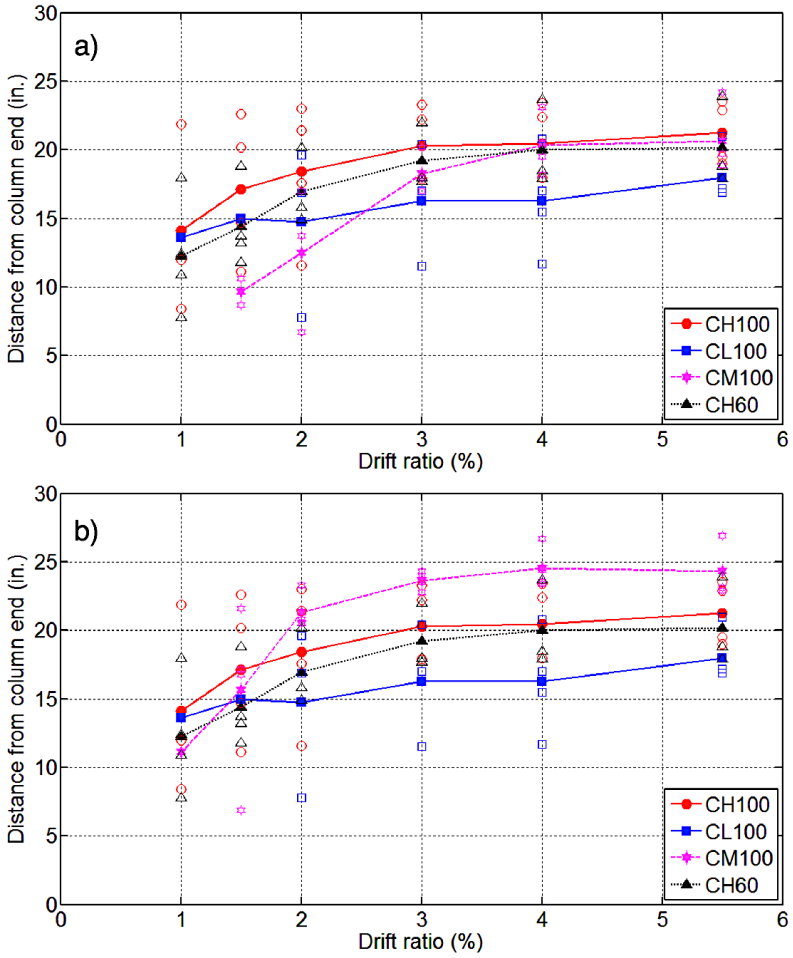

FIGURE 2-12: SPREAD OF INELASTIC STRAINS ON THE LONGITUDINAL BARS FOR EACH SPECIMEN: A) STRAIN AT THE END OF LINEAR RESPONSE IN CM100 CALCULATED USING THE 0.2% OFFSET RULE; B) STRAIN AT THE END OF LINEAR RESPONSE IN CM100 TAKEN AS THE STRAIN AT 100 KSI

Spread of strain demands over a higher length is beneficial to reduce strain concentrations and enhance member deformation capacity. Columns CH100 and CL100 had the same design and were both reinforced with grade 100 bars with similar stress-strain shapes, but with differing tangent modulus during strain hardening and tensile-to-yield strength (*T/Y*) ratios. Thus, the influence of inelastic properties of longitudinal bars on plasticity spread can be determined by comparing the results from these two column tests.

However, given the small difference in *T/Y* ratio (i.e. 1.27 for CH100 vs. 1.16 in CL100) between these two columns, the difference in the spread of inelastic strains away from the section of peak moment demand were relatively small. The column with grade 100 bars with the higher *T/Y* ratio resulted in slightly greater spread of inelastic deformations and strains away from the section of peak moment demand as compared to the column reinforced with grade 100 bars with a lower *T/Y* ratio, 21.2 in. vs 20.2 in., respectively. Column CH60, which had bars with a well-defined yield point but a higher *T/Y* ratio than the grade 100 bars, experienced similar spreads of inelastic bar strains as bars in CH100, 20.2 in. The lower shear stresses in CH60 compared to the columns with grade 100 bars may have limited the beneficial effects of the tension shift phenomenon on plasticity spread in this member.

By the end of testing, inelastic strains in the longitudinal bars of all members were recorded up to similar distances away from the section of peak moment. These distances were at least equal to the section height of the cross-section. CH100 had spread of inelastic strains on average up to 21.2 inches or 1.18 times the section height (h= 18 in.) from the section of peak moment. Inelastic strains spread up to similar average distance of 1.12h for all longitudinal bars of CH60, or up to 20.2 inches. In CL100, inelastic strains were limited to a height of 18 inches on average, or h. The rate of increase in the length over which inelastic strains were measured slowed at lower drifts for members with a lower *T/Y* ratio, i.e., CH100 and CL100. The spread in plasticity was more gradual with respect to drift demand in members with higher *T/Y* ratios, as observed in members CM100 and CH60.

The lack of a well-defined yielding point and a relatively steep inelastic hardening tangent modulus of bars produced a different strain distribution behavior for CM100 than in other columns. The measured strains in the longitudinal bars indicated that the inelastic demands spread over a significantly larger distance from column ends in CM100 than in other columns. The length over which inelastic bar strains (i.e. strains higher than strain corresponding to a stress in the bar of 100 ksi) were recorded to reach on average 24.3 in. or 1.33h in CM100, with one longitudinal bar spreading its inelastic strain up to 27 inches or 1.5h from column end.

Observing the flexural cracking patterns lead to similar conclusion regarding the plasticity spread and strain demands on longitudinal bars (Figure 2-8). Column CM100, in which plasticity spread farthest and peak strain demands were lowest on the longitudinal bars, had a larger number of narrower flexural cracks that spread farther away from the regions of peak moment. Column CH60 exhibited wider critical cracks at moderate drift levels than other columns. This corroborates the findings of higher strain demands in the longitudinal bars of CH60 at moderate drift levels (1.5% to 3.0%) compared with other columns.

The observed length over which inelastic bar demands were recorded in CH60, CH100, and particularly CM100 exceeded the length prescribed in ACI 318-14 (l_0 = 18 in.) over which larger amounts of transverse reinforcement is required at column ends to satisfy Special Moment Frame requirements (1.12l_0 for CH60, 1.18l_0 for CH100, and 1.33l_0 for CM100).

2.5 COMPARISON WITH ANALYTICAL MODELS

2.5.1 Moment Strength

ACI 318-14 allows the use of a bilinear elastic-plastic behavior for reinforcement when estimating flexural strength of a concrete section. A maximum usable concrete compressive strain of 0.003 is allowed in ACI 318-14, while the specified yield strength of the longitudinal bars (f_{ys}) is used to obtain the nominal moment strength (M_{ns}) and $1.25f_{ys}$ when calculating the probable moment strength (M_{prs}). Measured concrete compressive strength at the day of column testing was used in calculations. Yield strain was taken at f_{ys}/29,000 (in ksi units). The moment strength of each member calculated using the above assumptions are presented in Table 2-3. Additionally, the nominal (M_{nm}) and probable (M_{prm}) moment strengths were estimated using the same assumptions as M_{ns} and M_{prm} but with measured yield and tensile strength values of bars, respectively, and are also presented in Table 2-3. All computed values account for a concentric axial load of 15% of the gross sectional capacity. The experimentally obtained moment at first longitudinal bar yield (M_{ye}) and the peak moment recorded experimentally (M_{ue}) and the drift ratios at which they occur are also presented in Table 2-3.

TABLE 2-3: EXPERIMENTAL AND CALCULATED MOMENT STRENGTHS OF COLUMNS

Specimen	M_{ns}[§]	M_{nm}	M_{prs}	M_{prm}	M_{ye}	M_{ue}	M_{ye}/M_{nm}	M_{ue}/M_{prs}	Δ_{ye}	Δ_{ue}
	kip-in								(%)	(%)
CH100	3810	3890	4160	4270	4230	4800	1.09	1.15	1.0	2.0
CL100	3810	3950	4160	4200	3950	4570	1.00	1.10	1.0	1.5
CM100	3810	4330	4160	4840	4720	5760	1.09	1.39	1.5	3.0
CH60	3200	3150	3460	3560	3260	4080	1.03	1.18	0.6	1.5

[§] *M_{ns} – nominal moment capacity of the section calculated per ACI 318-14 procedures and specified steel yield strength; M_{nm} – nominal moment capacity of the section calculated per ACI 318-14 procedures and measured steel yield strength; M_{prs} – probable moment calculated per ACI 318-14 procedures and 1.25 times the specified steel yield strength; M_{prm} – moment capacity calculated per ACI 318-14 procedures and measured steel tensile strength; M_{ye} – moment corresponding to experimental first yield; M_{ue} – peak recorded moment during experiments; Δ_{ye} – drift ratio at first recorded bar yield; Δ_{ue} – drift ratio at peak recorded moment during experiments.*

The nominal moment strengths calculated using measured material properties were within 10% of the yield strengths recorded experimentally for all four members. However, when using specified material properties, the nominal moment strength of CM100 was underestimated by 24% due to the measured yield strength of the CM100 bars being 124.2 ksi or 24% larger than the specified 100 ksi value. The nominal moment strength based on specified material properties (M_{ns}) of CH60 was evaluated to be 3200 kip-in. (362 kN-m), while for the columns reinforced with grade 100 reinforcement that strength was 19% larger at 3810 kip-in. However, the measured moment at first yield of CH100 and CL100

were about 30% larger than that of column CH60, while the experimental peak moments of CH100 and CL100 were about 18% larger than that of column CH60.

The probable moment strengths, M_{prs}, of columns CH60, CH100, and CL100 were respectively 15%, 13%, and 9% lower than their measured peak moment strengths. Due to the hardening behavior of the ASTM A1035 bars in CM100, its probable moment strength, M_{prs}, was underestimated by 28% when using the specified yield strength of 100 ksi ($1.25f_{ys}$ = 125 ksi) in calculations. Results therefore indicate that a factor higher than 1.25 may be warranted when estimating the probable moment strength of columns, especially those reinforced with A1035 longitudinal bars.

2.5.2 Shear Demands

Shear strengths calculated using ACI 318-14 are compared to column measured peak shear demands (V_{ue}) in Table 2-4. The contributions of both concrete and steel to shear strength were included because column axial load exceeded $0.05A_g f'_c$ (clause 18.7.6.2 in ACI 318-14). The concrete contribution was calculated using the simplified equation for the concrete contribution of nonprestressed members with axial compression (V_c from section 22.5.6.1 in ACI 318-14), and the detailed procedure ($V_{c\text{-}det}$ from Table 22.5.6.1 in ACI 318-14). The transverse reinforcement contribution to the shear strength was calculated using section 22.5.10.5.3 of ACI 318-14. All values were computed using measured material properties and measured applied forces (i.e. M_u, N_u, and V_u). No strength reduction factors were included in the calculations. As can be seen in Table 2-4, the columns were subjected to low shear demands as compared with their estimated shear strengths.

TABLE 2-4: EXPERIMENTAL PEAK SHEAR DEMANDS AND CALCULATED SHEAR STRENGTHS OF COLUMNS

Specimen	V_c[¿]	$V_{c\text{-}det}$	V_s	V_n	$V_{n\text{-}det}$	V_{ue}	V_c / V_{ue}	$V_{c\text{-}det} / V_{ue}$
	kip							
CH100	58	44	280	338	324	82	0.71	0.54
CL100	58	44	234	292	278	81	0.72	0.54
CM100	62	45	388	450	433	98	0.63	0.46
CH60	53	41	147	200	188	64	0.83	0.64

[¿] *V_c – concrete shear contribution calculated using equation 22.5.6.1 in ACI 318-14; $V_{c\text{-}det}$ – concrete shear contribution calculated using Table 22.5.6.1 of ACI 318-14; V_s – transverse reinforcement contribution to the shear strength as calculated by equation 22.5.10.5.3 of ACI 318-14; $V_n = V_c + V_s$; $V_{n\text{-}det} = V_{c\text{-}det} + V_s$; V_{ue} – measured peak applied shear force*

2.5.3 Effective Stiffness

The secant lateral stiffnesses to first yield extracted from experimental results are compared to the values suggested in ASCE/SEI 41 (2017) and ACI 318-14 in Table 2-5. Assuming the columns were restrained against rotation at both ends and had a linear variation of curvature over their height prior to yield, the measured effective lateral stiffness ($EI_{eff\text{-}exp}$) of each specimen was calculated as:

EQUATION 2-1: EFFECTIVE LATERAL STIFFNESS

$$EI_{eff-exp} = \frac{F_y L^3}{12\Delta_y}$$

where F_y is the applied shear at first yield; L is the span length of the members; Δ_y is the displacement at first yield. The values of F_y and Δ_y can be found in

Table 2-2.

Column effective stiffnesses from Equation 2-1 were normalized to the gross section stiffnesses (E_cI_g) in Table 2-5. To obtain values in Table 2-5, E_c was taken as $57000\sqrt{f_c'}$ (in psi units). Experimental values of the effective stiffness were closer to the prediction from ASCE/SEI 41-17 than ACI 318-14, especially for CH60 for which the experimental effective lateral stiffness was estimated at $0.28E_cI_g$ (compared with $0.35E_cI_g$ obtained from ASCE/SEI 41-17). This was expected considering that the ASCE/SEI 41-17 lateral stiffness recommendations were calibrated to experimental data from members reinforced mainly with grade 60 steel (Elwood and Eberhard 2009). The experimental

effective stiffnesses of CH100 and CL100 were about 30% lower than that of CH60 and around $0.20E_cI_g$. Due to the higher assumed strain at yield for CM100, its experimental effective stiffness was even lower at $0.15E_cI_g$. The effective stiffness from ACI 318-14 overestimated the experimental values by a factor exceeding 2 for all columns.

TABLE 2-5: EXPERIMENTAL AND STANDARD EFFECTIVE LATERAL STIFFNESSES

Specimen	$EI_{eff\text{-}exp}/E_cI_g$	ASCE/SEI 41 (EI_{eff}/E_cI_g)	ACI 318-14 (EI_{eff}/E_cI_g)
CH100	0.19	0.35	0.7
CL100	0.21		
CM100	0.15		
CH60	0.28		

2.5.4 ASCE/SEI 41 Drift Capacity

The total drift capacity at 20% loss of lateral strength was estimated for the four columns using the 2013 and 2017 versions of ASCE/SEI 41 Seismic Evaluation and Retrofit of Existing Buildings (2013, 2017). In calculating the total drift capacity, the elastic portion of the drift was obtained assuming a lateral stiffness of $0.35E_cI_g$ per both versions of ASCE/SEI 41, while the end of the elastic range was taken at the nominal flexural strength calculated using the measured material properties (M_{nm}), in lieu of expected properties as defined in ASCE/SEI 41. Strength at drift capacity was taken as M_{prm}.

The lateral load versus drift plots as estimated from ASCE/SEI 41 are overlaid on the measured experimental response envelopes in Figure 2-13. The procedures in ASCE/SEI 41 were able to capture reasonably well the overall behavior of the members. The standard procedures underestimated column drift capacities, predicting loss of lateral strength at a drift ratio of about 4% in all columns. However, all four tested columns were able to complete at least one cycle to 5.5% drift ratio prior to losing more than 20% lateral strength.

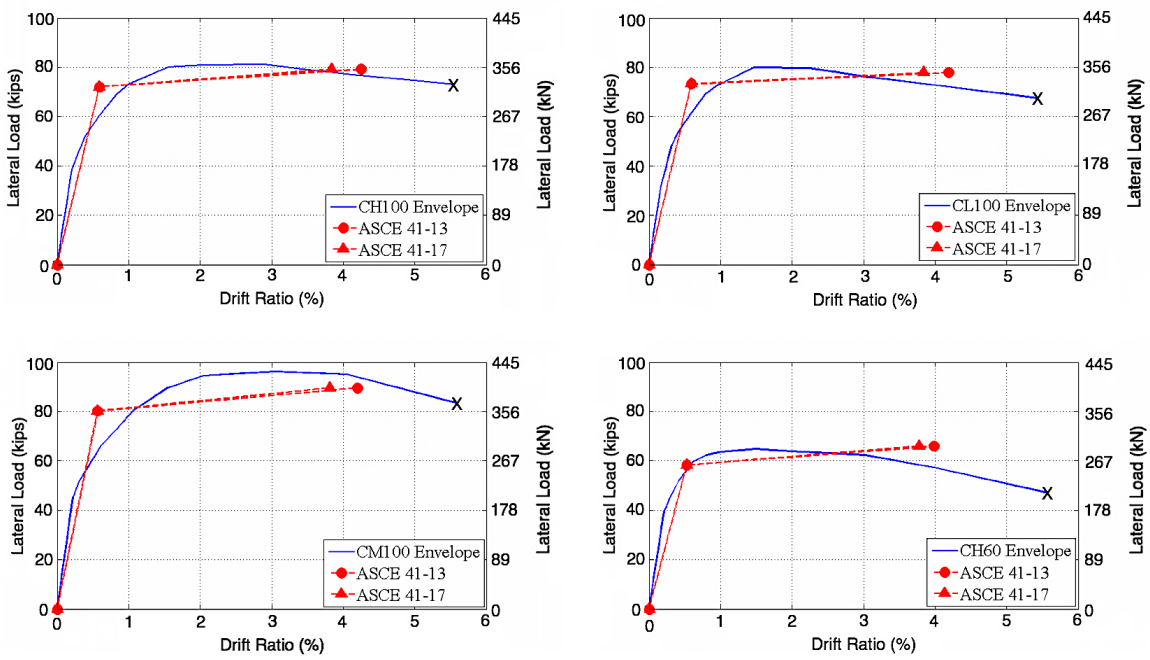

FIGURE 2-13: DISPLACEMENT CAPACITY ENVELOPE AS PREDICTED FROM ASCE/SEI 41-13 AND ASCE/SEI 41-17 VS. RESPONSE ENVELOPES OF TESTED COLUMNS (X – DRIFT AT WHICH 20% LATERAL STRENGTH WAS LOST)

2.6 CONCLUSIONS

A targeted structural testing program was carried out to identify any major issues in the performance of newly developed high strength reinforcing bars (HSRB) in concrete members, as well as provide necessary data to set material specifications for HSRB. The experiments conducted in this study were designed to push the new HSRB to large strain demands in concrete columns. Of particular interest was quantifying the effects of the shape of the stress-strain curve and the tensile-to-yield (*T/Y*) strength ratio of high-strength longitudinal bars on the behavior of concrete columns and the strain demands in the longitudinal bars.

Three columns were designed and built with grade 100 reinforcing bars produced using different production techniques. CH100 was reinforced with grade 100 bars having a relatively high *T/Y* strength ratio, CL100 was reinforced with grade 100 bars have a relatively low *T/Y* strengthratio, and CM100 was reinforced with ASTM A1035 bars. A fourth specimen CH60 was designed and built using grade 60 ASTM A706 bars. All four columns were tested cyclically under a constant axial load of about 15% of the gross axial capacity. Concrete strength was around 5 ksi for all columns.

The key findings are:

- All specimens exhibited flexural degradation characterized by longitudinal bar yielding, concrete crushing, varying degrees of longitudinal bar buckling, and eventually longitudinal bar fracture. Comparable drift capacities were observed between the four specimens. The four tested columns completed at least one full

cycle to a drift ratio of 5.5% prior to bar fracture and 20% loss in lateral strength. The four columns tested can therefore be considered to have acceptable materials for designs in regions of high seismicity.

- The uniform and fracture elongations of longitudinal bars did not have a determining role in the drift capacity of the four tested columns. Bar fractures were consequential to buckling and the low cycle fatigue life of the bars.
- The adjusted hoop spacing of 4.7 longitudinal bar diameters ($4.7d_b$) in the columns with grade 100 bars offset the detrimental effects of the higher bar strength and their buckling propensity, such that columns with the higher-grade bars exhibited a similar drift capacity to the column with grade 60 bars which had hoops spaced at $6.0d_b$. Using a larger hoop spacing for grade 100 bars, up to those currently permitted in ACI 318-14 for grade 60 bars (i.e., $6.0d_b$), is therefore not advised as that could produce lower drift capacities for columns reinforced with grade 100 bars than for those reinforced with grade 60 bars.
- First bar fracture in longitudinal bars of columns CH100, CL100, and CH60 occurred within the buckled length between the first and second hoop from member end in a middle bar. These bars were supported by 90-degree cross-ties which eventually opened up, increasing the unsupported length of the bar leading to more pronounced buckling and earlier fracture as compared to the corner bars of the same columns. Therefore, it may be prudent to explore means to mitigate the 90-degree

cross-ties and tie every bar in SMF columns in order to achieve higher lateral deformation capacities.

- Strain concentrations in longitudinal bars at flexural cracks were influenced by the shape of the stress-strain curve of the longitudinal bars. Generally, longitudinal-bar strain demands increased more rapidly with increasing lateral drifts in columns reinforced with bars having a lower *T/Y* strength ratio. Strains in the ASTM A1035 longitudinal bars were lower over most of the drift range than in bars of all other columns. This is possibly due to the relatively large tangent modulus of the A1035 bars in the inelastic range compared to other bars, which may have allowed strains in the A1035 bars to spread away from critical cracks more effectively.
- Inelastic strains in the longitudinal bars of all members were recorded up to similar distances away from the section of peak moment. These distances were at least equal to the section height of the cross-section. These plastic hinge lengths were on the order of 1.0 of the section height (h) for CL100, 1.18h for CH100, and 1.12h for CH60. The lack of a well-defined yielding point and a relatively steep inelastic hardening tangent modulus of bars produced a different strain distribution behavior for CM100 than in other columns. The length over which inelastic bar strains (i.e. strains higher than strain corresponding to a stress in the bar of 100 ksi) were recorded to reach on average 24.3 in. or 1.33h in CM100, with one longitudinal bar spreading its inelastic strain up to 27 inches or 1.5h from column end. The observed length over which inelastic bar demands were recorded in CH60, CH100, and

particularly CM100 exceeded the length prescribed in ACI 318-14 (l_0 = 18 in.) over which larger amounts of transverse reinforcement is required at column ends to satisfy Special Moment Frame requirements.

- The secant lateral stiffness to first yield of the columns reinforced with grade 100 bars was at least 30% lower than that of the column reinforced with grade 60 bars, indicating that effective stiffnesses prescribed in ACI 318-14 and ASCE/SEI 41-17 may need to be revised to account for higher grades of reinforcement.
- Results indicate that an over-strength factor higher than 1.25 on the yield strength of longitudinal bars may be warranted when estimating the probable moment strength of all columns, and especially of those reinforced with ASTM A1035 longitudinal bars.
- ASCE/SEI 41-17 drift capacities at loss of 20% of moment strength were found to reasonably represent the drift capacity of the columns and were about 25% lower than those observed in the experiments.

3. PAPER 2: FROM GLOBAL TO LOCAL DEFORMATIONS OF CONCRETE SPECIAL MOMENT FRAME MEMBERS[1]

Simulating the nonlinear response of structures to seismic demands is becoming a more widespread practice with the popularization of nonlinear simulation tools and performance-based seismic design standards and guides. Performance-based documents provide modeling guidance as well as acceptance criteria, which are used to judge the adequacy of the performance of structural members. Current acceptance criteria mainly consist of deformation limits on members (e.g., plastic rotation limits), but are being converted to strain limits in many instances. The use of strain limits has the advantages of providing more reliable estimates of material damage and strength degradation, as well as improving consideration of variations in member boundary conditions (e.g., axial load). However, achieving reliable estimates of member seismic deformations and converting those member deformations to local material strains is challenging due to the paucity of physical models and test data at the local strain level.

A computational framework based on fiber-section elements and mechanics-based behavioral models is proposed to accurately estimate both member-level deformations and

[1] *Part of the material presented in this chapter and the corresponding appendices has been reproduced from Limantono (2016) with the author's and his advisor's permission. Additionally, part of this material has been presented in the Eleventh U.S. National Conference on Earthquake Engineering: Sokoli, D., Limantono A., Hogsett G., Al-Teraffy D., To D.V., Moehle J.P., and, Ghannoum, W.M., "Critical Strain Demands for Performance Evaluation of High-Strength Reinforcing Bars," 11NCEE, June 2018. D. Sokoli was the lead student investigator of the project, responsible for carrying the analysis and writing the manuscript. A. A. Limantono assisted with the analysis and part of the writing. G. Hogsett and Al-Teraffy D. carried material testing. D.V. To and J.P. Moehle provided the data from experimental research (Series 4) and reviewed the manuscript. W. M. Ghannoum supervised the research, and reviewed and edited the manuscript.*

strain demands in longitudinal bars and the concrete surrounding them within the plastic hinge regions of frame members. Particularly, the effects of the mechanical properties and steel grade of reinforcing bars on these strain demands are quantified experimentally and estimated by the proposed framework. This work was part of a larger study investigating the fatigue fracture potential of newly introduced high-strength reinforcing bars in seismic applications, for which accurate estimates of strain demands related to bar fracture demands were required.

3.1 INTRODUCTION

As prescriptive seismic design standards give way to more flexible and transparent performance-based standards, the need for reliable numerical simulations is increasing, as is the desire to achieve higher fidelity in the simulation tools that are the cornerstone of performance-based methodology. Performance-based documents, such as the ASCE/SEI 41 (2017) and ACI 369 (2017) standards, or the Guidelines for Performance-Based Seismic Design of Tall Buildings (Tall Building Initiative 2017) and the Guidelines for Nonlinear Structural Analysis for Design of Buildings (ATC Part I, Part IIa, and Part IIb, 2017), give nonlinear modeling guidance and acceptance criteria to judge the adequacy of performance of structural members. Current acceptance criteria mainly consist of deformation limits on members (e.g., plastic rotation limits), but are undergoing conversions to strain limits in many instances. The use of strain limits has the advantages of providing more reliable estimates of material damage and strength degradation, as well as improving consideration

of variations in member boundary conditions (e.g., axial load). However, achieving reliable estimates of member seismic deformations and converting those member deformations to local material strains is challenging due to the paucity of physical models and test data at the local strain level.

A computational framework based on fiber-section elements and mechanics-based behavioral models is proposed to accurately estimate both member-level deformations and strain demands in longitudinal bars and the concrete surrounding them within the plastic hinge regions of frame members. The proposed behavioral models scale strain estimates obtained using a calibrated force-formulation fiber-section computational element (Limantono 2016) to achieve the desired strain estimates.

A fiber-section computational element was selected over a lumped plasticity model, as the first one provides some estimate of strain demands in the longitudinal bars. Additionally, it was the scope of this work to produce the model using open-source software and readily available material models, such that the framework can be easily reproduced by researchers and practicing engineers in the area of Earthquake Engineering.

The framework is calibrated using 12 cyclic experimental tests conducted on concrete columns and beams that were cycled to large damage states and in some cases bar fracture. The experimental beam and column dataset contained members reinforced with regular strength, or grade 60 reinforcing bars, as well as higher strength bars of grades 80 and 100. In this work, grade refers to the specified yield strength of a reinforcing bar.

The resulting computational framework is capable of matching the global deformation behavior of reinforced concrete frame members, through the fiber-section element, and provides reliable strain demands in the longitudinal bars and surrounding concrete through the full range of expected inelastic deformations. Particularly, the effects of the mechanical properties and steel grade of reinforcing bars on their strain demands are quantified experimentally and estimated by the proposed framework.

This work was part of a larger study investigating the fatigue fracture potential of newly introduced high-strength reinforcing bars in seismic applications, for which accurate estimates of strain demands related to bar fracture were required. However, the proposed framework is intended to be applicable beyond fracture fatigue problems and aid in the development of the next generation of performance-based standards.

3.2 EXPERIMENTAL DATA

The experimental data used to calibrate the proposed framework was extracted from four series of tests carried on twelve reinforced-concrete members.

- Series 1 tests were carried to understand the fundamental behavior of moderately confined columns sustaining shear and axial failure (Leborgne, 2012). The two columns in Series 1 (2L06, 2H06) were nominally identical in design. Both were reinforced with grade 60 ASTM A615 (2016) bars. Columns were loaded under the same lateral cyclic protocol but a different axial load was applied to each. Series 1 columns sustained significant flexural yielding prior to shear and axial failures.
- Series 2 tests (CS60, CS80, CS100) were carried to investigate the ability of high-strength transverse reinforcement in maintaining confinement integrity and the shear strength of concrete columns during inelastic demands (Sokoli 2014, Sokoli and Ghannoum 2016). These three columns were constructed using different grades of reinforcement: grade 60 ASTM A706 (2016) bars for CS60, grade 80 ASTM A706 (2016) bars for CS80, and grade 100 bars that did not have ASTM specifications at the time of testing for CS100. Series 2 columns were well confined and satisfied ACI 318-15 Special Moment Frame provisions. Columns CS60 and CS80 sustained significant flexural yielding prior to shear and axial failures. The column reinforced with grade 100 steel (CS100) sustained a bond failure mechanism, which is not beneficial for the purpose of this study. This member was not used to calibrate the proposed model.

- Series 3 tests (CH100, CL100, CM100, CH60) were conducted to investigate the effects of the different shapes of the steel stress-strain relation, the tensile-to-yield strength ratios, and fracture elongations of the longitudinal bars on the plasticity spread and deformation capacity of concrete columns (Sokoli et al. 2017). All columns were geometrically identical, reinforced with the same bar layout and sizes. Three of these columns were reinforced with grade 100 steel sourced from different steel manufacturing processes, which led to different post-yield stress-strain curves. Column CM100 was reinforced with grade 100 ASTM A1035 (2016) bars having a rounded stress-strain relation. Columns CH100 and CM100 on the other hand were reinforced with grade 100 bars having a distinct yield point. Column CH60 was reinforced with grade 60 A706 bars (2016). All specimens sustained a flexural mode of degradation characterized by concrete crushing, varying degrees of longitudinal bar buckling, and eventually longitudinal bar fracture.
- Series 4 tests were the beam equivalent (BH100, BL100, BM100, BH60) of Series 3 columns (To and Moehle, 2017). The beams had nominally identically dimensions and concrete material properties, but were designed to maintain the same nominal moment strength across bar grades.

Relevant structural parameters for each specimen are summarized in Table 3-1. Additional information about the design, material properties, and loading protocol of each specimen is presented in APPENDIX C. All tests were carried on large scale specimens, with sectional depth ranging from 13.5 in. to 21.75 in. Longitudinal reinforcement bar sizes varied from #6 to #10, with longitudinal reinforcement ratios ranging from 0.7% to 4.7%. Transverse reinforcement spacing was as low as 4.4 longitudinal bar diameters and as high as 6 bar diameters. The reinforcing bar grades ranged from 60 to 100. The grade 100 bars used in this study encompassed the full range of HSRB under production in the United States as of the date of this publication. Therefore, the results were able to capture the effect of different mechanical properties present in HSRB. All specimens were constructed with moderate to low concrete compressive strengths, ranging from 3.13 ksi to 5.58 ksi.

Column specimens were tested in symmetric double curvature, whereas the beam specimens were tested as cantilevers. Details of the loading protocols for each series of tests can be found in APPENDIX C. The beams were not subjected to axial load, whereas the axial load ratio (axial load divided by the gross-sectional compressive capacity) for the column members ranged from 0.15 to 0.41 (Table 3-1). The maximum applied shear stresses varied from $3.13\sqrt{f_c'}$ to $10.55\sqrt{f_c'}$ (in psi units) (Table 3-1).

TABLE 3-1: STRUCTURAL PARAMETERS FOR EACH SPECIMEN

Member	Section Effective Depth (d)[1] (in.)	Concrete Comp. Strength (psi)	Axial Load Ratio[2]	Shear Stress[3] ($\sqrt{f_c'}$ psi)	Shear Span / Section Depth	Long. Bar Dia. (in.)	Long. Reinf. Ratio[4]	Long. Bar Yield Strength (psi)	*T/Y*[5] Strength Ratio	Tie Spacing / Bar Dia.
2L06	13.50	3130	0.19	4.46	4.00	1.00	0.025	65500	1.64	6.0
2H06	13.50	3340	0.41	4.74	4.00	1.00	0.025	65500	1.64	6.0
CS60	15.27	3830	0.30	10.55	2.75	1.25	0.047	67300	1.41	4.4
CS80	15.44	4290	0.27	9.86	2.72	1.13	0.037	79100	1.35	4.9
CH100	16.13	5160	0.15	4.00	3.60	0.75	0.011	84600	1.27	4.7
CL100	16.13	5210	0.15	3.93	3.60	0.75	0.011	100000	1.16	4.7
CH60	16.13	4570	0.15	3.15	3.60	0.75	0.011	68500	1.45	6.0
BH100	21.75	5000	0.00	3.13	4.31	1.00	0.007	102120	1.25	5.0
BL100	21.75	5100	0.00	2.91	4.31	1.00	0.007	105730	1.17	5.0
BH60	21.70	5340	0.00	3.69	4.31	1.13	0.011	65130	1.47	4.4
CM100	16.13	5580	0.15	4.55	3.60	0.75	0.011	124200	1.27	4.7
BM100	21.75	5470	0.00	3.82	4.31	1.00	0.007	100420	1.63	5.0

[1] *The section effective depth (d) is taken as the distance measured from the extreme compression fiber to the centroid of the outermost layer of longitudinal tension reinforcement.*

[2] *Axial load ratio is taken as the applied axial load divided by the gross sectional area and the measured concrete compressive strength at the day of column testing*

[3] *Shear stress is taken as the peak applied lateral load divided by member depth, width, and the square-root of concrete compressive strength*

[4] *Longitudinal reinforcement ratio is taken as the area of longitudinal steel divided by gross sectional area for column members, and tension layer of reinforcement divided by gross sectional area for beam members.*

[5] *T/Y = Tensile-to-yield strength ratio*

Specimens were instrumented to measure strains at the point of maximum demand in the longitudinal bars, and in some instances strain demands along the length of bars. While different layouts for strain gauge placement were used in different series, the mean values recorded from multiple strain gages located at peak demand sections are reported in this paper. Tests in Series 2 and 3 were monitored with a digital image correlation (DIC) system developed by the authors (Sokoli et al. 2014, Sokoli and Ghannoum 2016). The DIC system was used to monitor surface deformations, which were useful in calibrating the propose framework.

3.2.1 Behavioral Milestones

To aid in understanding the behavior of each member and to calibrate the mechanics-based local deformation models, member behavioral milestones were extracted along with the drift ratio levels at which they occurred for tests of Series 1, 2 and 3 (Table 3-2). The information was not available for specimens in Series 4. Drift ratio is defined as the lateral drift divided by member clear span.

The reported behavioral milestones of interest are: the first flexural crack (FFC), the first inclined crack (FIC), the longitudinal bar yield (LBY), the first transverse reinforcement yield (FTBY), spalling damages state 1 (SDS1), spalling damages state 2 (SDS2), and spalling damages state 3 (SDS3).

The FFC, FIC, MLBY, and FTBY were originally reported by Leborgne 2012, Sokoli 2014, Sokoli and Ghannoum 2016 and Sokoli et al. 2017. FFC, FIC and FTBY were identified by surface strains acquired from the DIC system and verified by visual

inspection. LBY was identified from strain gauges installed at the interfaces of the columns and footings where the demands were expected to be the largest.

Spalling damages states (SD1, SD2, SD3) were first reported in Limantono (2016) and obtained by tracking the maximum of horizontal surface strains in the plastic hinge region at the approximate location of longitudinal bars (Figure 3-1). The milestone SD1 was defined as the first significant increase in the horizontal strain near the face of the column (i.e. Row #1 in Figure 3-1) and represented when the first hairline spalling crack occurred. SD2 was taken at the point in loading history when any horizontal strain (Row 1 – 5) jumped above a strain equal to 0.02. SD3 was taken at the point in loading history when any horizontal strain jumped above 0.04, representing severe damage in the column (Figure 3-1). A more detailed discussion can be found in Limantono (2016).

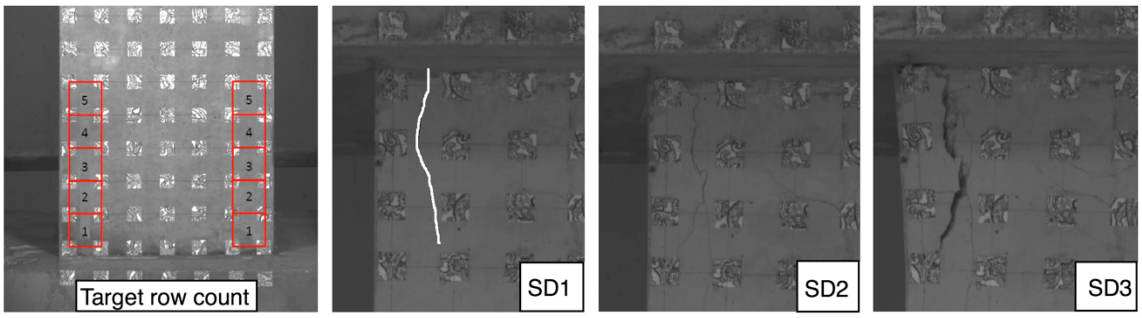

FIGURE 3-1: EXAMPLE OF SURFACE STRAIN TRACKING LOCATIONS AND DAMAGE STATES

TABLE 3-2: DRIFT RATIOS AT BEHAVIORAL MILESTONES

Specimen	FFC	FIC	LBY	FTBY	SD1	SD2	SD3
	All Values in Drift Ratio (%)						
2L06	0.69	0.92	0.90	N/A	N/A	N/A	N/A
2H06	0.65	1.62	1.30	N/A	N/A	N/A	N/A
CS60	0.30	0.60	2.00	3.00	0.60	1.32	1.67
CS80	0.40	0.60	1.05	2.00	1.00	1.41	2.00
CH100	0.20	0.60	1.01	N/A	1.50	2.87	3.00
CL100	0.20	0.60	1.00	N/A	1.50	2.70	3.12
CM100	0.20	0.60	N/A	N/A	3.00	4.00	N/A
CH60	0.20	0.60	0.60	N/A	1.00	2.68	3.99
BH100	N/A	N/A	1.25	N/A	N/A	N/A	N/A
BL100	N/A	N/A	1.25	N/A	N/A	N/A	N/A
BM100	N/A	N/A	N/A	N/A	N/A	N/A	N/A
BH60	N/A	N/A	0.90	N/A	N/A	N/A	N/A

N/A == data not available

3.2.2 Measured Strains in Longitudinal Bars

The measured longitudinal bar strains presented in this section were obtained from the strain gauge readings on bars farthest away from the flexural neutral axis and at the sections of highest moment, i.e., at both ends of the columns or the support end of the beams. Sample plot of measured strains versus drift ratios at critical sections for longitudinal bars in members CS80, CH100, BH100 and BM100 are shown in Figure 3-2.

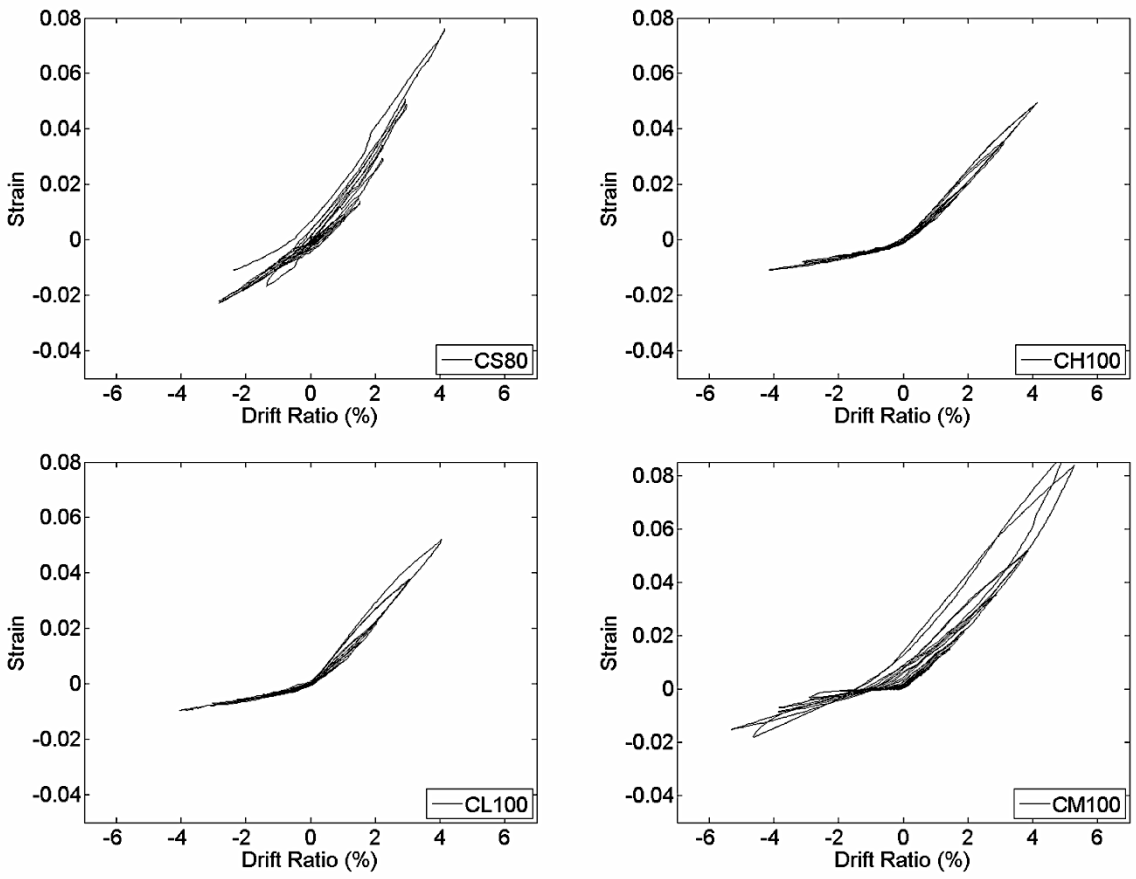

FIGURE 3-2: SAMPLE STRAIN GAUGE RECORDING FOR FOUR OF THE MEMBERS (POSITIVE STRAIN VALUES INDICATE TENSILE STRAINS)

Mean largest strains (ε_{MB}) of bars were calculated as the mean value of each reliable strain gauge measurement on corner bars at the sections of largest moments and at each drift target level, taking the average of both cycles to a certain drift target. Mean largest tension strains are plotted for all members versus drift ratio in Figure 3-3, while mean largest compression strains are shown in Figure 3-4. One of the variables that influences the value of strain in longitudinal bar is the effective depth (d) of the member section in the direction of loading. The larger the effective depth, the larger the longitudinal bar strain

value is at a given lateral drift. The measured strains normalized by effective depth versus the lateral drift ratios are provided for more direct comparison between all members in Figure 3-3 and Figure 3-4. The mean largest strains were only presented in Figure 3-3 and Figure 3-4 up to the drift ratios at which they were deemed to be reliable. In tests 2L06 and 2H06, the strain measurement beyond shear failure at a drift ratio of about 3.3% are not presented. Shear failure occurred in CS60 and CS80 only after drift ratios of 5.5%.

Important observations can be made based on Figure 3-3 and Figure 3-4:

1- The largest inelastic tensile strain demands on longitudinal bars vary significantly from member to member at a given drift ratio. That is true even for columns that were designed to be nominally identical in dimensions and detailing, and subjected to the same axial load ratio (e.g., CH100, CL100, and CM100). In Series 2 and 3, reinforcing steel mechanical properties were found to alter inelastic strain demands in bars of nominally identical members by as much as 60%. Additional discussion on strain demands difference can be found in Sokoli and Ghannoum (2016) for Series 2, Sokoli et. al. (2017) and APPENDIX C for Series 3 and To and Moehle (2017) for Series 4.

2- Other parameters besides the reinforcing bar properties appear to alter the tensile strain demand difference between the various members, which lead to strain demands several folds different at any given drift ratio in Figure 3-3. The subsequent section discussing the strain prediction model investigates the influence of various parameters on the stain demands.

3- In columns with compressive axial loads, longitudinal bar strains did not vary significantly from cycle to cycle to the same drift target (Sokoli 2014, Sokoli and Ghannoum, 2014, Sokoli et. al 2018). On the other hand, the measured bar strains in the beams that were not subjected to axial loads were highly dependent on the lateral loading history. After longitudinal bars yield in tension, loading reversal begins to compress residual tensile strains while flexural cracks begin to close. Depending on the magnitude of the tensile strains and member axial loads, bars can reach compressive stresses prior to cracks closing during load reversal, and prior to reaching compression strains. Therefore, it is possible for the longitudinal bars that have yielded in tension to experience only tensile strains (i.e. positive strain) during symmetrical cyclic lateral loading history. This was observed in beams specimens, where strains in longitudinal bars were seen to gradually increase in tension during cyclic loading. It is noteworthy that beams were not restrained longitudinally during testing, while such beams cast monolithically with slabs would be restrained and therefore may not experience such gradually increasing strains during cycling.

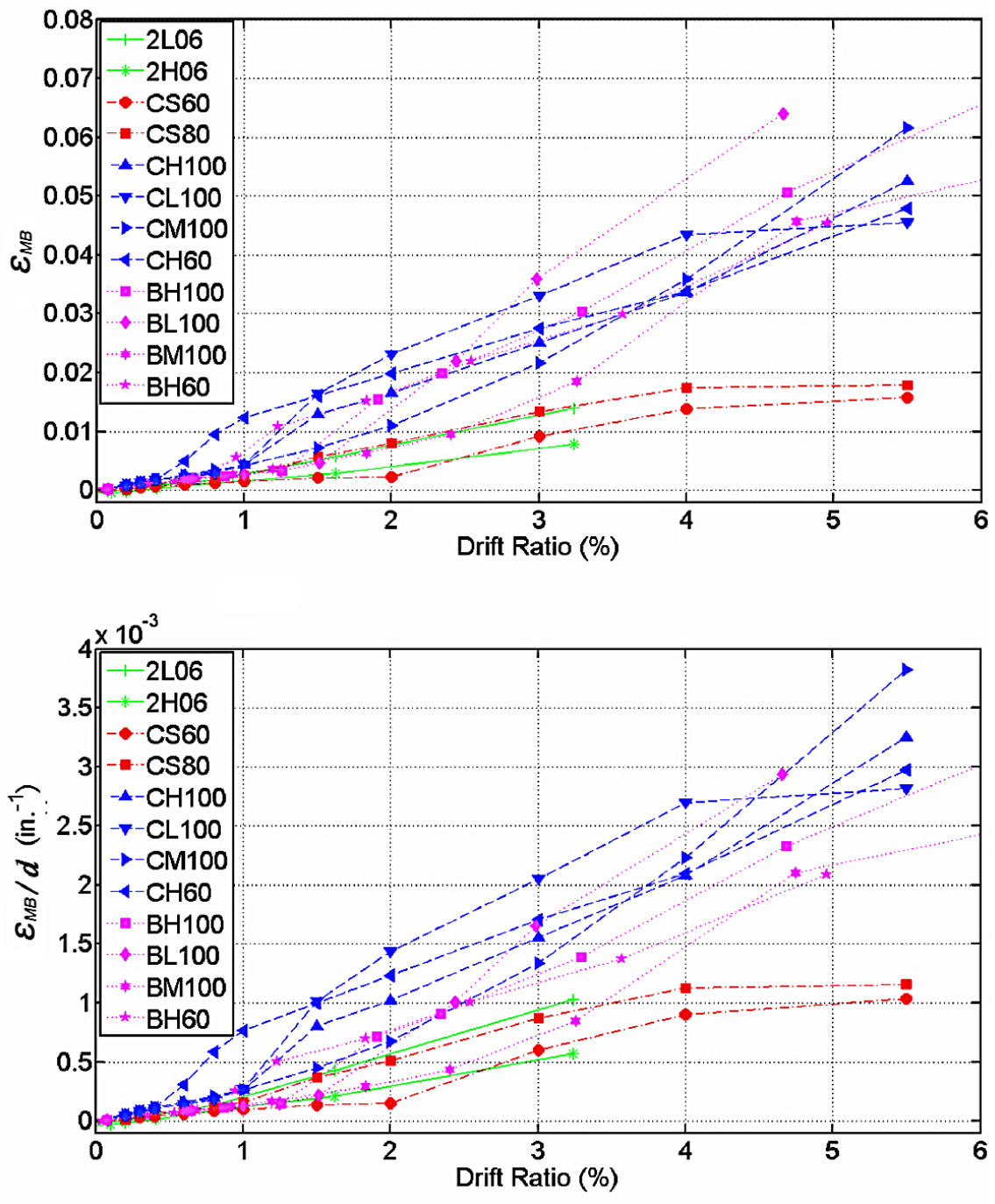

FIGURE 3-3: MEAN LARGEST TENSILE STRAIN DEMANDS (ε_M) VERSUS DRIFT RATIOS (UP), AND ε_M NORMALIZED TO SECTION DEPTH VERSUS DRIFT RATIOS (DOWN) FOR ALL SPECIMENS

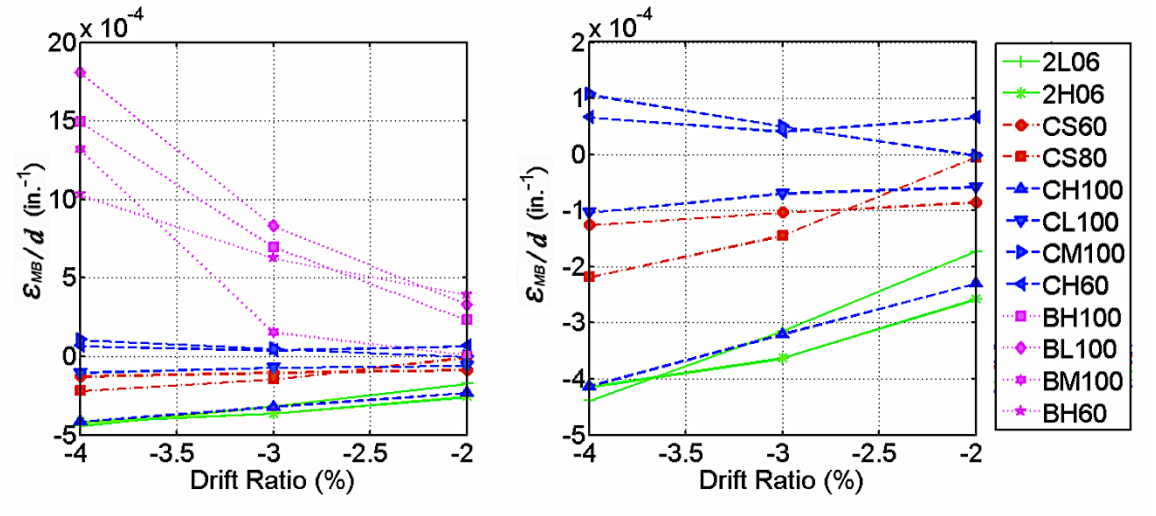

FIGURE 3-4: MEAN MEASURED STRAINS IN COMPRESSION FOR ALL MEMBERS (LEFT) AND COLUMNS ONLY (RIGHT)

3.2.3 Measured Surface Strains in Plastic Hinge Regions

Longitudinal strains on the concrete surface were monitored along the outermost longitudinal bars at column ends (Figure 3-5). This data was available for six column specimens, namely, CS60, CS80, CH100, CL100, CM100 and CH60. The strains were extracted between targets on the footings and targets 7 in. from the column/footing interface. This height represents the approximate location of the second hoop in the members. The measurements included deformations due to slip of bars from the foundations caused by strain penetration effects. Sample surface strains versus member drift ratio are presented in Figure 3-6.

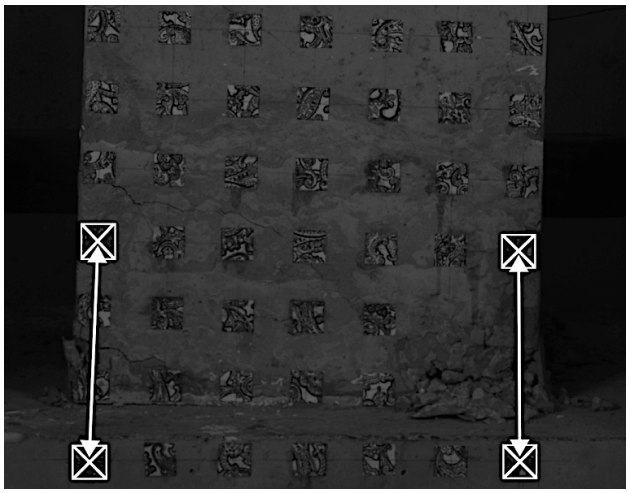

FIGURE 3-5: SCHEMATICS OF MONITORED STRAINS ON CONCRETE SURFACE

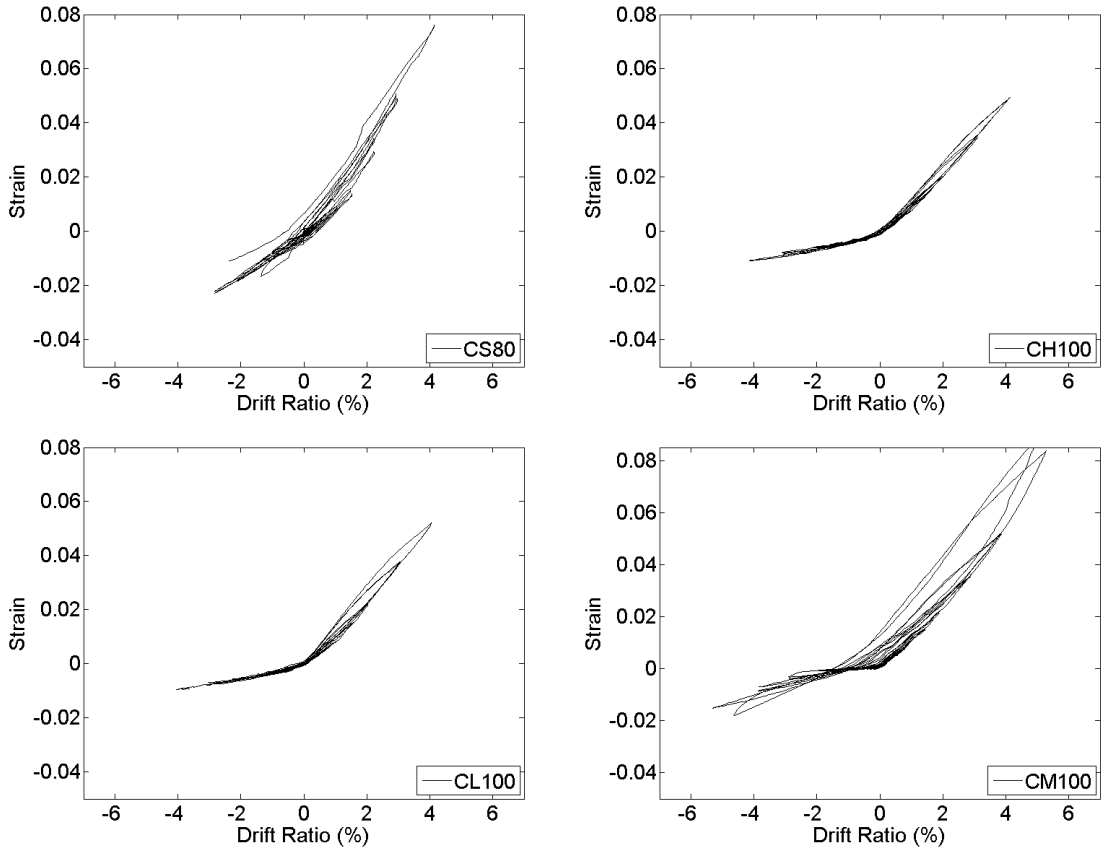

FIGURE 3-6: SAMPLE LONGITUDINAL SURFACE STRAINS IN MEMBER PLASTIC HINGE REGIONS

Measured surface longitudinal stains were fairly similar between the two consecutive half-cycle to the same drift ratio (Figure 3-6). This trend is similar to the one observed in the longitudinal-bar strains recorded in the same columns. The mean of the surface strains at each drift target (ε_{MS}) are plotted in Figure 3-7 for all specimens for which the data were available. Similar to strains in the longitudinal bars, members subjected to higher axial loads (CS60 and CS80) experienced higher compressive strains and lower tensile strains on average.

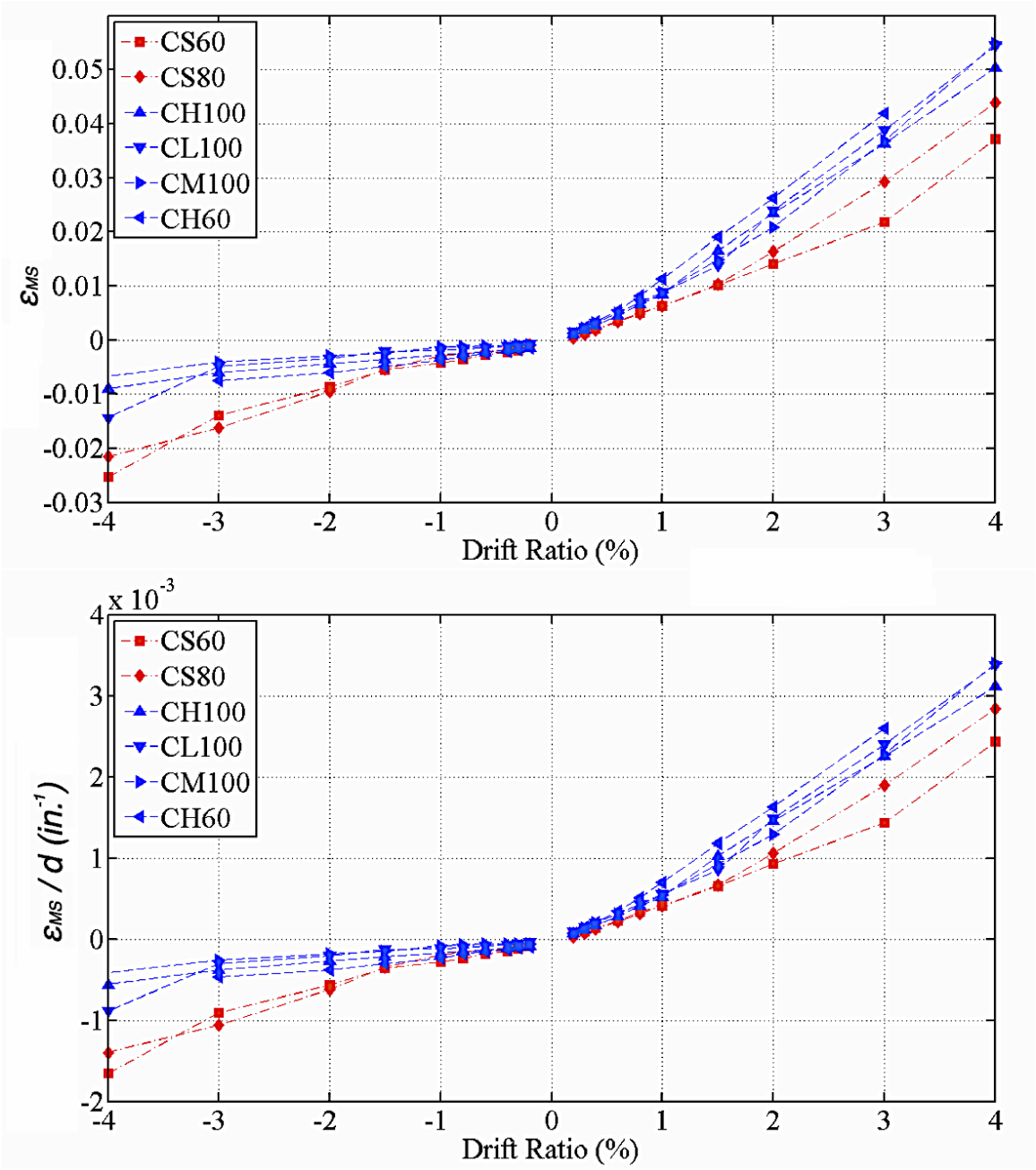

FIGURE 3-7: MEAN CONCRETE SURFACE STRAIN DEMANDS (UP) AND NORMALIZED TO SECTION DEPTH (DOWN) FOR SIX OF THE SPECIMENS

3.2 FIBER-SECTION COMPUTATIONAL MODEL

A fiber-section line-element computational model was calibrated to obtain reliable member-level deformations. The model also provides strain estimates for longitudinal bars and the surrounding concrete within the plastic hinge region, which reflect at least partially, the effects axial loads and material properties. Nonlinear monotonic and cyclic pushover analyses were conducted for each specimen to calibrate the computational model. Results from monotonic analyses were used for the sensitivity analyses in order to save computation time. Model parameters including the layout of the fibers in the section, number of integration points, and material constitutive models, were selected to achieve reliable member deformations for the 12 tests considered. The open source simulation software OpenSees (McKenna 2000) was used in analyses.

3.2.1 Fiber-Section Distributed Plasticity Element

A distributed plasticity fiber-section force based formulation element was used to model the column flexural behavior (Spacone et al., 1996), with the suggested changes by Coleman and Spacone (2001) (Figure 3-8). This element is formulated with constant curvature between integration points, which generates constant strains around each integration point, unlike displacement-based elements that typically have linear curvature assumptions along the element. Additionally, one force-based element is sufficient to capture the column global deformation and strain demands in the nonlinear range of behavior, as opposed to requiring several displacement-based elements to achieve the same accuracy (Neuenhofer and Filippou 1997, Scott and Fenves 2006, Addessi and Ciampi

2007). Elastic rotational springs were added at the end of the distributed plasticity line element to simulate the softening effect of strain penetration of longitudinal bars in the adjacent footings. Elastic shear springs were introduced as well at the ends of the distributed plasticity element to capture shear flexibility. Nonlinear geometry effects were treated in the analyses.

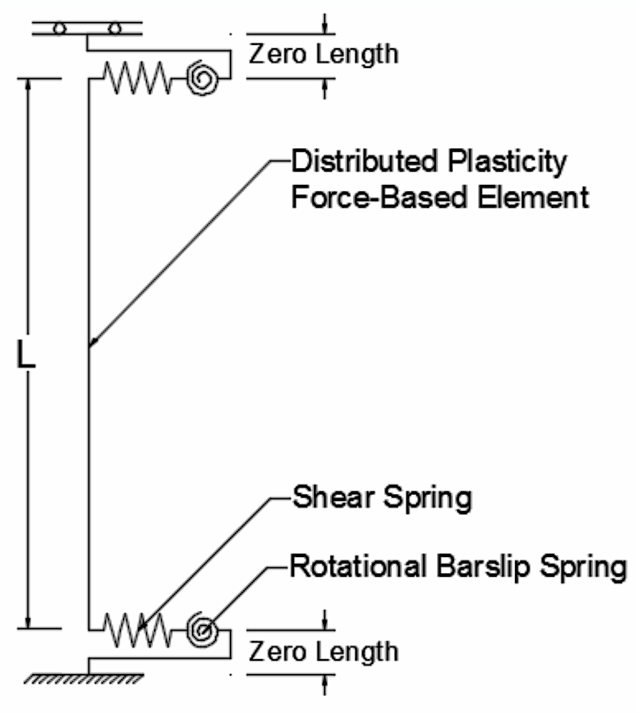

FIGURE 3-8: DISTRIBUTED PLASTICITY FIBER-SECTION MODEL

3.2.2 Fiber Discretization

The column section was discretized into fibers modeling the cover concrete, core concrete, and steel reinforcement (Figure 3-9). Considering that the number of fibers affects computational time, a sensitivity study was conducted to determine the optimal number of concrete fibers required to capture column lateral response and provide a

reasonable starting point for tension strains in longitudinal bars for all type of sections investigated in this study. Details of the sensitivity study can be found in Limantono (2016). Ten fibers in the core and side covers were selected based on the study, while two fibers were selected for the outermost covers in the direction of loading for all members (Figure 3-9).

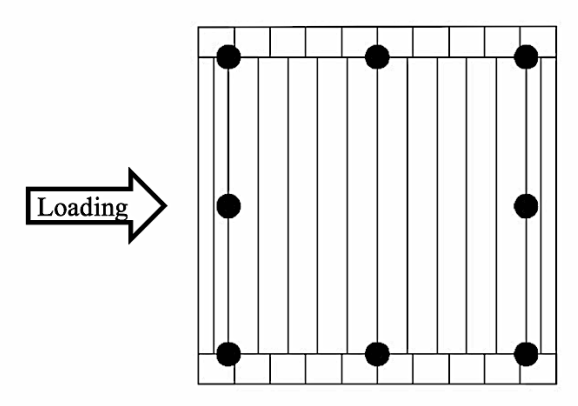

FIGURE 3-9: FIBER SECTION CONFIGURATION FOR ALL MODELED MEMBER

3.2.3 Material Models

Concrete

The stress-strain response of the cover concrete was modeled using the Concrete02 material model in OpenSees, which is based on the work by Kent and Park (1971) and utilizes linear tension degrading behavior. To avoid rapid and unrealistic softening of the member response due to localization of deformations occurring in force-based elements (Scott and Fenves 2006, Scott and Hamutcuoglu 2008), the softening branch of the concrete cover material model was regularized to adjust the strain (ε_{20}) at which the concrete stress drops to 0.2 $f'c$ in the softening branch (Coleman and Spacone, 2001) (Figure 3-10); with

$f'c$ being the peak compressive stress in the model. The regularization process accounts for the length over which the curvature of the end fiber-sections are integrated. For example, that length is 5% of the length of the column element for 5 Gauss-Lobatto integration points (Lp in Equation 1-1). Based on work in Colman and Spacone, 2001, ε_{20} can be estimated as:

EQUATION 3-1: STRAIN AT CONSTANT ENERGY INITIATION

$$\varepsilon_{20} = \frac{G_f^c}{0.6 f'c\ Lp} - \frac{0.8\ f'c}{E_c} + \varepsilon_0$$

where G_f^c is the material fracture energy under the material stress strain curve as illustrated in Figure 3-10; E_c is the modulus of elasticity of the concrete, ε_0 is strain at peak stress $f'c$, L_p is plastic hinge length, which is equal to the weighted length for the first integration point in the force-based element. The fracture energy of plain regular strength concrete cylinders tested under axial compression typically range from 0.11 kip/in. to 0.17 kip/in. (Coleman and Spacone 2001). The higher value of fracture energy (G_f^c) used for regularization results in higher strain ε_{20}. Higher values of ε_{20} or G_f^c reduce the softening slope in the lateral member response, or can even produce a hardening behavior (Figure 3-11). A sensitivity analysis carried for all members suggested that a value of G_f^c equal to 0.342 kip/in. would capture the post-yield slope of the lateral force versus lateral drift response of the test specimens (Figure 3-11).

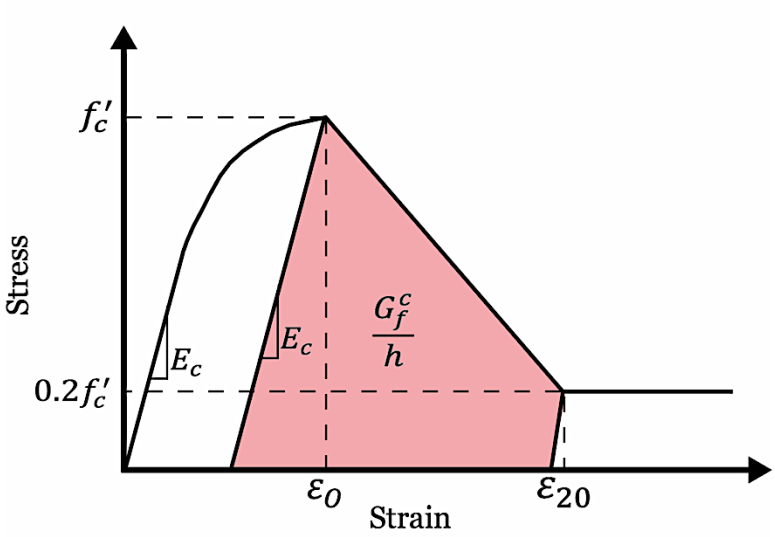

FIGURE 3-10: STRESS-STRAIN MODEL WITH FRACTURE ENERGY IN COMPRESSION AS HIGHLIGHTED AREA (ADAPTED FROM KENT-PARK 1971)

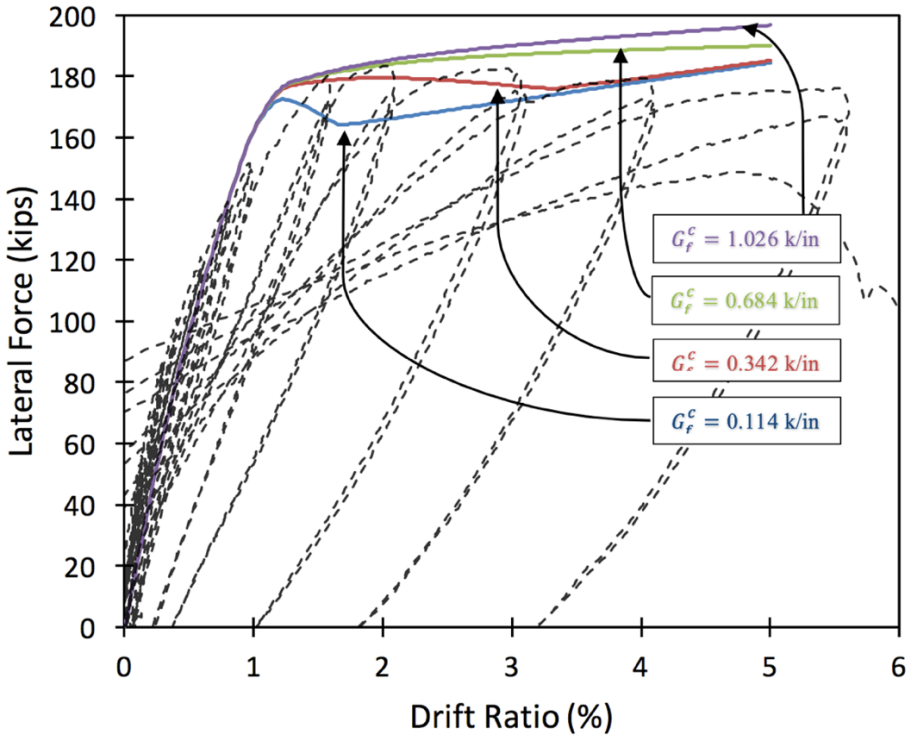

FIGURE 3-11: LATERAL RESPONSE SENSITIVITY TO G_F^C FOR CS80

To illustrate the regularization process, the adjusted concrete cover material model in compression is plotted in Figure 3-12 for the concrete of column CL100. On the same plot, the measured concrete compressive behaviors from three cylinder tests are shown. In regularizing the concrete model, the parameters in Equation 1-1 were taken as: G_f^c = 0.342 kip/in., f_c' = 5110 psi, E_c = 4075 ksi, ε_0 = -0.0027 (Ghannoum et al. 2008), and L_p=5.4 in (for five integration points with the Gauss-Lobatto integration scheme for the force-formulation fiber element), and ε_{20} of -0.022 (compression). The difference in the pre-peak behavior between the measured cylinder response in compression and the regularized model is attributed to the single value peak strain selected (ε_0 = -0.0027) for all members.

The tensile response of concrete was modeled with a loading stiffness of $(2f'c/\varepsilon_0)$. The tension strength (f_t) was calculated with Eq. 19.2.3.1 in ACI 318-14. The linear softening slope (E_t) in tension was taken as 10% of the loading stiffness.

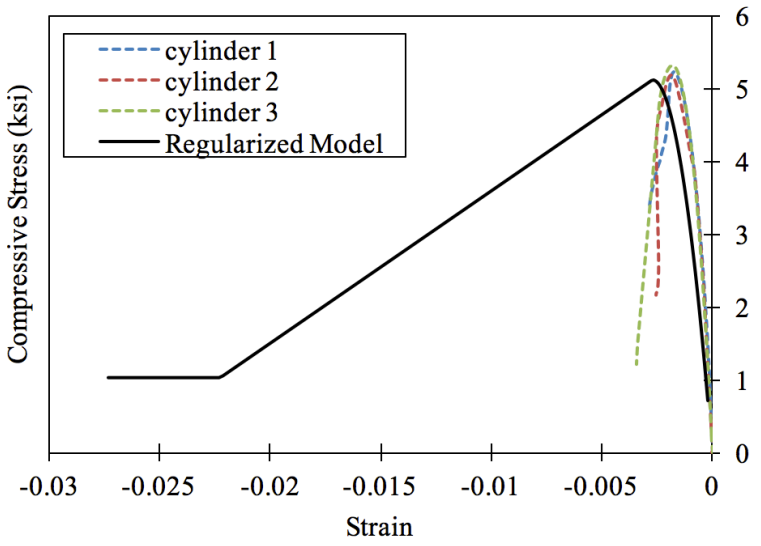

FIGURE 3-12: COMPARISON BETWEEN CYLINDER TEST AND REGULARIZED MODEL FOR CL100

The core concrete stress-strain response was modeled using the Concrete04 material model in OpenSees. This Popovics (1973) concrete material is characterized by a degraded linear unloading/reloading stiffness according to the work of Karsan-Jirsa (1969) and tensile strength with exponential decay. The maximum stress value for the material model was calculated in accordance with recommendations of Mander et al. (1988). The strain at crushing was modelled using the empirical maximum strain equation suggested by Qi and Moehle (1991). Additional details about core and cover concrete modeling can be found in Limantono (2016). Figure 3-13 compares the cover and core concrete material models in compression for column CS80.

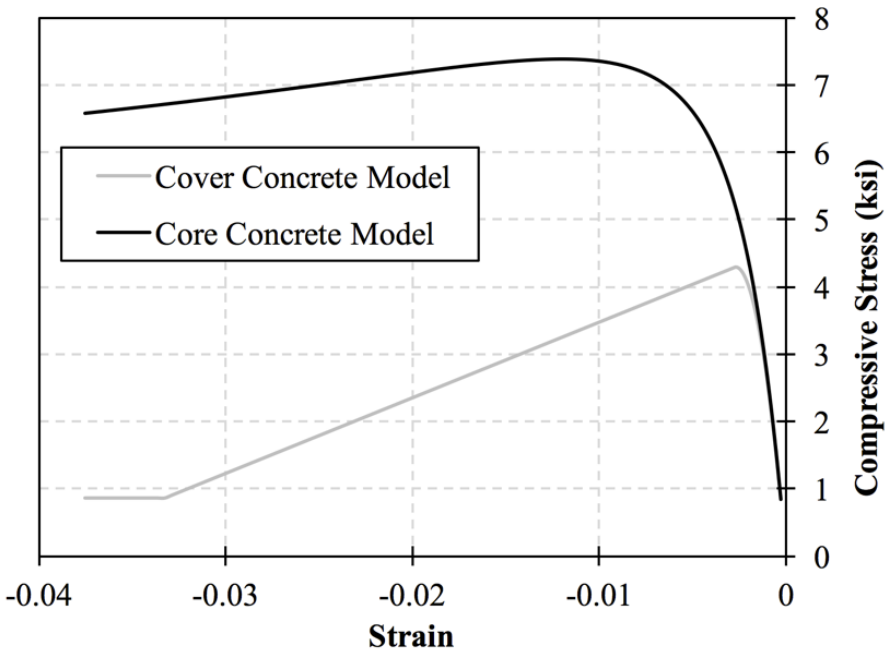

FIGURE 3-13: COVER AND CORE CONCRETE MODEL

Steel Material Model

The behavior of reinforcing bars was modeled using the Steel02 material model in OpenSees, which is a bi-linear Giuffre-Menegotto-Pinto (1972) model that captures the Bauschinger effect (Bauschinger, 1886). The strain hardening ratio (b), which is the ratio between post-yield tangent stiffness and initial elastic stiffness was calculated using data from Table 3-1 in Equation 3-2:

EQUATION 3-2: CALCULATING STRAIN HARDENING RATIO

$$b = \frac{f_y\left[\left({}^{T}/_{Y}\right) - 1\right](ksi) \Big/ (\varepsilon_u - \varepsilon_y)}{29000}$$

where f_y , ε_y and ε_u are the measured yield strength, yield strain, and uniform strain, respectively, and were obtained from tension test results of the longitudinal bars.

The calculated strain hardening ratio values were found to be consistent with recommendations from previous research (Berry and Eberhard 2007), being close to 1% for grade 60 bars (Table 3-3). This value was used for specimens reinforced with grade 60 bars and for which the full stress-strain curve data was not available (i.e., 2L06 and 2H06). The hardening ratio was lower than 1% for bars having a yield strength higher than 60 ksi (420MPa) and having a distinct yield point. The ratio was higher than 1% for members reinforced with ASTM A1035 steel due to that steel's rounded stress-strain shape. Figure 3-14 compares the Steel02 monotonic stress-strain curves for longitudinal bars of CH100 and CM100, overlaid on a typical experimental stress-strain curve.

TABLE 3-3: STRAIN HARDENING RATIO

Column	2L06	2H06	CS60	CS80	CL100	CH100	CM100	CH60	BH100	BL100	BM100	BH60
b (%)	1.00*	1.00*	0.96	1.09	0.71	1.28	2.58	0.86	0.97	1.00	4.2	0.94

**Assumed values based on literature and estimated values in similar bar types*

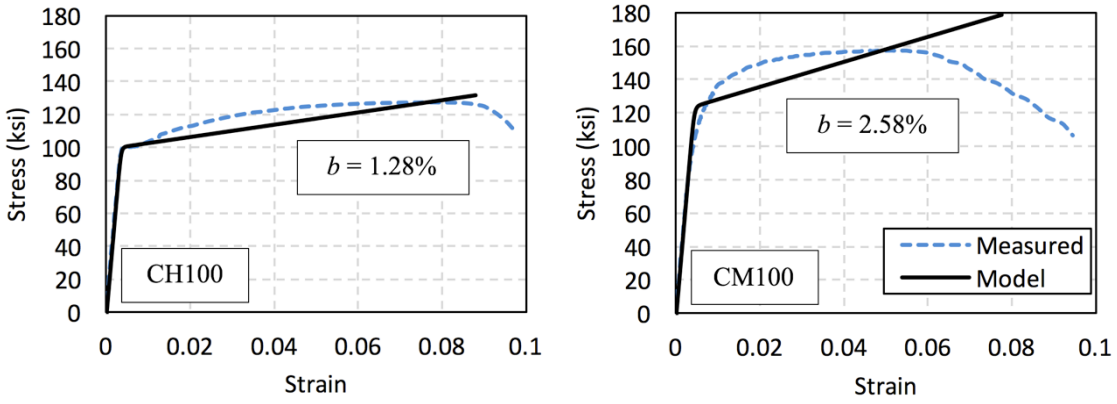

FIGURE 3-14: COMPARISON OF MEASURED AND MODELED STRESS-STRAIN CURVES FOR BARS IN CH100 AND CM100

The Reinforcing Steel material model in OpenSEES simulates the post-yield behavior of reinforcing bars much more closely than the Steel02 model. The comparison of Steel02 and Reinforcing Steel material models, however, demonstrated insignificant response differences for both high shear – high axial load columns (e.g., CS80) and low shear – low axial load columns (e.g., CL100) in (Figure 3-15). The Steel02 material model was selected in this work because similar bi-linear steel models are commonly available in most simulation software.

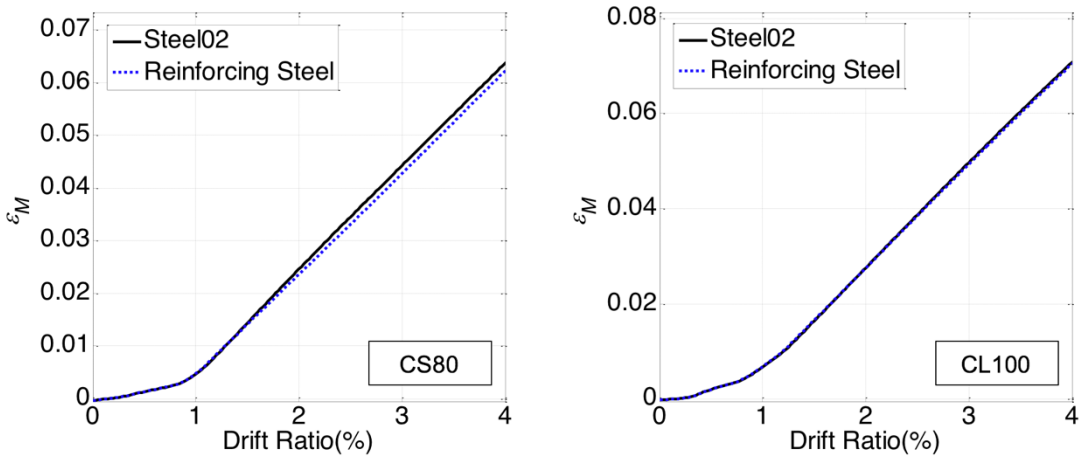

FIGURE 3-15: TENSION STRAIN COMPARISON FOR STEEL02 AND REINFORCING STEEL MATERIAL MODELS

3.2.4 Shear Deformations

Measured shear deformations were relatively small compared with total lateral deformations for all tested specimens. Given the low impact of shear deformations on total deformation, shear deformation was modeled using a shear spring with an elastic stiffness given by:

EQUATION 3-3: SHEAR SPRING STIFFNESS

$$k_{shear} = \frac{(5/6)GA_g}{L}$$

where G is the shear modulus calculated as $G = \frac{E_c}{2(1+v)}$, A_g is gross section area, L is the column length, E_c is the concrete material elastic modulus and is calculated as $57{,}000\sqrt{f'c}$ psi as per ACI 318-14 provisions, v is the Poisson Ratio of concrete and was taken as 0.25.

3.2.5 Bar Slip Deformations

Slip of longitudinal bars due to strain penetration in adjacent footings, or longitudinal bar slip, accounted for around 30 to 50% of the total lateral drift of the frame members considered (Figure 3-16) (Sokoli et al. 2017). As can be seen in Figure 3-16, bar slip deformations tend to maintain their ratio to total deformations even within the inelastic range of behavior, indicating the bar-slip deformations undergo inelastic behavior as well.

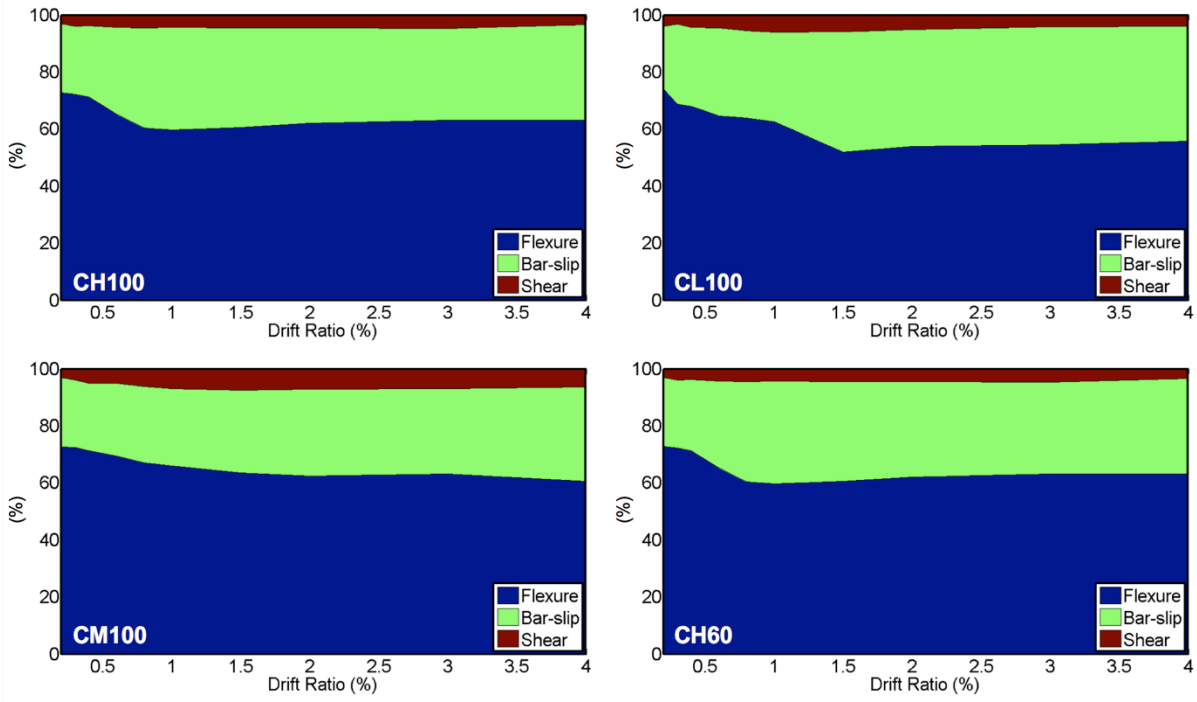

FIGURE 3-16: DEFORMATION COMPONENTS AT DRIFT TARGETS FOR COLUMNS OF SERIES 3

However, bar slip deformations were introduced through linear zero-length rotational springs at member ends. In this fashion, all nonlinear lateral drift behavior is simulated by the fiber-section element. Nonlinear bar slip behavior was not modeled to avoid numerical issues related to having two nonlinear elements in series when the fiber-section element

exhibits a negative softening stiffness. This approach resulted in reasonable estimates of global member deformations as will be shown subsequently. Assuming a constant bond stress between bar and surrounding concrete in the footing (Sezen and Moehle 2004, and Ghannoum and Moehele 2012), the rotational stiffness of the slip springs can be derived as:

EQUATION 3-4: BAR-SLIP SPRING STIFFNESS

$$k_{slip} = \frac{8u\, M_y}{d_b f_y\, \phi_y}$$

where u represents the constant bond stress between bars and adjacent concrete, M_y represents moment at first yield, ϕ_y represents the section's curvature at first yield, d_b represents longitudinal bar diameter, and f_y represents longitudinal bar stress at first yield. M_y, ϕ_y, and f_y can be estimated from moment curvature analyses, and were demonstrated experimentally to provide accurate measures using DIC data of columns tests (Sokoli et al. 2014). Recommendations for the constant bond stress parameter (u), however, vary greatly in the literature and depend on many factors, including whether the longitudinal bars are anchored in footings or in beam-column joints, and the level of damage or cracking the anchoring member.

Values of constant bond stress between bars and adjacent concrete have been reported in literature. Twelve concrete column tests carried by Lynn et. al. (1996) and Sezen and Setzler (2008), exhibited a mean u value of $11.4\sqrt{f'c}$. The same mean value for the constant bond stress ($11.4\sqrt{f'c}$) was also reported for six column tests by Melek et. al.

(2003). Similar values were reported from beam tests by Sozen and Moehle (1990), where the mean u values for 35 beams tested under monotonic loading was calculated to be $10\sqrt{f'c}$.

For the column tests considered in this study, matching member lateral stiffness prior to yielding produced u values from $9\sqrt{f'c}$ to $18\sqrt{f'c}$, with a mean of $13.9\sqrt{f'c}$, and a standard deviation $2.9\sqrt{f'c}$. Limantono (2016) investigated the effect of varying the elastic bond stress parameter between the low and high end of the range identified above and found that it resulted in less than 5% difference in the inelastic strain demands in longitudinal bars produced by the fiber-section element. Therefore, the same value of bond stress (u) of $14\sqrt{f'c}$ was used in this study for column members, while a value of $11\sqrt{f'c}$ was used for beam members. It is noteworthy that the test members were connected to large footings that remained essentially undamaged during testing, which resulted in bond stresses on the higher end of the range provided in the literature. However, when considering moment frames, the lower value of $9.6\sqrt{f'c}$ recommended by Elwood and Eberhardt (2009) and Kwon (2016) may be more appropriate.

3.2.6 Flexural Deformations

The flexural deformation component was modeled using a distributed-plasticity, force-based, fiber beam-column element. The fiber beam-column element is a line element with a fiber-section assigned at each integration point, with each fiber-section defining the moment curvature response at that point. A force-based formulation always satisfies

equilibrium along the length of the element. Equilibrium is satisfied by force interpolation functions. Deformations along the length of the element are obtained by weighted integration of the fiber-section deformations (Spacone et al. 1996).

Inelastic deformations in reinforced concrete columns typically occur in the end sections of the columns. In order to account for that scenario, a Gauss-Lobatto integration scheme is used in the element since it has integration points at the ends of the element, which coincide with the sections of highest inelastic deformation. The Gauss-Lobatto integration method is a numerical integration approximation of the definite integral of a function, which is evaluated as the sum of weights multiplied by function values at the integration points within the domain of integration. The Gauss-Lobatto integration method matches the exact results of polynomials of degree 2N-1 (with N being the number of integration points). Thus, the Gauss-Lobatto integration method has a specific weight and integration point locations for each number of integration points (N) to match exactly the polynomials of degree 2N-1. However, local flexural deformations along the length of reinforced concrete columns do not follow any polynomial function because of cracks, damage, and inelastic deformation that occur along the length of a column. Therefore, deformation delivered by a Gauss-Lobatto intergration scheme for fiber-section curvatures can only approximate the actual distribution of flexural deformations along a column length.

The measured and modeled flexural deformations using different number of integration points were compared for all specimens at two force levels: first yield and at

80% of that value. First yield was taken as recommended by Benzoni et al. (1996) as the first point at which the tension reinforcement yielded or the maximum concrete compressive strain reached a value of 0.002. The lateral force versus drift response of column CS80 as measured from the experiment and modeled in OpenSees with different number of integration points is plotted in Figure 3-17. Based on the results of the sensitivity analysis, five Gauss-Lobatto integration points produced reasonably small errors for all members, typically on the order of 5% across the full drift range of the tests.

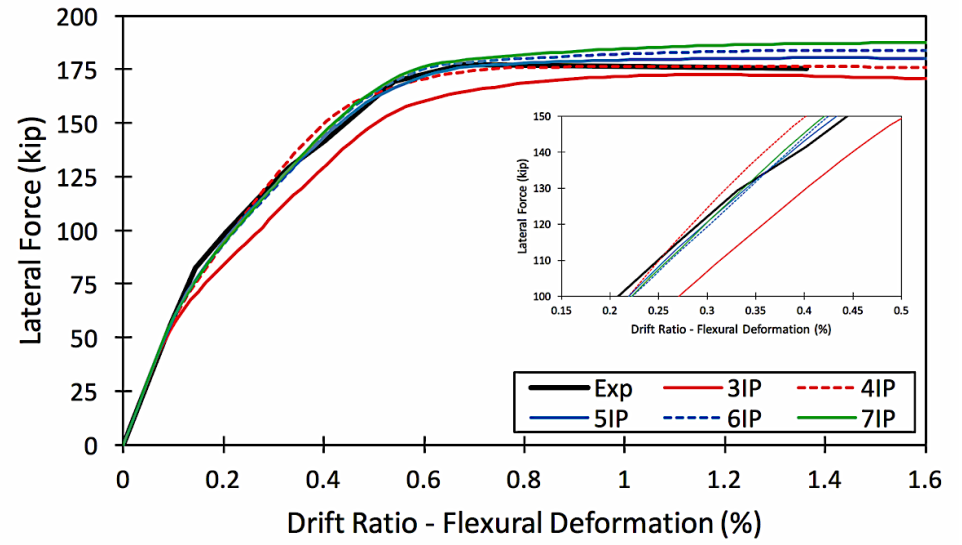

FIGURE 3-17: MEASURED AND MODELED FLEXURAL DEFORMATION COMPONENT OF CS80

It was also observed that five integration points deliver the least amount of errors in tensile strains in longitudinal bars before longitudinal bar yield (Figure 3-18). As can be seen in Figure 3-18, the strain in longitudinal bars localized significantly after yielding as the number integration points increased. The first integration point has a finite length proportional to the integration weight times the length of the element. Therefore, larger

numbers of integration points generate smaller first integration weight (or length) where the plasticity is concentrated. This results in larger strains due to larger curvatures.

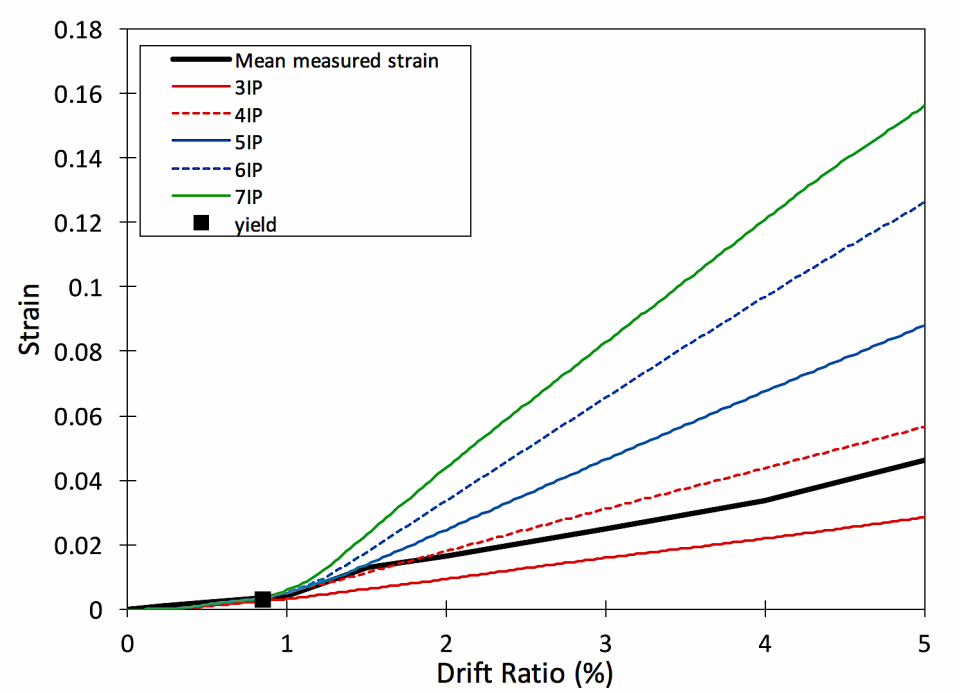

FIGURE 3-18: CH100 - INFLUENCE OF NUMBER OF INTEGRATION POINTS ON THE TENSILE STRAINS IN LONGITUDINAL BARS

Based on the above observations, five integration points are recommended per element to simulate the global column behavior and estimate the strains in longitudinal bars prior to yielding. However, when columns experience yielding, the associated fiber-section strain results become less reliable. In subsequent sections, an adjustment factor is proposed to modify the strains obtained from the five integration-point computational model after initial yielding occurs.

3.2.7 Simulated Member-Level Behavior

Due to the use of simplified elastic relations for bar slip and shear deformations, the estimated elastic stiffness before first yield was typically lower than the measured column global lateral stiffness, as shown in Figure 3-19. Nevertheless, the estimated total drift before first yield can be considered acceptable and represents the measured stiffness after softening occurred due to cycling and past the point of first yield.

The mean measured tension strain demands at target drifts and those from fiber-section analyses are plotted for all member in Figure 3-21. In the figure, the assumed drifts at which the computational and experimental strains diverge are highlighted. This strain corresponds to the point in loading at which the bars in the analyses yield. As can be seen in Figure 3-21, the ratio between inelastic tensions strains from analyses and experiments varies greatly from member to member and can exceed a factor of 4.

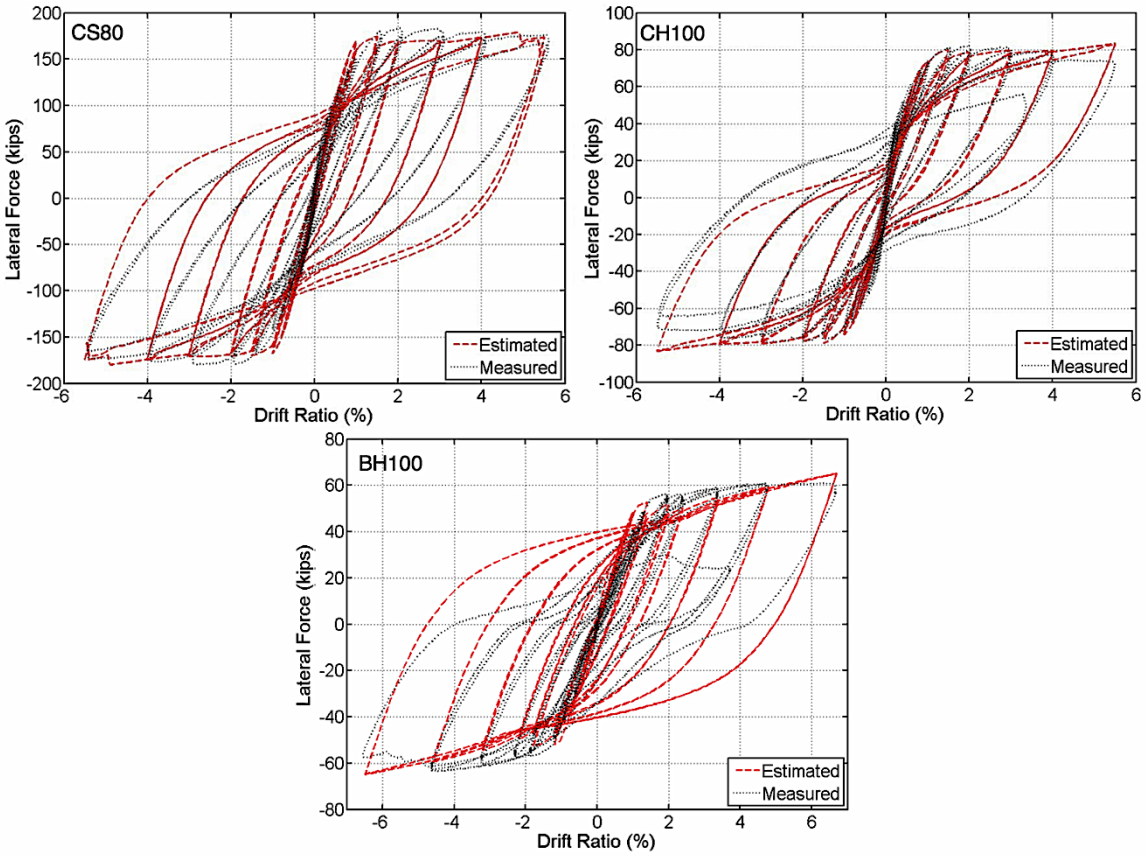

FIGURE 3-19: GLOBAL BEHAVIOR PREDICTION – CS80, CH100, BH100

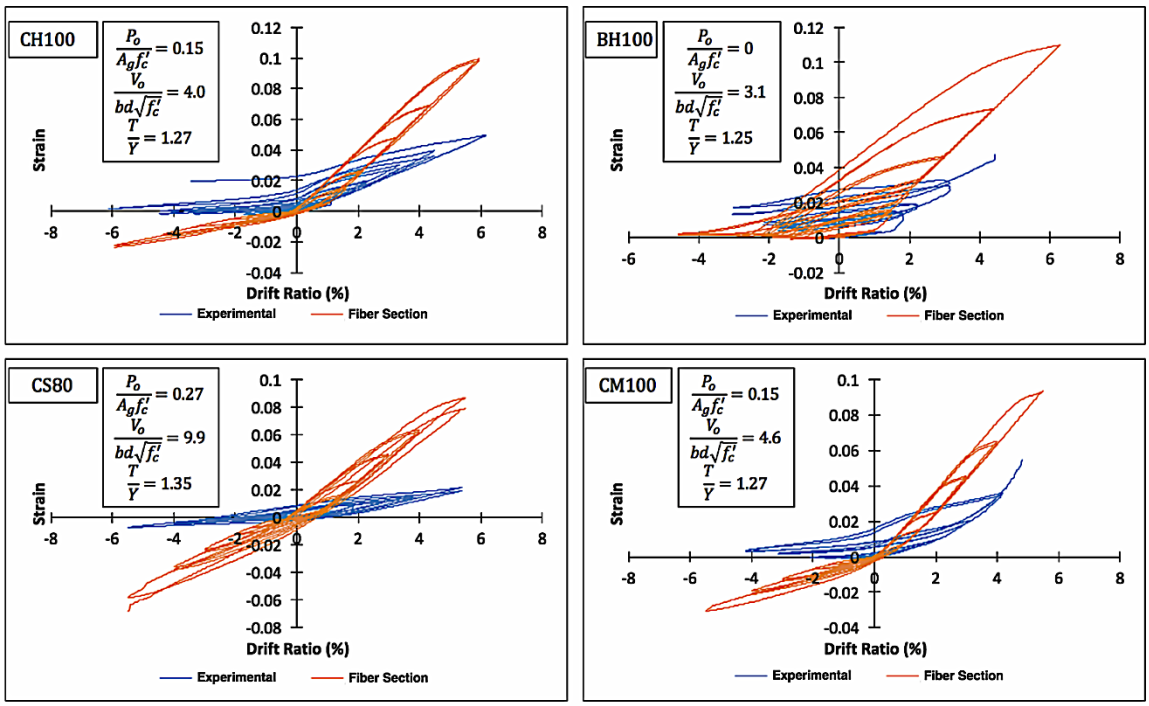

FIGURE 3-20: COMPARISON OF A TYPICAL CYCLIC STRAIN GAUGE READING AND CORRESPONDING RESULT FROM ANALYSES

The tested specimens where the only variable was the axial load ratio were columns 2L06 and 2H06 (Figure 3-21). Column 2L06 was tested with an axial load ratio of 0.19 and column 2H06 with an axial load ratio of 0.41. In these tests, higher axial loads delayed the longitudinal bar yielding to a larger drift, and produced lower strain increases with increasing drift after yielding. Even though the fiber-section model accounted partly for that effect, it did not capture the extent of the axial load influence on inelastic bar strains. Possibly, the assumption of perfect bond between steel and concrete in the fiber-section model could not capture the effects of degrading bond between longitudinal bars and concrete in the inelastic range due to concrete damage and spalling.

The tested specimens where the only variable was the strain hardening ratio (b) of the longitudinal reinforcement were columns CL100, CH100, and CH60, as well as beams BL100, BH100, and BH60. The strain measurements from experiments indicated that the longitudinal bar strain progression after bar yielding was related to the T/Y ratio of the bars. A higher T/Y ratio produced a lower strain progression with increasing drift. Even though the strain hardening ratio was adjusted for the steel material model, the computational results showed approximately the same rate of strain progression with increasing drifts for all columns (Figure 3-21). On the other hand, the computational model captured the effects of the bar yield strength, with lower yield strengths yielding at earlier drift ratios.

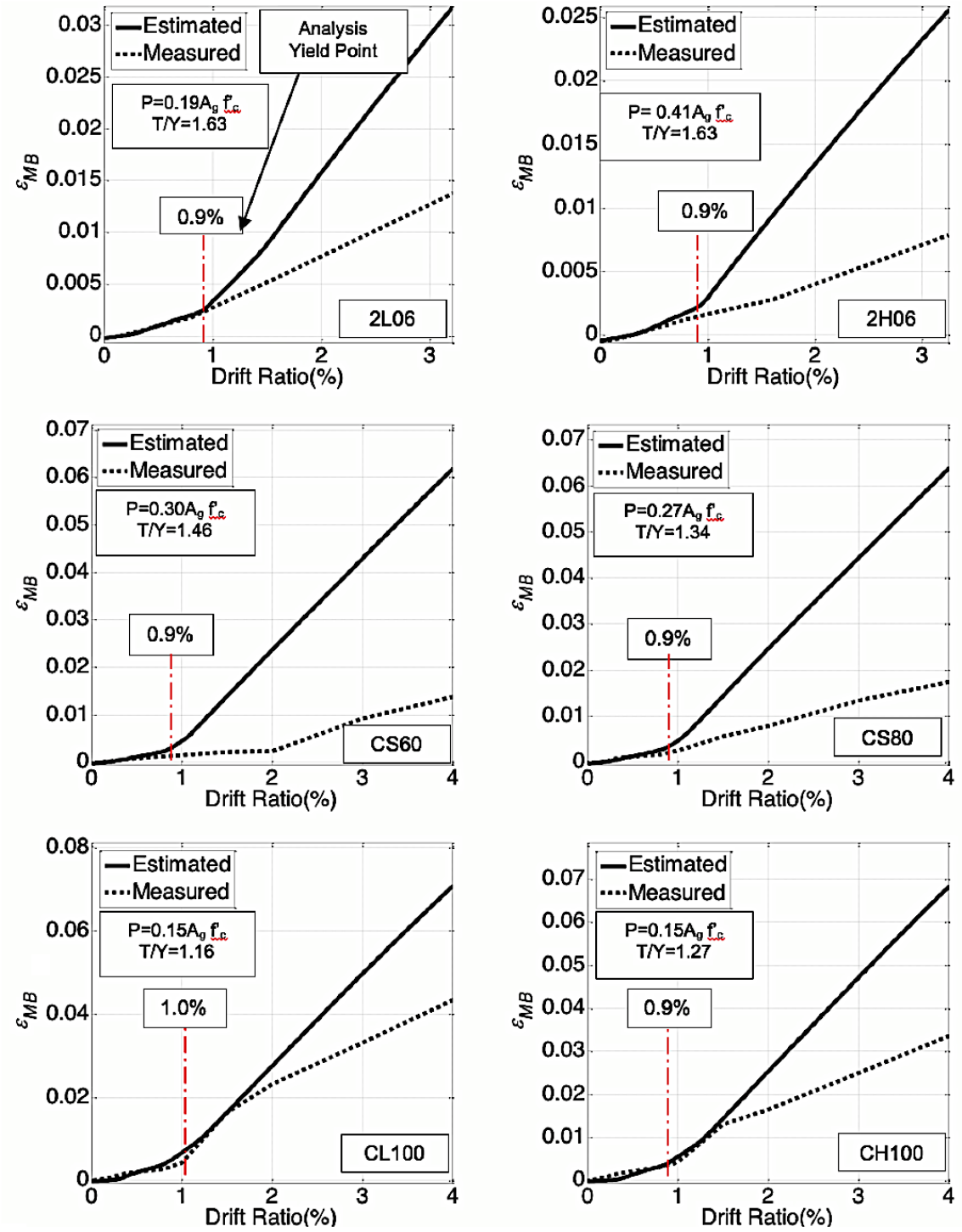

FIGURE 3-21: CONTINUES INTO NEXT PAGE

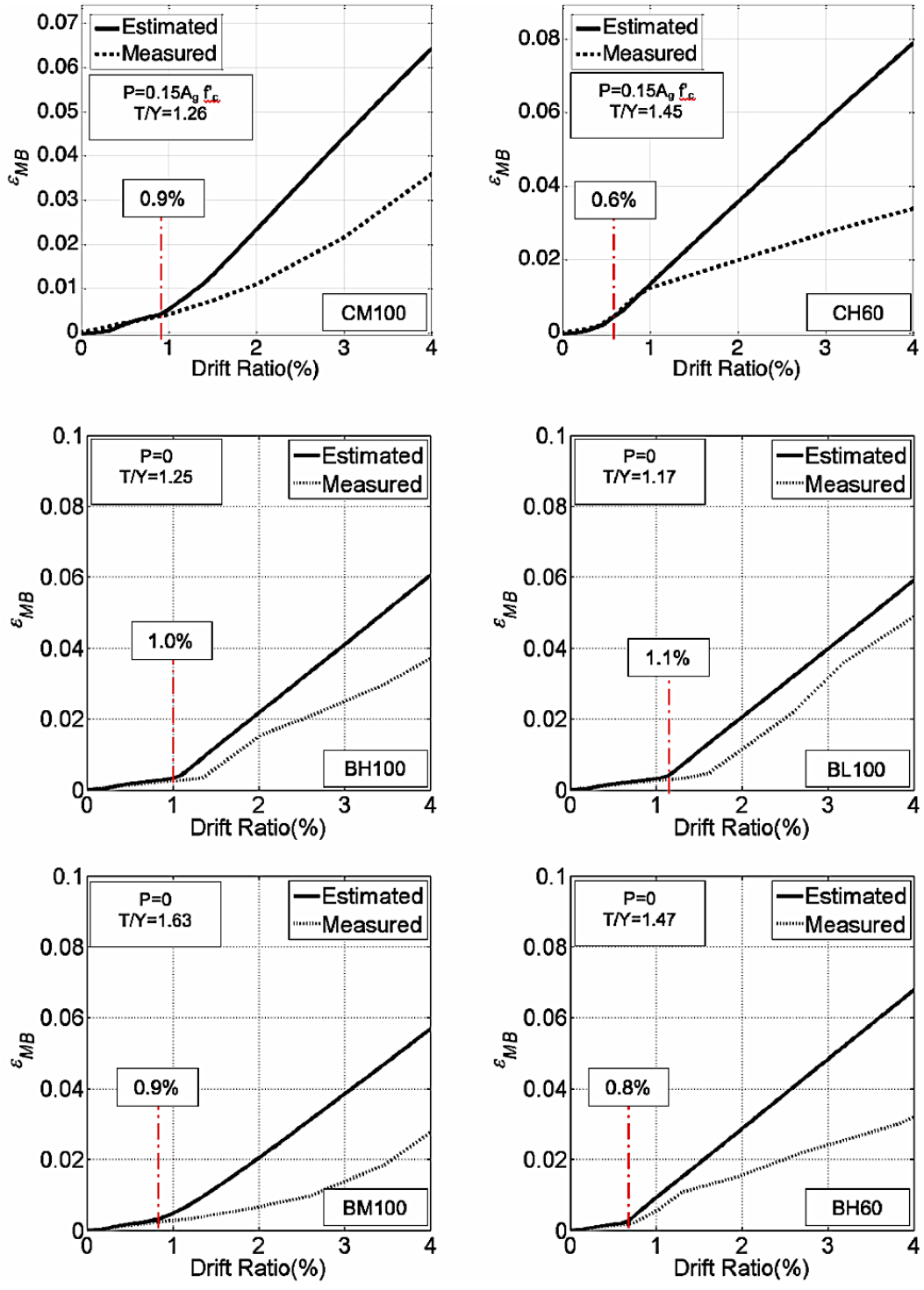

FIGURE 3-21: CONTINUES INTO NEXT PAGE

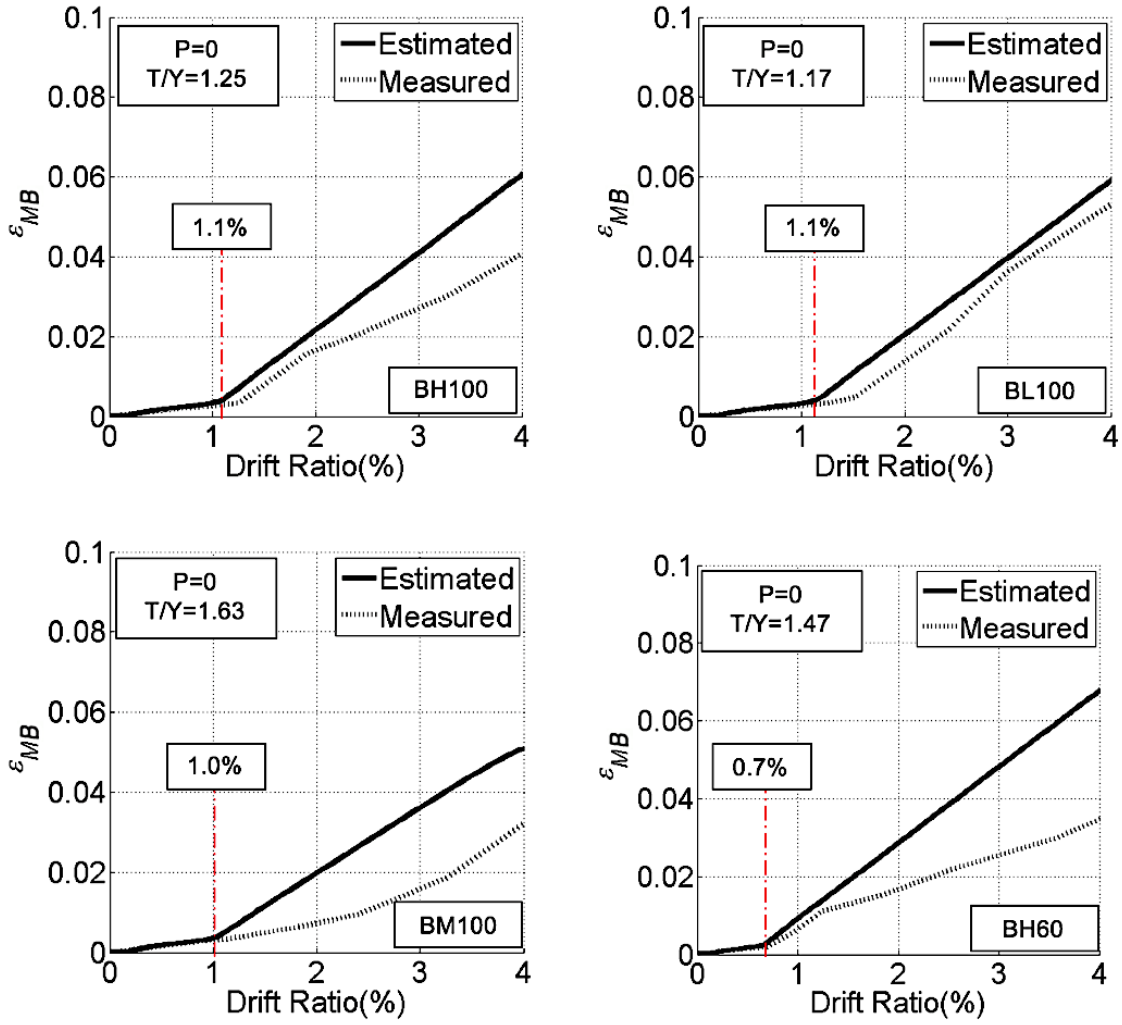

FIGURE 3-21: TENSILE STRAINS FROM ANALYSIS AND MEASURED FOR ALL MEMBERS

3.3 ESTIMATING STRAINS IN REINFORCING BARS

3.3.1 Tensile Strains

Estimated tensile strains were always larger than the measured strains at the sections of peak flexural demand after a "divergence point". Limantono (2016) concluded that the "divergence point" closely coincide with the drifts at first yield and observed associated debonding or spalling cracks around longitudinal bars. The cracking of concrete at the longitudinal reinforcement appeared to allow for inelastic bar strains to spread over a larger length of the bar away from flexural cracks, thereby reducing the peak strain demands from those generated by a fiber-section model that assumes perfect bond. For simplicity and because strains at this level of loading are low enough to not induce damage in the longitudinal bars, the yield strain from analyses was taken as the divergence point between measured and analysis strain results.

Post-yield tension strains in longitudinal bars were scaled through a Tension Scaling Factor (*TSF)*. For each test, the *TSF* factor was obtained at different lateral drift targets in accordance with Equation 3-5:

EQUATION 3-5: TENSILE STRAIN SCALING PROCEDURE

$$\varepsilon_{i-end} = \varepsilon_{i-analysis} \qquad for\ \varepsilon_{i-analysis} \leq \frac{f_y}{29000}$$

$$\varepsilon_{i-end} = \frac{f_y}{29000} + TSF(\varepsilon_{i-analysis} - \frac{f_y}{29000}) \qquad for\ \varepsilon_{i-analysis} > \frac{f_y}{29000}$$

where ε_i is the estimated strain demand at a given lateral drift ratio; $\varepsilon_{i-analysis}$ is the strain demand from the fiber-section analysis at the same lateral drift ratio for the same member, f_y is the yield strength of the longitudinal reinforcement.

The resulting *TSF* values for drift targets of 2.0%, 4.0% and 4.0% are plotted in Figure 3-22. As can be seen in Figure 3-22, the *TSF* was similar between the drift ratios of 2.0% and 4.0% for a given test, but varied greatly from test to test. The final *TSF* to be used in the scaling procedure was calibrated to achieve the highest accuracy at a drift target of 3.0%, where strain levels are also most critical for low-cycle fatigue failures. Moreover, this drift level corresponds to the drift limit specified in ASCE/SEI 7 (2016) for the Maximum Considered Earthquake scenario.

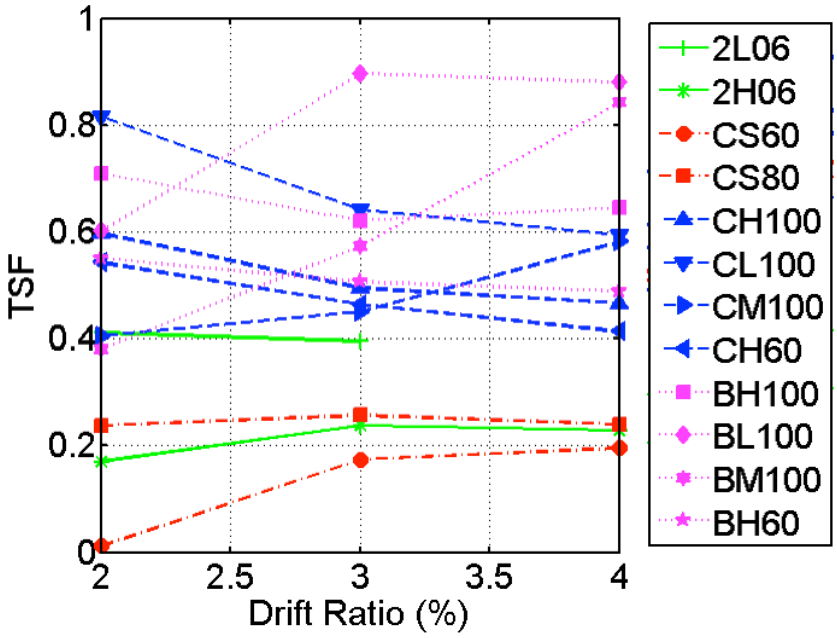

FIGURE 3-22: EXTRACTED *TSF* AT DRIFT RATIOS OF 2%, 3% AND 4%

The estimated *TSF* at 3% drift is plotted versus the most correlated test parameters in Figure 3-23. These parameters were member axial load ratio, member shears stress, and the *T/Y* ratio of the longitudinal bars. Higher axial load demands affect the strain demands in longitudinal bars of concrete members, with a higher axial load ratio having a compressing effect on the tensile strains, and generating greater damage in concrete around the bars at any given drift level. The *TSF* was found to decrease with increasing axial load ratio, thereby reducing strain demands with increasing axial load. Higher shear stresses decrease the scaling factor, or conversely decrease bar strains. This is attributed to the increased concrete damage caused by higher shear stresses, as well as the effects of the tension shift mechanism on plasticity spread (Park and Paulay 1975). Additionally, larger values of the tensile to yield (*T/Y*) ratio of longitudinal bars reduced the scaling factor, which reduces the strain demands in the bars. This indicates that lower *T/Y* ratios concentrate strains in longitudinal bar at the critical flexural crack. This behavior is consistent with observations from laboratory tests (Macchi et al. 1996, Aoyama 2001, Sokoli 2014, Sokoli and Ghannoum 2014).

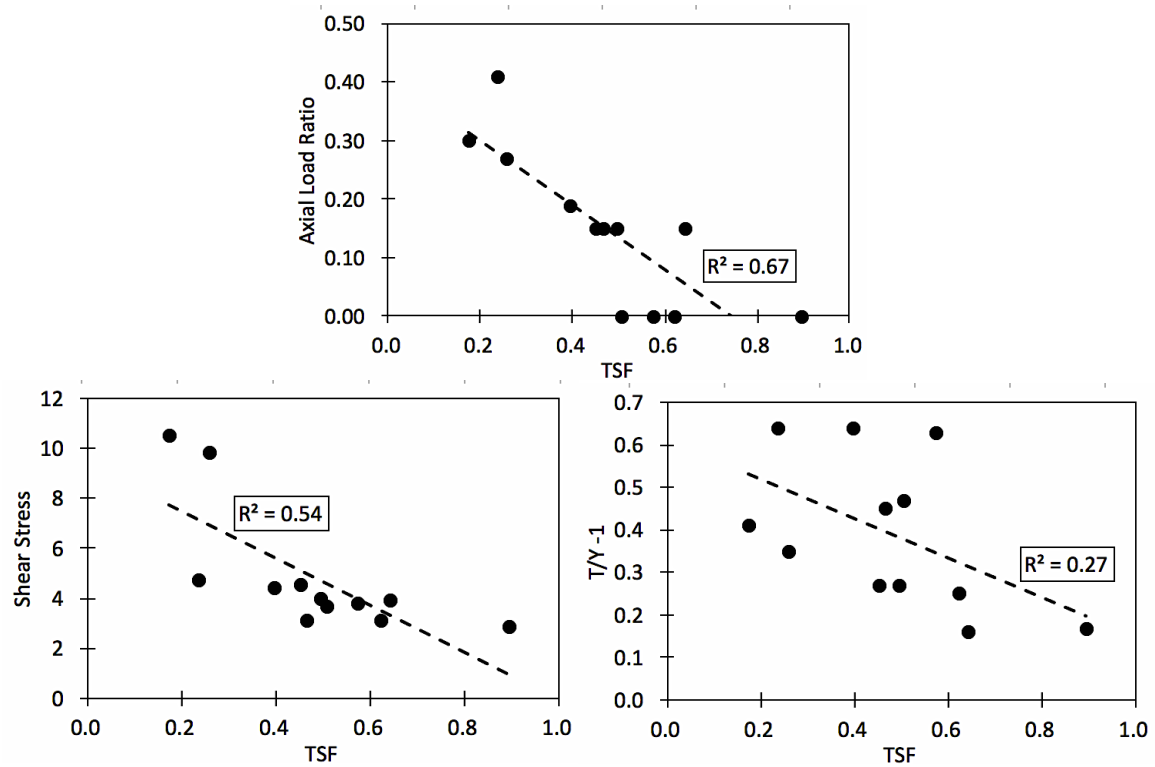

FIGURE 3-23: INFLUENTIAL PARAMETERS ON *TSF*

Equation 3-6 was produced through linear regression to calculate the *TSF* based on the three influential parameters discussed above. Results from Equation 3-6 serve as input in Equation 3-5 to scale fiber-section strains.

EQUATION 3-6: TENSILE STRAIN FACTOR

$$TSF = \frac{9}{10} - \frac{2}{3}\frac{P_o}{A_g f_c'} - \frac{1}{30}\frac{V_o}{bd\sqrt{f_c'}} - \frac{2}{5}\left(\frac{T}{Y} - 1\right)$$

where P_o is the applied axial load (in lb, positive in compression); $A_g$the gross sectional area (in.^{2}); f_c' is the concrete compressive strength (in psi); V_o the maximum expected shear demand and can be obtained from fiber-section analysis (in lb); b and d are

the cross-sectional width and effective depth in inches, respectively; and T/Y is the tensile to yield strength ratio for the longitudinal reinforcement.

The extracted *TSF* at a drift ratio of 3% (as calculated from strain from analysis and mean measured strain), and the estimated *TSF* (calculated using Equation 3-6) are compared in Figure 3-24. The mean error ratio calculated as the ratio of the estimated *TSF* to matched *TSF* was 1.02. The standard deviation was 0.12. The measured and predicted tensile strains up to 4% drift ratio are compared in APPENDIX C.

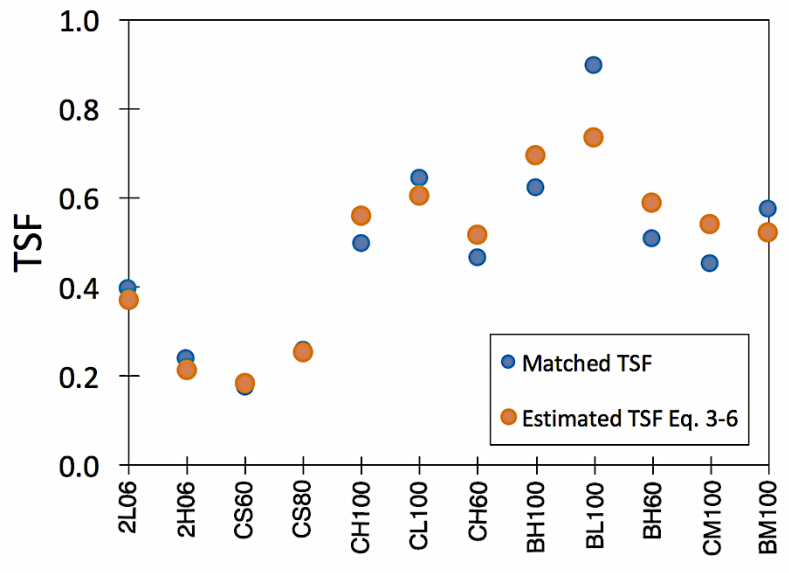

FIGURE 3-24: MATCHED VS. ESTIMATED TSF

3.3.2 Compressive Strains

A behavioral model was developed to estimate compression strains in longitudinal bars. The model is based on observed trends in the compression strains in the column tests. Longitudinal reinforcing bars in beams experienced inelastic strains when the surrounding concrete was in compression that ranged from 0 to positive 4% (i.e., tensile strains). The beams were not restrained longitudinally during testing, which allowed them to elongate as they were cycled laterally. However, beams in a moment frame are typically restrained by a slab and columns or walls and therefore are not able to elongate to the same extent as in the laboratory tests. As such bar strains in beams may be closer to those obtained from the fiber-section analysis in structural systems. Moreover, high variability was observed in compression strains between members and even on bars of the same member, due to the highly variable distribution of concrete damage.

The best predictor of bar stains in compression was found to be axial load (Figure 3-25).

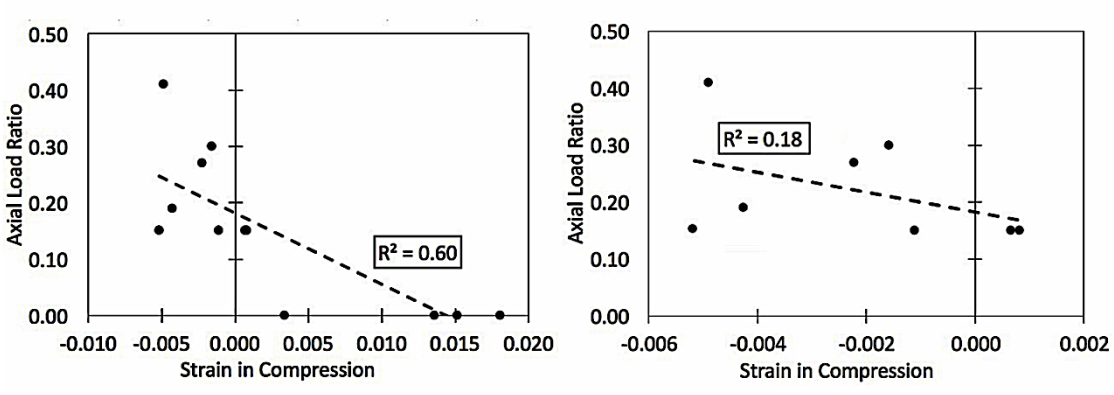

FIGURE 3-25: MEAN MEASURED STRAIN IN COMPRESSION AT 3% DRIFT RATIO VS. AXIAL LOAD RATIO (LEFT) ALL MEMBERS, (RIGHT) COLUMNS ONLY

To constrain the model, for members that are not designed to carry axial loads, the strain in bars when concrete surrounding them is in compression was taken as zero at a drift ratio of 3%. Following observed experimental trends in columns, the strain in compression at a drift ratio of 3% was taken as -0.5% for a member loaded at an axial load ratio of 50%. For axial load ratios between 0 and 50%, strain in the bars at a drift ratio of 3% can be obtained by linear interpolation as given in Equation 3-7:

EQUATION 3-7: STRAIN IN COMPRESSION AT A DRIFT RATIO OF 3%

$$\epsilon_{EC} = \frac{P_o}{100\, A_g\, f_c'}$$

Scaling of the strains in the compression strain region obtained from fiber-section analyses for all drift levels can be accomplished by using a Compression Strain Factor (*CSF*) as follows:

EQUATION 3-8: COMPRESSION STRAIN SCALING PROCEDURE

$$\varepsilon_i = CSF \times \varepsilon_{i-analysis} \qquad for\ 0 > \varepsilon_{i-analysis}$$

EQUATION 3-9: COMPRESSION STRAIN SCALING FACTOR

$$CSF = \frac{\epsilon_{EC}}{\epsilon_{CA3}}$$

where ϵ_{CA3} is the compression strain from fiber-section analysis taken at a drift ratio of 3%.

3.3.3 Cyclic Strain Demands

To obtain the cyclic strain history for longitudinal bars at the critical moment sections of frame members, the Tension Scale Factor (*TSF*) and Compression Scale Factor (*CSF*) are to be applied per Equation 3-10. Scaling of bar strain is not necessary until bars exceed their yield strain for the first time as the fiber-section model is able to accurately capture those strains. In theory, after first yield all tension strains are to be scaled, but it is assumed here that strains between zero and tension yield are relatively small and therefore are not scaled (Figure 3-26).

EQUATION 3-10: SUMMARY OF SCALING PROCEDURE FOR STRAINS IN LONGITUDINAL BARS

$$\varepsilon_{i-end} = CSF \times \epsilon_{i-analysis} \qquad for\ \varepsilon_{i-analysis} < 0$$

$$\varepsilon_{i-end} = \epsilon_{i-analysis} \qquad for\ 0 \le \varepsilon_{i-analysis} \le \frac{f_y}{29000}$$

$$\varepsilon_{i-end} = \frac{f_y}{29000} + TSF(\varepsilon_{i-analysis} - \frac{f_y}{29000}) \qquad for\ \varepsilon_{i-analysis} > \frac{f_y}{29000}$$

where:

$$CSF = \frac{\epsilon_{EC}}{\epsilon_{CA3}};\ \epsilon_{EC} = \frac{P_o}{100\ A_g\ f_c'}$$

$$TSF = \frac{9}{10} - \frac{2}{3}\frac{P_o}{A_g f_c'} - \frac{1}{30}\frac{V_o}{bd\sqrt{f_c'}} - \frac{2}{5}(\frac{T}{Y} - 1)$$

A comparison between scaled fiber-section strains and typical measured strains from beam and column tests is presented in Figure 3-27.

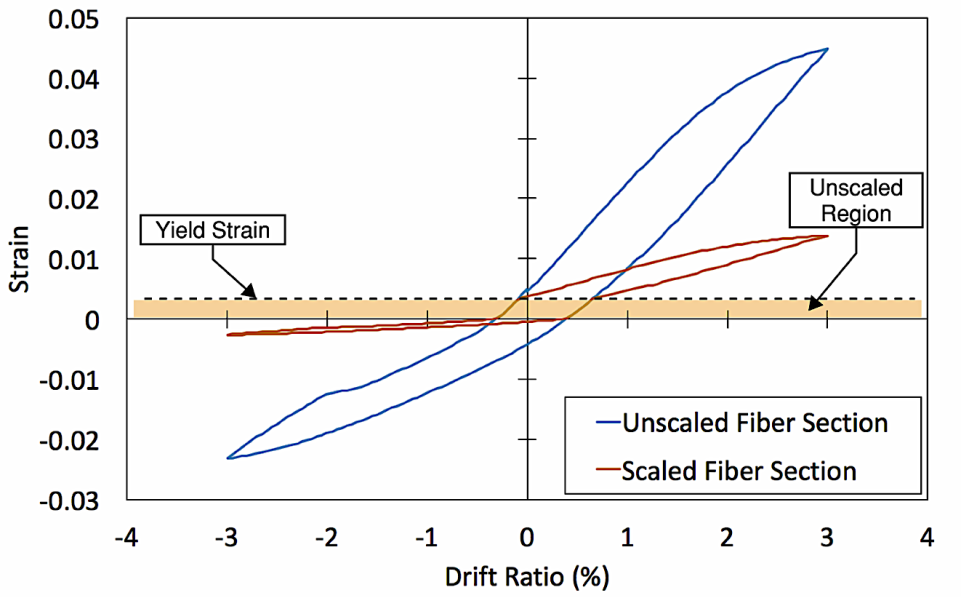

FIGURE 3-26: COMPARISON OF UNSCALED VS. SCALED STRAIN DEMANDS FROM ANALYSIS FOR A CYCLE OF LOADING IN CS80

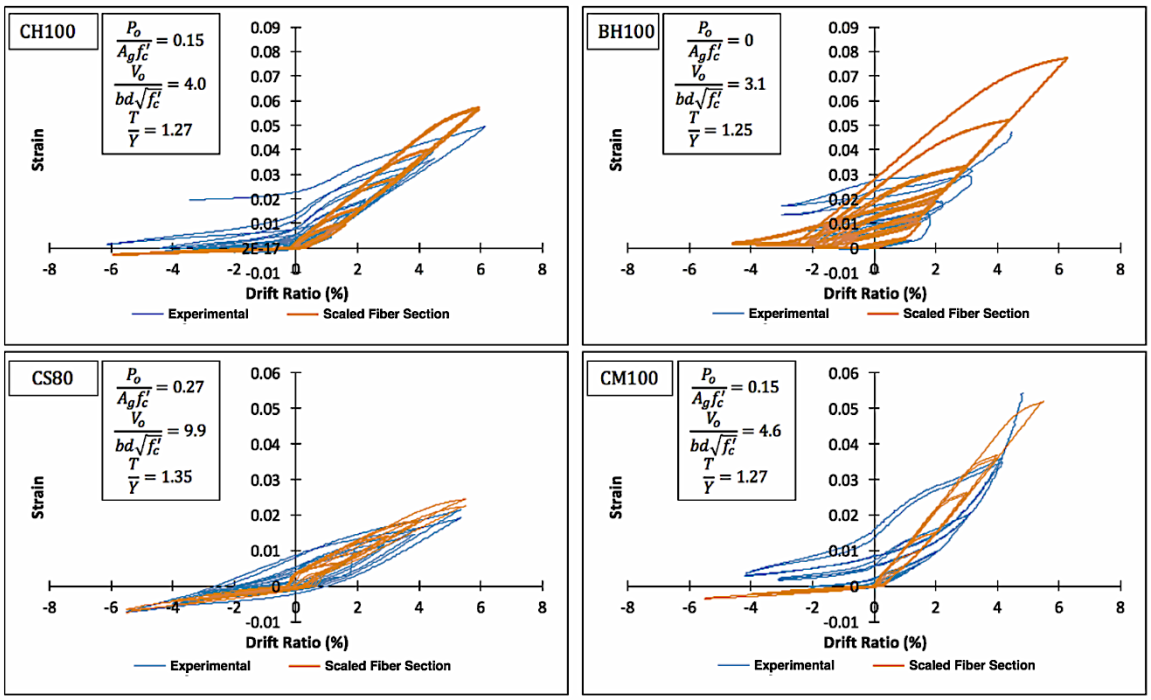

FIGURE 3-27: COMPARISON OF A TYPICAL CYCLIC STRAIN GAUGE READING AND CORRESPONDING SCALED RESULT FROM FIBER-SECTION ANALYSES

3.4 CONCRETE SURFACE STRAINS

In several applications, it is useful to estimate the smeared longitudinal strain in the concrete or steel bar over a member length approximating the location of peak strain concentrations. One such application consists of estimating the smeared longitudinal bar strain over it potential buckling length, from member end where moments are maximum to the location of the second hoop (for inter-hoop buckling). This could be used to identify the potential point of bar buckling initiation. Relations to estimate such strains from fiber-section bar strains extracted at the section of peak moment are presented in this section.

3.4.1 Tensile Strains

Tensile surface strains in the plastic hinge region versus strains from analysis in the reinforcing bars at the section of maximum demand are plotted in Figure 3-28 for six of the members for which the experimental data was available. These strains included the bar-slip crack at the interface of the member to the footing and were measured over a gage length of 7 inches, which is about 8.5% of the member length for CS60 and CS80 and 6.5% of the member length for CH100, CL100, CM100, and CH60. The analytical model included a plastic hinge of 5% of the length of each member, with deformation concentrated at the end of the member.

Because the scope of the study to obtain accurate estimates of strain demands at higher drift ratios that contribute more to the damage in the section, a similar approach to

the scaling of strains in the longitudinal bars was taken assuming that estimated strains from analysis diverge at first yield from measured strains.

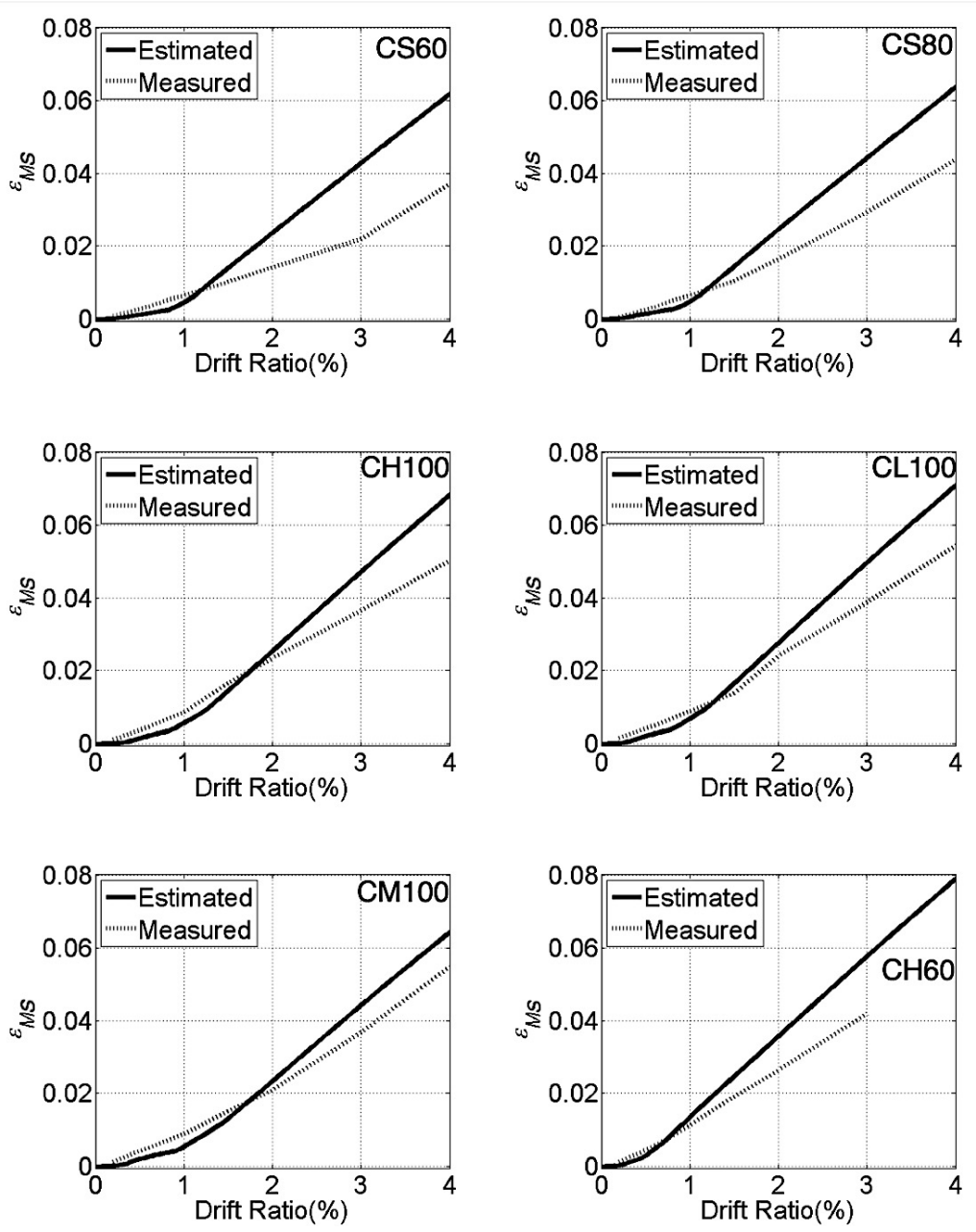

FIGURE 3-28: MEAN MEASURED TENSILE SURFACE STRAINS VS. ESTIMATED STRAINS FROM ANALYSIS

Post-yield tension strains in longitudinal bars at the critical section were scaled through a Surface Tension Scaling Factor (*STSF).* The *STSF* was obtained in accordance with Equation 3-11:

EQUATION 3-11: TENSILE STRAIN SCALING PROCEDURE

$$\varepsilon_{i-buckling} = \varepsilon_{i-analysis} \qquad for\ 0 \leq \varepsilon_{i-analysis} \leq \frac{f_y}{29000}$$

$$\varepsilon_{i-buckling} = \frac{f_y}{29000} + STSF(\varepsilon_{i-analysis} - \frac{f_y}{29000}) \qquad for\ \varepsilon_{i-analysis} > \frac{f_y}{29000}$$

where ε_i is the estimated strain demand at a given lateral drift ratio; $\varepsilon_{i-analysis}$ is the strain demand from the fiber-section analysis at the same lateral drift ratio for the same member, f_y is the yield strength of the longitudinal reinforcement.

The resulting *STSF* values for drift targets of 2.0%, 3.0%, and 4.0% are plotted in Figure 3-29. As can be seen in Figure 3-29, the S*TSF* was observed to be similar between the drift ratios of 2.0% and 4.0% for a given test, but varied from test to test. The final *STSF* was calibrated to the for higher accuracy at a lateral drift target of 3.0%.

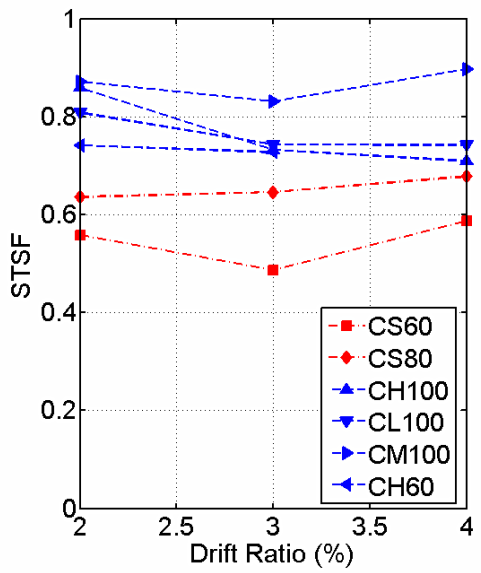

FIGURE 3-29: EXTRACTED *STSF* AT DRIFT RATIOS OF 2%, 3% AND 4%

The *STSF* at 3% drift was found to correlate with the axial load ratio. The *STSF* decreased with increasing axial load ratio, thereby reducing strain demands with increasing axial load.

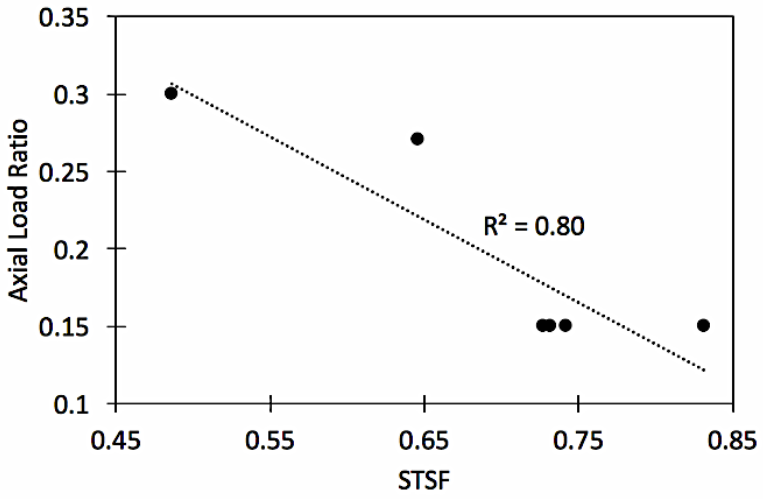

FIGURE 3-30: INFLUENTIAL PARAMETER ON *STSF*

Equation 3-12 was produced through linear regression to calculate the *STSF* based on column axial load ratio. Other terms considered, such as the longitudinal reinforcement yield strength and concrete compressive strength improved the accuracy of the relation, but the increase in accuracy did not justify the increase in complexity. The equation converges to a *STSF* of 1 for members with zero axial load.

EQUATION 3-12: TENSILE STRAIN FACTOR

$$STSF = 1 - 1.5\frac{P_o}{A_g f_c'}$$

where P_o is the applied axial load (in lb, positive in compression); $A_g$the gross sectional area (in.^{2}); f_c' is the concrete compressive strength (in psi);

The mean error ratio calculated as the ratio of the estimated *STSF* to matched *STSF* was 1.02. The standard deviation was 0.08. The measured and predicted tensile strains up to 4% drift ratio are compared in APPENDIX C.

3.4.2 Compressive Strains

Compression surface strains in the plastic hinge region versus strains from analysis in the reinforcing bars at the section of maximum demand are given in Figure 3-31 for six of the members for which the experimental data was available. Measured strains were measured over a gage length of 7 inches, same as the tension surface strains.

Equation 3-13 can be used to obtain the surface compression strains from strains from analysis through the Surface Compression Strain Factor (*SCSF*).

EQUATION 3-13: TENSILE STRAIN SCALING PROCEDURE

$$\varepsilon_{si} = SCSF \times \varepsilon_{i-analysis} \qquad for\ \varepsilon_{i-analysis} < 0$$

where ε_{si} is the estimated surface strain demand at a given lateral drift ratio; $\varepsilon_{i-analysis}$ is the strain demand from the fiber-section analysis at the same lateral drift ratio for the same member.

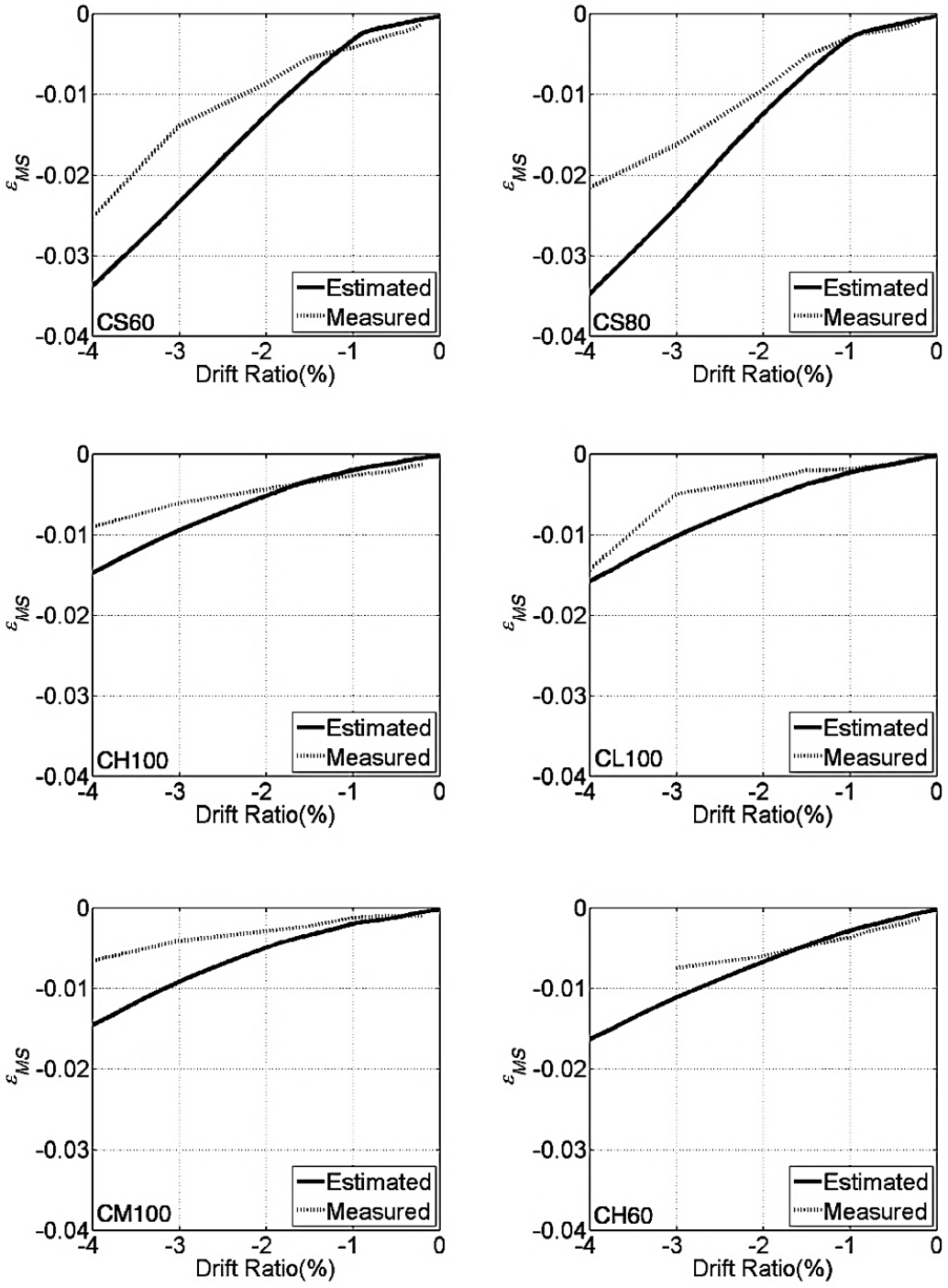

FIGURE 3-31: MEAN MEASURED COMPRESSION SURFACE STRAINS VS. ESTIMATED STRAINS FROM ANALYSIS

The resulting *SCSF* values for drift targets ranging from 2.0% to 4.0% are plotted in Figure 3-32. As observed in Figure 3-32, the S*CSF* was similar between the drift ratios of 2.0% and 4.0% for a given test. No clear correlation was found between the *SCSF* and test parameters. Therefore, the mean value of *SCSF* at 3% drift was taken between the six members, leading to a value of 0.6.

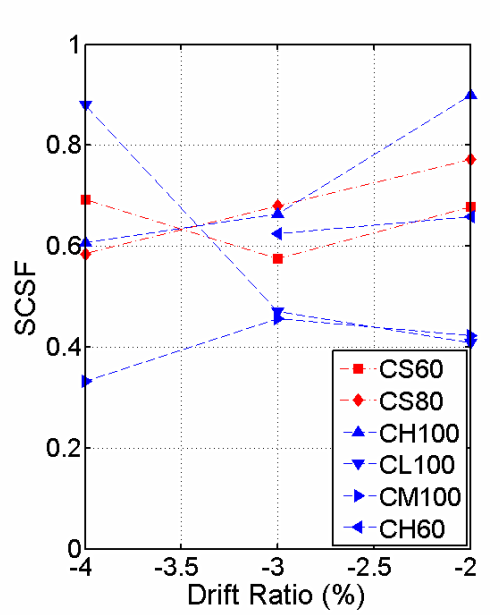

FIGURE 3-32: EXTRACTED *STSF* AT DRIFT RATIOS OF 2%, 3% AND 4%

EQUATION 3-14: COMPRESSION STRAIN FACTOR

$$SCSF = 0.6$$

The mean error ratio calculated as the ratio of the estimated *SCSF* to matched *SCSF* was 1.07. The standard deviation was 0.2.

3.4.3 Cyclic Strain Demands

To obtain the cyclic surface strain history over a height of about 7% of column length, the Surface Tension Scale Factor (*STSF*) and Surface Compression Scale Factor (*SCSF*) are applied per Equation 3-15 to scale strains from the proposed fiber-section analysis at the location of maximum moment. Scaling of bar strain is not necessary until bars exceed their yield strain for the first time as the fiber-section model is able to accurately capture strains up to that point. In theory, after first yield all tension strains are to be scaled, but it is assumed here that strains between zero and tension yield are relatively small and therefore are not scaled (Figure 3-33).

EQUATION 3-15: SUMMARY OF SCALING PROCEDURE FOR SURFACE CONCRETE STRAINS

$$\varepsilon_{si} = SCSF \times \epsilon_{i-analysis} \qquad for\ \varepsilon_{i-analysis} < 0$$

$$\varepsilon_{si} = \epsilon_{i-analysis} \qquad for\ 0 \leq \varepsilon_{i-analysis} \leq \frac{f_y}{29000}$$

$$\varepsilon_{si} = \frac{f_y}{29000} + STSF(\varepsilon_{i-analysis} - \frac{f_y}{29000}) \qquad for\ \varepsilon_{i-analysis} > \frac{f_y}{29000}$$

where:

$$SCSF = 0.6$$

$$STSF = 1 - 1.5\frac{P_o}{A_g f_c'}$$

A typical measured cyclic strain in the concrete surface of CH100 is compared to the corresponding unscaled and scaled results from fiber-section analysis in Figure 3-34.

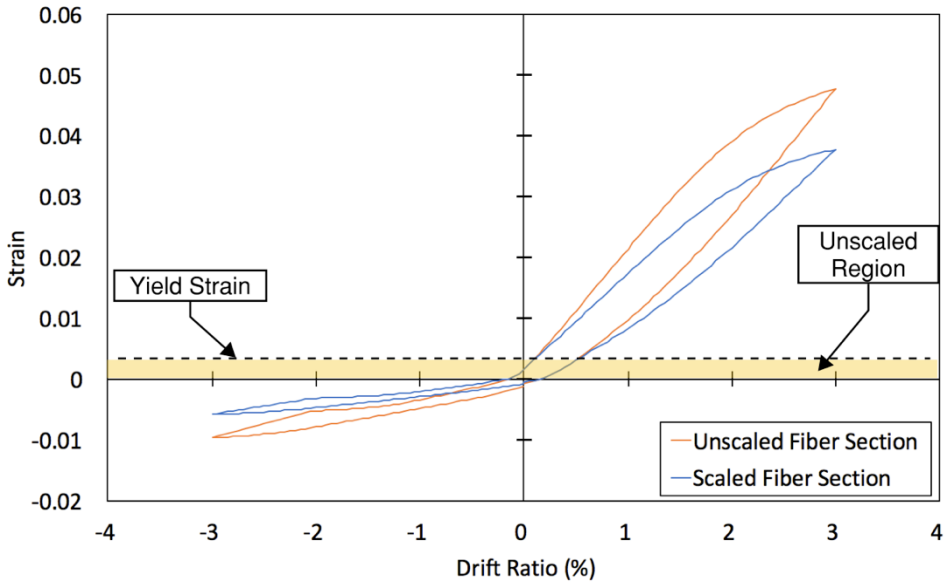

FIGURE 3-33: COMPARISON OF UNSCALED VS. SCALED STRAIN DEMANDS FROM ANALYSIS FOR A CYCLE OF LOADING IN CH100

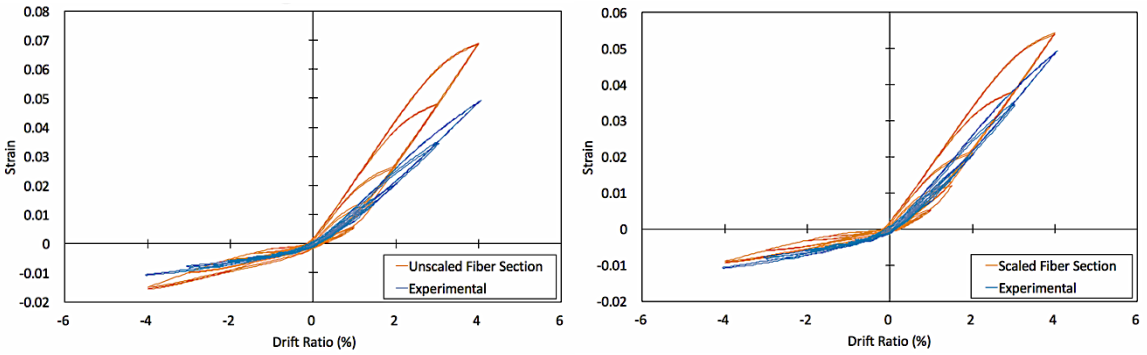

FIGURE 3-34: COMPARISON OF A TYPICAL MEASURED CYCLIC STRAIN IN THE CONCRETE SURFACE OF CH100 VS. CORRESPONDING UNSCALED AND SCALED RESULTS FROM FIBER-SECTION

3.5 SUMMARY AND CONCLUSIONS

A behavioral model is proposed to scale strain estimates obtained from a calibrated force-formulation fiber-section computational element to achieve desired representative strain estimates. The framework is calibrated using 12 cyclic experimental tests conducted on concrete columns and beams that were cycled to large damage states and in some cases bar fracture. The resulting computational framework is capable of matching the global deformation behavior of reinforced concrete members through the fiber-section element, and provides reliable strain demands in the longitudinal bars and surrounding concrete through the full range of expected inelastic deformations. It was found that:

- Tension strains in longitudinal bars depend on the axial load ratio, shear stress, and tensile-to-yield-strength ratio of the steel.
- Compression strains in bars depend on the axial load ratio
- Tension strains in the concrete surface within the plastic hinge region depend on axial load ratio
- No clear correlation was found between test parameters and the ratio of concrete surface compression strains to strains from analysis.

The accurate estimate of strains in the longitudinal bars and surrounding concrete at the point of maximum demands provides reliable estimates of material damage and strength degradation, particularly for applications considering longitudinal bar fracture and buckling.

3.6 LIMITATIONS AND RECOMMENDATION FOR FUTURE WORK

It was the purpose of this study to use results from well-controlled and instrumented lateral load tests of concrete members incorporating different grades and types of reinforcement. As such, a limited number of tests were available. As more tests on concrete members with different grades and types of steel are carried, future work should focus on increasing the accuracy in strain demand prediction, by calibrating and validating the framework to a larger dataset. Also, it may be useful to distinguish strain models for bars with a rounded stress-strain relation (e.g., ASTM A1035) and those with a distinct yield point (e.g., ASTM A706).

4. PAPER 3: BUCKLING AND FRACTURE OF HSRB IN SPECIAL MOMENT FRAME MEMBERS [1]

Special Moment Frame (SMF) members undergoing typical flexural degradation under seismic loads are subjected to longitudinal bar yielding, concrete crushing, longitudinal bar buckling and/or fracture. While longitudinal bar fracture has typically not been of major concern in concrete members of SMF, it is gaining more attention as higher strength reinforcing bars (HSRB) with lower fracture elongation and low-cycle fatigue life are introduced to the market. A methodology for predicting longitudinal bar buckling initiation and fracture in SMF members is proposed. The methodology is based on estimates of local strain demands in longitudinal bars of SMF members. A buckling initiation model is proposed that accounts for the mechanical properties of the reinforcing bars, as well as the loading history the bars and surrounding concrete experience prior to buckling. Material specific bar fatigue relations calibrated through material test results are used to predict the number of half-cycle to bar fracture based on accumulation of strain demands prior and after buckling, if it occurs.

[1] *The material presented in this chapter and the corresponding appendices has not been published elsewhere. However, the manuscript is to be submitted for review with the following authors: Sokoli, D., Hogsett, G., Slavin, C., Limantono A., To D.V., Moehle J.P., and, Ghannoum, W.M. D. Sokoli was the lead student investigator of the project, responsible for carrying the analysis and writing the manuscript. G. Hogsett and C. Slavin carried material testing. A. A. Limantono assisted with the analysis. D.V. To and J.P. Moehle provided the data from experimental testing (Series 4) and reviewed the manuscript. W. M. Ghannoum supervised the research, reviewed and edited the manuscript.*

4.1 INTRODUCTION

Special Moment Frame (SMF) members undergoing typical flexural degradation under seismic loads are subjected to longitudinal bar yielding, concrete crushing, longitudinal bar buckling and/or fracture. While longitudinal bar fracture has typically not been of concern in concrete members of SMF, it is gaining more attention as higher strength reinforcing bars (HSRB) with lower fracture elongation and low-cycle fatigue life are introduced to the U.S. market. A methodology for predicting longitudinal bar buckling initiation and fracture in SMF members is proposed. The methodology is based on estimates of local strain demands in longitudinal bars of SMF members and accounts for member properties and loading conditions, as well as the mechanical properties of reinforcing bars.

The proposed methodology is intended for use with reinforced concrete beams and columns that satisfy ACI 318-14 Special Moment Frame requirements. For this reason, it is assumed that one or both of the following strength degradation mechanisms occur (Figure 4-1):

1. The strain history demand at the point of maximum moment leads to the longitudinal bars fracturing at that location (typically at member end).
2. Longitudinal bars buckle between hoops (typically between the first and second hoops from member ends), which generates strain concentrations within the buckled length and eventually lead to bar fracturing within the buckled length, typically at a distance equal to spacing of the ties from the end of the member.

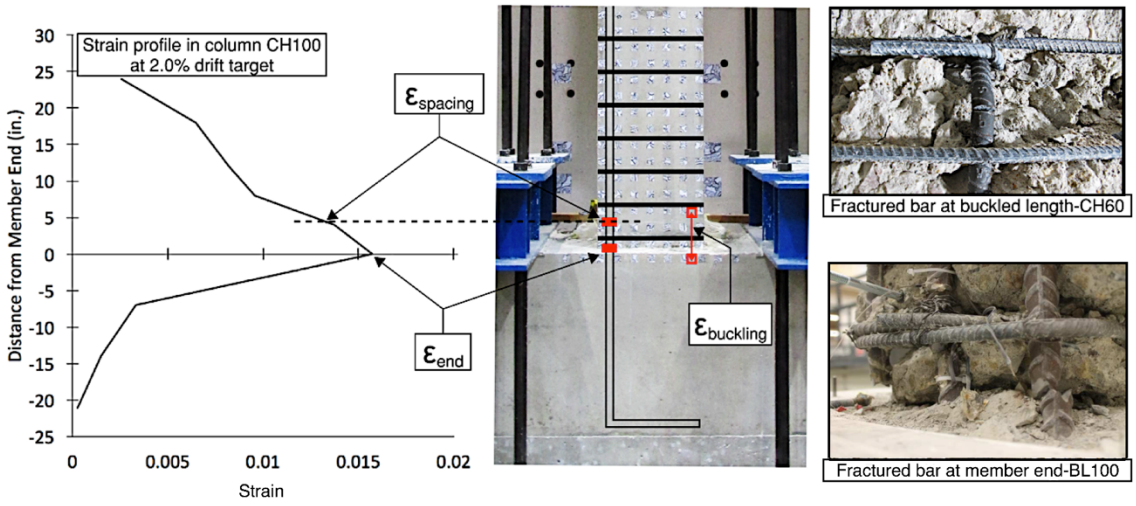

FIGURE 4-1: TYPES OF REPRESENTATIVE STRAINS AND BAR FRACTURE LOCATIONS

The sequence of the two listed possible events is tracked in the proposed methodology in order to determine if and which occurs first, as illustrated in the flow chart in Figure 4-2. The starting point for the methodology is estimating the deformation or strain histories of frame members during a simulated seismic event. If the frame members are modeled using lumped plasticity elements in the structural simulation, then a fiber-section representation of each member is generated and run through the deformation and loading history of the member. The framework introduced in Chapter 3 for deriving accurate strain demands is then used to scale fiber-section strains to obtain representative longitudinal bar strain histories at the section of maximum moment and at mid-span of the potential bar-buckled shape (i.e., half way between the first two hoops from member end), as well as longitudinal strain histories for the concrete around the potential bar buckling region. Alternatively, if the structural model is constructed directly using fiber-section elements in accordance with recommendations in Chapter 3, then representative bar and concrete

strains could be obtained by directly scaling the fiber-section element strains per Chapter 3. The strain scaling procedure is described in more detail in Section 4.3.

At the location of maximum moment, bar buckling cannot occur (Figure 4-1). Therefore, strain histories at that location are used to estimate bar damage due to fatigue using a Coffin-Manson (Manson 1953, Coffin 1954) type relation that was calibrated using fatigue tests on essentially unbuckled bars (Ghannoum and Slavin 2016, Hogsett 2017). If the damage index calculated using the fatigue model reaches a value of 1.0 during an earthquake scenario, then bars are deemed to fracture at the member end during that scenario, unless bar fracture occurs at the bar buckle first.

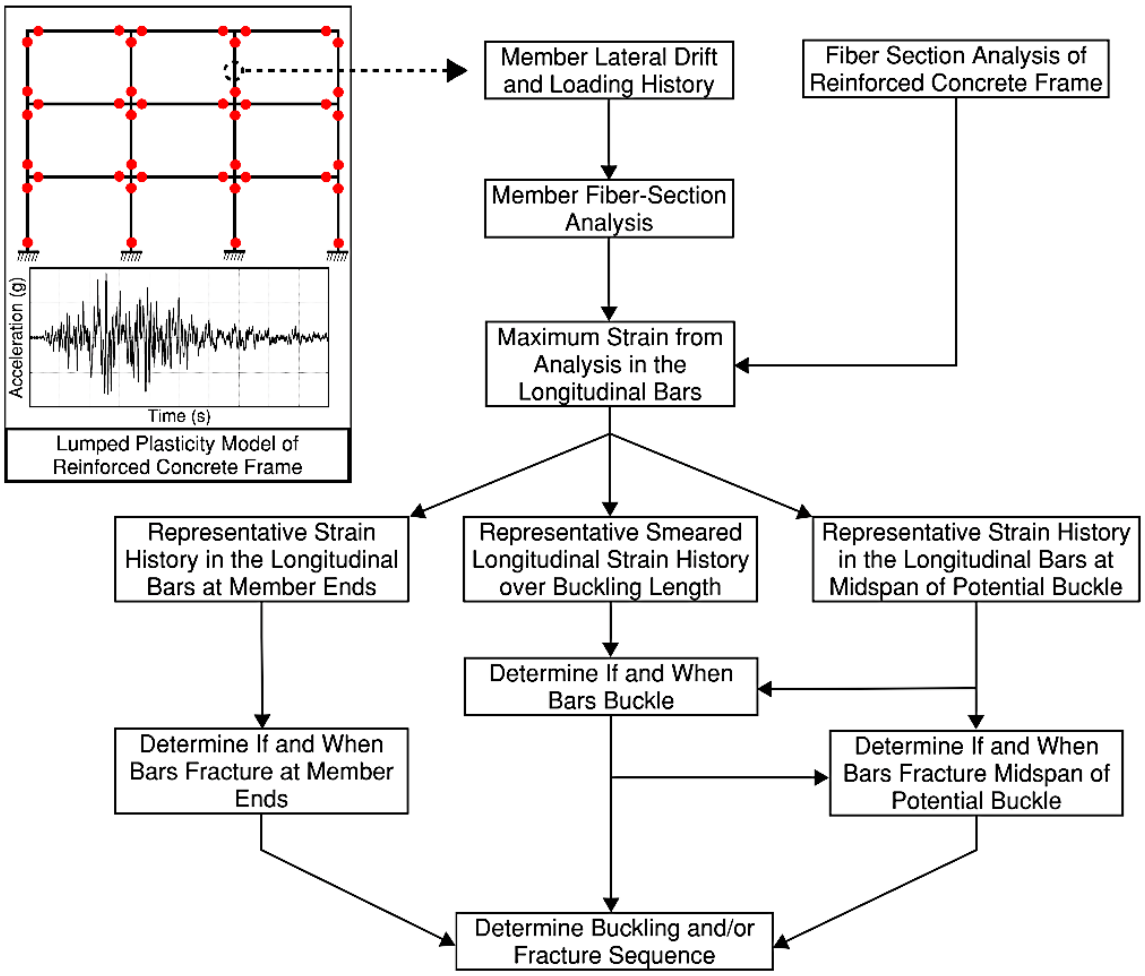

FIGURE 4-2: FLOW-CHART FOR PREDICTING BAR FRACTURE IN SMF MEMBERS

At mid-span of the potential buckled shape, however, strain demands in the longitudinal bar are lower than those at the section of maximum moment until bar buckling occurs (Figure 4-1). Therefore, fracture at that location cannot materialize if bar buckling does not occur. Once bar buckling occurs, curvature demands tend to localize at that weakened location, while strain concentrations increase in the bars due to the buckled

shape (Figure 4-3). Therefore, after buckling, strain demands in the longitudinal bars within the buckled length can outpace those at the section of maximum moment, forcing the damage index to exceed 1.0 and bars to fracture at the buckled location. The proposed methodology requires tracking the damage index due to pre and post buckling strain demands at both potential locations of fracture to determine if and where bar fracture will occur during an earthquake scenario (Figure 4-2). A buckling initiation model is also proposed to determine if and when bar buckling occurs during an earthquake scenario.

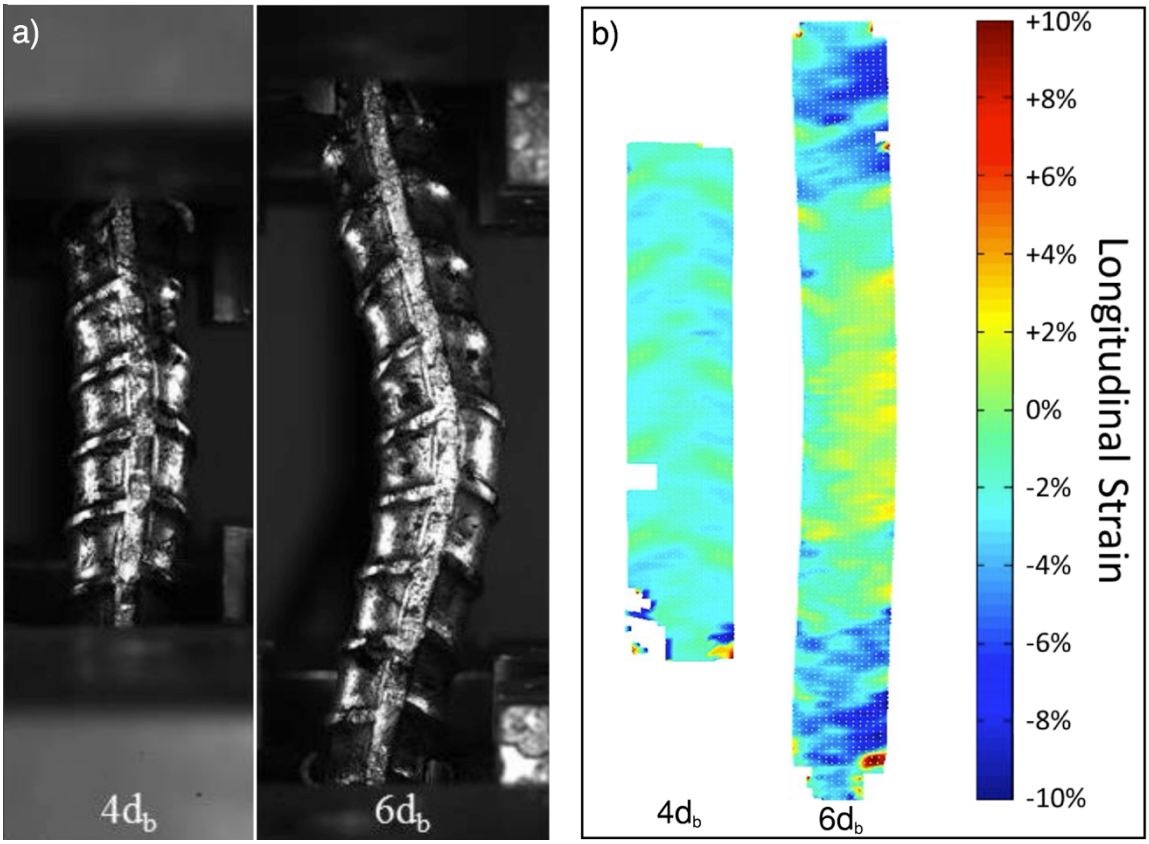

FIGURE 4-3: LOW CYCLE FATIGUE TESTS OF BARS GRIPPED AT SPANS OF 4 AND 6 BAR DIAMETER: A) PICTURES OF GRADE 100 BARS DURING TESTING B) MEASURED LONGITUDINAL STRAINS IN GRADE 80 BARS DURING TESTING (ADOPTED FROM GHANNOUM AND SLAVIN 2016)

4.2 EXPERIMENTAL DATA

The experimental data used to calibrate the proposed buckling initiation model and validate the bar fracture methodology was extracted from four series of tests carried on twelve reinforced-concrete beams and columns having various reinforcing steel grades and stress-strain properties.

- Series 1 reversed cyclic tests were conducted on moderately confined columns sustaining shear and axial failure (Leborgne, 2012). The two columns in Series 1 (2L06, 2H06) were nominally identical in design and detailing. Both were reinforced with grade 60 ASTM A615 bars. In this publication, grade refers to the specified yield strength of steel bars. Columns were loaded under the same lateral cyclic protocol but a different axial load was applied to each. Series 1 columns sustained significant flexural yielding prior to shear and axial failures. Bar buckling was not observed in these columns prior to shear failure.
- Series 2 tests (CS60, CS80) investigated the ability of high-strength transverse reinforcement in maintaining confinement integrity and the shear strength of concrete columns during inelastic demands (Sokoli 2014, Sokoli and Ghannoum 2016). These two columns were designed to have equivalent moment strength and constructed using different grades of reinforcement: grade 60 ASTM A706 bars for CS60, and grade 80 ASTM A706 bars for CS80. Hoop spacing varied between the columns. Series 2 columns were well confined and satisfied ACI 318-14 Special Moment Frame provisions. Columns CS60 and CS80 sustained flexural yielding

prior to shear and axial failures. Bar buckling was not observed in these columns prior to shear failure.

- Series 3 tests (CH100, CL100, CM100, CH60) investigated the effects of varying stress-strain relations of the longitudinal bars on the plasticity spread and deformation capacity of concrete columns (Sokoli et al. 2017). All columns were geometrically identical, reinforced with the same longitudinal bar layout and size. Three of these columns were reinforced with grade 100 steel sourced from different steel manufacturing processes, which led to different post-yield stress-strain curves. Column CH60 was reinforced with grade 60 A706 bars. Hoop spacing was tighter for the columns with grade 100 steel than for the column with grade 60 steel to mitigate the higher buckling propensity of higher strength bars. The four specimens sustained a flexural mode of degradation characterized by concrete crushing, varying degrees of longitudinal bar buckling, and eventually longitudinal bar fracture. Column CM100 reinforced with ASTM A1035 steel exhibited almost no bar buckling prior to bar fracture at column end where moment demands were largest. All other columns sustained longitudinal bar fracture with the buckled length after significant buckling.
- Series 4 tests were conducted on four beams (BH100, BL100, BM100, BH60) reinforced with the same steel as Series 3 columns (To and Moehle 2017). The beams had nominally identically dimensions and concrete material properties, but were designed to maintain the same nominal moment strength across bar grades.

Hoop spacing was also tighter in this series for beams with grade 100 bars than for the beam with grade 60 reinforcement. All members failed at relatively high lateral deformation demands due to bar fracture or global instability. Limited buckling of longitudinal bars was observed in the beam tests.

Relevant structural parameters for each specimen are summarized in Table 3-1, and observed failure modes in Table 4-2 and Table 3-2. Additional information about the design, material properties, and loading protocol of each specimen is presented in APPENDIX C.

TABLE 4-1: STRUCTURAL PARAMETERS FOR EACH SPECIMEN

Member	Section Effective Depth (d)[1] (in.)	Concrete Comp. Strength (ksi)	Axial Load Ratio[2]	Shear Stress[3] ($\sqrt{f_c'}$ psi)	Shear Span to Section Depth Ratio	Long. Bar Dia. (in.)	Long. Reinf. Ratio[3]	Long. Bar Yield Strength (ksi)	T/Y[4] Strength Ratio	Hoop Spacing / Long. Bar Dia.
2L06	13.50	3.13	0.19	4.46	4.00	1.00	0.025	65.5	1.64	6.0
2H06	13.50	3.34	0.41	4.74	4.00	1.00	0.025	65.5	1.64	6.0
CS60	15.27	3.83	0.30	10.55	2.75	1.25	0.047	67.3	1.41	4.4
CS80	15.44	4.29	0.27	9.86	2.72	1.13	0.037	79.1	1.35	4.9
CH100	16.13	5.16	0.15	4.00	3.60	0.75	0.011	84.6	1.27	4.7
CM100	16.13	5580	0.15	4.55	3.60	0.75	0.011	124.2	1.27	4.7
CH60	16.13	4.57	0.15	3.15	3.60	0.75	0.011	68.5	1.45	6.0
BH100	21.75	5.00	0.00	3.13	4.31	1.00	0.007	102.1	1.25	5.0
BL100	21.75	5.10	0.00	2.91	4.31	1.00	0.007	105.7	1.17	5.0
BH60	21.70	5.34	0.00	3.69	4.31	1.13	0.011	65.1	1.47	4.4
BM100	21.75	5.47	0.00	3.82	4.31	1.00	0.007	100.4	1.63	5.0

[1] *The section effective depth (d) is taken as the distance measured from the extreme compression fiber to the centroid of the outermost layer of longitudinal tension reinforcement.*

[2] *Axial load ratio is taken as the applied axial load divided by the gross sectional area and the measured concrete compressive strength at the day of column testing*

[3] *Longitudinal reinforcement ratio taken as the area of longitudinal steel divided by gross sectional area for column members, and tension layer of reinforcement divided by gross sectional area for beam members.*

[4] *T/Y = Tensile-to-yield strength ratio of the longitudinal reinforcement*

Test members are divided in two groups in Table 4-2 and Table 3-2, based on their failure modes. Members listed in Table 4-2 failed due to bar buckling and/or bar fracture and were used to calibrate the buckling initiation model and to verify the fracture prediction methodology. Members listed in Table 4-2 failed in shear, axial, and/or global instability and were used to validate the buckling and fracture models. Members reinforced using ASTM A1035 were not included at this stage as their material tests needed to obtain fatigue and mechanical properties of those bars were not available at the time of writing.

TABLE 4-2: DRIFT RATIOS AT BEHAVIORAL MILESTONES FOR MEMBERS THAT SUSTAINED BAR BUCKLING/FRACTURE

Specimen	D1[1]			D2[1]		
	Mode	Drift Target Event[2] (%)	Half-Cycle to Drift Target	Mode	Drift Target Event[2] (%)	Half-Cycle to Drift Target
CH100	BB[3]	5.5	2	BF[4]	5.5	4
CL100	BB	5.5	3	BF	7.0	1
CH60	BB	5.5	2	BF	5.5	3
BL100	BF	4.9	2	BF	6.5	2

[1] *D1 = First damage mode; D2 = Second damage mode*
[2] *Drift target towards which the damage mode took place*
[3] *Bar buckling from observation*
[4] *Bar fracture*

TABLE 4-3: DRIFT RATIOS AT BEHAVIORAL MILESTONES FOR MEMBERS WHICH DID NOT SUSTAIN BAR BUCKLING/FRACTURE

Specimen	D1[1]		D2	
	Maximum Drift Ratio Prior to D1[2] (%)	Mode	Maximum Drift Ratio Prior to Event[2] (%)	Mode
2L06	4.0	SH[3]	7.6	A[4]
2H06	3.4	SH	3.4	A
CS60	5.5	SH	5.5	A
CS80	7.0	SH	7.0	A
BH100	6.5	GI[5]	-	-
BH60	4.9	GI	-	-

[1] *D1 = First damage mode; D2 = Second damage mode*
[2] *Member completed the half-cycle to that drift ratio prior to damage mode*
[3] *Shear failure = initiation of lateral strength loss due to shear strength degradation*
[4] *Axial failure = member was not able to sustain the prescribed axial load*
[5] *Global instability due to buckling over several ties, or torsional instability.*

4.3 From Fiber-Section Strains To Representative strains

As mentioned previously, this work utilizes the fiber-section based computational approach proposed in Chapter 3 to obtain longitudinal strain demands that are representative of experimentally measured strains on longitudinal bars at member ends and in the surrounding concrete within the plastic hinge region. This methodology is further expanded in this work to deliver strain demands in the longitudinal bars at the mid-span location of potential bar buckling (Figure 4-1), or approximately one hoop spacing from member end.

The force-formulation fiber section model proposed in Chapter 3 provides longitudinal strain estimates for longitudinal bars and the surrounding concrete at member end, which partially reflect axial loads and material properties. As demonstrated in Chapter 3 however, additional empirical scaling is then required to obtain strains that are representative of experimentally measured values at the locations of interest (Figure 4-1), namely:

- Representative strain histories in longitudinal bars at member end, ε_{end}
- Representative smeared longitudinal strain histories in the concrete or longitudinal bars over the span of a potential bar buckle, $\varepsilon_{buckling}$. This region tends to concentrate curvature and longitudinal strains after bar buckling, as will be demonstrated later.
- Representative strain histories in longitudinal bars at mid-span of a potential bar buckle, or approximately at a distance equal to one hoop spacing from member end, $\varepsilon_{spacing}$.

4.3.1 Representative strain histories in longitudinal bars at member ends

To obtain the representative cyclic strain histories for longitudinal bars at the critical moment sections (ε_{end}) of frame members, the Compression Scale Factor (*CSF*) and the Tension Scale Factor (*TSF*) are applied to the compression and tension strain history outputs at member ends from fiber-section analysis ($\varepsilon_{analysis}$). The scaling relations and their effects on fiber-section longitudinal bar strains in column CH100 are presented in Figure 4-4. For this member, CSF was equal to 0.12 and TSF equal to 0.56.

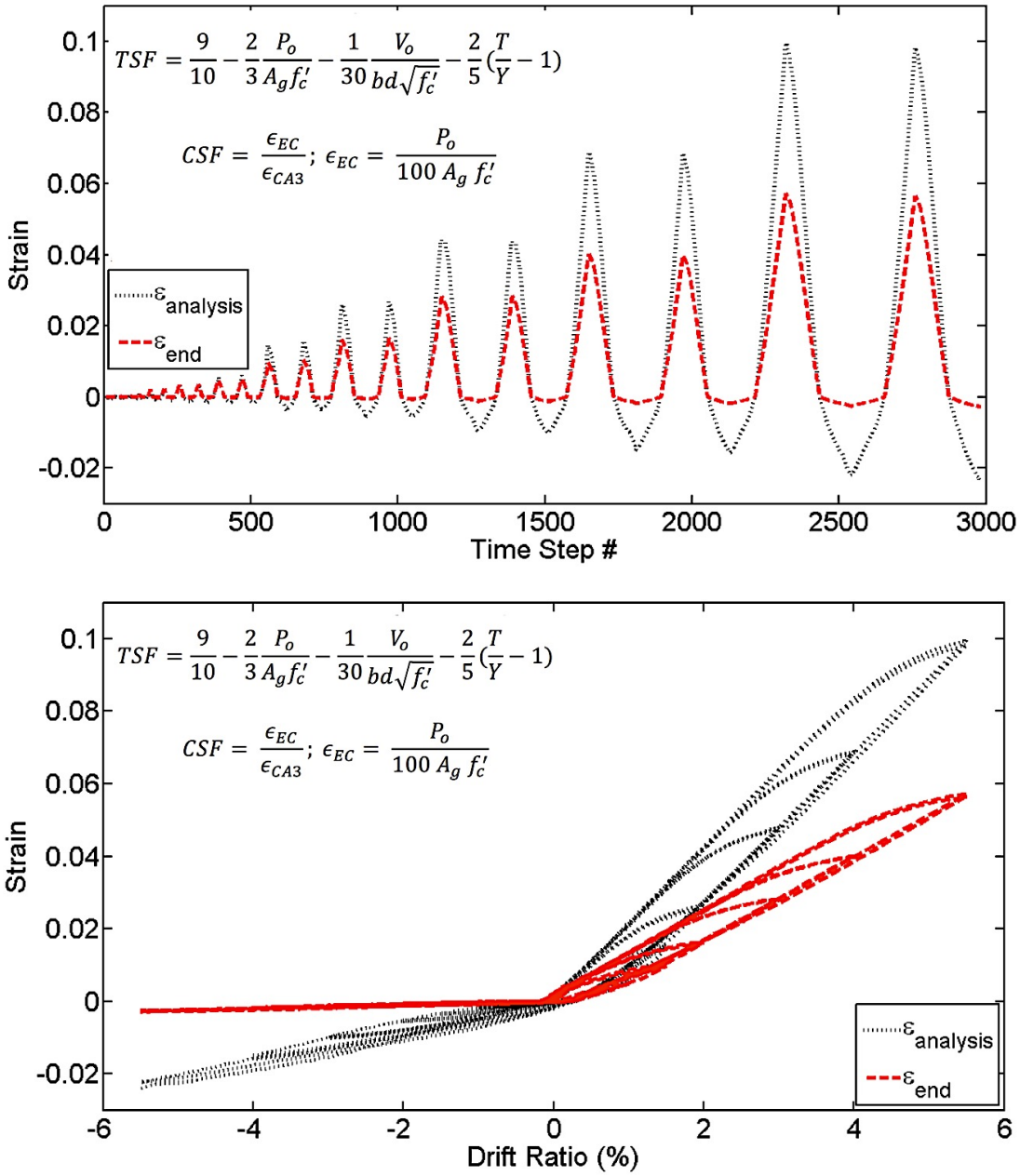

NOTE: TSF is the Tensile Strain Factor used to get the representative tensile strains over at the member end from strains from analysis; CSF is the Compression Strain Factor used to get the representative compression strains over at the member end from strains from analysis; P_o is the applied axial load (in lb, positive in compression); A_g the gross sectional area (in.^{2}); f_c' is the concrete compressive strength (in psi); V_o the maximum expected shear demand and can be obtained from fiber-section analysis (in lb); b and d are the cross-sectional width and effective depth in inches, respectively; and T/Y is the tensile to yield strength ratio for the longitudinal reinforcement, ϵ_{CA3} is the compression strain from fiber-section analysis taken at a drift ratio of 3%.

FIGURE 4-4: REPRESENTATIVE STRAIN HISTORY IN LONGITUDINAL BARS AT MEMBER ENDS SCALED FROM STRAIN FROM ANALYSIS

4.3.2 Representative smeared longitudinal strain histories over buckling length

To obtain the representative smeared longitudinal strain histories in the concrete or steel bars over the span of bar buckling, ($\varepsilon_{buckling}$), the Surface Compression Scale Factor (*SCSF*) and the Surface Tension Scale Factor (*STSF*) are applied to the compression and tension strain history outputs at member ends from fiber-section analysis ($\varepsilon_{analysis}$). These scaling factors were calibrated from surface strain measurements on test members at the location illustrated in Figure 4-1. The scaling for column CH100 is presented in Figure 4-5.

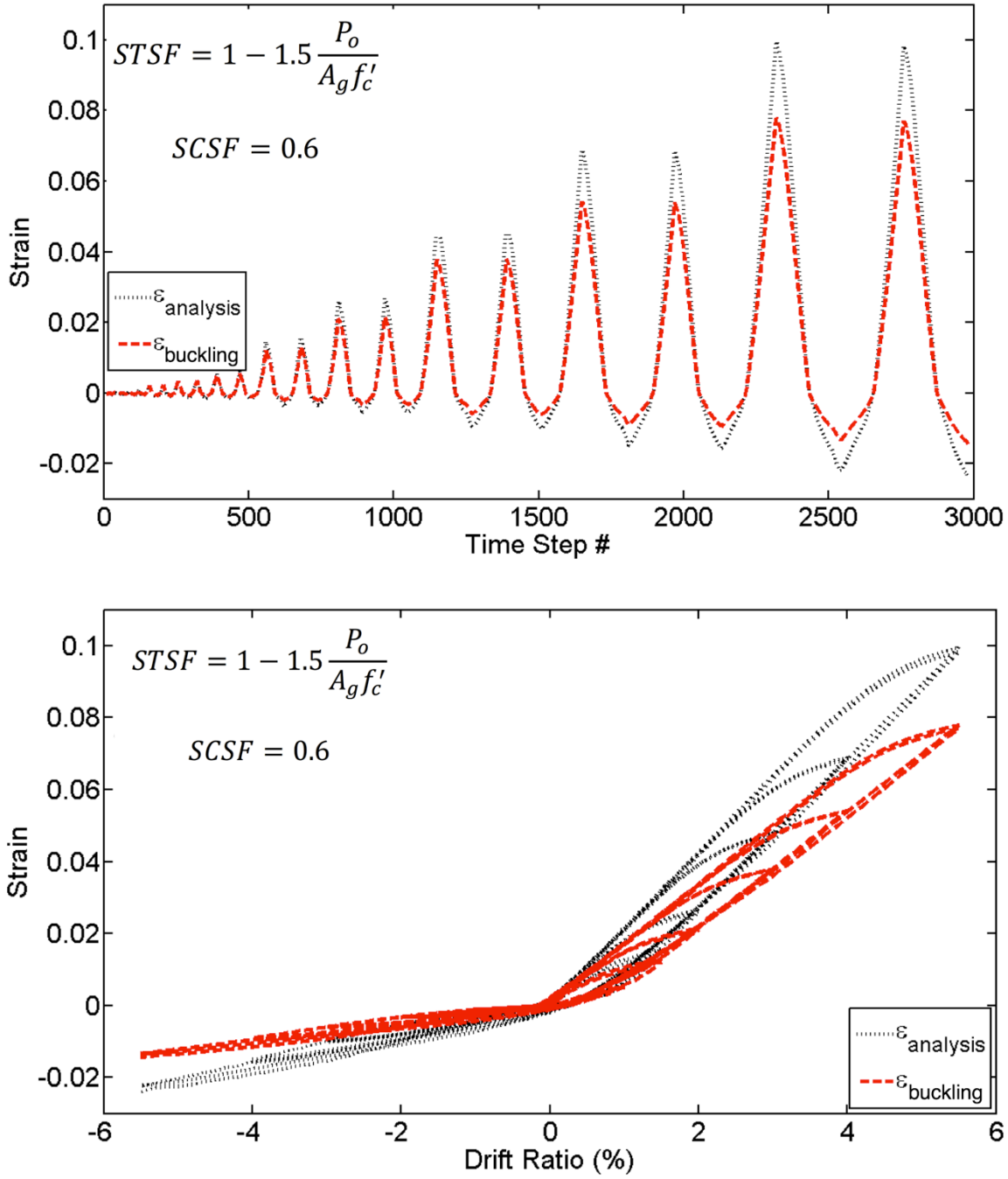

NOTE: STSF is the Tensile Strain Factor used to get the representative tensile strains over the buckling length from strains from analysis; SCSF is the Compression Strain Factor used to get the representative compression strains over the buckling length from strains from analysis.

FIGURE 4-5: REPRESENTATIVE STRAIN HISTORY IN CONCRETE SURFACE VS. STRAIN FROM ANALYSIS

Figure 4-6 shows the measured surface strain readings with and without bar-slip deformations for column CH100. The point at which bar buckling initiated is highlighted on the figure. Significant differences between strain measurements with and without bar-slip deformations can be seen in Figure 4-6 up to the initiation of bar buckling. This is particularly true for tension strain measurements. However, once bar buckling initiates, both readings become similar, which indicates that the bar-slip component reduces substantially and strains, or conversely curvatures, concentrate within the buckling length. For this reason, the longitudinal bar strain demands over the buckled length can be assumed after buckling to be approximately the same as the representative smeared longitudinal strains measured over the concrete surface including the bar slip region, $\varepsilon_{buckling}$.

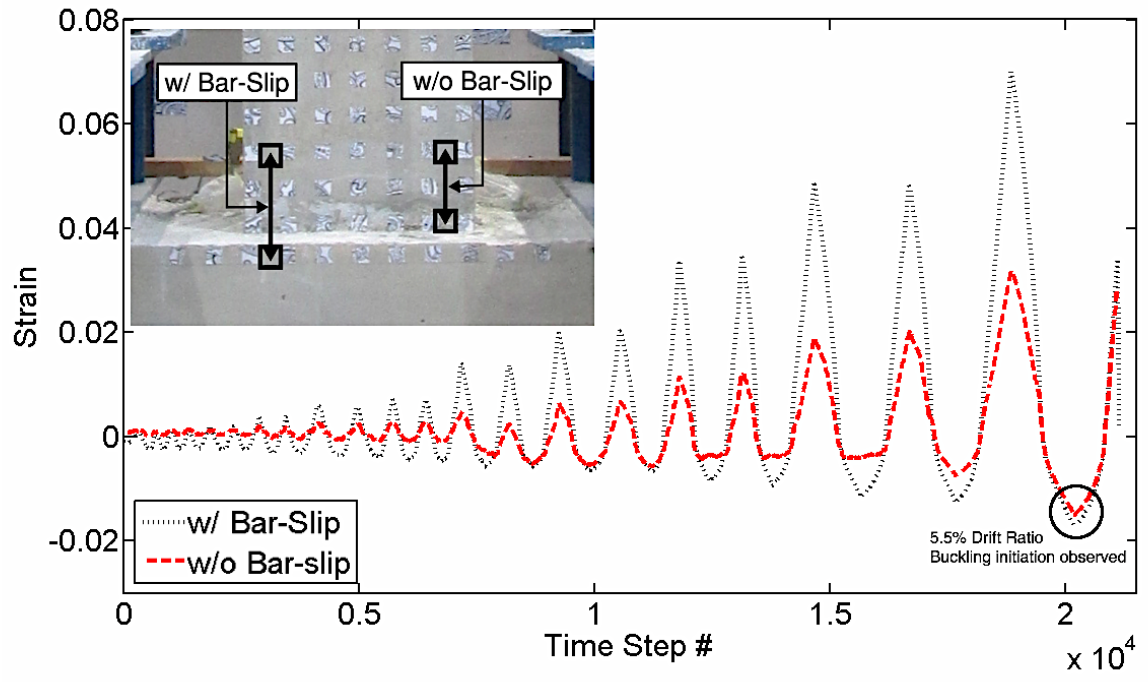

FIGURE 4-6: MEASURED SURFACE STRAINS FROM EXPERIMENT IN COLUMN CH100 WITH AND WITHOUT BAR-SLIP DEFORMATION

4.3.3 Representative strain histories in longitudinal bars at hoop-spacing distance from member ends

The procedure to scale strain in the longitudinal bars from analysis to get the representative strain history in longitudinal bars at mid-span of a potential bar buckle or approximately at a hoop-spacing distance from member ends ($\varepsilon_{spacing}$) is discussed in this section. This strain measure is not included in Chapter 3. Six of the specimens had available and reliable strain gauge data for strains along the length of the longitudinal bars, namely CH100, CL100, CH60, BH100, BL100, and BH60.

A schematic representation of the strain profile over the plastic hinge length is illustrated in Figure 4-7 and is assumed to be linear from the section of maximum moment

until the strain drops to the yield strain. The linear profile assumption is in agreement with experimental data as shown in Figure 4-1.

The length over which inelastic tension strains spread away from the section of maximum demand was identified from experiments at the first cycle to each drift target (h_p). It is noteworthy that measured bar strains were slightly lower in the following cycles to the same drift level. h_p was taken as the mean distance from member end to the section the strain in instrumented bars went down to a value equal to the yield strain (ε_y). Bar yield strains were obtained from material tension testing.

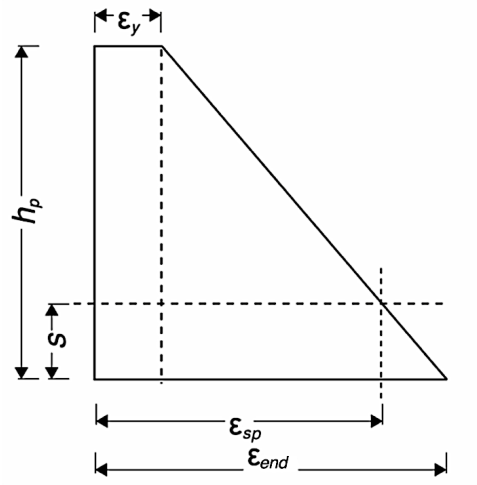

FIGURE 4-7: SCHEMATIC OF CALCULATING STRAIN AT A DISTANCE SPACING FROM BASE

Based on experimental values of h_p, the strains at a hoop spacing from member end ($\varepsilon_{spacing}$) could be obtained using Equation 4-1:

EQUATION 4-1: ESTIMATING STRAIN AT A DISTANCE SPACING FROM BASE

$$\varepsilon_{spacing} = \varepsilon_y + (\varepsilon_{end} - \varepsilon_y)(\frac{h_p - s}{h_p})$$

The Spacing Strain Factor (*SSF*) was then calculated for each member and at various drift targets as $\frac{\varepsilon_{end}}{\varepsilon_{spacing}}$. Results for *SSF* at different lateral drift ratio targets are given in Figure 4-8. For the specimens under consideration, the values of *SSF* varied from 0.74 to 0.99 at a drift ratio target of 1%. At higher drift ratios, the range of *SSF* narrowed to about 0.81 to 0.88. At a drift ratio of 3%, the mean value for the *SSF* was 0.85, with a standard deviation of 0.03. For simplicity, this constant scale factor of 0.85 is proposed to convert from tension strains at the section of maximum moment to tension strains at a hoop-spacing distance member end as defined in Equation 4-2. Compression strains were assumed to remain the same at a hoop-spacing distance from the member ends and member ends, based on the limited available test data (Equation 4-2).

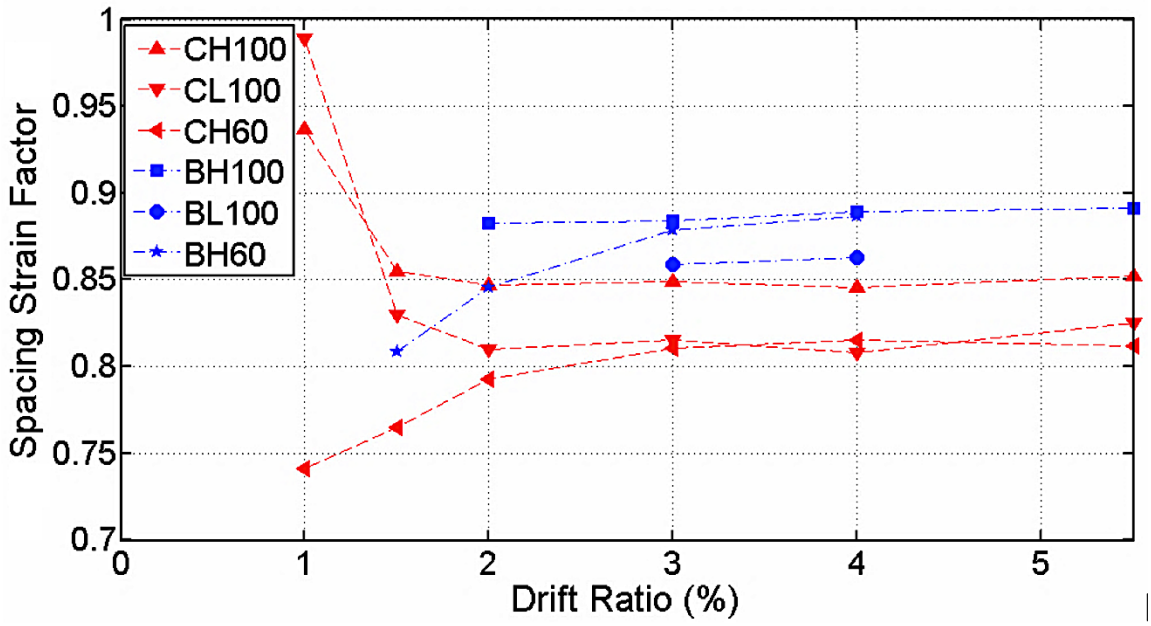

FIGURE 4-8: SSF – STRAIN SPACING FACTOR AT VARIOUS TARGET DRIFT RATIOS

EQUATION 4-2: TENSILE STRAINS AT A DISTANCE SPACING FROM BASE

$$\varepsilon_{i-spacing} = 0.85\ \varepsilon_{i-end} \quad for\ \varepsilon_{i-end} > 0$$

$$\varepsilon_{i-spacing} = \varepsilon_{i-end} \quad for\ \varepsilon_{i-end} < 0$$

4.4 BUCKLING INITIATION MODEL

4.4.1 Prior Buckling Initiation Models

Buckling of longitudinal bars in reinforced concrete columns subjected to gravity loads only has been attributed to compression strains in the plastic hinge region, while the magnitude of the compression strain required to trigger buckling has been related to the geometric configuration of both the longitudinal and transverse reinforcement (Bresler 1961, Scribler 1986, Papia et. al 1988, Papia and Russo 1989, Pantazopoulou 1998). The primary focus in those studies has been to set an adequate spacing of stirrups to prevent bar buckling. Additionally, Papia et. al (1988) concluded that compression strains experienced in longitudinal bars of uniaxially loaded members at the onset of buckling can be higher than the compression yield strain, depending on the provided spacing of transverse reinforcement.

Differences between bar buckling under monotonic lateral loads and buckling under cyclic loading have been recognized in experimental studies and summarized by Brown et. al (2007). First, strains in the compressed bars subjected to monotonic loading are relatively small, and therefore buckling is unlikely to take place because the concrete carries most of the compression demand. When subjected to cyclic loads, a large flexural crack may be present, which in the next consecutive cycle may lead the bar to buckle before the crack closes (Wang and Restrepo 1996, Brown et. al 2007, Goodnight et al. 2012). Second, the cyclic nature of loading may change the local stress-strain properties of the

steel due to the Bauschinger effect, leading to a lower tangent modulus of the material which in return reduces the inelastic buckling load of the bar.

Additionally, the influence of the maximum experienced tensile strain on the buckling initiation of reinforcing bars has been corroborated by various authors (Wang and Restrepo 1996, Rodriguez et. al. 1999, Moyer and Kowalsky 2003, Brown et. al 2007, Goodnight et al. 2012, Feng et. al 2014). Rodriguez et. al. (1999) concluded through monotonic and cyclic axial tests on bars that reinforcing bars are more susceptible to buckling upon reversal from cycles of significant tension strains. They cited that the onset of buckling of steel bars could occur in the tensile region of the hysteresis cycle. Moyer and Kowalsky (2003) and Feng et. al (2014) supported the idea behind the influence of the loading history of the bars and especially that of the tensile strains on the onset of bar buckling, and proposed a tension-based buckling mechanism in circular bridge columns. Additionally, they argued on the importance of quantifying the compression load capacity associated with bar buckling, since bar buckling occurs under compression.

Dhakal and Maekawa (2002) related buckling initiation to the compression strain demand in core concrete coupled with the buckling tendency of the longitudinal bars at such demands lead to cover spalling. Therefore, the inherent assumption that spalling is caused due to buckling. The authors recognized the importance of considering the loading history and the tensile strains the bar may have experienced, however the compression strain at spalling was calibrate for monotonic cases only.

Berry and Eberhardt (2005) established a statistical drift-based bar buckling initiation model. The model includes the effect of the confinement ratio, axial-load ratio, aspect ratio, and longitudinal bar diameter on the required lateral deformation for bar buckling. The dataset to which the empirical equation was calibrated did not contain bars with yield strength higher than 75 ksi.

Tension-based models were primarily calibrated with results from circular bridge piers with spiral reinforcement. These members have typically high confinement and are subjected to low axial loads. The design parameters in such members are significantly different from concrete members of SMF and therefore could not upon verification capture buckling initiation in the members part of this study. Additionally, the effect of higher-strength reinforcing bars was not treated in any of the above-mentioned references. Therefore, a buckling initiation model is proposed here that accounts for the mechanical properties of the reinforcing bars, as well as the tension and compression loading histories experienced by the bars and surrounding confining concrete prior to buckling.

4.4.2 Proposed Buckling Initiation Model

A model is proposed to predict the point in a loading history at which longitudinal bar buckling initiates. The proposed buckling initiation model assumes that the restraint provided by hoops is sufficient to prevent the longitudinal reinforcing bars from buckling across multiple hoops or prior to compression yield. The model accounts for the mechanical properties of the reinforcing bars, as well as the loading history the bars and surrounding confining concrete experience prior to buckling. The proposed model takes on

the form of the Euler's buckling equation for critical buckling stress, but modified through factors α and β to account for the cyclic nature of seismic loading and the associated damage progression (Equation 4-3). Factors α and β degrade the critical buckling stress by reducing the effective restrained length of the bar as the concrete surrounding the bar reaches higher levels of compressive and tensile strains, respectively. Whenever the stress in a longitudinal bar reaches the degrading critical buckling stress evaluated using Equation 4-3 then buckling is deemed to initiate.

EQUATION 4-3: CRITICAL STRENGTH OF THE BAR AT BUCKLING INITIATION

$$f_{cr} = \frac{\pi^2 E_{tp}}{(\alpha\beta \frac{L}{r})^2}$$

where f_{cr} is the critical stress at which a longitudinal bar is expected to buckle; E_{tp} is the tangent modulus of elasticity of the bar at a given strain demand, and is calculated as described in Section 4.4.3; L is the effective buckled length, which based on experimental tests is taken as 1.25 times the center-to-center spacing between the seismic hoops (Figure 4-9); r is the radius of gyration taken as $d_b/4$ with d_b being the diameter of the bar; and α and β are factors calibrated to account for the loading history experienced by the concrete surrounding the bar prior to buckling, and are discussed in more detail in Section 4.4.4.

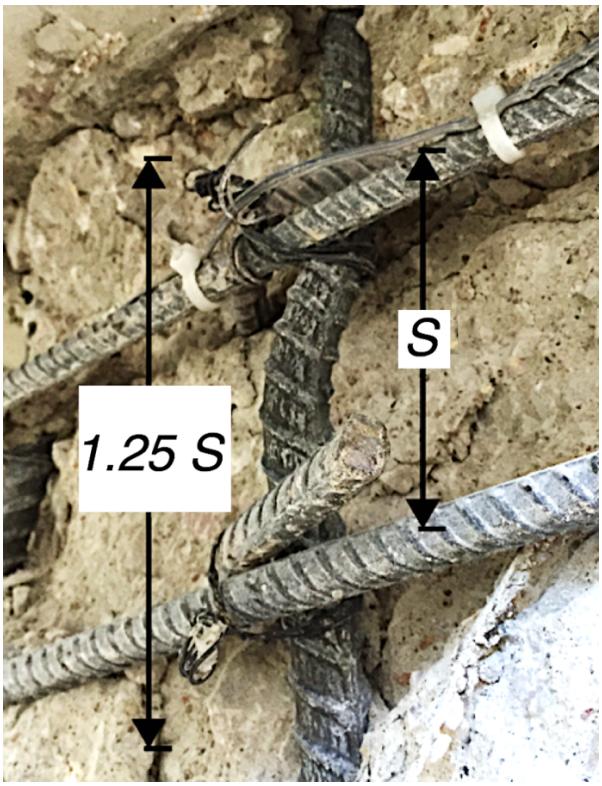

FIGURE 4-9: EFFECTIVE LENGTH OF BUCKLED BAR

The stress history of a longitudinal bar can be obtained from the fiber-section analysis of the member and that value compared with the degrading critical buckling stress to determine if and when a bar will buckle. However, given that bar stresses vary within the inelastic range of behavior between the yield stress (f_y) and the ultimate stress (f_u), the stress in a bar at buckling initiation (f_{ub}) can be simply estimated as the average of the tensile and ultimate stress as per (Equation 4-4) with limited loss in resolution.

EQUATION 4-4: ASSUMED STRESS IN THE BAR AT BUCKLING INITIATION

$$f_{ub} = \frac{f_u + f_y}{2}$$

Using the proposed model, buckling in well confined frame members satisfying the ACI 318-14 Special Moment Frame provisions is therefore triggered by the following mechanisms:

- Increased compressive strains that cause loss of confinement, damage in the core concrete after spalling, and opening of 90-degree cross-ties captured by the α factor
- Increased peak tensile strains experienced by the longitudinal bar in the previous cycles, which increases flexural crack widths and bar instability, and is captured by the β factor
- Increased differential between the tensile and compressive strains experienced by the bar and surrounding concrete, which increases concrete damage and bar instability, and is captured by the product of α and β

4.4.3 Reinforcing Bar Tangent Modulus of Elasticity

An empirical relation was derived for the tangent modulus of elasticity of the reinforcing bars subjected to compression strains in the inelastic range of behavior. Data from low-cycle fatigue tests on #8 Grade 60 and 100 bars sourced from two different manufacturers were used to calibrate the tangent modulus model (Ghannoum and Slavin 2016, Slavin 2015). Manufacturer 1 (M1) high-strength bars were produced using the micro-alloying process, while Manufacture 2 (M2) bars were produced using the quenching and tempering process (Ghannoum and Slavin 2016). The bars for which cyclic stress-strain data was used to calibrate the tangent modulus model were sourced from the same manufacturers as the bars used in the concrete members considered in this study,

except those reinforced with ASTM A1035 bars. The grade 60 and 100 bars selected had tensile-to-yield-strength ratios varying from 1.18 to 1.68, and monotonic tangent moduli at initiation of strain hardening ranging from 661 to 1452 ksi. Properties of the bars selected for the calibration process are listed in Table 4-4.

Stress-strain results were taken for calibration from a loading protocol cycling between strains of -1% in compression to 4% in tension (Figure 4-10). This strain range was the most representative of strains observed in the reinforcement of the concrete beams and columns around the point at which bar buckling occurred (Chapter 3). The cyclic fatigue tests considered were performed in a universal test machine with a spacing between the grips of 4 bar diameters or 4 inches, which lead to bars sustaining practically no buckling in compression.

TABLE 4-4: PROPERTIES OF BARS TESTED IN LOW CYCLE FATIGUE

	G60M1	G100M1	G60M2	G100M2
	Manufacturer 1		Manufacturer 2	
	Grade 60	Grade 100	Grade 60	Grade 100
f_y (ksi)	63.2	101.5	61.5	104.6
f_u ksi)	93.7	128.5	103.1	123.8
T/Y	1.48	1.27	1.68	1.18
ε_y	0.0026	0.0038	0.0026	0.0040
ε_u	0.1	0.081	0.095	0.062
E_s (ksi)	26900	30100	25800	31400
E_{sh} (ksi)	315	350	449	331
E_{tm} (ksi)	861	945	1452	661

! *f_y is the yield strength of the bars in tension, f_u is the tensile strength of the bars, T/Y is the ratio of the tensile-to-yield strength, ε_y is the yield strain of bars, ε_u is the uniform elongation measured per ASTM E8 procedures, E_{sh} is the inelastic secant modulus estimated as ($f_u - f_y$)/($\varepsilon_u - \varepsilon_y$), and E_{tm} is the tangent modulus of the bars tested in tension taken at the beginning of the strain hardening region.*

The tangent modulus (E_{tp}) of the bars cycled to inelastic strains was taken as the slope of the stress-strain curve in the second cycle to the compression target strain during the fatigue test (Figure 4-10).

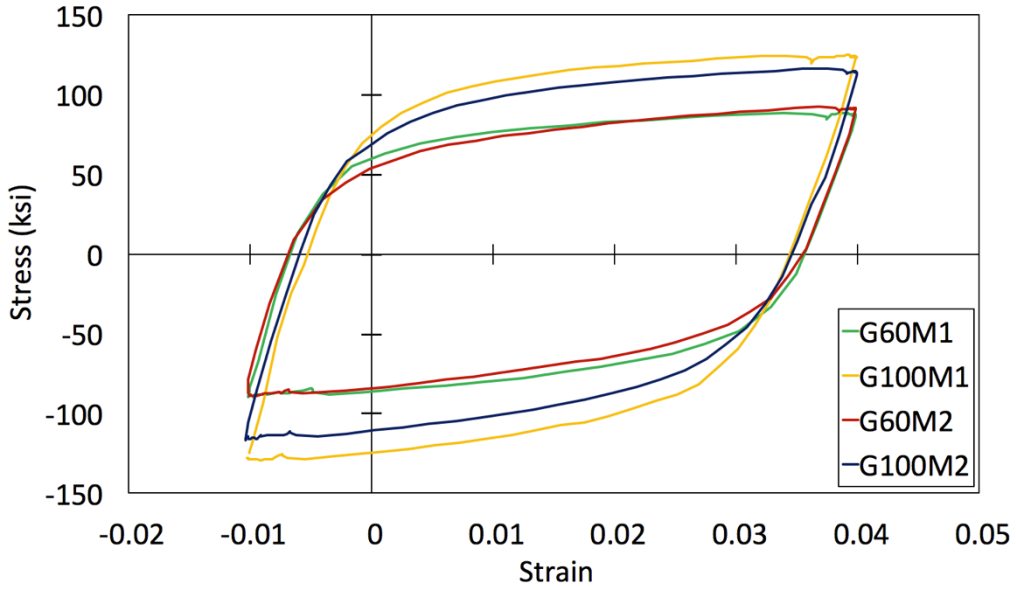

FIGURE 4-10: STRESS-STRAIN CURVE OF BARS IN THE SECOND LOADING CYCLE

In Figure 4-11, the tangent modulus E_{tp} is plotted versus the strain increment from the peak tensile strain at which the cyclic protocol reversed direction ($\Delta\varepsilon$). The curves in Figure 4-11 represent average values from at least three successful tests per bar type. As can be seen in the figure, the tangent modulus is higher for reinforcing bars with higher yield strength in the initial strain range after load reversal. This can be attributed to the lower yield strain of grade 60 bars, which leads the stress-strain curve of these bars to soften at a lower strain level as compared to grade 100 bars. In the higher inelastic strain range after load reversal, the tangent moduli were found to converge at similar values for all grades (Figure 4-11).

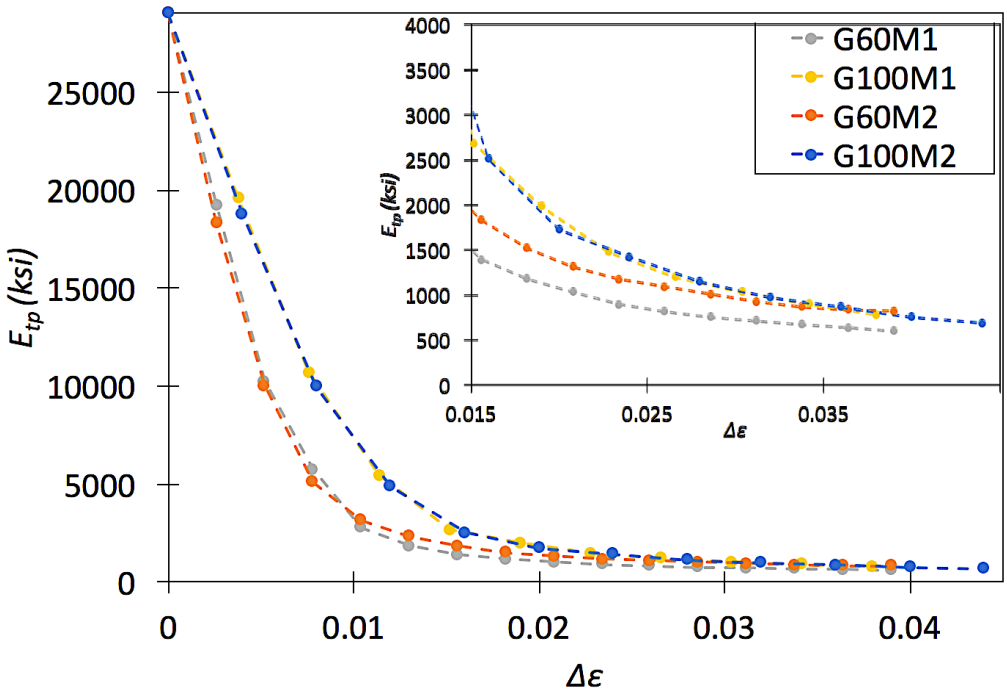

FIGURE 4-11: TANGENT MODULUS VS. STRAIN INCREMENT FROM LOAD REVERSAL

The strain reversal values were normalized to the yield strain (ε_y) in Figure 4-12. This led to the lines converging throughout the monitored strain range, with differences becoming pronounce at high strain values. The grade 60 bars from Manufacturer 2, G60M2, displayed the higher modulus values in the normalized plot, whereas the grade 100 from Manufacturer 2, G100M2, had the lowest values. This corresponds with their inelastic properties from monotonic tension tests, with G60M2 having the highest *T/Y* ratio and E_{sh} values, and G100M2 having the lowest values (Table 4-4).

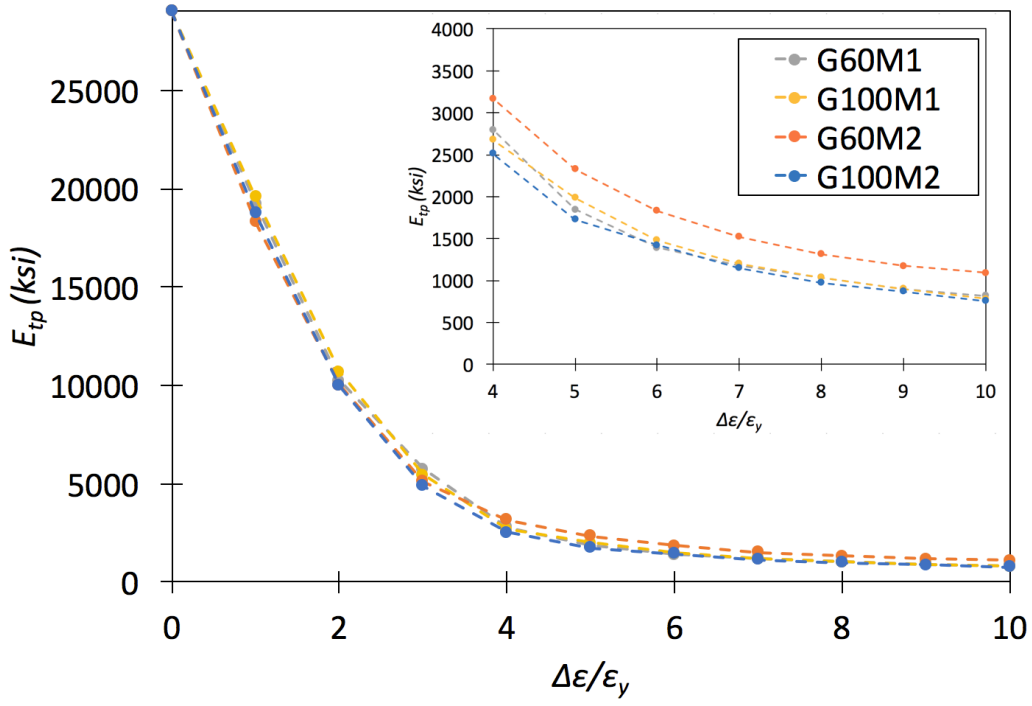

FIGURE 4-12: TANGENT MODULUS VS. NORMALIZED STRAIN INCREMENT FROM LOAD REVERSAL TO YIELD STRAIN

Equation 4-5 was derived through nonlinear regression analysis to estimate the tangent modulus of reinforcing bars subjected to inelastic strains. The model captures the effects of varying bar strength, as well as bar inelastic properties, such as the T/Y ratio and E_{sh}. Using both these properties in the equation was found to increase the accuracy of estimates, as opposed to using only the secant modulus, E_{sh} or the tangent modulus, E_{tm}.

EQUATION 4-5: TANGENT MODULUS AT INELASTIC STRAINS

$$E_{tp} = (E_{sh} \times \frac{f_u}{f_y}) + \frac{E_s - (E_{sh} \times \frac{f_u}{f_y})}{1 + (\frac{5}{7}\frac{\Delta\varepsilon}{\varepsilon_y})^{2.3}}$$

In Figure 4-13, the tangent modulus values from material testing are compared to the tangent modulus estimates using Equation 4-5 for G60M2 and G100M2 bars, which respectively represent the highest and the lowest T/Y ratio and E_{sh} values. The mean error ratio of the 4 bar types calculated as the ratio of the estimated tangent modulus from Equation 4-5 over the tangent modulus taken from the material testing at $\frac{\Delta\epsilon}{\epsilon_y}$ of 1 to 10 was 1.04. The standard deviation was 0.07.

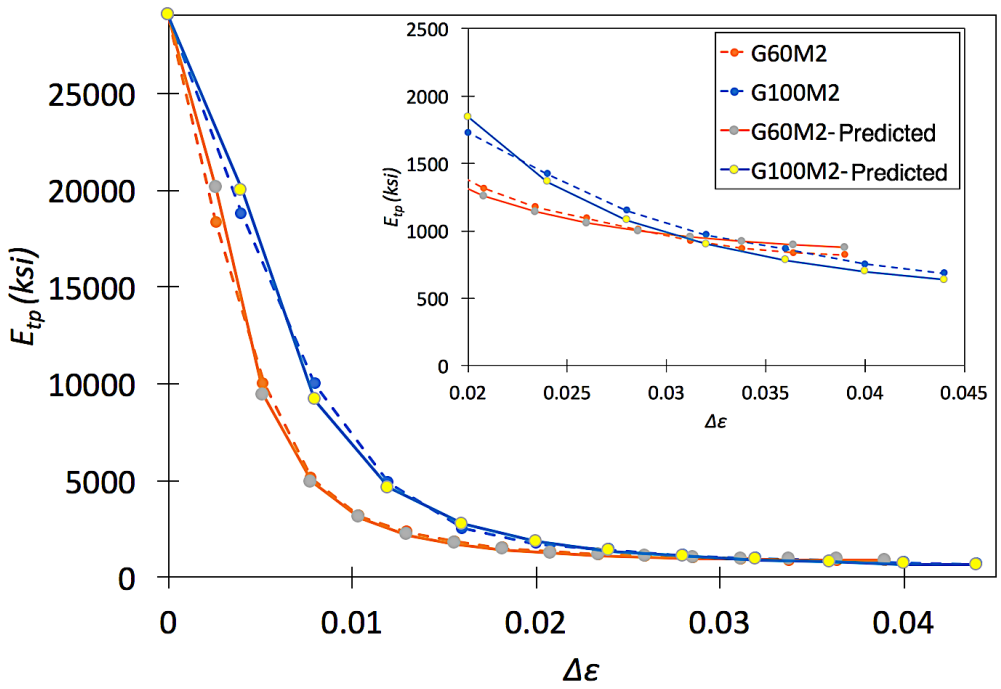

FIGURE 4-13: TANGENT MODULUS FROM MATERIAL TESTING COMPARED TO PREDICTION FROM EQUATION 4-5

4.4.4 Alpha and Beta Factors

Members CH100, CL100, and CH60 exhibited buckling of longitudinal bars between two consecutive ties at relatively large lateral deformation demands. Buckling was observed well after the bars had yielded in compression. As the members were cycled to higher lateral deformation demands, the damage in the concrete cover and core increased. It is postulated that this concrete damage reduced the effective bracing of the longitudinal bars leading to bar buckling once the damage was severe enough. Additionally, at high compressive demands in the longitudinal bars the 90-degree cross-ties are prone to opening up leading to increased unsupported length.

The mechanics of such degradation in the plastic hinge region is captured by factors α and β in Equation 4-3. The variation of factors α and β with longitudinal strain demands on the concrete around the longitudinal bars in the plastic hinge region are presented in Figure 4-14. The values were calibrated such that Equation 4-3 captures buckling in members CH100, CL100 and CH60, and no buckling is predicted up to the end of the loading protocol for the rest of the members.

Factor α accounts for the loss of lateral support due to damage and spalling caused by compressive strain demands, and was calibrated using the smeared longitudinal strain histories in the concrete over the span of bar buckling, $\varepsilon_{buckling}$. Factor α was determined to vary from 0.2 to 1.0 as $\varepsilon_{buckling}$ goes from 0 to -0.03. Beyond a compression strain of -0.03 the factor remains at 1.0. Maximum damage is therefore assumed to occur at a compression strain of -0.03 as that value constitutes an upper bound on the compressive

strain achievable by concrete in a well confined core prior to significant strength loss (Moehle 2015).

Factor β accounts for the peak tensile strain experienced by the longitudinal bar in the previous cycles, which can contribute to bar instability (Wang and Restrepo 1996, Rodriguez et. al. 1999, Moyer and Kowalsky 2003, Brown et. al 2007, Goodnight et al. 2012, Feng et. al 2014). β was calibrated using the tensile strain demands in the bar at mid-span of a potential buckle or a distance equal to spacing of hoops from the member ends, $\varepsilon_{spacing}$. Factor β was determined to vary from 0.2 to 1, as the tensile strain demand, $\varepsilon_{spacing}$, goes from 0 to a maximum of 0.1. A tensile strain of 10% was chosen for maximum damage as that values is representative of the uniform or fracture elongations of the reinforcing bars considered in this study. Therefore, tension strain demands in bars could not exceed this threshold without a high risk of bar fracture.

The calculations carried to predict buckling initiation based on the proposed model are presented in Table 4-5. It is noted that the α factor is evaluated continuously during a cyclic loading protocol whereas the β factor is updated only if the peak tension strain experienced by a bar exceeds the prior recoded peak. The model was able to predict buckling accurately for all members, i.e., buckling was predicted to occur in members CH100, CL100 and CH60 at the correct peak drift excursion, and no buckling was predicted in the other members up to the end of their loading protocols. For members CH100 and CL100 buckling is predicted to occur at the end of the first cycle to a drift ratio of 5.5%. For member CH60, buckling initiation is predicted earlier, at the first excursion

to the first half-cycle to +5.5% drift, meaning that the maximum tensile strain the bar experienced when the member was cycled at 4% drift ratio combined with compression strain the bar experienced at 5.5% drift ratio resulted in large enough product of α and β that triggered buckling. During the experimental testing of these members, buckling was observed at the end of the first cycle to 5.5% drift ratio for members CH100 and CH60, and at the third half-cycle excursion of the second cycle for CL100.

The proposed buckling initiation model is intended to capture the fundamentals of the mechanisms and parameters leading to buckling of longitudinal bars in the well confined concrete frame members. It was however calibrated to a limited dataset, as few tests were conducted using bars of various strengths and mechanical properties. This model should be further validated or adjusted when additional data becomes available.

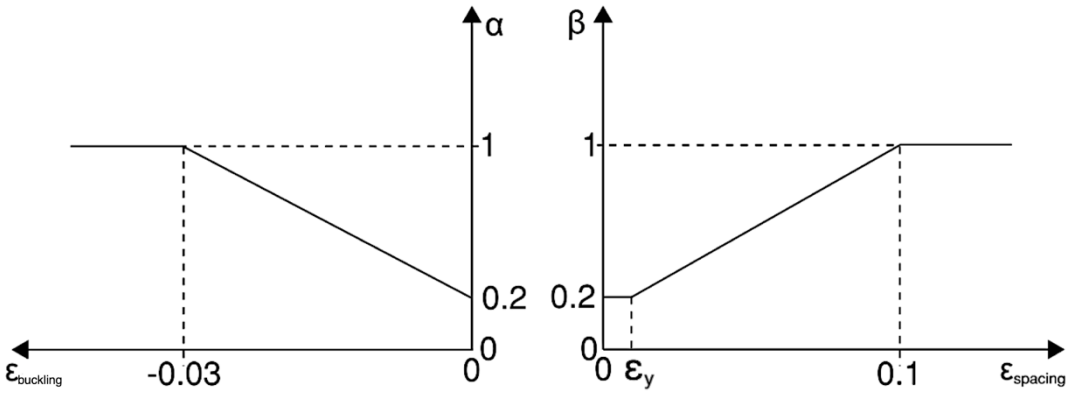

FIGURE 4-14: VARIATION OF FACTOR α AND β WITH STRAIN DEMAND (NEGATIVE VALUES REPRESENT COMPRESSION STRAINS)

TABLE 4-5: BUCKLING INITIATION PREDICTION CALCULATIONS FOR ALL MEMBERS

	Drift Ratio*	$\varepsilon_{buckling}$	$\varepsilon_{spacing}$	$\Delta\varepsilon/\varepsilon_y$	E_{tp}	f_y (ksi)	f_u (ksi)	ε_y	T/Y	E_{sh} (ksi)	s (in)	d_b (in)	α	β	$\alpha\beta$	*Eq. 1-3:* f_{cr}	*Eq. 1-4:* $(f_y+f_u)/2$	Check** $(f_y+f_u)/2/f_{cr}$
CH100	4.0%	0.051	0.034			100	127.0	0.0034	1.27	375	3.5	0.75					113.5	
	-4.0%	-0.009	-0.002	10	758								0.451	0.454	0.205	327.5		0.3
	5.5%	0.075	0.049	11	742								0.557	0.454	0.253	209.8		0.5
	-5.5%	-0.013	-0.003	15	601								0.557	0.574	0.320	106.2		1.1
CL100	4.0%	0.055	0.037			106.4	123.4	0.0037	1.16	210	3.5	0.75					114.9	
	-4.0%	-0.009	-0.002	11	513								0.453	0.478	0.217	198.3		0.6
	5.5%	0.079	0.052	11	499								0.569	0.478	0.272	122.0		0.9
	-5.5%	-0.014	-0.003	15	365								0.569	0.606	0.345	55.6		2.1
CH60	4.0%	0.060	0.033			64.4	93.4	0.0022	1.45	260	4.5	0.75					78.9	
	-4.0%	-0.011	-0.002	16	488								0.487	0.445	0.217	114.0		0.7
	5.5%	0.085	0.049	16	482								0.602	0.445	0.268	73.6		1.1
	-5.5%	-0.015	-0.003	23	422								0.602	0.575	0.346	38.6		2.0
2L06	5.5%	0.040	0.019	10	1015	65.5	107.4	0.0023	1.64	450	6	1	0.733	0.325	0.238	195.6	86.5	0.4
	-5.5%	-0.020	-0.005															
2H06	4.0%	0.016	0.008	8	1246	65.5	107.4	0.0023	1.64	450	6	1	1.000	0.238	0.238	240.8	86.5	0.4
	-4.0%	-0.035	-0.010															
CS60	5.5%	0.048	0.015	9	808	67.3	94.9	0.0023	1.41	315	5.5	1.25	1.000	0.296	0.296	187.8	81.1	0.4
	-5.5%	-0.032	-0.007															
CS80	7.0%	0.065	0.020	10	763	79.1	106.8	0.0027	1.35	320	5.5	1.13	1.000	0.337	0.337	111.5	92.9	0.8
	-7.0%	-0.045	-0.006															
BH100	6.5%	0.073	0.044	12	535	102.1	127.6	0.0035	1.25	280	5	1	0.200	0.536	0.107	734.1	114.9	0.2
	-6.5%	0.000	0.000															
BL100	6.5%	0.076	0.048	13	504	105.7	123.7	0.0036	1.17	290	5	1	0.200	0.569	0.114	612.8	114.7	0.2
	-6.5%	0.000	0.000															
BH60	4.9%	0.082	0.042	19	478	65.1	95.7	0.0022	1.47	275	5	1.13	0.200	0.518	0.104	897.9	80.4	0.1
	-4.9%	0.000	0.000															

**Negative values represent compression*

***Values greated than 1.0 indicate Eq. 1-3 predicted buckling*

Buckling observed in experimental test

Eq. 1-3 predicts buckling

Eq. 1-3 does not predict buckling

4.5 DAMAGE ACCUMULATION INDEX AND FRACTURE

4.5.1 Fatigue Fracture Models

The low-cycle fatigue life and the accumulated strain demand of reinforcing bars have been related in models by many authors (Mander et al. 1994, Brown and Kunnath 2004, Hawileh et al. 2010, Slavin 2015, Ghannoum and Slavin 2016). However, the work presented by Slavin et. al. (2015), Slavin (2015), Ghannoum and Slavin (2016) and Hogsett (2017) are the only studies that capture the effect of HSRB currently in production in the U.S. Moreover, the types of bars tested by Slavin et. al. (2015) were sourced from the same manufacturers as the bars used to reinforce concrete members considered in this study (Table 4-6).

Slavin et. al. (2015) used a power function of the form described in Equation 4-6, with coefficients "c" and "d" calibrated per the material properties to relate the number of half-cycles to fracture, $2N_f$, to the total strain range over which bars are cycled, ε_a.Values of coefficients "c" and "d" for different manufacturers, grades, and clear spans between machine grips are presented in Table 4-6. The parameters were calibrated using results from #8 bars tested in low-cycle fatigue up to fracture. These bars were cycled to total strain ranges of 4% and 5%, which are representative of the peak strain range experienced by the longitudinal bars in the concrete members considered.

In this study, the fatigue model coefficients "c" and "d" used to represent the fatigue life of bars prior to buckling were those from $4d_b$ clear span tests, as bars did not experience significant buckling at that test clear span. After a bar is deemed to have buckled based on

the buckling initiation model, coefficients "c" and "d" are taken from $5d_b$, $6d_b$, or $8d_b$, based on the 1.25 times the spacing of the transverse reinforcement in the concrete member. Because data was not available for tests on grade 60 bars tested at $8d_b$, the value was interpolated linearly from $4d_b$ and $6d_b$ values. Linear interpolation was also used for an assumed buckled length in between the reported clear testing spans. It is noteworthy that the fatigue life of bars decreased as the clear span in testing increased due to increased strain concentrations caused by the buckled shape (Figure 4-3). By taking the fatigue model coefficients corresponding to the buckled length of a bar in a concrete member, the effects of the strain concentration due to buckling are captured indirectly by the reduced fatigue life estimated by the adjusted "c" and "d" coefficients.

EQUATION 4-6: RELATION OF STRAIN RANGE TO THE NUMBER OF HALF-CYCLES TO FAILURE

$$2N_f = c \times {\varepsilon_a}^d$$

TABLE 4-6: SUMMARY OF MATERIAL COEFFICIENTS FOR FATIGUE LIFE EQUATION

Manufacturer	Grade	Member	Clear Span	c	d
1	60	CH60, CS60, BH60	$4d_b$	5.14E-03	-2.87
			$6d_b$	7.92E-03	-2.59
	80	CS80	$4d_b$	2.48E-03	-2.97
			$6d_b$	6.60E-03	-2.43
	100	CH100, BH100	$4d_b$	2.40E-05	-4.62
			$6d_b$	1.49E-06	-3.03
2	100	CL100, BL100	$4d_b$	1.90E-06	-5.42
			$6d_b$	1.65E-05	-4.46

Based on the work by Miner (1945), Equation 4-7 is used to calculate the accumulation of damage index, a model that assumes a linear summation of damage as a function of the number of half-cycle the bar is loaded at a certain deformation amplitude. A bar is assumed to fracture when the damage index factor D in Equation 4-7 reaches a value of 1.0 in a tensile half-cycle.

EQUATION 4-7: COFFIN-MANSON CUMULATIVE DAMAGE INDEX

$$D = \sum D_i = \sum_{i=1}^{N} \frac{n_i}{2N_{fi}}$$

where n_i is the number of half cycles a bar is cycled to a certain total strain range of ε_a, $2N_{fi}$ is the number of half cycles to fracture to the same strain range of ε_a.

4.5.2 Predicting Fracture

Predicting the fracture of longitudinal bars in frame members using the proposed methodology requires tracking the damage indices of the longitudinal bars at the locations of expected highest moments (typically at member ends) and about one hoop spacing from member ends, which corresponds to the mid-span of the bar buckled shape. Damage index calculations should therefore typically be performed at four sections in frame members and for all longitudinal bars at those sections. The four sections to consider are: both member ends and at one hoop spacing away from both member ends. All these checks may be necessary because it is not always evident which member end will experience the largest rotation demands during a seismic event or which longitudinal bars will experience the highest damage index at a particular section. For the sections at a hoop spacing from

member ends, the damage index ($D_{spacing}$) is incremented for each bar at each loading step using $\varepsilon_{spacing}$ and the unbuckled fatigue model parameters "c" and "d". At the same time, the buckling initiation check is performed at each loading step. For a given bar, if buckling is not predicted at any point in the loading history, then this location will not govern and fracture can only occur at the section of maximum moment. If buckling is predicted, then after buckling the damage index ($D_{spacing}$) is incremented using $\varepsilon_{buckling}$ and the bar fatigue model parameters "c" and "d" corresponding to the expected buckled shape. At the same time, the damage index for longitudinal bars at the sections of highest moment demands (D_{end}) is incremented at each loading step using ε_{end} and the unbuckled fatigue model parameters "c" and "d". Fracture will occur at the bar and location at which the damage index exceeds 1.0 first.

The methodology predicted buckling of the outermost longitudinal bars in member CH100 at the end of the first cycle to a drift ratio of 5.5% (Table 4-5), followed by fracture at the same location two half cycles later. Estimated representative strain demands in the outermost longitudinal bars of member CH100 at a hoop spacing away from the end are given through the loading history in Figure 4-15. Up to buckling initiation, $\varepsilon_{spacing}$ is used at a hoop spacing from member end. After buckling initiation is triggered, the smeared longitudinal strain in the concrete or steel bars over the span of bar buckling, $\varepsilon_{buckling}$, is used. The strain demands ε_{end} at the critical moment section are also given in Figure 4-15 for the outermost longitudinal bars.

The cumulative damage indices $D_{spacing}$ and D_{end} in the longitudinal bars of member CH100 are plotted against the number of half cycles in Figure 4-16. D_{end} shown in Figure 4-16 reaches a maximum of 0.30 at the point where $D_{spacing}$ reaches 1.0. The cumulative damage index $D_{spacing}$ exceeds the value of 1.0 at the last half cycle to a drift ratio of 5.5% (i.e. the end of the second cycle to 5.5% drift ratio). This concurs with the recorded fracture during experimental testing, at the end of the second cycle to 5.5% drift ratio.

The methodology predicts that about 80% of the damage leading to fracture at a hoop spacing from member end is induced after buckling takes place. A similar high damage value is predicted after buckling initiates for members CL100 and CH100. This is a plausible scenario because all these three members during testing sustained fracture of the longitudinal bars at similar drift ratios of about 5.5%, although the mechanical properties and the strain demands in the bars were significantly different.

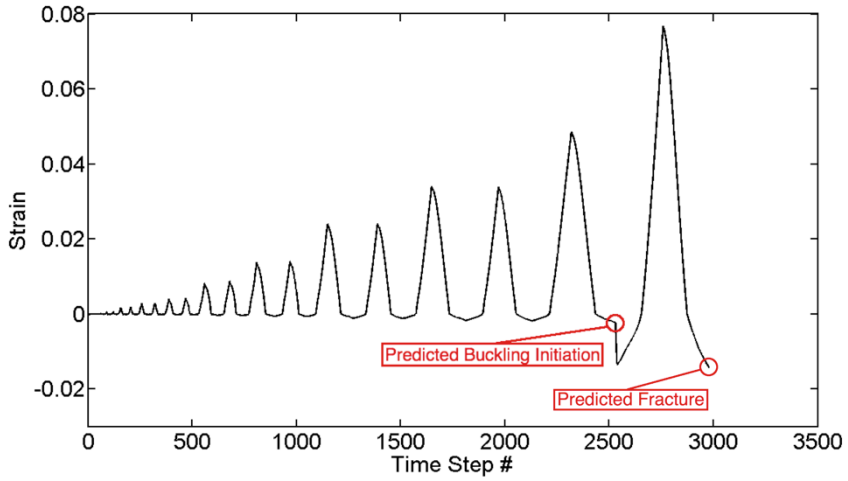

FIGURE 4-15: REPRESENTATIVE STRAIN DEMANDS IN THE LONGITUDINAL BARS OF MEMBER CH100 THROUGH THE LOADING HISTORY

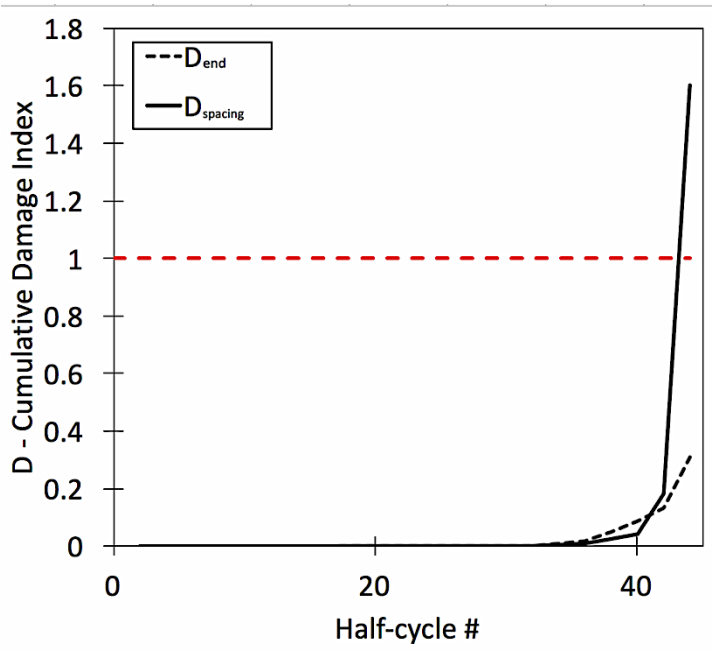

FIGURE 4-16: ACCUMULATION OF DAMAGE INDEX IN THE LONGITUDINAL BARS OF CH100 AS THE COLUMN IS CYCLED LATERALLY

The methodology predicted that bar fracture in member BL100 takes place at the end of the first excursion to a drift ratio of 6.5% (Table 4-7). Fracture was observed in the experimental testing at the end of the first cycle to 4.9% drift ratio. Additionally, fracture of the longitudinal bars at the member ends was predicted at the same point in the loading protocol in member BH100, and no fracture was observed in the experiments. However, at this drift, member BH100 sustained global buckling.

TABLE 4-7: SUMMARY OF EXPERIMENTALLY OBSERVED AND PREDICTED BUCKLING AND FRACTURE

	Experimnetal Observed Buckling		Methodology Predicted Buckling		Experimental Observed Fracture			Methodology Predicted Fracture		
	Drift Target Towards which Buckling Observed (%)	Half Cycle #	Drift Target Towards which Buckling Predicted (%)	Half Cycle #	Drift Target Towards which Fracture Observed (%)	Half Cycle #	Location	Drift Target Towards which Fracture Predicted (%)	Half Cycle #	Location
CH100	5.5	2	5.5	2	5.5	4	At Buckle	5.5	4	At Buckle
CL100	5.5	3	5.5	2	5.5**	5	At Buckle	5.5	4	At Buckle
CH60	5.5	2	5.5	1	5.5	3	At Buckle	5.5	4	At Buckle
BL100	Did Not Buckle		Did Not Buckle		4.9	2	At End	6.5	1	At End
2L06	Did Not Buckle		Did Not Buckle		Did Not Fracture			Did Not Fracture		
2H06	Did Not Buckle		Did Not Buckle		Did Not Fracture			Did Not Fracture		
CS60	Did Not Buckle		Did Not Buckle		Did Not Fracture			Did Not Fracture		
CS80	Did Not Buckle		Did Not Buckle		Did Not Fracture			Did Not Fracture		
BH100	Did Not Buckle		Did Not Buckle		Did Not Fracture			6.50%	1	At End
BH60	Did Not Buckle		Did Not Buckle		Did Not Fracture			Did Not Fracture		

** End of loading protocol assumed in order to compare dammage index*

**Fracture was observed at a drift ratio of 5.5% as the member was being pushed towards the first half-cycle to 7.0% drift target

4.6 SUMMARY AND CONCLUSIONS

A methodology for predicting longitudinal bar buckling initiation and fracture in SMF members is proposed. The methodology is based on estimates of local strain demands in longitudinal bars of SMF members. A buckling initiation model is proposed that accounts for the mechanical properties of the reinforcing bars, as well as the loading history the bars and surrounding concrete experience prior to buckling. Material specific bar fatigue relations calibrated through material test results are used to predict the number of half-cycles to bar fracture for buckled and un-buckled bars based on accumulation of strain demands prior and after buckling, if it occurs.

Conclusions and contributions also include:

- The proposed methodology predicted both buckling initiation and fracture of the longitudinal bars within a half-cycle of loading compared to the bar buckling initiation and fracture observed in the tests. The proposed buckling initiation model accounts for both bar properties and member design properties: decrease in steel tangent modulus with increase in compression strain demand, hoop spacing, axial load demand, local loading history of the bar and the surrounding concrete.
- Local deformation measurements of longitudinal strains around the buckled bars indicate that curvatures concentrate within this region after bar buckling. Once buckling is initiated, bar-slip deformations are reduced.
- An empirical relation was derived for the tangent modulus of elasticity of grade 60 to 100 reinforcing bars subjected to compression strains in the inelastic range of

behavior. This relation was found to be dependent on the yield strength of the longitudinal bars, as well as bar inelastic properties, such as the T/Y ratio and secant modulus, E_{sh}. At low inelastic compressive strain demands, the tangent modulus of elasticity of grade 60 bars was lower than that of the higher strength bars. This can be attributed to the lower yield strain of the grade 60 bars, which results in the stress-strain curve of these bars softening at a lower strain level compared to grade 100 bars. At high compression strains, the tangent modulus was found to converge to a value of about $E_{sh} \times \frac{f_u}{f_y}$ for all bar grades and types considered.

The proposed methodology indicates that curvature and bar-strain concentrations after bar buckling can increase fatigue damage in longitudinal bars leading to bar fracture shortly after bar buckling.

4.7 LIMITATIONS AND RECOMMENDATION FOR FUTURE WORK

It was the purpose of this study to use results from well-controlled and instrumented cyclic load tests of concrete members incorporating different grades and types of reinforcement. As such, a limited number of tests were available. As more tests on concrete members with different grades and types of steel are carried, future work should focus on increasing the accuracy in buckling initiation demand prediction, by calibrating parameters α and β to a larger dataset. Additionally, as steel mills get closer to a final product for grade 80 and100 bars, the Coffin-Manson equation parameters could be re-evaluated to remain representative of bar production in the U.S.

5. SUMMARY, CONCLUSIONS, AND DISCUSSION

The behavior of Special Moment Frame (SMF) members with high-strength reinforcing bars (HSRB) subjected to large inelastic demands was investigated through laboratory testing and analytical examination. The experimental program consisted of four SMF concrete columns reinforced with HSRB tested under constant axial load and reverse cyclic lateral loading of increasing amplitudes until fracture of longitudinal bars. In the analytical examination, a computational framework based on fiber-section elements and mechanics-based behavioral models is proposed to accurately estimate both member-level deformations and strain demands in longitudinal bars and the concrete surrounding them within the plastic hinge regions of frame members. Strain demands derived through the proposed analytical framework were used to track the damage progress of longitudinal bars up to buckling and fracture.

The research work is presented in this dissertation in the form of three collated technical papers. Conclusions from each paper are reproduced below.

5.1 PAPER 1

The structural testing program was carried out to identify any major issues in the performance of newly developed HSRB in concrete members, as well as provide necessary data to set material specifications for HSRB. The experiments conducted in this study were designed to push the new HSRB to large strain demands in concrete columns. Of particular interest was quantifying the effects of the shape of the stress-strain curve and the tensile-to-yield (*T/Y*) strength ratio of high-strength longitudinal bars on the behavior of concrete columns and the strain demands in the longitudinal bars.

Three columns were designed and built with grade 100 reinforcing bars achieved using different production techniques. CH100 was reinforced with grade 100 bars having a relatively high T/Y ratio, CL100 was reinforced with grade 100 bars have a relatively low T/Y ratio, and CM100 was reinforced with ASTM A1035 bars. A fourth specimen CH60 was designed and built using grade 60 ASTM A706 bars. All four columns were tested cyclically under a constant axial load of about 15% of the gross axial capacity. Concrete strength was around 5 ksi for all columns. The key findings are listed below:

- All specimens exhibited flexural degradation characterized by concrete crushing, varying degrees of longitudinal bar buckling, and eventually longitudinal bar fracture. Comparable drift capacities were observed between the four specimens. The four tested columns completed at least one full cycle to a drift ratio of 5.5% prior to bar fracture and 20% loss in lateral strength. The four columns tested can

therefore be considered to have acceptable materials for designs in regions of high seismicity.

- The uniform and fracture elongations of longitudinal bars did not have a determining role in the drift capacity of the four tested columns. Bar fractures were consequential to buckling and the low cycle fatigue life of the bars.
- The adjusted hoop spacing of 4.7 longitudinal bar diameters ($4.7d_b$) in the columns with grade 100 bars offset the detrimental effects of the higher bar strength and their buckling propensity, such that columns with the higher-grade bars exhibited a similar drift capacity to the column with grade 60 bars which had hoops spaced at $6.0d_b$. Using a larger hoop spacing for grade 100 bars, up to those currently permitted in ACI 318-14 for grade 60 bars (i.e., $6.0d_b$), is therefore not advised as that could produce lower drift capacities for columns reinforced with grade 100 bars than for those reinforced with grade 60 bars.
- First bar fracture in longitudinal bars of columns CH100, CL100, and CH60 occurred within the buckled length between the first and second hoop from member end in a middle bar. These bars were supported by the 90-degree cross-ties which eventually opened up, increasing the unsupported length of the bar leading to more pronounced buckling and earlier fracture as compared to the corner bars of the same columns. Therefore, it may be prudent to explore means to mitigate the 90-degree cross-ties and tie every bar in SMF columns in order to increase the lateral deformation capacity.

- Strain concentrations in longitudinal bars at flexural cracks were influenced by the shape of the stress-strain curve of the longitudinal bars. Generally, longitudinal-bar strain demands increased more rapidly with increasing lateral drifts in columns reinforced with bars having a lower *T/Y* ratio. Strains in the ASTM A1035 longitudinal bars were lower over most of the drift range than in bars of all other columns. This is possibly due to the relatively large tangent modulus of the A1035 bars in the inelastic range compared to other bars, which may have allowed strains in the A1035 bars to spread away from critical cracks more effectively.
- Inelastic strains in the longitudinal bars of all members were recorded up to similar distances away from the section of peak moment. These distances were at least equal to the section height of the cross-section. However, longitudinal bars with a higher *T/Y* ratio resulted in a greater spread of inelastic deformations and strains away from the section of peak moment demand. The length over which inelastic strains were recorded generally increased with increasing drift demands albeit at a slower rate for members with a lower *T/Y* ratio. These plastic hinge lengths were on the order of 1.0 of the section height (h) for CL100, 1.18h for CH100, and 1.12h for CH60. The lack of a well-defined yielding point and a relatively steep inelastic hardening tangent modulus of bars produced a different strain distribution behavior for CM100 than in other columns. The length over which inelastic bar strains (i.e. strains higher than strain corresponding to a stress in the bar of 100 ksi) were recorded to reach on average 24.3 in. or 1.33h in CM100, with one longitudinal bar

spreading its inelastic strain up to 27 inches or 1.5h from column end. The observed length over which inelastic bar demands were recorded in CH60, CH100, and particularly CM100 exceeded the length prescribed in ACI 318-14 (l_0 = 18 in.) over which larger amounts of transverse reinforcement is required at column ends to satisfy Special Moment Frame requirements.

- The secant lateral stiffness to first yield of the columns reinforced with grade 100 bars was at least 30% lower than that of the column reinforced with grade 60 bars, indicating that effective stiffnesses prescribed in ACI 318-14 and ASCE/SEI 41-17 may need to be revised to account for higher grades of reinforcement.
- Results indicate that an over-strength factor higher than 1.25 on the yield strength of longitudinal bars may be warranted when estimating the probable moment strength of all columns, and especially of those reinforced with A1035 longitudinal bars.
- ASCE/SEI 41-17 drift capacities at loss of 20% of moment strength were found to reasonably represent the drift capacity of the columns and were about 25% lower than those observed in the experiments.

5.2 PAPER 2

A behavioral model is proposed to scale strain estimates obtained using a calibrated force-formulation fiber-section computational element to achieve the desired strain estimates. The framework is calibrated using 12 cyclic experimental tests conducted on concrete columns and beams that were cycled to large damage states and in some cases bar fracture. The resulting computational framework is capable of matching the global deformation behavior of reinforced concrete members, through the fiber-section element, and provides reliable strain demands in the longitudinal bars and surrounding concrete through the full range of expected inelastic deformations. It was found that:

- Tension strains in longitudinal bars depend on the axial load ratio, shear stress, and tensile-to-yield-strength ratio of the steel.
- Compression strains in bars depend on the axial load ratio
- Tension strains in the concrete surface within the plastic hinge region depend on axial load ratio
- No clear correlation was found between test parameters and the ratio of concrete surface compression strains to strains from analysis.

The accurate estimate of strains in the longitudinal bars and surrounding concrete at the point of maximum demands can provide more reliable estimates of material damage and strength degradation, particularly for applications considering longitudinal bar fracture and buckling.

The framework is calibrated using 12 cyclic experimental tests conducted on concrete columns and beams that were cycled to large damage states and in some cases bar fracture. The experimental beam and column dataset contained members reinforced with regular strength, or grade 60 reinforcing bars, as well as higher strength bars of grades 80 and 100.

5.3 PAPER 3

A methodology for predicting longitudinal bar buckling initiation and fracture in SMF members is proposed. The methodology is based on estimates of local strain demands in longitudinal bars of SMF members. A buckling initiation model is proposed that accounts for the mechanical properties of the reinforcing bars, as well as the loading history the bars and surrounding concrete experience prior to buckling. Material specific bar fatigue relations calibrated through material test results are used to predict the number of half-cycle to bar fracture for buckled and un-buckled bars based on accumulation of strain demands prior and after buckling, if it occurs.

Conclusions and contributions also include:

- The proposed methodology predicted both buckling initiation and fracture of the longitudinal bars within a half-cycle of loading compared to the bar buckling and fracture observed in the tests. The proposed buckling initiation model accounts for both bar properties and member design properties: decrease in steel tangent modulus with increase in compression strain demand, hoop spacing, axial load demand, local loading history of the bar and the surrounding concrete.
- Local deformation measurements of longitudinal strains around the buckled bars indicate that curvatures concentrate within this region after bar buckling Once buckling is initiated, bar-slip deformations are reduced.
- An empirical relation was derived for the tangent modulus of elasticity of grade 60 to 100 reinforcing bars subjected to compression strains in the inelastic range of

behavior. This relation was found to be dependent on the yield strength of the longitudinal bars, as well as bar inelastic properties, such as the T/Y ratio and secant modulus, E_{sh}. At low inelastic compressive strain demands, the tangent modulus of elasticity of grade 60 bars was lower than that of the higher strength bars. This can be attributed to the lower yield strain of the grade 60 bars, which results in the stress-strain curve of these bars softening at a lower strain level compared to grade 100 bars. At high compression strains, the tangent modulus was found to converge to a value of about $E_{sh} \times \frac{f_u}{f_y}$ for all bar grades and types considered.

- The proposed methodology indicates that curvature and bar-strain concentrations after bar buckling can increase fatigue damage in longitudinal bars leading to bar fracture shortly after bar buckling.

6. APPENDIX A: EXPERIMENTAL PROGRAM INFORMATION

6.1 DESIGN CALCULATIONS AND CHECKS PER ACI 318-14

Columns Reinforced with Grade 100 Steel – CH100, CL100, CM100

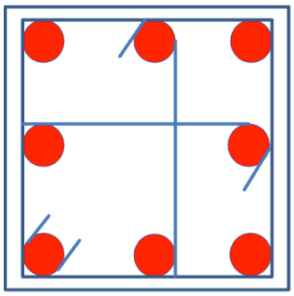

$cv := 1in$ $db := 0.75 \cdot in$ $dt := 0.5in$

$fc := 5ksi$ $Ab := db^2 \cdot \frac{3.14}{4}$ $At := dt^2 \cdot \frac{3.14}{4}$

$l := 108 \cdot in$

$fyl := 104ksi$ $fyt := 105ksi$

$E := 29000ksi$

$Ec := 57000 \cdot \frac{\sqrt{fc \cdot 1000ksi}}{1000} = 4.031 \times 10^3 \cdot ksi$

1. Checks from ACI 318-14

18.7.2.1 Shortest cross sectional dimension: >12 in $b := 18in$ $h := 18in$

18.7.2.1 Short to long dimension ratio > 0.4

$\frac{b}{h} = 1$ $d := h - cv - dt - \frac{db}{2} = 16.125 \cdot in$

18.7.4 Area of longitudinal reinforcement:

$Amin := 0.01 \cdot b \cdot h = 3.24 \cdot in^2$

$Amax := 0.06 \cdot b \cdot h = 19.44 \cdot in^2$ $Ast := 8 \cdot Ab = 3.532 \cdot in^2$

18.7.5 Transverse Reinforcement

$l0 := \max\left(18in, \frac{l}{6}, d\right) = 18 \cdot in$

18.7.5.2 Spacing of crossties or legs of rectilinear hoops:

$hxmax := 14in$

$hx := \frac{(b - 2cv - dt)}{2} = 7.75 \cdot in$

18.7.5.3 Spacing of transverse reinforcement:

$s0 := \min\left[6 \cdot db, 4in + \frac{(14in - hx)}{2}, \frac{h}{4}\right] = 4.5 \cdot in$

Chosen spacing: $s := 3.5in$

Forces in each reinforcing layer:

$$F1 := \begin{cases} \frac{\varepsilon s3}{|\varepsilon s3|} \cdot fyl \cdot A1 & \text{if } |\varepsilon s1| > \frac{fyl}{E} \\ \varepsilon s1 \cdot E \cdot A1 & \text{otherwise} \end{cases} = 117.852 \cdot kip$$

$$F2 := \begin{cases} \frac{\varepsilon s3}{|\varepsilon s3|} \cdot fyl \cdot A2 & \text{if } |\varepsilon s2| > \frac{fyl}{E} \\ \varepsilon s2 \cdot E \cdot A2 & \text{otherwise} \end{cases} = -53.826 \cdot kip$$

$$F3 := \begin{cases} \frac{\varepsilon s3}{|\varepsilon s3|} \cdot 1.25 fyl \cdot A3 & \text{if } |\varepsilon s3| > \frac{fyl}{E} \\ \varepsilon s3 \cdot E \cdot A3 & \text{otherwise} \end{cases} = -172.209 \cdot kip$$

Compression force from concrete: $Fc := 0.85 \cdot \beta \cdot fc \cdot b \cdot c = 361.08 \cdot kip$

$F := F1 + F2 + F3 + Fc = 252.897 \cdot kip$

$$Mpr := Fc \cdot \left(\frac{-\beta \cdot c}{2} + \frac{h}{2} \right) + F1 \cdot \left(-d1 + \frac{h}{2} \right) + F2 \cdot \left(-d2 + \frac{h}{2} \right) + F3 \cdot \left(-d3 + \frac{h}{2} \right) = 4.609 \times 10^3 \cdot kip \cdot in$$

Mpr from OpenSees:

$Mpr := 4490 kip \cdot in$

$$\gamma := \frac{F}{b \cdot h \cdot fc} = 0.156$$

Shear: $\lambda := 1$

$$Ve := \frac{2Mpr}{l} = 83.148 \cdot kip$$

$$Vnrequired := \frac{Ve}{0.75} = 110.864 \cdot kip$$

$$\tau := \frac{\frac{Ve}{kip} \cdot 1000}{\frac{b}{in} \cdot \frac{d}{in} \cdot \sqrt{\frac{fc}{ksi} \cdot 1000}} = 4.051$$

Check ACI 21.6.5.2 Shall we account for Vc?

a) Induced shear force represents more than one-half of the shear strength
b) Factored axial load:

$$F = 252.897 \cdot kip \qquad \sigma := b \cdot h \cdot \frac{fc}{20} = 81 \cdot kip$$

Axial compression is more than 5% of the capacity, thus we should consider Vc.

$$Vc := 2 \cdot \left(1ksi + \frac{F \cdot 1000}{2000 \cdot b \cdot h}\right) \cdot \lambda \cdot \sqrt{fc \cdot \frac{1000}{ksi}} \cdot b \cdot \frac{\left(h - cv - dt - \frac{db}{2}\right)}{1000} = 57.067 \cdot kip$$

$$Vsrequired := Vnrequired - Vc = 53.797 \cdot kip$$

$$Vsprovided := 3 \cdot At \cdot fyt \cdot \frac{(h - cv)}{s} = 300.263 \cdot kip \qquad Avrequired := \frac{Vsrequired \cdot s}{fyt \cdot \left(h - cv - dt - \frac{db}{2}\right)} = 0.111 \cdot in^2$$

$$Vnprovided := Vc + Vsprovided = 357.33 \cdot kip \qquad Avprovided := 3 \cdot At = 0.589 \cdot in^2$$

$$\rho_w := \frac{Avrequired}{Avprovided} = 0.189$$

Detailing

Minimum Hook Lengths:

For longitudinal reinforcement hooks: 90* hook length: $lb1 := 12 \cdot db = 9 \cdot in$

180* hook length: $lb2 := 4 \cdot db = 3 \cdot in$

For tie hooks: $lv := 6 \cdot dt = 3 \cdot in$

Minimum Bend Diameters:

For longitudinal reinforcement: $\theta l := 6 \cdot db = 4.5 \cdot in$

For ties: $\theta v := 4 \cdot dt = 2 \cdot in$

Confined concrete

1. Confining Pressure

$$bc := b - 2\cdot cv - 2\cdot\frac{dt}{2} = 15.5\cdot in \qquad hc := bc = 15.5\cdot in$$

$$frx := \frac{3\cdot At\cdot fyt}{s\cdot bc} = 1.14\cdot ksi \qquad fry := frx = 1.14\cdot ksi$$

2. Effective Area

$$wi := \frac{bc - 2\cdot cv - 2\cdot dt - 3\cdot db}{2} = 5.125\cdot in$$

$$Aineff := \frac{8\cdot wi^2}{6} = 35.021\cdot in\cdot(in) \qquad s1 := s - 2\cdot\frac{dt}{2} = 3\cdot in$$

$$Aeff := (bc\cdot hc - Aineff)\left(1 - \frac{s1}{2\cdot bc}\right)\cdot\left(1 - \frac{s1}{2\cdot hc}\right) = 167.429\cdot in\cdot in$$

$$Acc := hc\cdot bc - 8\cdot Ab = 236.718\cdot in\cdot in$$

3. Effective confinement coefficient

$$ke := \frac{Aeff}{Acc} = 0.707$$

4. Effective lateral confining pressure

$$freff := ke\cdot frx = 0.806\cdot ksi \qquad \frac{freff}{fc} = 0.161 \text{ ---------->>>>>}$$

$$fcc := 1.85\cdot fc = 9.25\cdot ksi$$

5. Strain at ultimate stress

$$\varepsilon cc := \varepsilon co\cdot\left[1 + 5\cdot\left(\frac{fcc}{fc} - 1\right)\right] = 0.011 \qquad \varepsilon co := 0.002 \quad \text{Ref: Mander et al}$$

6. Maximum strain capacity of confined concrete

$$\rho s := \frac{At\cdot bc\cdot 6}{Acc\cdot s} = 0.022$$

$$\varepsilon cmax := 0.004 + 0.1\cdot\frac{\rho s\cdot fyl}{fc} = 0.05$$

Column Reinforced with Grade 60 Steel - CH60

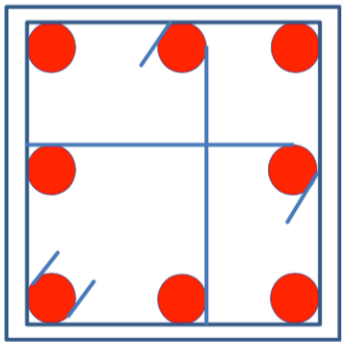

$cv := 1in$ $db := 0.75 \cdot in$ $dt := 0.5in$

$fc := 5.0ksi$ $Ab := db^2 \cdot \frac{3.14}{4}$ $At := dt^2 \cdot \frac{3.14}{4}$

$l := 108 \cdot in$

$fyl := 64ksi$ $fyt := 65ksi$

$E := 29000ksi$

$$Ec := 57000 \cdot \frac{\sqrt{fc \cdot 1000ksi}}{1000} = 4.031 \times 10^3 \cdot ksi$$

1. Checks from ACI 318-14

18.7.2.1 Shortest cross sectional dimension: >12 in $b := 18in$ $h := 18in$

18.7.2.1 Short to long dimension ratio > 0.4

$$\frac{b}{h} = 1 \qquad d := h - cv - dt - \frac{db}{2} = 16.125 \cdot in$$

18.7.4 Area of longitudinal reinforcement:

$$Amin := 0.01 \cdot b \cdot h = 3.24 \cdot in^2$$

$$Amax := 0.06 \cdot b \cdot h = 19.44 \cdot in^2 \qquad Ast := 8 \cdot Ab = 3.532 \cdot in^2$$

18.7.5 Transverse Reinforcement

$$l0 := \max\left(18in, \frac{l}{6}, d\right) = 18 \cdot in$$

18.7.5.2 Spacing of crossties or legs of rectilinear hoops:

$$hxmax := 14in$$

$$hx := \frac{(b - 2cv - dt)}{2} = 7.75 \cdot in$$

18.7.5.3 Spacing of transverse reinforcement:

$$s0 := \min\left[6 \cdot db, 4in + \frac{(14in - hx)}{2}, \frac{h}{4}\right] = 4.5 \cdot in$$

Chosen spacing: $s := 4.5in$

b) Cross sectional area:

$$Ash1 := 0.3 \cdot s \cdot (b - 2cv) \cdot \frac{(b \cdot h) - (b - 2cv)(h - 2cv)}{(b - 2cv)(h - 2cv)} \cdot \frac{fc}{fyt} = 0.441 \cdot in^2$$

$$Ash2 := 0.09 \cdot s \cdot (b - 2 \cdot cv) \cdot \frac{fc}{fyt} = 0.498 \cdot in^2$$

$$Ash := \max(Ash1, Ash2) = 0.498 \cdot in^2 \qquad Ashprovided := 3 \cdot At = 0.589 \cdot in^2$$

2. Calculate M_{pr}:

Longitudinal bar layer position relative to the top concrete fiber of the section, and area per layer:

$$d1 := cv + \frac{db}{2} = 1.375 \cdot in \qquad A1 := 3 \cdot Ab = 1.325 \cdot in^2$$

$$d2 := d1 + \frac{(h - 2 \cdot d1)}{2} = 9 \cdot in \qquad A2 := 2 \cdot Ab = 0.883 \cdot in^2$$

$$d3 := d2 + \frac{(h - 2 \cdot d1)}{2} = 16.625 \cdot in \qquad A3 := 3 \cdot Ab = 1.325 \cdot in^2$$

Concrete compression block parameter: (ratio of max stress to avg stress)

$$\beta := 0.85 - 0.05 \cdot \left(-4 + \frac{fc}{ksi}\right) = 0.8$$

Assume NA depth: $c := 5.3in$

Assume strain at top fiber concrete is (conservative): $\varepsilon cu := 0.004$

Assuming plain sections remain plain, the strain in each reinforcing layer is:

$$\varepsilon s1 := \varepsilon cu \cdot \frac{(c - d1)}{c} = 2.962 \times 10^{-3}$$

$$\varepsilon s2 := \varepsilon cu \cdot \frac{(c - d2)}{c} = -2.792 \times 10^{-3}$$

$$\varepsilon s3 := \varepsilon cu \cdot \frac{(c - d3)}{c} = -8.547 \times 10^{-3}$$

Forces in each reinforcing layer:

$$F1 := \begin{cases} \frac{\varepsilon s1}{|\varepsilon s1|} \cdot fyl \cdot A1 & \text{if } |\varepsilon s1| > \frac{fyl}{E} \\ \varepsilon s1 \cdot E \cdot A1 & \text{otherwise} \end{cases} = 84.78 \cdot kip$$

$$F2 := \begin{cases} \frac{\varepsilon s2}{|\varepsilon s2|} \cdot fyl \cdot A2 & \text{if } |\varepsilon s2| > \frac{fyl}{E} \\ \varepsilon s2 \cdot E \cdot A2 & \text{otherwise} \end{cases} = -56.52 \cdot kip$$

$$F3 := \begin{cases} \frac{\varepsilon s3}{|\varepsilon s3|} \cdot 1.25 fyl \cdot A3 & \text{if } |\varepsilon s3| > \frac{fyl}{E} \\ \varepsilon s3 \cdot E \cdot A3 & \text{otherwise} \end{cases} = -105.975 \cdot kip$$

Compression force from concrete: $Fc := 0.85 \cdot \beta \cdot fc \cdot b \cdot c = 324.36 \cdot kip$

$F := F1 + F2 + F3 + Fc = 246.645 \cdot kip$

$$Mpr := Fc \cdot \left(\frac{-\beta \cdot c}{2} + \frac{h}{2} \right) + F1 \cdot \left(-d1 + \frac{h}{2} \right) + F2 \cdot \left(-d2 + \frac{h}{2} \right) + F3 \cdot \left(-d3 + \frac{h}{2} \right) = 3.686 \times 10^3 \cdot kip \cdot in$$

Mpr from OpenSees:

$Mpr := 3525 kip \cdot in$

$$\gamma := \frac{F}{b \cdot h \cdot fc} = 0.152$$

Shear: $\lambda := 1$

$Ve := \frac{2Mpr}{l} = 74.074 \cdot kip$

$Vnrequired := \frac{Ve}{0.75} = 98.765 \cdot kip$

$\tau := \frac{\frac{Ve}{kip} \cdot 1000}{\frac{b}{in} \cdot \frac{d}{in} \cdot \sqrt{\frac{fc}{ksi} \cdot 1000}} = 3.609$

Check shall we account for Vc?

a) Induced shear force represents more than one-half of the shear strength
b) Factored axial load:

$F = 246.645 \cdot kip \quad \sigma := b \cdot h \cdot \frac{fc}{20} = 81 \cdot kip$

Axial compression is more than 5% of the capacity, thus we are allowed to consider Vc.

$Vc := 2 \cdot \left(1ksi + \frac{F \cdot 1000}{2000 \cdot b \cdot h}\right) \cdot \lambda \cdot \sqrt{fc \cdot \frac{1000}{ksi}} \cdot b \cdot \frac{\left(h - cv - dt - \frac{db}{2}\right)}{1000} = 56.671 \cdot kip$

$Vsrequired := Vnrequired - Vc = 42.094 \cdot kip$

$Vsprovided := 3 \cdot At \cdot fyt \cdot \frac{(h - cv)}{s} = 144.571 \cdot kip$

$Avrequired := \frac{Vsrequired \cdot s}{fyt \cdot \left(h - cv - dt - \frac{db}{2}\right)} = 0.181 \cdot in^2$

$Vnprovided := Vc + Vsprovided = 201.242 \cdot kip$

$Avprovided := 3 \cdot At = 0.589 \cdot in^2$

$\rho_w := \frac{Avrequired}{Avprovided} = 0.307$

Detailing

Minimum Hook Lengths:

For longitudinal reinforcement hooks: 90* hook length: $lb1 := 12 \cdot db = 9 \cdot in$
180* hook length: $lb2 := 4 \cdot db = 3 \cdot in$

For tie hooks: $lv := 6 \cdot dt = 3 \cdot in$

Minimum Bend Diameters:

For longitudinal reinforcement: $\theta l := 6 \cdot db = 4.5 \cdot in$

For ties: $\theta v := 4 \cdot dt = 2 \cdot in$

Confined concrete

1. Confining Pressure

$$bc := b - 2\cdot cv - 2\cdot\frac{dt}{2} = 15.5\cdot in \qquad hc := bc = 15.5\cdot in$$

$$frx := \frac{3\cdot At\cdot fyt}{s\cdot bc} = 0.549\cdot ksi \qquad fry := frx = 0.549\cdot ksi$$

2. Effective Area

$$wi := \frac{bc - 2\cdot cv - 2\cdot dt - 3\cdot db}{2} = 5.125\cdot in$$

$$Aineff := \frac{8\cdot wi^2}{6} = 35.021\cdot in\cdot in \qquad s1 := s - 2\cdot\frac{dt}{2} = 4\cdot in$$

$$Aeff := (bc\cdot hc - Aineff)\left(1 - \frac{s1}{2\cdot bc}\right)\cdot\left(1 - \frac{s1}{2\cdot hc}\right) = 155.684\cdot in\cdot in$$

$$Acc := hc\cdot bc - 8\cdot Ab = 236.718\cdot in\cdot in$$

3. Effective confinement coefficient

$$ke := \frac{Aeff}{Acc} = 0.658$$

4. Effective lateral confining pressure

$$freff := ke\cdot frx = 0.361\cdot ksi \qquad \frac{freff}{fc} = 0.072 \qquad \text{---------->>>>>}$$

$$fcc := 1.46\cdot fc = 7.3\cdot ksi$$

5. Strain at ultimate stress

$$\varepsilon cc := \varepsilon co\cdot\left[1 + 5\cdot\left(\frac{fcc}{fc} - 1\right)\right] = 6.6\times 10^{-3} \qquad \varepsilon co := 0.002$$

Ref: Mander et al

6. Maximum strain capacity of confined concrete

$$\rho s := \frac{At\cdot bc\cdot 6}{Acc\cdot s} = 0.017$$

$$\varepsilon cmax := 0.004 + 0.1\cdot\frac{\rho s\cdot fyl}{fc} = 0.026$$

6.2 DETAILED DRAWINGS OF THE SPECIMENS

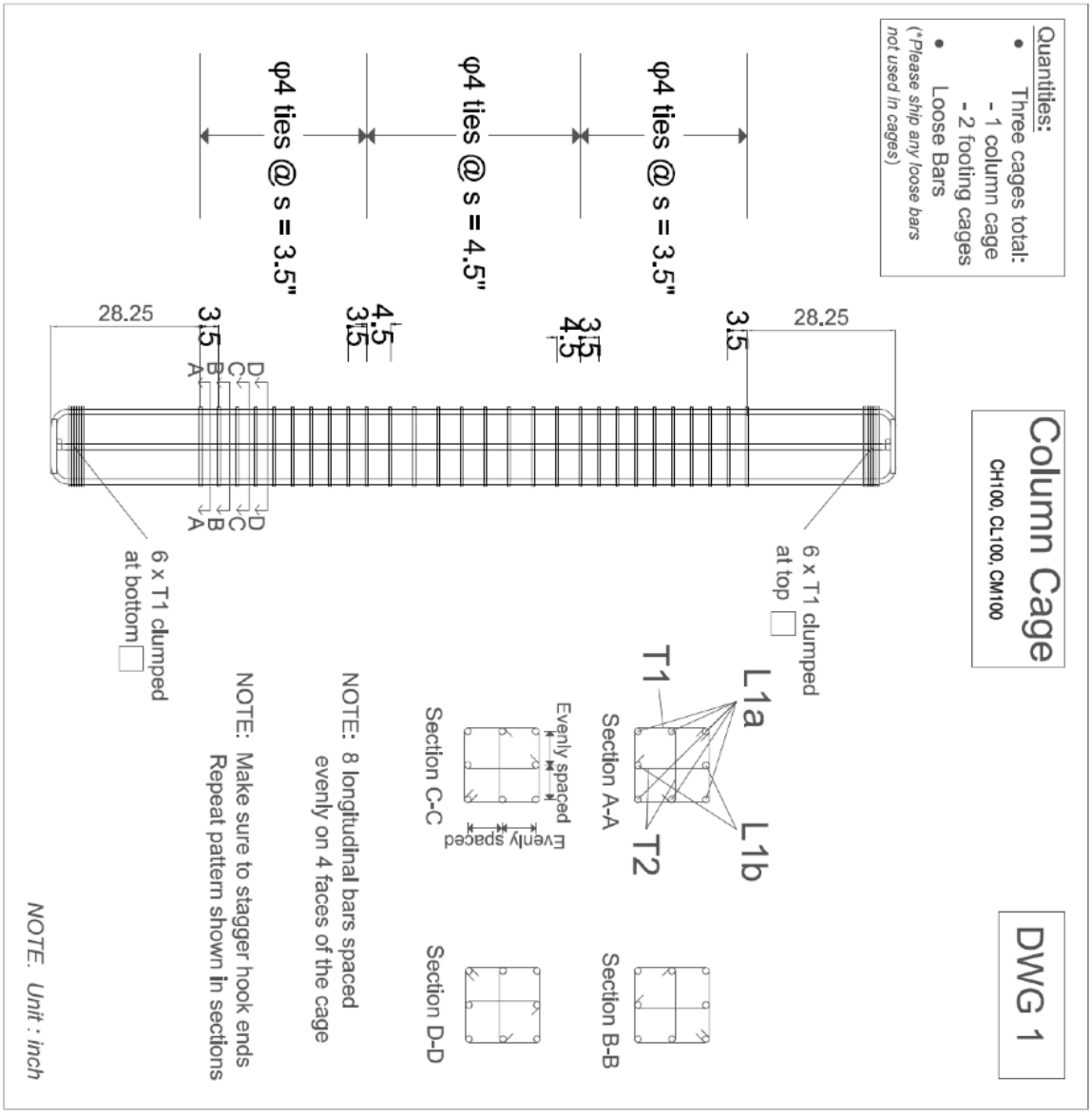

Quantities:

- Three cages total:
  - 1 column cage
  - 2 footing cages
- Loose Bars

(**Please ship any loose bars not used in cages*)

Column Cage
CH60

DWG 1b

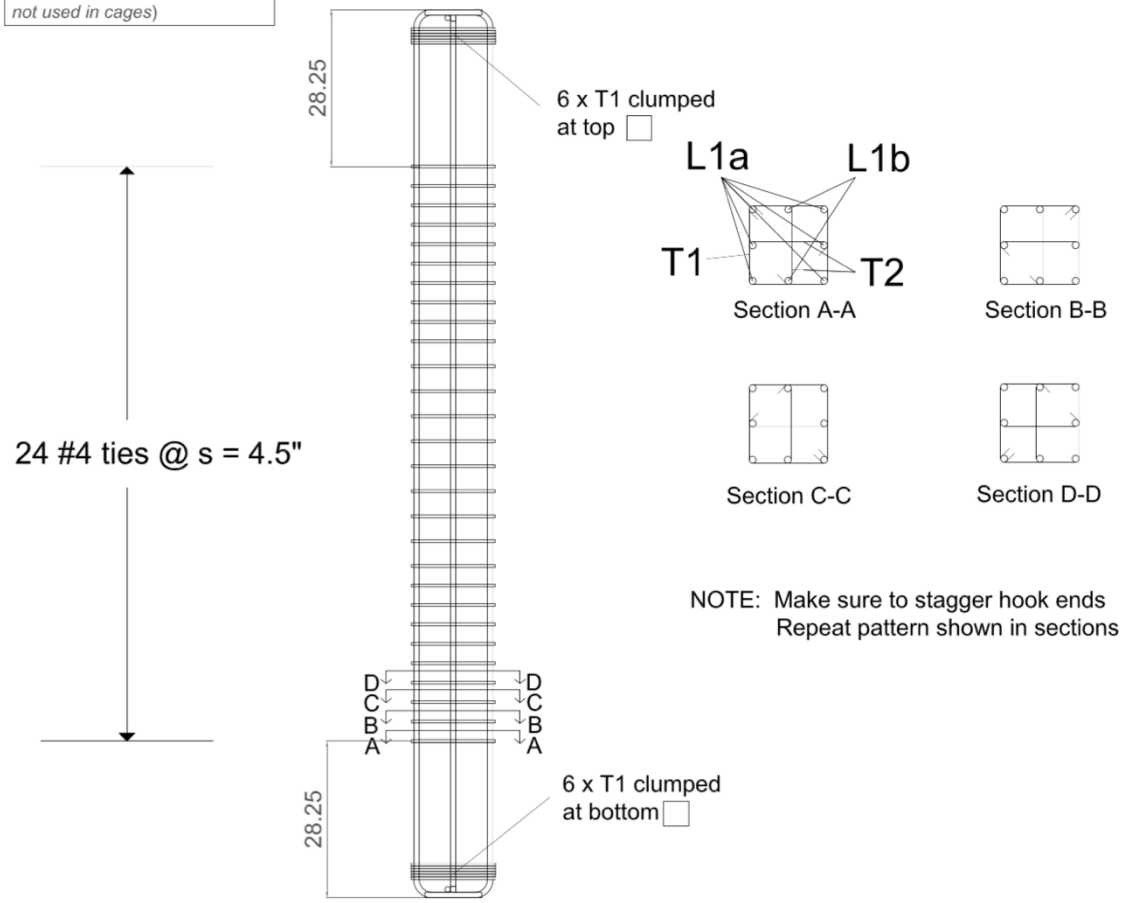

Section A-A

Section B-B

Section C-C

Section D-D

NOTE: Make sure to stagger hook ends
Repeat pattern shown in sections

NOTE. Unit : inch

Quantities:

- Three cages total:
  - 1 column cage
  - 2 footing cages
- Loose Bars

(*Please ship any loose bars not used in cages)

Footing Cages

Quantity = 2

DWG 2

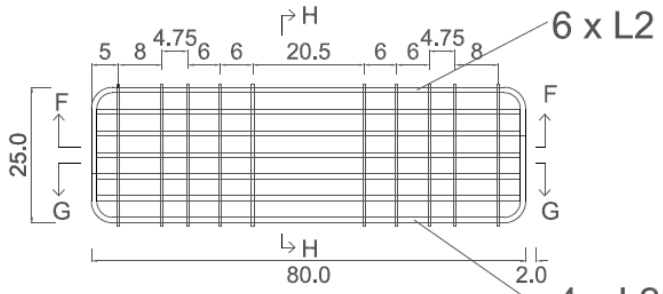

Side view of Top footing

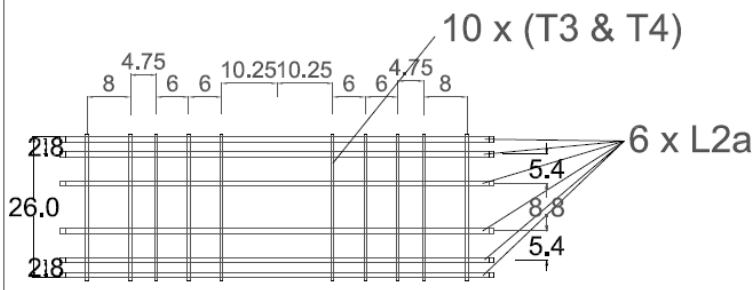

Section F-F

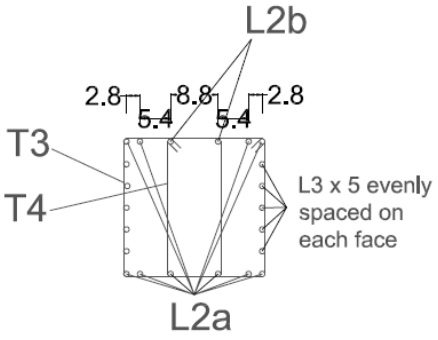

Section H-H

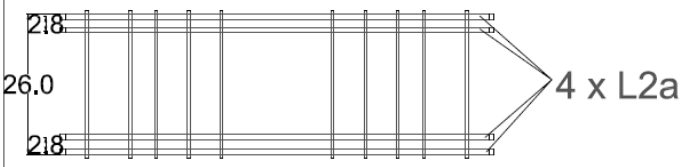

Section G-G

NOTE: Make sure to stagger hook ends

NOTE. Unit : inch

DWG 3

Tolerances:
T1, T2 +- **1/4** "
All others +-1/2 "

Bar schedule

GR60 Bars A706 or A615
GR100 Bars Special Grade

Note. Unit : Inch
T1, T2, CP1 must be from same heat
L1a, L1b, and CP2 must be from same heat

L1a	L1b	L2a	L2b	L3	L4	L5	
#6 **Gr 100** bar x 6	#6 **Gr 100** bar x 2	#8 Gr 60 bar x 20	#8 Gr 60 bar x 4	#4 Gr 60 bar x 20	#4 Gr 60 bar x 24	#4 Gr 60 bar x 32	
		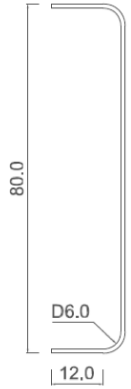	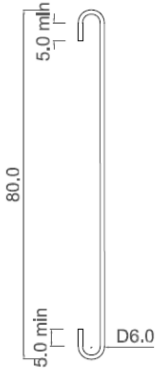 ***		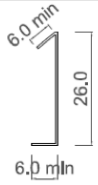 ***	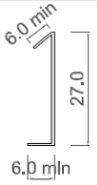 ***	
				NOTE: Bend inside diameter = 3.0" for #4 bars Bend inside diameter = 4.5" for #6 bars As specified - for other bars			

*** Please ship any loose bars not used in cages.

NOTE. Unit : inch

DWG 4

Tolerances:
T1, T2 +- **1/4** "
All others +-1/2 "

Bar schedule

GR60 Bars A706 or A615
GR100 Bars Special Grade

Note. Unit : Inch
T1, T2, CP1 must be from same heat
L1a, L1b, and CP2 must be from same heat

T1	T2	T3	T4				
#4 **Gr 100** bar x 40	#4 **Gr 100** bar x 80	#4 Gr 60 ties x 20	#4 Gr 60 ties x 20				
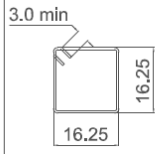	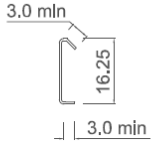	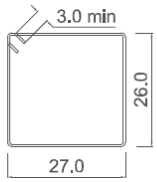	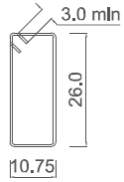				

NOTE. Bend inside diameter = 3.0" for #4 bars

NOTE. Unit : inch

6.3 Pictures from Specimen Construction and Test Setup

Columns were cast in an upright position in three stages, simulating a typical construction sequence. The bottom footing and column cage were tied together and placed in steel forms (Figure 6-1; Figure 6-3). The bottom footing was cast first and the concrete surface at the interface with the column was roughened. The bottom footing was allowed to cure for several days before casting the column concrete. The top footing cage was then placed in the forms along with PVC pipes that created holes in order to enable the attachment to the loading frame and for lifting. More than 28 days were allowed for each concrete column to cure before testing.

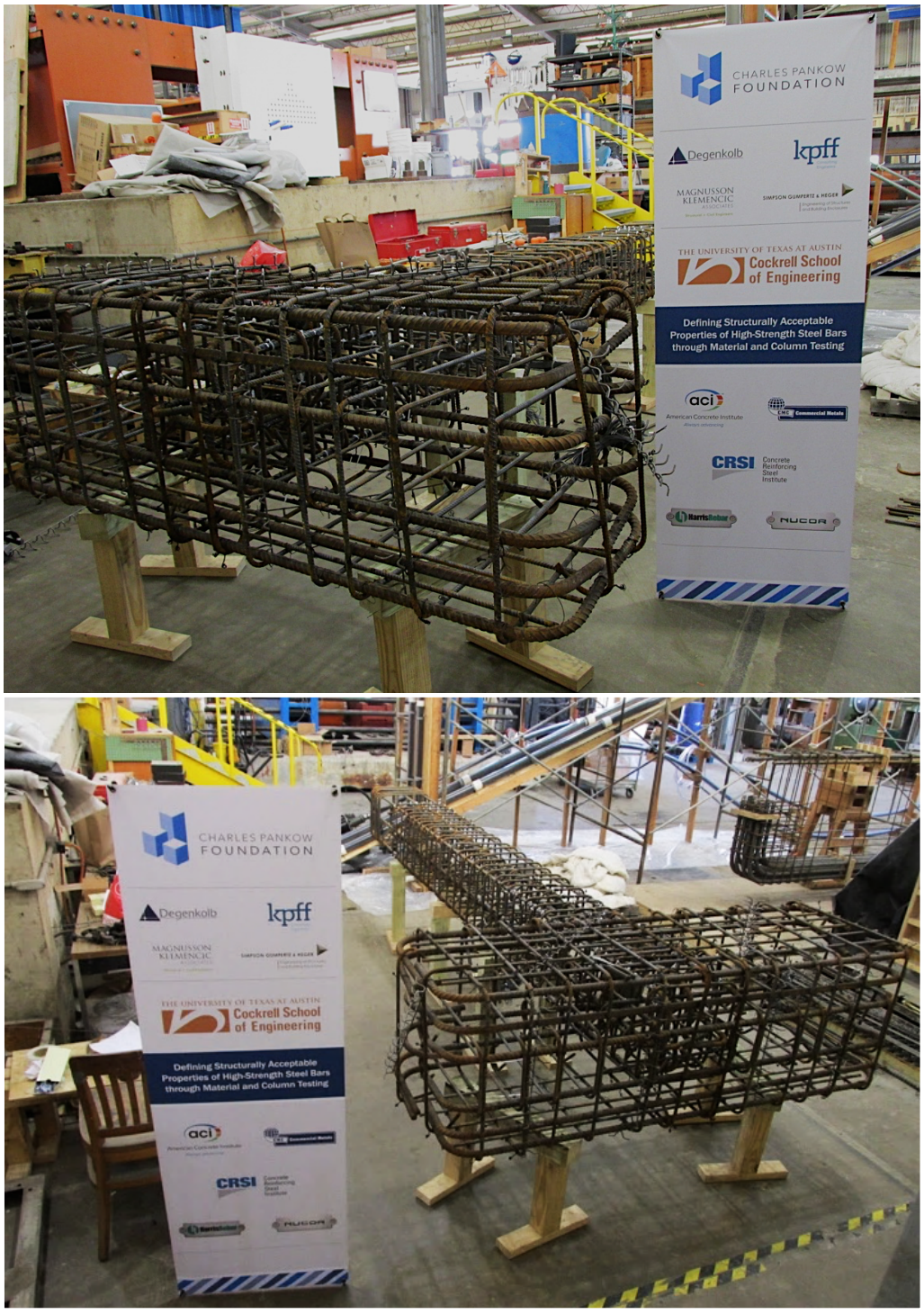

FIGURE 6-1: STEEL CAGE ASSEMBLY AND STRAIN GAUGE INSTALLATION

FIGURE 6-2: SLUMP TEST AND CONCRETE CYLINDER PREPARATION FOR A TYPICAL CAST

Figure 6-3: Column casting process

FIGURE 6-4: TEST SETUP

6.4 Concrete Mix Properties and Compressive Strength

The columns and footings supporting them had the same concrete mix design (Table 6-1). The concrete mix had a specified compressive strength of 5 ksi and a seven-inch slump. River gravel was used in both cases, with a specified maximum aggregate size of 1 in.

Table 6-1: Concrete mix design quantities

Material	Design Quantities
Type 1 cement	423 lb/yd^3
Fly ash – Class F	141 lb/yd^3
Sand	1343 lb/yd^3
1” max. river gravel aggregate	1950 lb/yd^3
Water	29.0 gal/yd^3
High Range Water Reducer	28.2 oz/ yd^3

Cylinders with a four-inch diameter were prepared for each cast and stored near their respective specimen to cure in the same environmental conditions. Concrete cylinders were left in plastic containers and covered with a plastic sheet for the same duration as formwork was left on the specimens. Concrete cylinders were removed from the plastic containers the same day the formwork was removed. Results from tested cylinders are presented below.

TABLE 6-2: CONCRETE CYLINDERS' COMPRESSIVE STRENGTH

		Cylinder 1	Cylinder 2	Cylinder 3	Average
CH100	7 days	4.1	4.0	4.0	4.0
	14 days	4.9	4.7	4.6	4.7
	21 days	5.0	4.9	4.7	4.9
	28 days	5.3	5.1	5.2	5.2
	Day of the test	5.2	5.2	5.2	5.2
CL100	7 days	3.9	4.1	4.0	4.0
	14 days	4.8	4.5	4.7	4.7
	21 days	5.0	5.1	5.0	5.0
	28 days	5.2	4.9	5.1	5.1
	Day of the test	5.3	5.1	5.1	5.2
CM100	7 days	5.0	4.8	4.9	4.9
	14 days	N/A	N/A	N/A	N/A
	21 days	N/A	N/A	N/A	N/A
	28 days	5.6	5.4	5.4	5.4
	Day of the test	5.6	5.5	5.6	5.6
CH60	7 days	3.3	3.4	3.3	3.4
	14 days	4.2	4.1	4.2	4.2
	21 days	4.4	4.3	4.4	4.4
	28 days	4.5	4.4	4.5	4.5
	Day of the test	4.5	4.7	4.5	4.6

6.5 Reinforcing Steel Tensile Test Results

In order to identify the material properties of the steel bars, monotonic tension tests were performed conforming to the procedures specified in *ASTM A370 – Standard Methods and Definitions for Mechanical Testing of Steel Products* and *ASTM E8 – Standard Test Methods for Tension Testing of Metallic Materials*. The complete force-strain response of a bar was recorded during each monotonic test. Stresses were calculated as the bar force divided by the nominal bar area. All strains used to generate bar stress-strain relations were measured over an 8-inch gauge length as specified in ASTM A370. The material properties obtained include: the modulus of elasticity, the yield strength, the tensile strength, the tensile-to-yield strength ratio, the uniform strain, and the fracture strain. The modulus of elasticity was measured as the slope of the initial elastic region of the stress-strain curve. Yield stress was calculated by the 0.2% offset method as detailed in ASTM E8. The ultimate tensile strength was measured as the maximum stress recorded in a test. The tensile-to-yield strength ratio was taken as the ratio of the ultimate tensile strength to the yield strength. Uniform strain is defined as the strain reached at tensile strength and immediately prior to the initiation of necking. Since the stress-strain curve can be assumed to be nearly flat in this region, the uniform strain was taken, in accordance with ASTM E8, as the middle point of the range of strains that led to stresses of at least 99.5% of the ultimate tensile strength. Fracture strain was measured just prior to loss of load-carrying capacity and, therefore, includes both the plastic and the elastic components of strain. Stress-strain curves and measured properties of all tested bars are presented below.

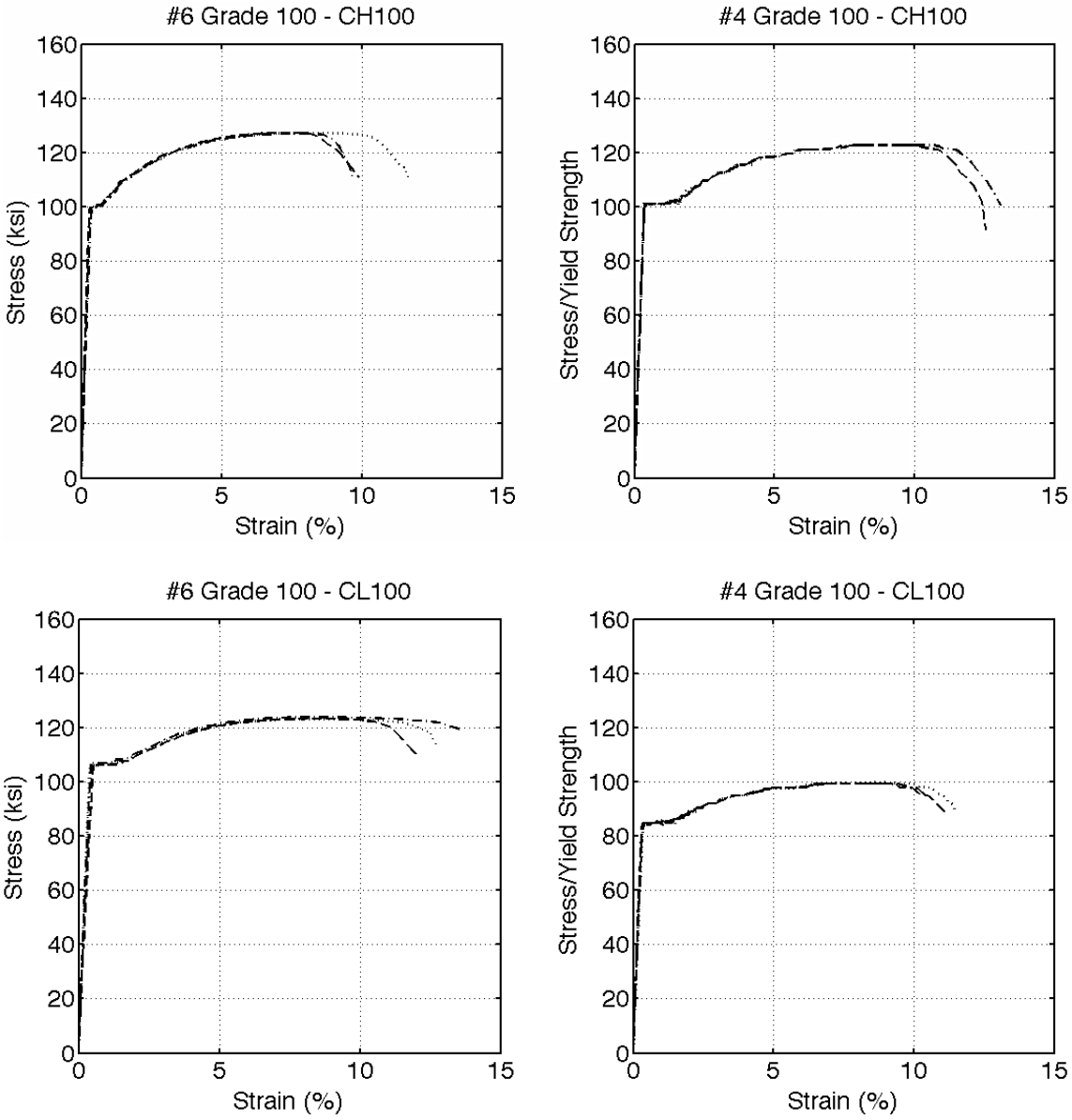

FIGURE 6-5: CONTINUES INTO NEXT PAGE

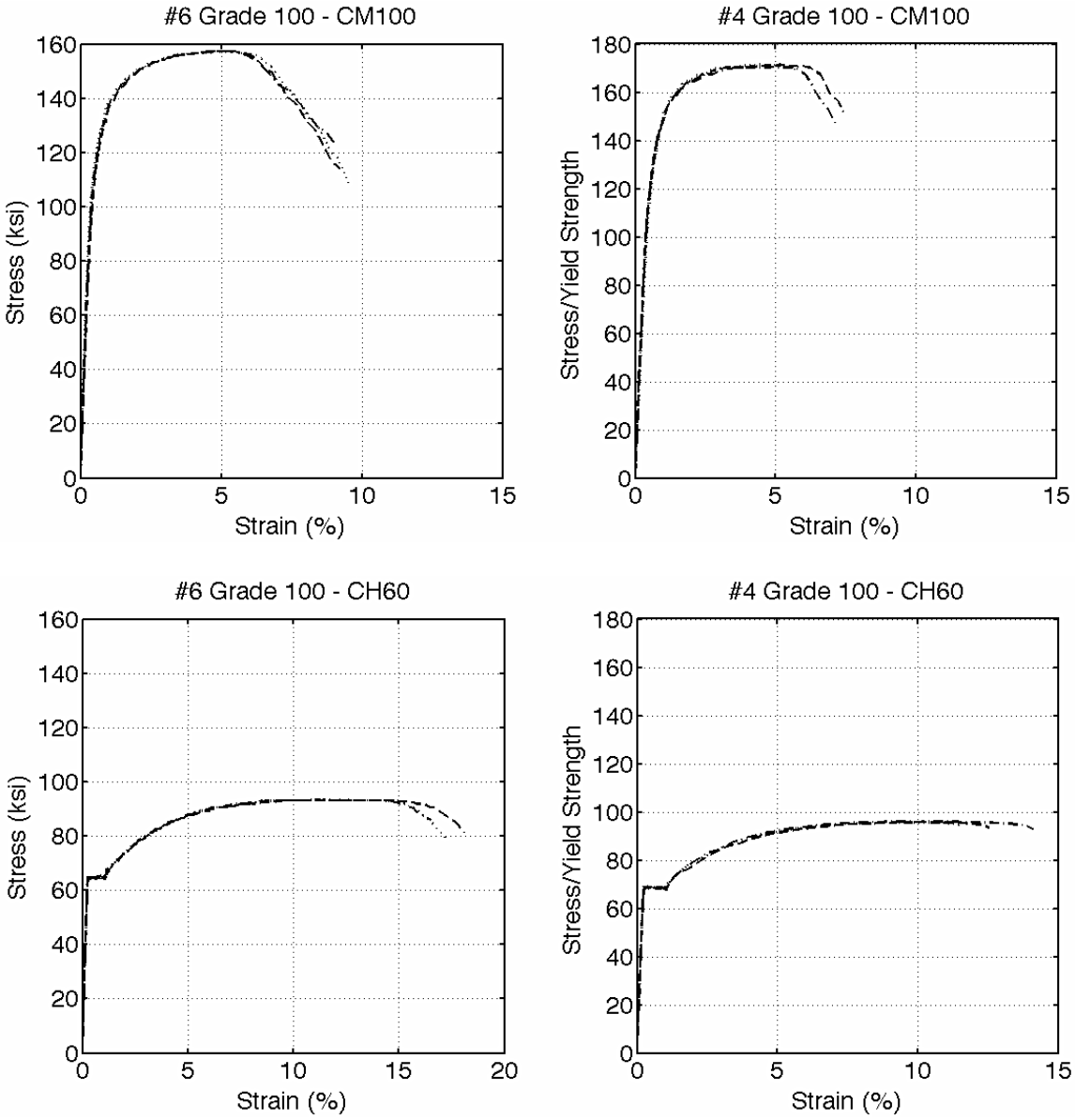

FIGURE 6-5: STRESS-STRAIN CURVES OF ALL LONGITUDINAL AND TRANSVERSE REINFORCING BARS UNDER MONOTONIC TENSION LOADING

TABLE 6-3: MECHANICAL PROPERTIES OF LONGITUDINAL AND TRANSVERSE REINFORCING BARS

Bar Size	Specimen	Trial Number	Yield Strength (ksi)	Tensile Strength (ksi)	Elastic Modulus (ksi)	Uniform Elongation (%)	Fracture Elongation (%)
#6	CH100	1	100	127.0	29,920	7.4	9.8
		2	99.8	127.2	30,170	8.2	11.7
		3	100.1	127.4	33,950	7.1	9.9
	CL100	1	106.9	123.9	25,150	8.9	12.7
		2	106.1	123.1	26,240	8.6	12.7
		3	106.3	123.2	20,374	8.4	12.0
	CM100	1	123.0	157.4	27,230	4.9	10.2
		2	125.0	157.4	28,480	5.0	9.7
		3	124.5	157.4	24,570	5.0	9.5
	CH60	1	64.5	93.4	25,640	11.4	16.9
		2	64.4	93.4	26,200	11.7	17.5
		3	64.4	93.2	27,000	12.2	18.4
#4	CH100	1	101.1	122.7	28,349	9.3	13.3
		2	101.1	N/A	28,740	N/A	N/A
		3	101.0	122.7	28,266	8.8	12.4
	CL100	1	84.4	99.3	25,986	8.0	11.3
		2	84.7	100.0	24,461	8.3	12.0
		3	84.7	99.4	28,346	7.8	11.4
	CM100	1	141.5	170.4	22,590	4.5	8.2
		2	141.7	171.7	21,890	4.5	8.0
		3	138.4	171.3	25,400	5.0	9.7
	CH60	1	66.6	96.2	30,400	N/A	N/A
		2	N/A	N/A	N/A	N/A	N/A
		3	67.8	94.7	30,900	N/A	N/A

6.6 TEST SETUP AND INSTRUMENTATION – ADDITIONAL INFORMATION

The setup consisted of three MTS actuators each having a 215-kip capacity in tension and 330-kip capacity in compression. The two vertical actuators applied a constant compressive load which equaled $0.15\ A_g f_c'$ in all columns, where f_c' was the concrete compressive strength measured at the day the corresponding column was tested. A third – horizontal – actuator pushed the columns in uni-directional quasi-static cyclic loading. The estimated self-weight of the top footing and hardware was accounted for when calculating the axial compression force that was applied by each actuator. The resulting axial loads applied at the bottom of each column were: 252 kips for CH100, 252 kips for CL100, 263 kips for CM100, and 232 kips for CH60.

Strain gauges were installed on the four corner bars at each column end, along four longitudinal bars within the footings and plastic hinge regions (Figure 6-6). Strain gauge installation followed manufacturer recommended procedures (Figure 6-7). Steel bars were ground to achieve a smooth surface at the location of a gauge. Great care was taken not to reduce bar cross-section in the grinding process. The cleared surface was then treated by removing any grease or dirt and was lightly polished with an abrasive #120 paper and wiped with acetone. CN-Y (Cyanoacrylate) adhesive was used to glue the gauges to the bar. After allowing for curing time, the gauge was wrapped with several protective layers as seen in Figure 6-7. Redundancy in strain gauge instrumentation allowed the omission of questionable measured strain data in when analyzing the results.

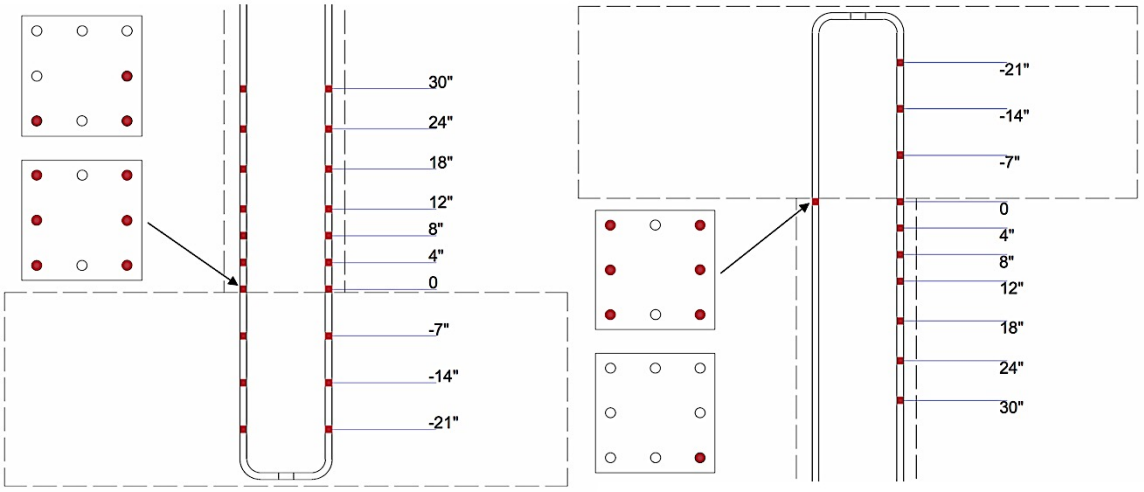

FIGURE 6-6: STRAIN GAGE LOCATIONS

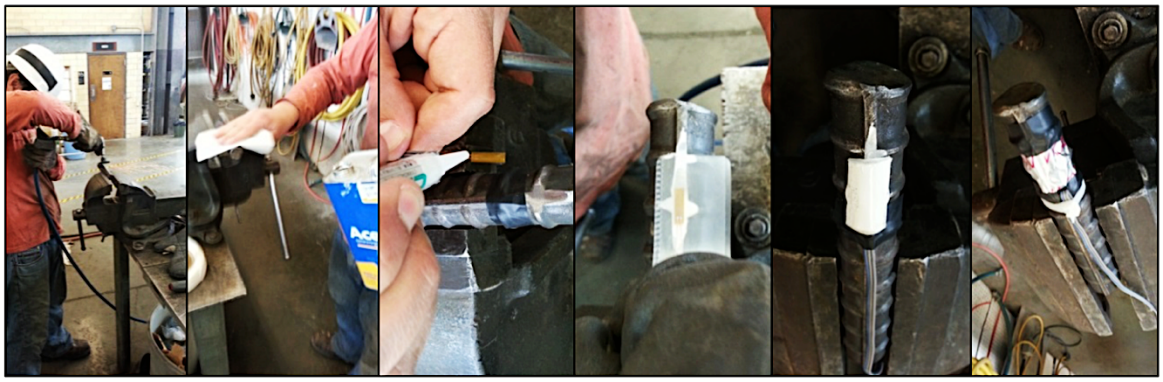

FIGURE 6-7: STRAIN GAUGE INSTALLATION PROCESS (SOKOLI, 2014)

7. APPENDIX B: ADDITIONAL EXPERIMENTAL RESULTS

This appendix presents an overview of the test results for each of the large-scale column tests. Post processing of the collected data is explained. The general behavior of each column is summarized and results regarding deformation components, strain demands, bar buckling history, energy dissipation and damage accumulation are presented. A comparative analysis between all specimens and a more detailed discussion of test results is provided in Chapter 2 of this dissertation.

7.1 DATA PROCESSING

Unless otherwise stated, the presented deformation data were measured using the Ghannoum Vision System (GVIS). The system used two cameras which recorded frames simultaneously at an average rate of 0.75 Hz. A script then ran through all the images extracting the image pixel coordinates of each target glued on the surface of the specimens. Targets were placed in a rectangular mesh spaced at 2.75 inches' center-to-center. Two-dimensional coordinates from each camera were then triangulated to produce the three-dimensional location of every target at each captured frame. Targets lost for short periods were linearly interpolated over the missing frames until the GVIS system recaptured the target. Targets permanently lost due to concrete spalling were ignored after being lost. The relatively low level of shear stress resulted in low damage in the column and at least 93% of targets remained on the column surface for the duration of all four experimental tests.

Frame data from the GVIS system were synchronized with the data gathered by the data acquisition system (DAQ) (i.e., strain gauge, load cell, and displacement transducer

data). For column CH100, 22,757 frames were recorded by the end of the test, for CL100 20,859 frames, for CM100 22,680 frames, and for CH60 24,726 frames. Due to the large number of data points gathered, the recordings from the GVIS and DAQ were smoothed by applying a 15-point moving average.

At the beginning of each test, the steel loading frame was leveled such that its weight was fully carried by the vertical actuators. Strain gauge readings and deformation quantities were zeroed at that stage. In all tests, positive drift values imply movement of the columns to the right (or the South direction) in images recorded by the optical measurement system.

7.1.1 Large Deformation Equilibrium

Applied base shear and axial load were computed by enforcing large-deformation equilibrium on the test frame using the recorded actuator loads and displacements. A free body diagram of the applied forces is shown in figure below. Column forces applied to the frame are assumed to be point loads applied from a single point on the actuator. The locations of the actuator's ends were measured prior to the test, in order for the initial angles to be tared accordingly. Potentiometers measured the movement of the frame needed to interpolate the angle differences and the resulting forces.

$$\theta_N = sin^{-1}\left(\frac{\Delta_H + \Delta_{H0N}}{\Delta_{VN} + \Delta_{V0N}}\right)$$

$$\theta_S = sin^{-1}\left(\frac{\Delta_H + \Delta_{H0S}}{\Delta_{VS} + \Delta_{V0S}}\right)$$

$$\theta_H = sin^{-1}\left(\frac{\Delta_{Vframe} + \Delta_{H0}}{\Delta_{Hact} + \Delta_{H0act}}\right)$$

$$V = H \cdot cos\theta_H + V_N \cdot sin\theta_N + V_S \cdot sin\theta_S$$

$$P = H \cdot sin\theta_H + V_N \cdot cos\theta_N + V_S \cdot cos\theta_S$$

Δ_H= $Horizontal\ displacement\ of\ the\ column$

Δ_{VN}= $Vertical\ movement\ of\ the\ north\ actuator$

Δ_{VS}= $Vertical\ movement\ of\ the\ south\ actuator$

ΔV_{frame} = $Vertical\ movement\ of\ the\ steel\ frame$

Δ_{Hact}= $Movement\ of\ horizontal\ actuator$

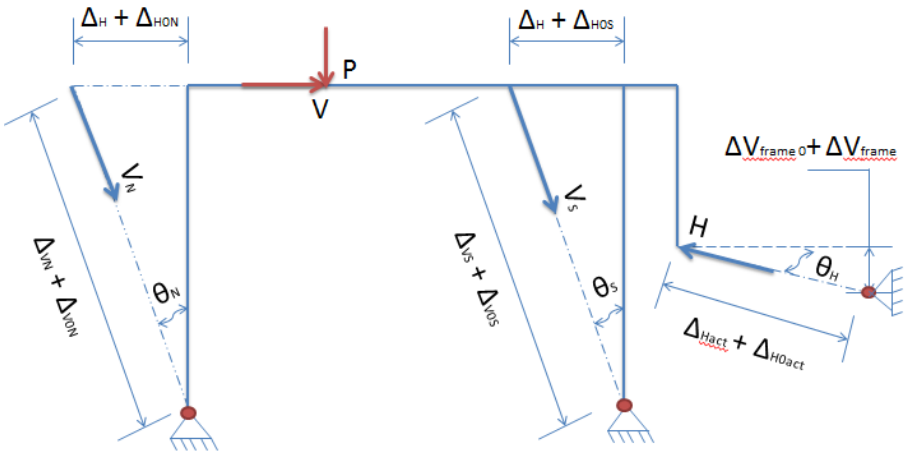

FIGURE 7-1: FREE-BODY DIAGRAM OF THE TEST SETUP

7.1.2 Deformation Measurements

The lateral drift (Δ_T - Figure 7-2) of each column was obtained by averaging the horizontal displacements of all available targets on the top footing and subtracting from them the average horizontal displacement of all available targets on the bottom footing. While the bottom footing did not slide during the test, this procedure removed any footing deformations from the column deformation data. In subsequent discussions, the term drift ratio refers to the lateral drift of a column divided by the clear span of the members (108 in.). Energy dissipated by columns in each cycle of every drift target were calculated from the area under the lateral drift versus average top and bottom column moment curves. The start of a cycle was taken as the point at which the column passed through the zero-lateral drift going from negative to positive drift (north-to-south).

The total lateral drift (Δ_T) of each column can be divided into three deformation components: flexural (Δ_{FL}), shear (Δ_{SH}), and bar-slip (Δ_{BS}) deformations (Figure 7-2).

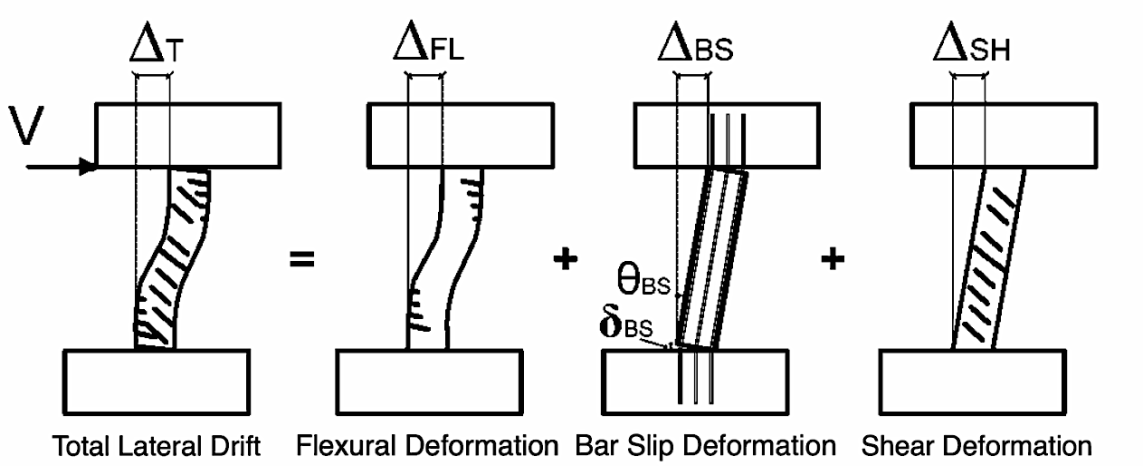

FIGURE 7-2: DEFORMATION COMPONENTS IN A CONCRETE MEMBER (SOKOLI ET AL. 2014)

Deformation components exhibit an essentially bilinear force-deformation relation at low demands, linear to first cracking and then linear to up to initiation of inelastic behavior at larger demands. Deformation components are sometimes coupled to the extent that one component entering the inelastic behavioral range may cause other components to exhibit an inelastic behavior. For example, as inelastic flexural deformations increase, so do shear deformations governed by expanding flexure-shear cracks.

Target displacement data from the GVIS were used to get rotations, curvatures, and deformation components over the height of the specimens, as described in Sokoli (2014) and Sokoli et al. (2014). A linear regression line was fit through each horizontal row of seven targets. Sectional rotations along column height were computed at each frame as the change in the slope of each target line with respect to the initial slope of the line prior to loading. Curvature profiles along column height were evaluated as the difference in angle of rotation between two target rows divided by the measured distance between the rows. Flexural deformations were evaluated from target displacement values by integrating those curvatures over the height of the column. The slip of column longitudinal bars from adjacent members causes rigid body rotations of the column about the interface between the column and the adjacent members. Lateral drifts generated by bar slip at the level of each target row were derived by multiplying the average rotation of the row of targets at column ends by the height of the target row considered. It is to be noted that at large deformations after concrete cover crushing, the measured bar slip becomes less reliable due to debonding between the longitudinal bar and the concrete cover. Shear deformations

along column height were extracted by subtracting the lateral drifts due to flexure and bar-slip from the total column lateral drift at each row of targets. The end result was the deconstruction of column drifts into three deformation components.

7.1.3 Strain Measurements

Given sufficiently high resolution, such as that achieved by the GVIS system, measurements of three-dimensional movements of known locations (i.e., targets) on a test specimen can be used to calculate surface material-strains. The GVIS can resolve surface strains to within 10^{-4} for a field of view of about 8ft (2.44m) and a gauge length of about 2.75 in.; a strain resolution that is on the order of the cracking strain of concrete. The surface targets arranged in a rectangular mesh were used as nodal points for bilinear-strain quadrilateral elements. Assuming that strains varied linearly between targets, the following element strain were calculated: the x-directional or horizontal strains (ε_x), the y-directional or vertical strain (ε_y), and the principal strains (ε_1 = largest principal strain and ε_2 = smallest principal strain), as well as the angle of inclination of the principal strains were determined. DIC measurements of surface strains were also used to estimate internal transverse reinforcement strains (Sokoli et al. 2014).

7.1.4 Damage Evaluation

Using GVIS surface-strain data, crack widths were estimated over the entire specimen surface, from which crack-width damage indices were evaluated. For a given frame, a crack was assumed to have formed within a quadrilateral surface-element when

the element's maximum principal tensile strain (ε_1) exceeded an assumed cracking strain, $\varepsilon_{cr}=f'_t/E_c=7.5/57000=1.3 \times 10^{-4}$ (with f'_t = concrete ultimate tensile strain, E_c = concrete modulus of elasticity, and their values based on provisions of ACI 318-14). After an initial crack formed in an element, the average elastic strain in adjacent uncracked concrete was assumed to be half the cracking strain. Thus, the crack width within surface elements can be calculated by subtracting half of the cracking strain from the maximum principal tensile strain and then multiplying the modified strain by the surface elements' length perpendicular to the crack. Since the surface elements are square, their lengths perpendicular to an inclined crack vary with crack inclination. An equivalent length ($L_{equiv.}$) was used for all crack inclinations to simplify the crack width evaluation procedure. The equivalent length was taken as the diameter of a circle of equivalent area to the square elements. The relation for crack width in each quadrilateral element is therefore given as:

EQUATION: CRACK-WIDTH CALCULATION USING DATA FROM GVIS

$$w_c=\left(\varepsilon_1-\varepsilon_{cr}/_2\right)*L_{equiv.}$$

7.1.5 Behavioral Milestones

The damage progression in the column specimens is presented in this report through the following major behavioral milestones: first flexural cracking (FFC), first inclined cracking (FIC), first longitudinal reinforcement yielding (FLRY), cover splitting crack (CSC), the peak shear force (PSF), longitudinal bar buckling (LBB), and longitudinal bar fracture (LBF) points. In plots of moment vs. lateral drift ratio, the peak applied moment (PAM) is given instead of peak shear force. Figure 7-3 shows the markers used in subsequent plots for each behavioral milestone.

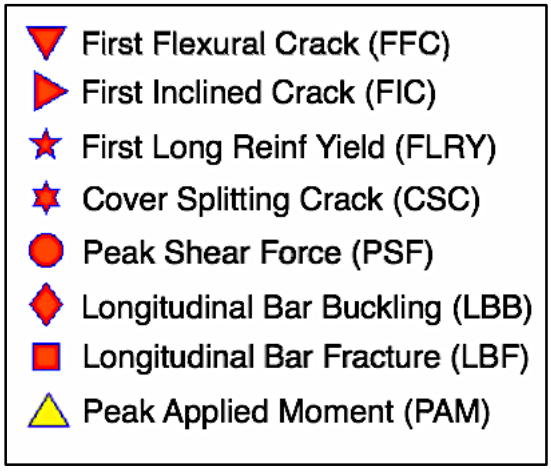

FIGURE 7-3: BEHAVIORAL MILESTONES NAMING AND CORRESPONDING MARKER

The yield strains of reinforcing bars were determined from material tests presented in Chapter 3. Yielding in longitudinal reinforcement was identified from strain gauges installed at the interfaces of the columns and footings where the demands were expected to be largest. First cracking was identified by monitoring the column surface for strain jumps above the concrete cracking strain, as described in Section 7.1.4. Flexural cracks were identified as having an angle of principal strain (ε_1) smaller than 25 degrees. Inclined

cracks were defined as cracks having an angle between 25°-65° based on the angle of principal strain (ε_1) from the horizontal line. The cover splitting crack was identified from surface x-direction (or horizontal) strains at column vertical edges in the plastic hinge regions. Bar buckling was identified from pictures taken at the end of each half-cycle. The exact point of initiation of bar buckling could therefore not be obtained while columns were being pushed laterally. Bar buckling markers are placed at the end of the half cycles during which buckling initiated. All the columns maintained the prescribed axial load throughout the test, so no milestone related to axial load was introduced.

7.2 TEST RESULTS FOR CH100

Results for column CH100 are reported in this section. Specimen CH100 was reinforced with grade 100 longitudinal and transverse bars. The longitudinal bars had a relatively high (H) *T/Y* ratio of 1.27. These bars were produced using the micro-alloying process. As for all specimens, CH100 was tested under displacement-controlled quasi-static cyclic lateral loading. The recorded lateral displacement history is shown in Figure 7-4. An axial load of 242 kips was applied by the vertical actuators which together with the 10-kips self–weight of the top footing and testing frame resulted in an effective axial load of 14.8% $A_g f_c'$ ($A_g f_c'$ = gross sectional capacity; where A_g= gross sectional area and f_c' = concrete compressive strength at the day of column testing) (Figure 7-5). The axial load was kept constant throughout the test as shown in Figure 7-5.

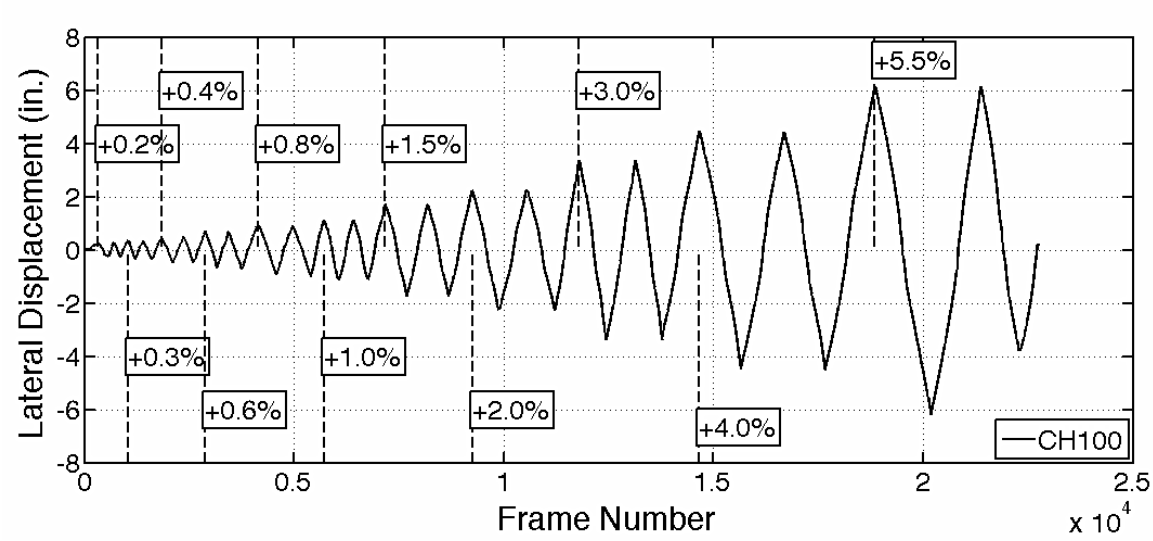

FIGURE 7-4: CH100 – MEASURED LATERAL DISPLACEMENT AT EVERY CAPTURED FRAME

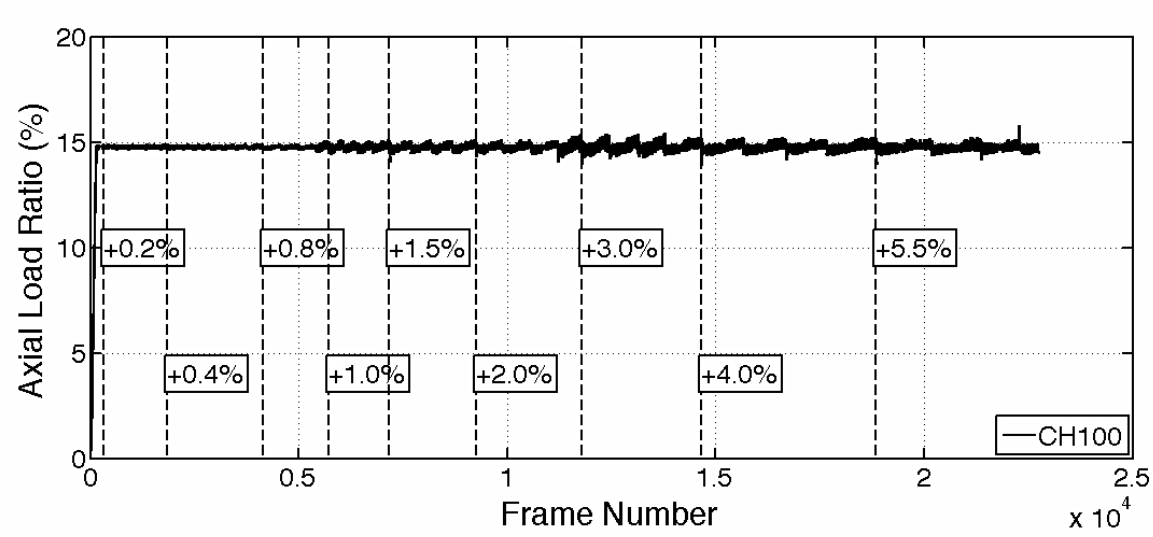

FIGURE 7-5: CH100 – APPLIED AXIAL LOAD RATIO AT EVERY CAPTURED FRAME

7.2.1 General Behavior

Prior to testing, no cracks were noticed on the specimen surface. The recorded lateral force versus drift ratio response of specimen CH100 is plotted in Figure 7-6. Table 7-1 summarizes the lateral force and drift values for all milestones for column CH100. The first flexural cracks formed at the end of the first cycle to +0.2% drift-ratio excursion (Figure 7-6, Figure 7-7). These cracks were noted through surface principal strains on the order of 0.002. The initial flexural cracks propagated closer to the centerline of the column leading to the formation of first inclined cracks at the end of the first half-cycle to a drift ratio of +0.6% (Figure 7-7).

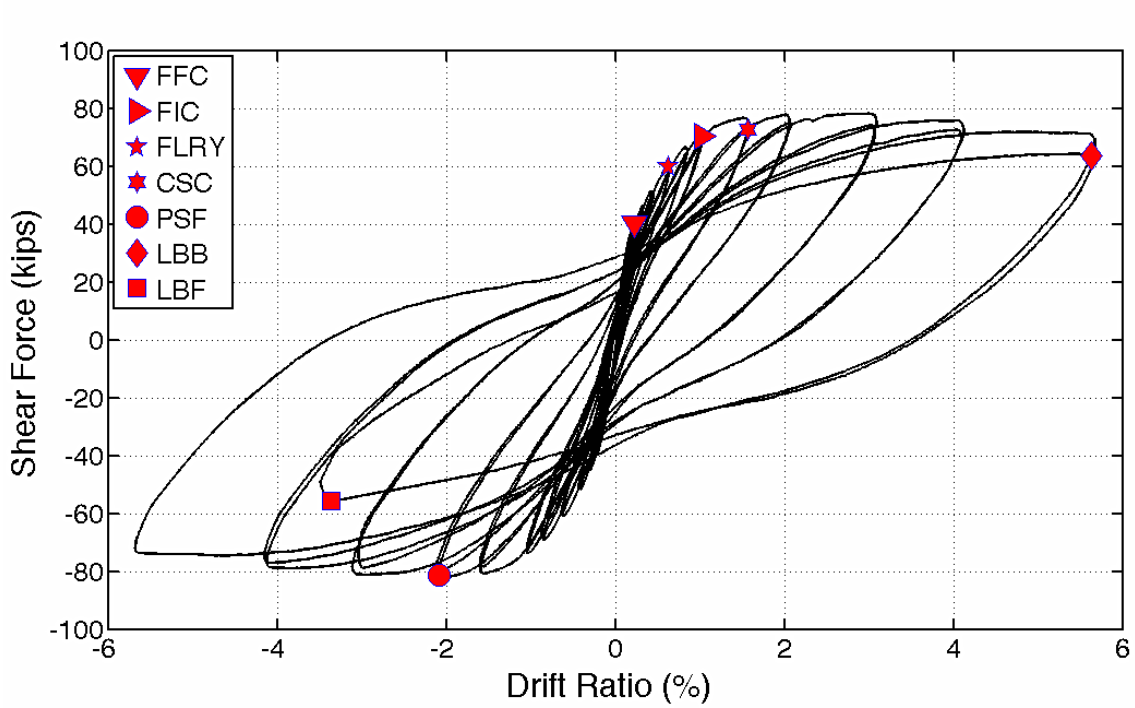

FIGURE 7-6: CH100 – LATERAL RESPONSE

TABLE 7-1: CH100 - BEHAVIORAL MILESTONES

Milestone	Drift Ratio (%)	Lateral Load (kips)
First Flexural Crack	+0.2	+40.2
First Inclined Crack	+0.6	+60.4
First Long. Reinf. Yield	-0.8	-69.5
Cover Splitting Crack	+1.5	+72.8
Peak Shear Force	-2.0	-81.9
Long. Bar Buckling	+5.5	+64.3
Long. Bar Fracture	-3.6	-55.6

First yield in the longitudinal reinforcement was identified from strain gauge readings at the end of the first cycle to a drift ratio of +1.0%. At this point during the loading protocol, the initial flexural cracks opened wider and additional cracks formed closer to the column mid-height (Figure 7-7). The maximum applied shear-force of 81.9 kips was recorded at the end of first cycle to a drift ratio of -2.0%. Beyond that drift cycle, the lateral load diminished slightly, driven by second order axial load effects and the accumulation of damage such as concrete spalling. Top and base moments versus lateral drift ratio are plotted in Figure 7-8. As can be seen in the figure, peak moment strength occurred at a drift ratio of 2.0%. Gradual degradation of moment strength occurred beyond that drift due to accumulation of damage in concrete. During the second cycle to a drift ratio of +5.5%, initiation of longitudinal bar buckling was observed and was associated with a gradual loss in the moment capacity during that half cycle (Figure 7-6).

As the column was pushed to drift ratios of 3.0%, 4.0%, and 5.5%, increasing crushing and spalling of the concrete cover was observed. Two main flexural cracks formed in each column-end plastic hinge region. These cracks were 9.5 inches from the ends of the specimen and reached 0.15 in. by the end of the first cycle to a drift ratio of 5.5%. At the same drift ratio, vertical cracks at the location of the longitudinal reinforcement propagated 14 in. from column ends, indicating some de-bonding between the longitudinal bars and the surrounding concrete. These cracks initiated a drift ratio of 1.5% drift ratio, which corresponded to a curbing of the rate of increase in longitudinal bars strains with increasing drift ratios. This behavior is discussed in more details in Section 4.2.3.

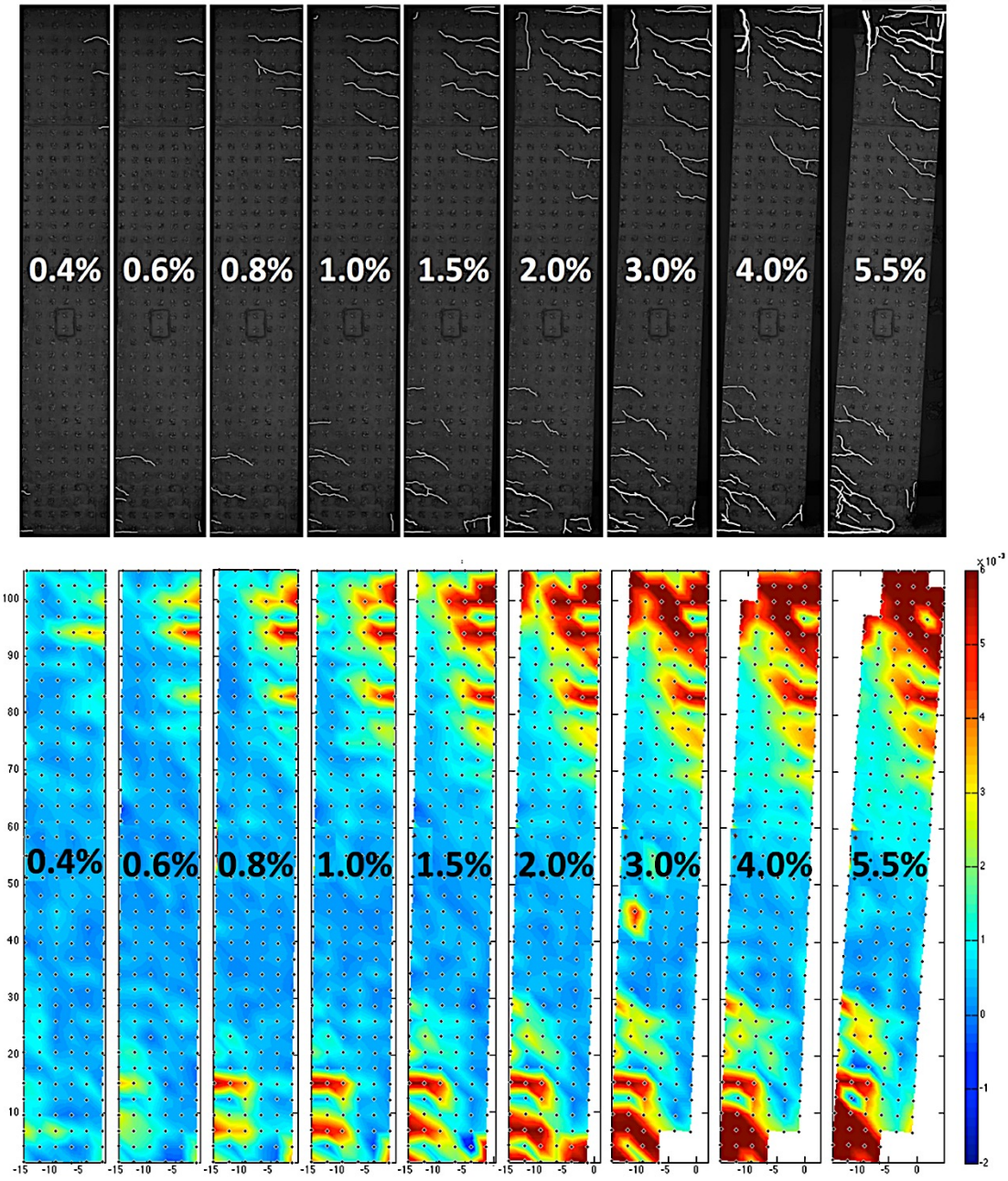

FIGURE 7-7: CH100 – CRACKING PATTERN (UP) AND MEASURED LARGEST PRINCIPAL STRAINS (DOWN) AT SEVERAL DRIFT RATIO TARGETS

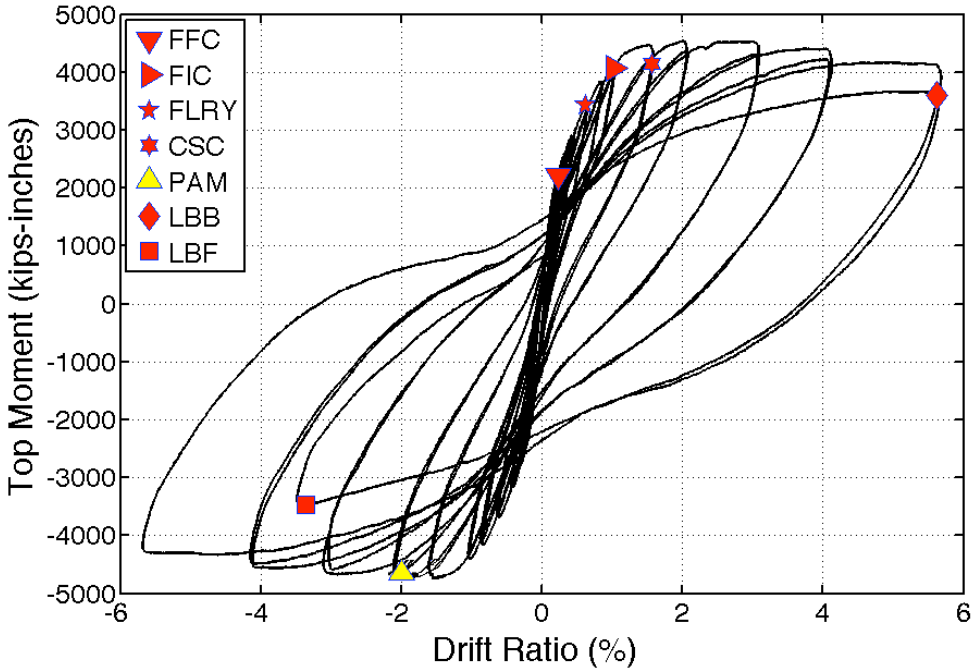

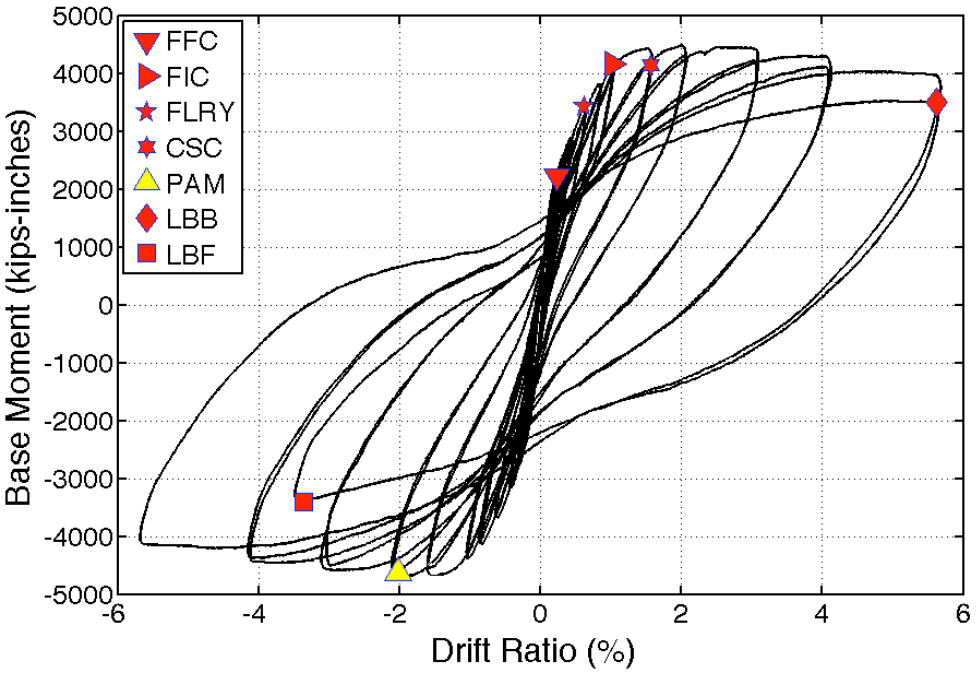

FIGURE 7-8: CH100 – BASE AND TOP MOMENT VS. DRIFT RATIO

The lateral load resistance of the column remained relatively stable and the column maintained axial load capacity past the first cycle to a drift ratio of +5.5% (Figure 7-9). During the second cycle to a drift ratio of +5.5%, the column experienced a 12% loss in moment resistance as compared to the previous half-cycle to the same drift target, and a 24% loss in moment resistance as compared to the peak lateral moment resistance. The significant loss in moment resistance was attributed to significant buckling of the longitudinal bars. By then, the cover concrete in the top and bottom plastic hinge regions had spalled to a distance of about 11.5 in. from column ends. As a result, on its way to completing two 5.5% drift cycles, one of the longitudinal bars fractured at the base of the column at a drift ratio of 3.6% (Figure 7-9; Figure 7-10). Just prior to first bar fracture, the column had lost 28% of its measured peak lateral moment resistance. The first bar fracture contributed to additional loss in lateral strength. Considering the considerable loss in lateral strength the test was stopped at this point. The column was able to carry the prescribed axial load throughout the test without showing signs of significant axial deformation even after longitudinal reinforcement fracture. It is noteworthy that the fractured bar was a middle bar. The 90-degree bend of the cross-tie restraining this bar had opened up significantly, during the previous half-cycle to a drift ratio of +5.5%, allowing the bar to buckle.

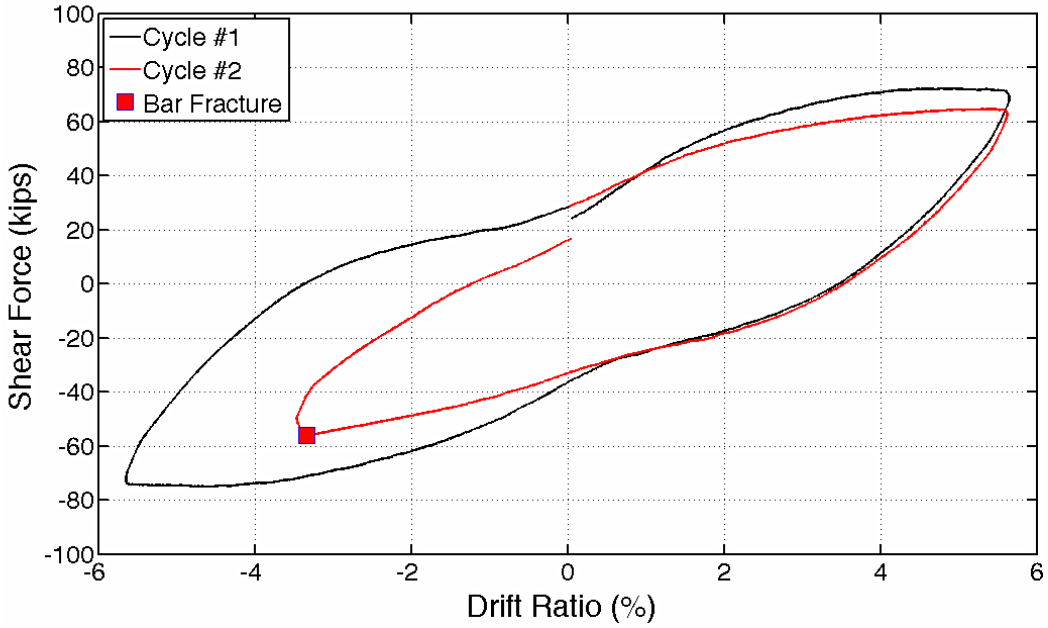

FIGURE 7-9: CH100 – LAST CYCLES RESPONSE

FIGURE 7-10: CH100 – PICTURES OF FRACTURED AND BUCKLED BARS

7.2.2 Deformation Components

Flexural deformations contributed most to the column lateral drift throughout the test (Table 7-2; Figure 7-11). At higher drifts, the relative weight of flexural deformations lowered as the bar-slip component increased from about 30% of the total drift at low drift levels, to about 40% in the post-yield cycles. Possibly, the observed increase in recorded bar-slip contribution was due to debonding of the longitudinal reinforcement from the surrounding concrete at larger levels of concrete damage. This debonding of longitudinal bars due to concrete damage could have decoupled the bar deformations from measured concrete surface movements. Shear deformations increased in absolute value, but remained relatively low at around 5% of total drift throughout the test. The low amount of shear deformations was due to the applied shear stresses being relatively low. Results for deformation components were not reliable after cycles to a drift ratio of 4.0%.

TABLE 7-2: CH100 – DEFORMATION COMPONENTS AS PERCENTAGE OF TOTAL

Total	Flexure	Bar-slip	Shear
0.2%	72.8%	24.1%	3.1%
0.3%	72.2%	23.9%	3.8%
0.4%	71.4%	24.9%	3.7%
0.6%	65.2%	30.4%	4.4%
0.8%	60.4%	35.1%	4.5%
1.0%	59.7%	35.9%	4.4%
1.5%	60.7%	34.8%	4.5%
2.0%	62.1%	33.4%	4.5%
3.0%	63.2%	32.1%	4.6%
4.0%	63.2%	33.4%	4.3%

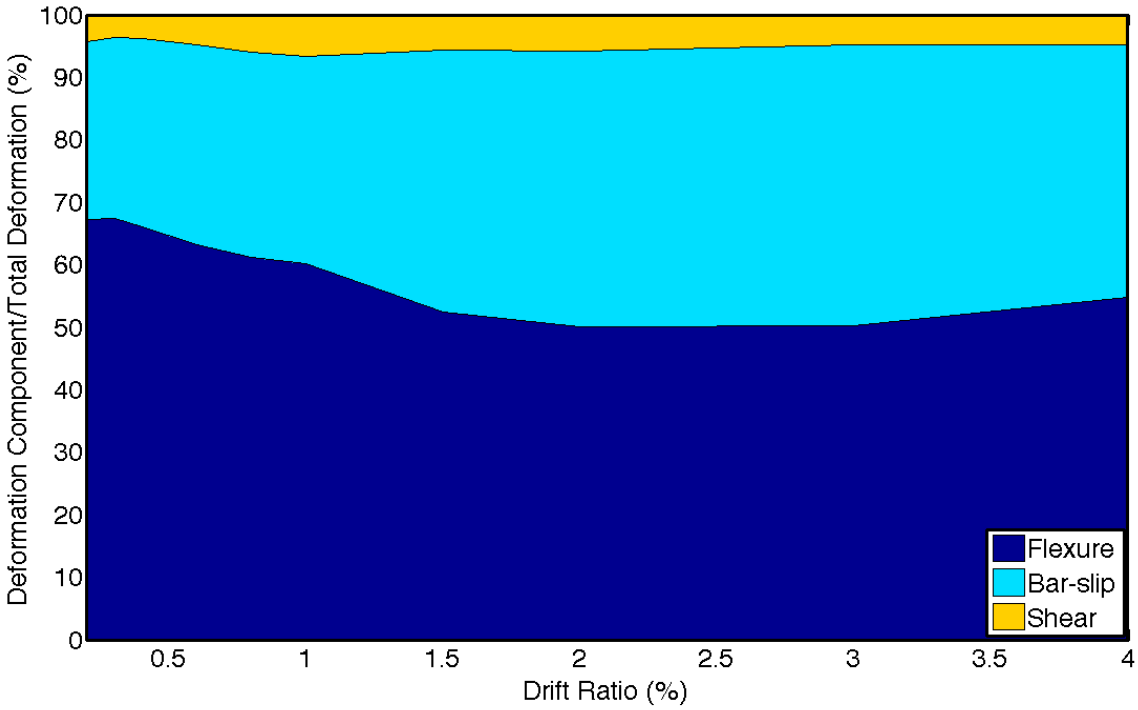

FIGURE 7-11: CH100 – DEFORMATION COMPONENTS

7.2.3 Strain History

Maximum strain demands were recorded at the interfaces between the column and footings. Figure 7-12 shows a typical strain versus lateral load response recorded on longitudinal bars at column ends. Figure 7-13 plots longitudinal bar tension strains at the end of each positive drift cycle target, measured at the top and bottom column interfaces with footings. The #6 bars used as longitudinal reinforcement in CH100 had a yield strain of 0.0032, as obtained from material testing. This strain was first reached at a drift ratio of +1.0% (Figure 7-13). After yield, the strain demands increased without significant increase in the lateral load. In general, strain demands of longitudinal bars were higher in the second

cycle to the same drift target, with the difference increasing at higher drifts. This difference was however relatively small, and on the order of 5% of the strain value.

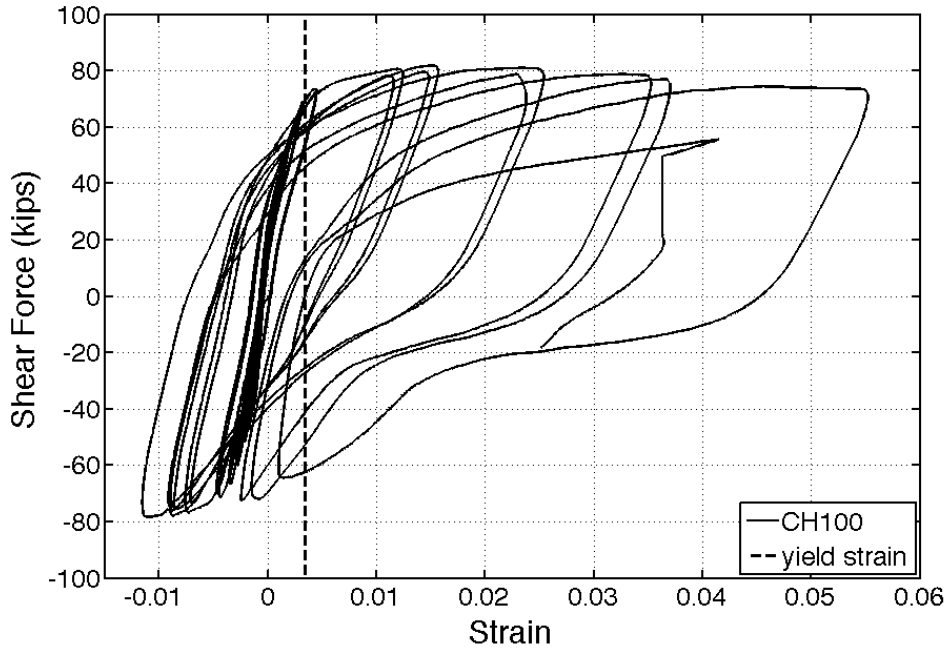

FIGURE 7-12: CH100 – STRAIN GAUGE L17NW (TOP NORTH-WESTERN CORNER) RECORDING AT THE INTERFACE BETWEEN THE COLUMN AND TOP FOOTING

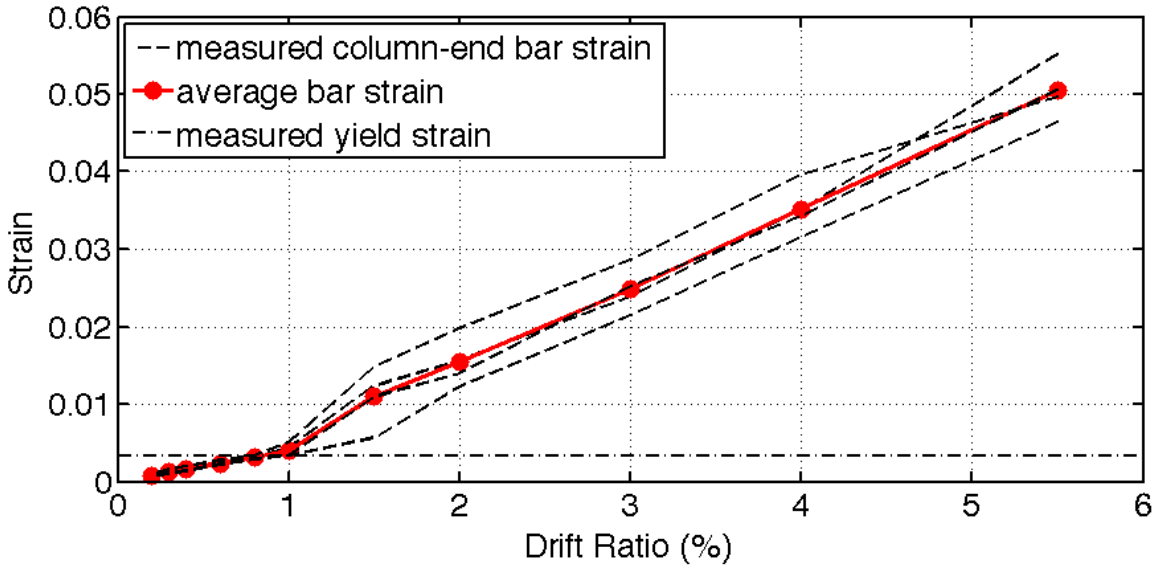

FIGURE 7-13: CH100 – COLUMN-END BAR STRAIN GAUGE RECORDINGS AT EACH DRIFT TARGET AND CALCULATED AVERAGE

Strain readings over the height of the top part of the north-western longitudinal bar are given in Figure 7-14. As can be seen in Figure 7-14, once flexural yielding occurs, strains tended to concentrate at column ends. However, as the column was pushed past first yield to higher drift targets, inelastic strains were able to spread to 23 inches from the end of the column.

.

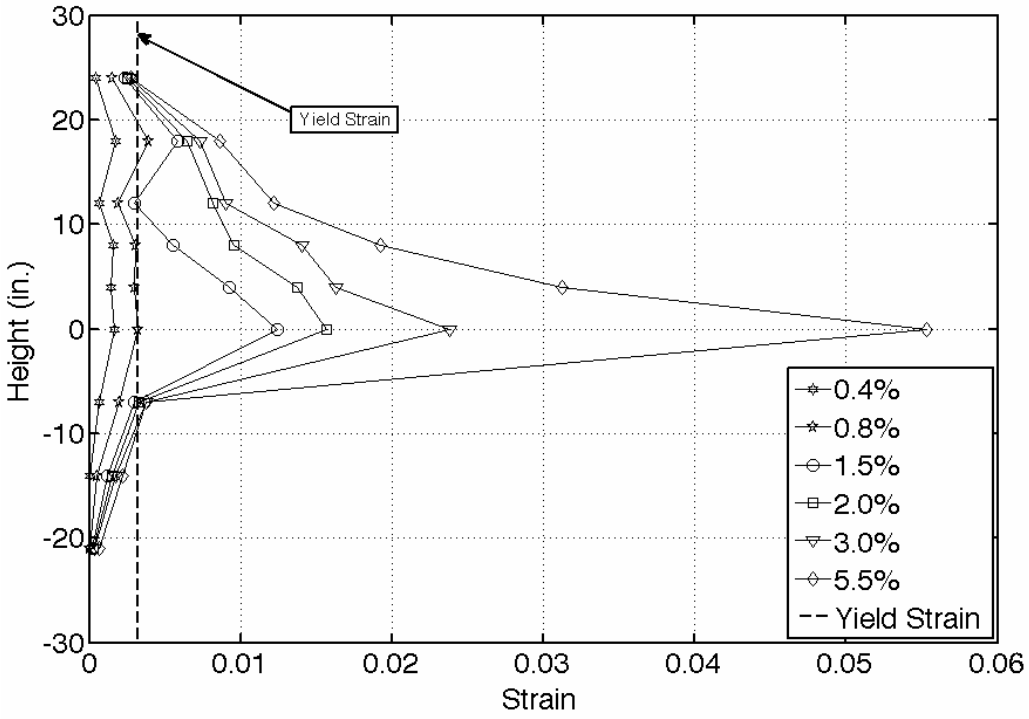

FIGURE 7-14: CH100 – LONGITUDINAL REINFORCEMENT STRAIN DEMANDS OVER HEIGHT AT DRIFT TARGETS

7.2.4 Crack Widths

Data from the GVIS was used to monitor the widths of the major flexural cracks at first yield were monitored. These cracks were identified as having a width of 0.008 inches or larger at first yield. Considering that ACI 318-14 intends to limit crack widths to 0.016 inches during service loading, half of this value was used conservatively as a threshold at first yield for cracks of concern. Cracks within seven quadrilateral target elements were identified as satisfying the above-mentioned criteria for each drift direction; three at the bottom half of the member, and four in the upper part (Figure 7-7). The number of cracks was the same between the north and south faces of the member as the column was cycled. During the first half cycle to a positive drift (column being pushed south, i.e. right on the pictures), flexural crack widths were measured in the bottom-south and top-north sides of the member. Strain readings of the second elements in from the column vertical surfaces were used to calculate the reported cracks width values. This was done as the outermost targets in the plastic-hinge region were lost at high demands due to cover crushing. The average of these cracks is plotted in Figure 7-15 and identified as cracks occurring during "Half Cycle 1". The same procedure was followed for other positive and negative drift half cycles for each drift target. At first yield, the average of all cracks was 0.012 inches. These cracks opened wider as the member was pushed passed yield. No significant difference in crack width was noticed between the successive half cycles in which the column was being pushed in the same direction. These critical cracks were all located within 16 inches from the ends of the member. As the column was pushed to higher drifts (past 2.0% drift ratio)

two large flexural cracks formed at each end of the member, 9.5 inches from its ends. Figure 7-16 plots the width of one of these cracks as measured throughout the test.

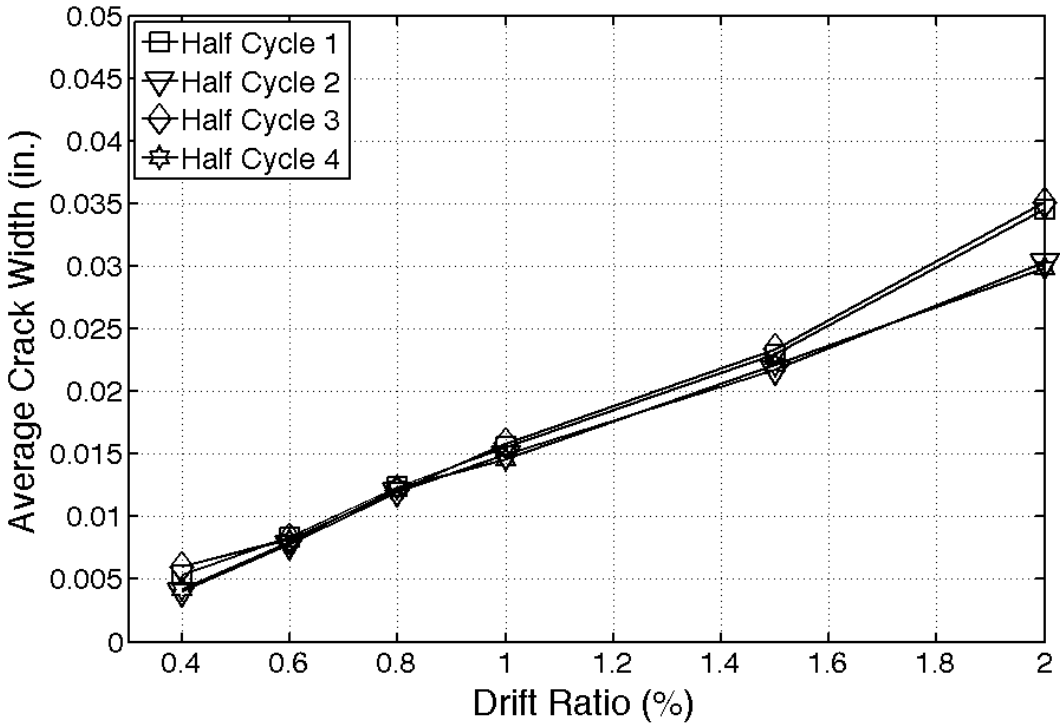

FIGURE 7-15: CH100 – AVERAGE VALUES OF LARGEST FLEXURAL CRACK WIDTHS AT DRIFT TARGETS

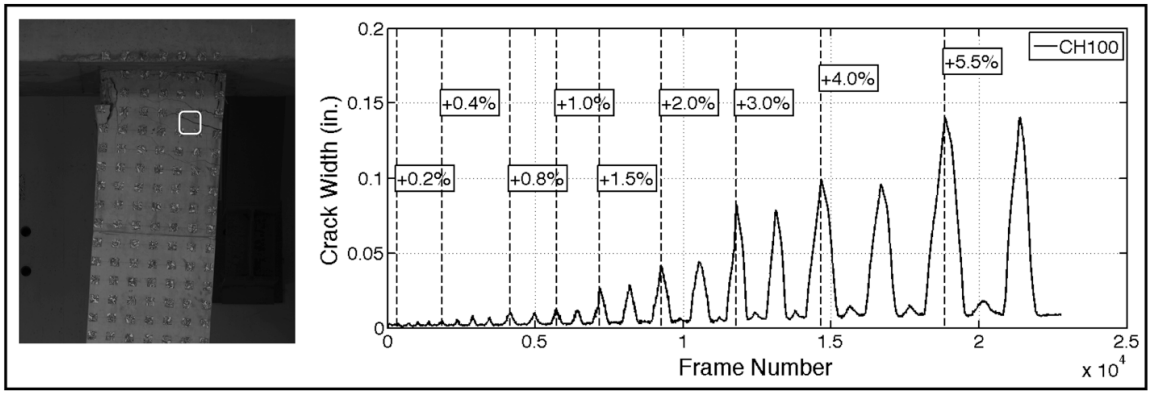

FIGURE 7-16: CH100 – WIDTH OF ONE OF THE TWO LARGEST FLEXURAL CRACKS

7.2.5 Buckling History

Buckling of the longitudinal reinforcement in CH100 was identified through the images taken at the end of each loading half-cycle. Buckling of the first longitudinal bars was observed at the second cycle to a drift ratio of +5.5% (Figure 7-17-left). The first bars to buckle were the middle bars that were restrained by the 90-degree hook of cross-ties, which opened up allowing the bar to buckling. At this point, the moment strength of the member had dropped by 28% as compared to the peak applied moment at the base. As the column was pushed back to a drift ratio of -5.5%, significant buckling took place, which lead to the lateral strength of the member having decreased from peak by 32% at the onset of the first bar fracture. The rotation of the row of targets located 9 inches over the base, or the 4th target row from the end) of the column is plotted in Figure 7-18. The location of this row of targets corresponds to the to the first row of targets above the observed buckling location. The rotation at this location seems to not have captured the progression of buckling.

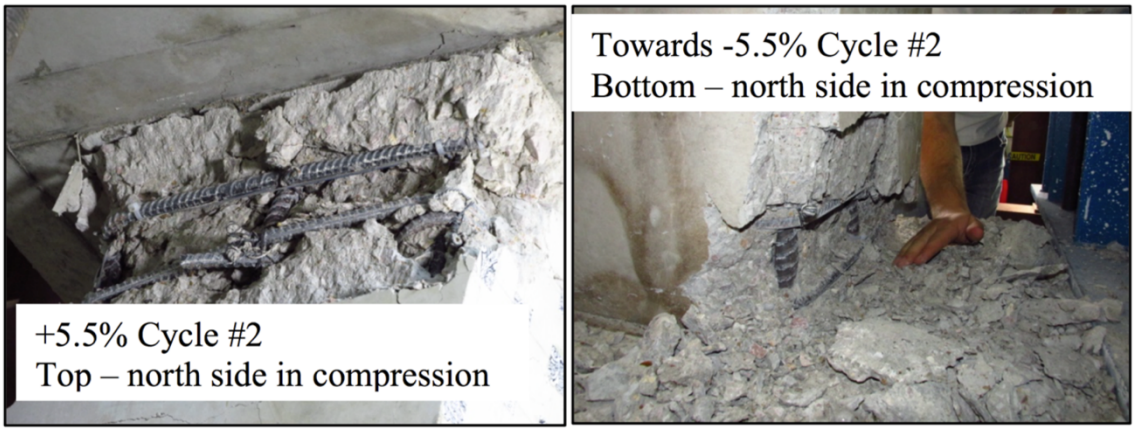

FIGURE 7-17: CH100 – LONGITUDINAL BAR BUCKLING

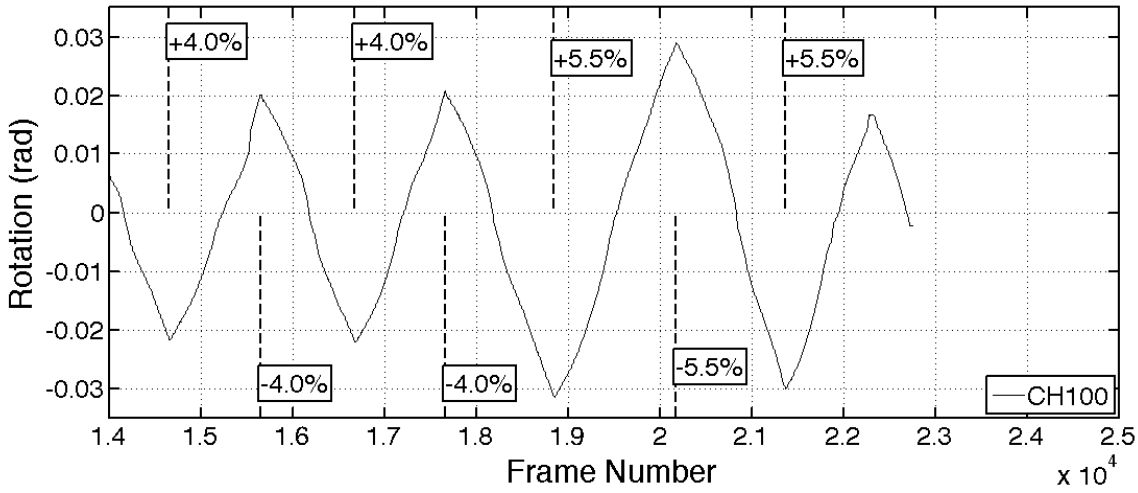

FIGURE 7-18: CH100 – ROTATION AT A DISTANCE 9 INCHES FROM THE BASE

7.2.6 Energy Dissipation

The dissipated energy, defined as the area under the average top and bottom moment versus lateral drift relation, is plotted in Figure 7-19 for each cycle. The average top and bottom moment was used to compute the dissipated energy as moment strength is more representative of column sectional strength, as opposed to lateral-load strength that is influenced by second order deformation effects. Prior to first yielding (drift ratio targets up to 0.8%) the amount of dissipated energy was similar between the two cycles at each target drift. As the column was pushed to higher drifts and damage accumulated, the difference in energy dissipation between the cycles increased. The difference between two consecutive post-yield cycles to the same drift ratio was in the range of 5 to 15%. The difference in cumulative dissipated energy between cycles at the end of the 4% drift ratio cycles was 10.7%.

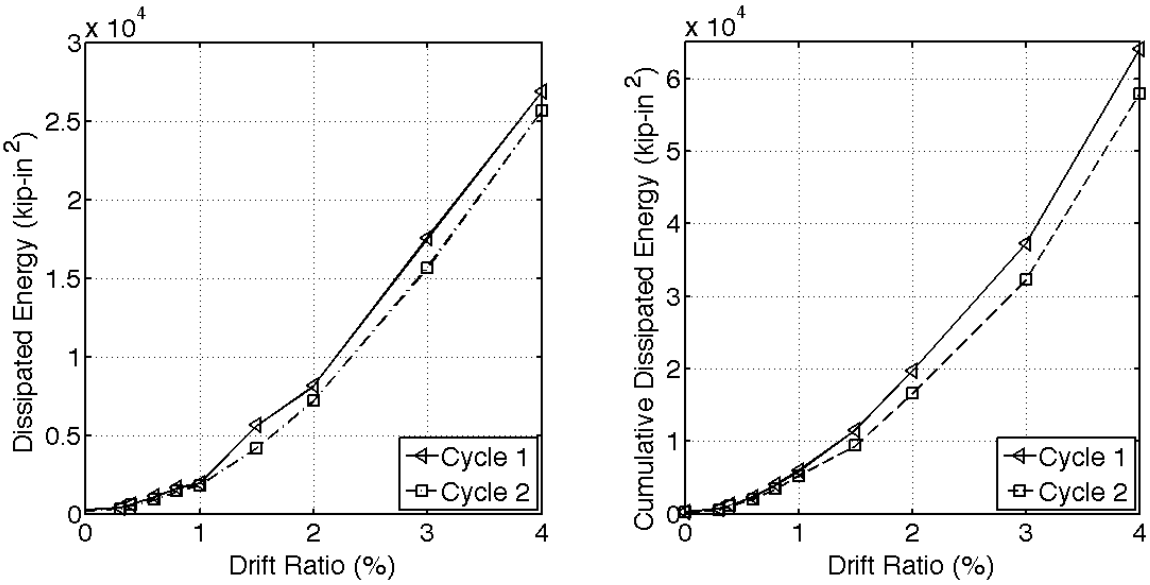

FIGURE 7-19: CH100 – DISSIPATED ENERGY AT DRIFT TARGETS FOR EACH CYCLE

7.3 TEST RESULTS FOR CL100

Results from testing of column CL100 are reported in this section. Specimen CL100 was reinforced with grade 100 longitudinal and transverse bars with a relatively low (L) *T/Y* ratio of 1.16. These bars were produced primarily using the quenching and tempering process. Specimen CL100 was tested under displacement-controlled quasi-static cyclic lateral loading. The recorded lateral displacement history of specimen CL100 is illustrated in Figure 7-20. An axial load of 242 kips was applied by the vertical actuators to this specimen which together with the 10-kip self–weight of the top footing and testing frame resulted in an effective axial load of $\sim 14.9\%\, A_g f_c'$ after performing large-deformation equilibrium. The load was kept constant throughout the test as shown in Figure 7-21.

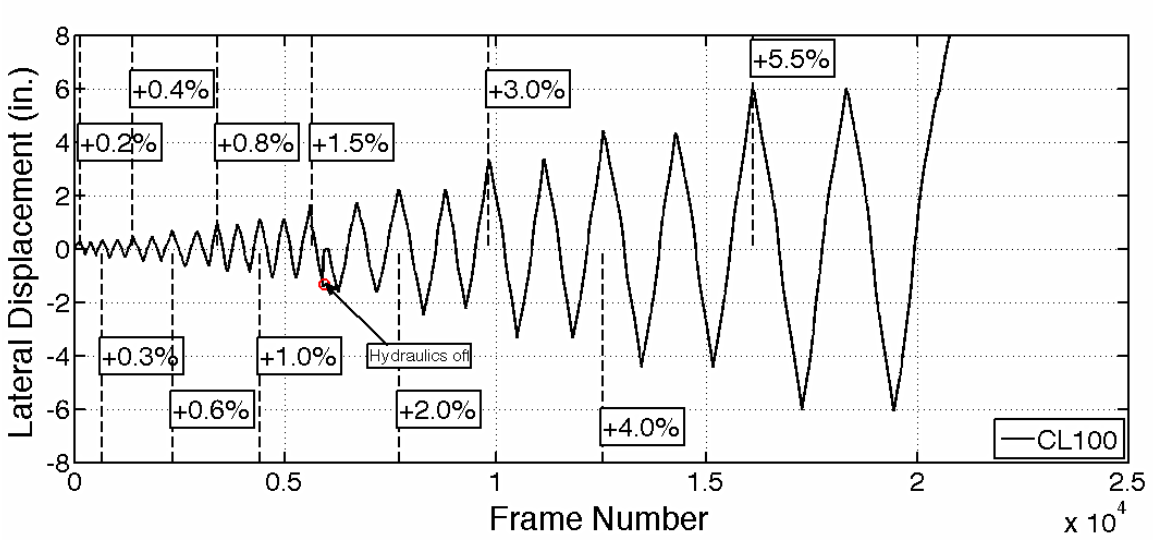

FIGURE 7-20: L100 – MEASURED LATERAL DISPLACEMENT AT EVERY CAPTURED FRAME

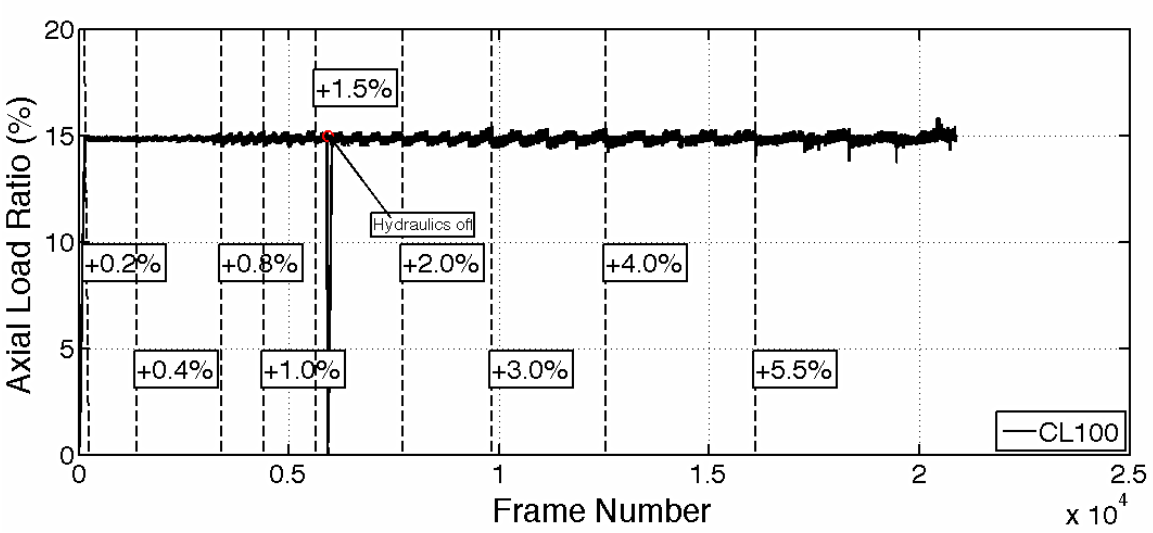

FIGURE 7-21: CL100 – APPLIED AXIAL LOAD RATIO AT EVERY CAPTURED FRAME

The loading protocol was disrupted during the test, as the specimen was being pushed towards the first half-cycle to a drift ratio of +1.5%. This took place at frame 5934 (Figure 7-20 & Figure 7-21), when the hydraulic system lost power. The column was reloaded axially and pushed to a drift ratio of +1.5% after being leveled. At the first cycle to a drift ratio of -2.0% the specimen was pushed 0.25 inches further than the target displacement. It is believed that these events did not affect the overall performance of the member.

7.3.1 General Behavior

Prior to testing, no cracks were noticed on the specimen surface. The recorded lateral force versus drift ratio response of specimen CL100 is plotted in Figure 7-22. Table 7-3 summarizes the lateral force and drift values for all milestones for column CL100. The first flexural cracks in column CL100 were visible at the end of the first cycle to +0.2%

drift-ratio excursion (Figure 7-22; Figure 7-23). These cracks were noted through surface principal strain on the order of 0.002 (Figure 7-23). The initial flexural cracks propagated closer to the centerline of the column leading to the formation of first inclined cracks at the end of the first half-cycle to a drift ratio of +0.6% drift ratio (Figure 7-23).

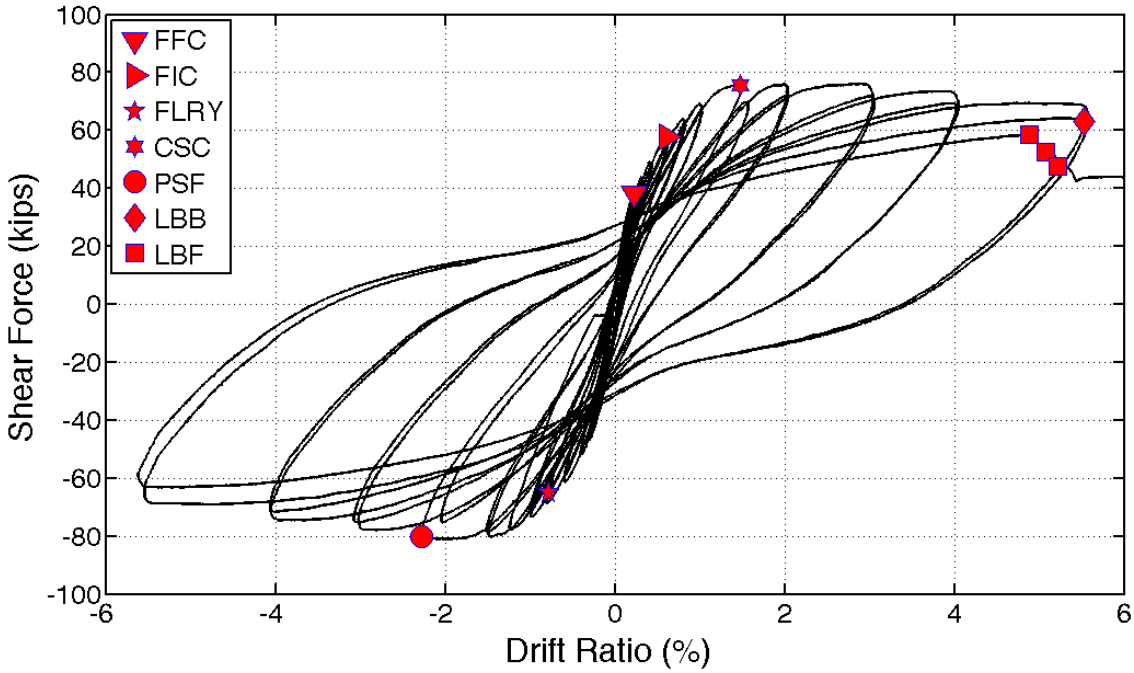

FIGURE 7-22: CL100 – LATERAL RESPONSE

TABLE 7-3: CL100 - BEHAVIORAL MILESTONES

Milestone	Drift Ratio (%)	Lateral Load (kips)
First Flexural Crack	+0.2	+38.2
First Inclined Crack	+0.6	+57.8
First Long. Reinf. Yield	+1.0	+78.4
Cover Splitting Crack	+1.5	+79.4
Peak Shear Force	-2.0	-80.8
Long. Bar Buckling	+5.5	64.0
Long. Bar Fracture	+4.8	+58.6

First yield in the longitudinal reinforcement was identified from strain gauge readings at the end of the first cycle to a drift ratio of +1.0%. As the column was pushed to the first cycle towards +1.0% drift the initial flexural cracks opened wider and additional cracks formed closer to the column mid-height (Figure 7-23). The maximum applied shear force of 80.8 kips was recorded at the end of first cycle to a drift ratio of -2.0%. Beyond that drift cycle, the lateral load diminished slightly, driven by second order axial load effects and the accumulation of damage such as concrete spalling. Top and bottom moments versus lateral drift ratio are plotted in Figure 7-24. As can be seen in the figure, peak moment strength occurred at a drift ratio of -1.5%. Gradual degradation of moment strength occurred beyond that drift due to accumulation of damage in concrete. At the second cycle to a drift ratio of +5.5%, initiation of longitudinal bar buckling was observed and was associated with a steeper degrading slope in the moment versus drift plots

As the column was pushed to drift ratios of 3.0%, 4.0% and 5.5%, increasing crushing and spalling of the concrete cover was observed. CL100 showed similar cracking pattern to CH100, with two main flexural cracks in the order of 0.15 inches at each plastic hinge region. These cracks were 10 inches from the end of the specimen and reached a width of 0.15 in. by the end of the first cycle to a drift ratio of 5.5%. At the same drift ratio, vertical cracks at the location of longitudinal reinforcement propagated 14 in. from column ends, indicating some de-bonding between the longitudinal bars and the surrounding concrete. These cracks initiated at a drift ratio of 1.5%, which corresponded to a curbing

of the rate of increase in longitudinal bars strains with increasing drift ratios. The behavior is discussed in more details in Section 4.3.3.

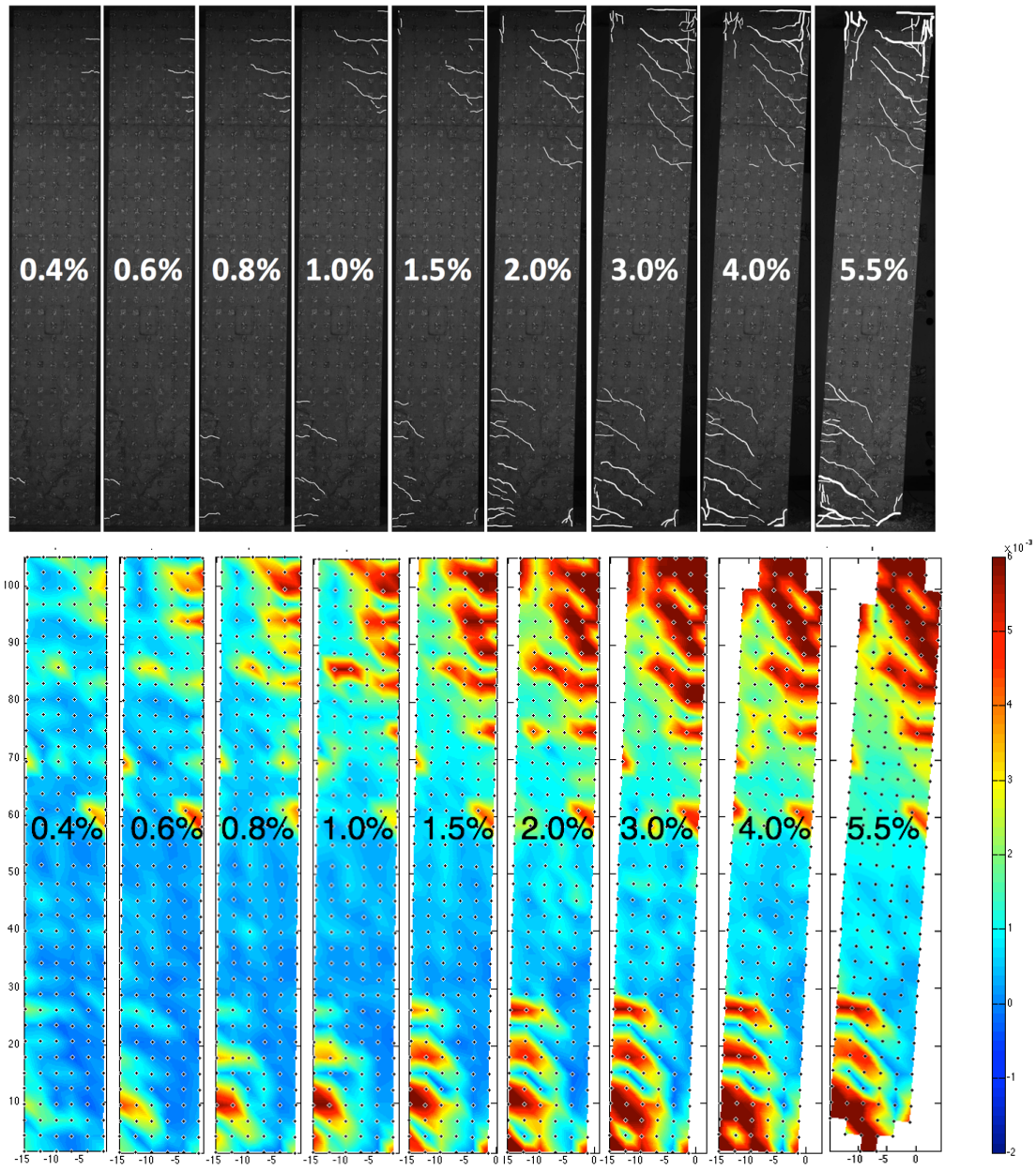

FIGURE 7-23: CL100 - CRACKING PATTERN (UP) AND MEASURED LARGEST PRINCIPAL STRAINS (DOWN) AT SEVERAL DRIFT RATIO TARGETS

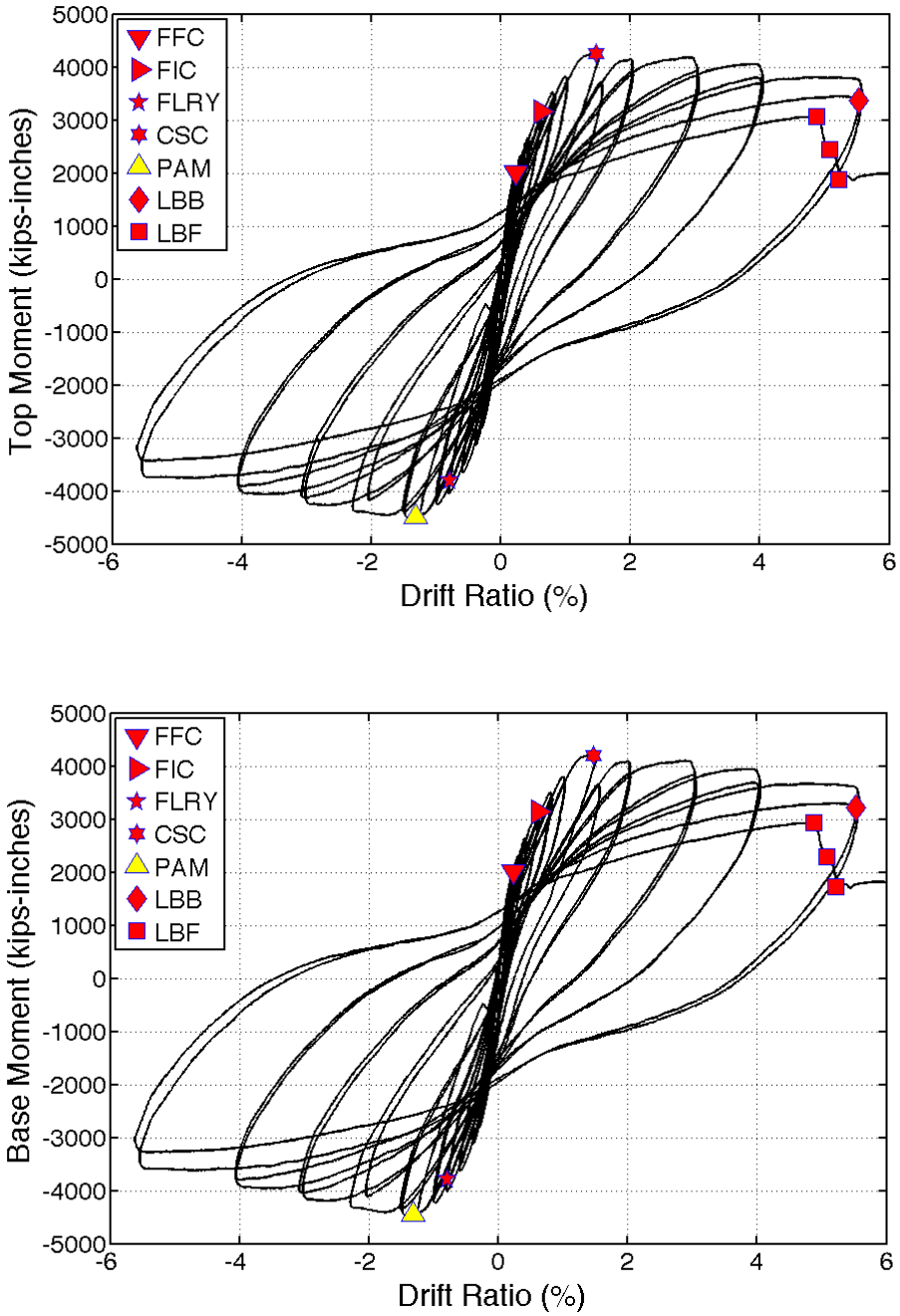

FIGURE 7-24: CL100 - BASE AND TOP MOMENT VS. DRIFT RATIO

The lateral load resistance of the column remained relatively stable and the column maintained axial load capacity past the first cycle to a drift ratio of 5.5% (Figure 7-25). During the second cycle to a drift ratio of +5.5%, the column experienced a 11% loss in moment resistance as compared to the previous half-cycle to the same drift target, or 29% loss as compared to the maximum peak moment resistance. This was due to significant buckling of longitudinal bars. By then, the cover concrete in the top and bottom plastic hinge regions had spalled to a distance of about 13 in. from column ends. The first 90-degree cross tie at the north-bottom face of the column had already opened up, contributing to the observed buckling. As a result, on its way to the first half-cycle to a drift ratio target of +7.0%, the first bar fractured at a drift ratio of 4.8% (Figure 7-25; Figure 7-26). Right before the first bar fractured, the lateral strength of the column was 34% lower as compared to the peak moment resistance (Figure 7-25; Figure 7-26). In an attempt to push the column towards a drift ratio of +7.0%, two more consecutive bar fractures occurred. The moment resistance at this point dropped below 50% of the peak moment resistance. The test was stopped after a fourth bar fractured at a drift ratio of +8.0%. The column was able to carry the prescribed axial load throughout the test without showing signs of significant axial deformation even after four-longitudinal reinforcement bars fractured.

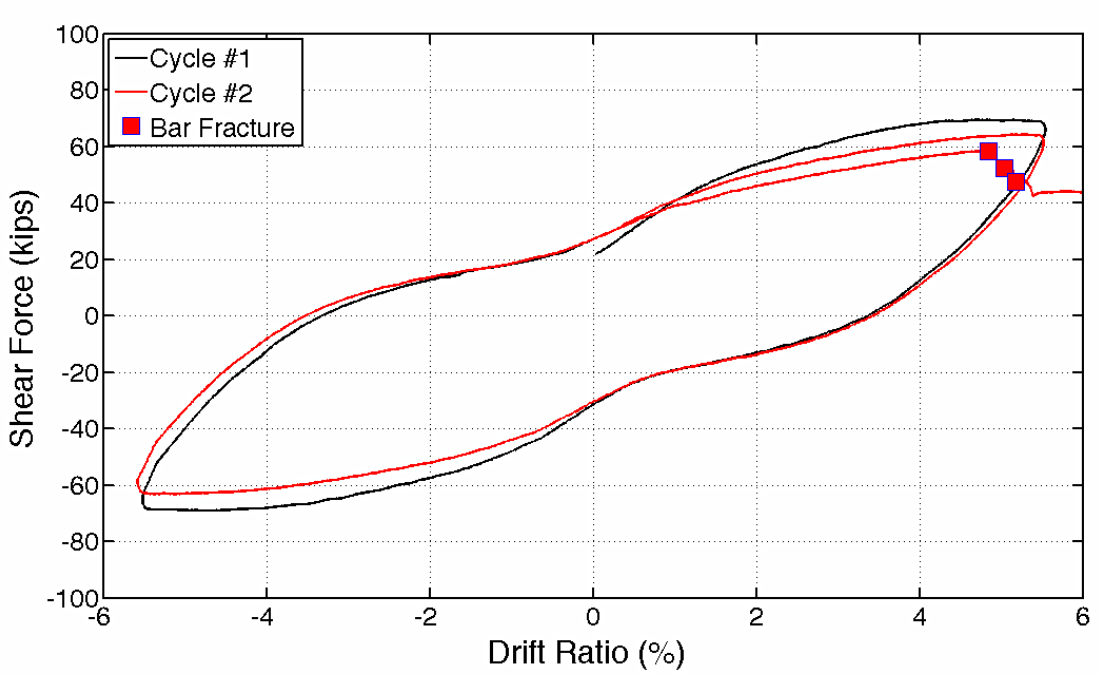

FIGURE 7-25: CL100 – LAST CYCLES RESPONSE

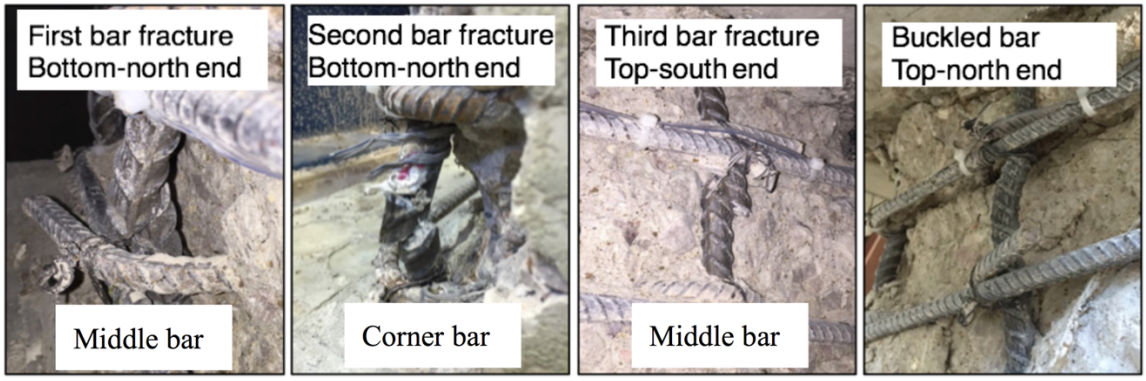

FIGURE 7-26: CL100 – PICTURES OF FRACTURED AND BUCKLED BARS AT THE END OF THE TEST

7.3.2 Deformation Components

Flexural deformations contributed most to the column lateral drift throughout the test (Table 7-4; Figure 7-27). At higher drifts, the relative weight of flexural deformations lowered as the bar-slip component increased from about 20% of the total drift at low drift levels, to about 40% in the post-yield cycles. Possibly, the observed increase in recorded bar-slip contribution was due to debonding of the longitudinal reinforcement from the surrounding concrete at larger levels of concrete damage. This debonding of longitudinal bars due to concrete damage could have decoupled the bar deformations from measured concrete surface movements, from which bar-slip deformations were extracted. Shear deformations increased in absolute value, but remained relatively low at around 5% of total drift throughout the test. The low amount of shear deformations was due to the applied shear stresses being relatively low. Results for deformation components were not reliable after cycle to a drift ratio of 4.0%.

TABLE 7-4: CL100 - DEFORMATION COMPONENTS AS PERCENTAGE OF TOTAL

Total	Flexure	Bar-slip	Shear
0.2%	74.0%	22.0%	4.0%
0.3%	68.7%	28.0%	3.3%
0.4%	67.9%	27.8%	4.2%
0.6%	64.7%	30.7%	4.6%
0.8%	63.9%	30.6%	5.5%
1.0%	62.7%	31.3%	6.0%
1.5%	52.0%	42.2%	5.8%
2.0%	53.9%	41.0%	5.0%
3.0%	54.6%	41.2%	4.3%
4.0%	55.8%	40.3%	3.9%

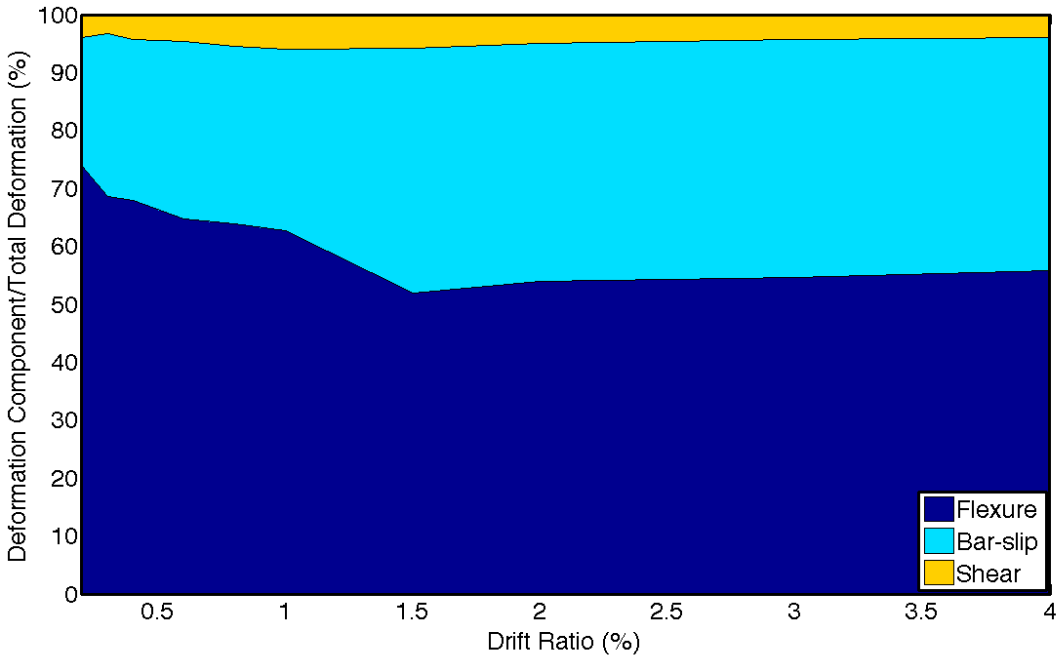

FIGURE 7-27: CL100 – DEFORMATION COMPONENTS

7.3.3 Strain History

Maximum strain demands were recorded at the interfaces between the column and footings. Figure 7-28 shows a typical strain versus lateral load response recorded on longitudinal bars at column ends. Figure 7-29 plots longitudinal bar tension strains at the end of each positive drift cycle target, measured at the top and bottom column interface with footings. The #6 bars used as longitudinal reinforcement in CL100 had a yield strain of 0.0032 as obtained from material testing. This strain was first reached at a drift ratio of -0.8%. However, the drift ratio of +1.0% was reported as the first yield, as an average between the available strain gauge recordings. After yield, the strain demands increased without significant increase in the lateral load. In general, strain demands on longitudinal bars were higher in the second cycle to the same drift target, with the difference increasing at higher drifts. This difference was however relatively small, and on the order of 5% of the strain value.

Strain gauge L4NE stopped recording right before the column was pushed to the first cycle to a drift ratio of 5.5%. The strain value at 5.5% drift ratio presented below was linearly interpolated. A linear behavior at these range of deformation demands was observed at all other measured strain data from other tests.

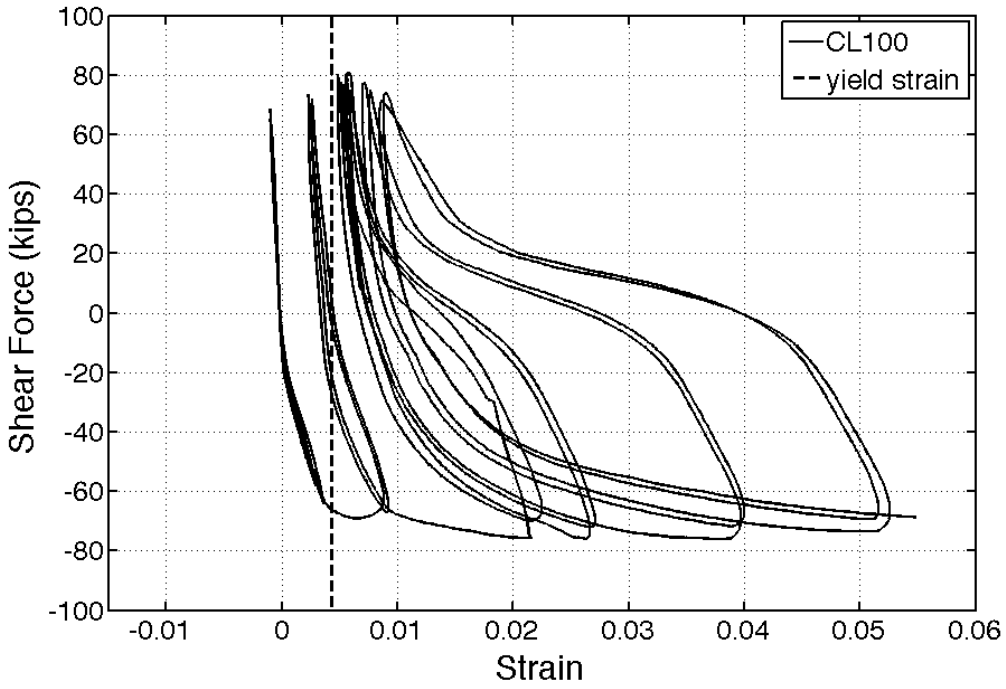

FIGURE 7-28: CL100 – STRAIN GAUGE L4NE (BOTTOM NORTH-EASTERN CORNER) RECORDING AT THE INTERFACE BETWEEN THE COLUMN AND BOTTOM FOOTING

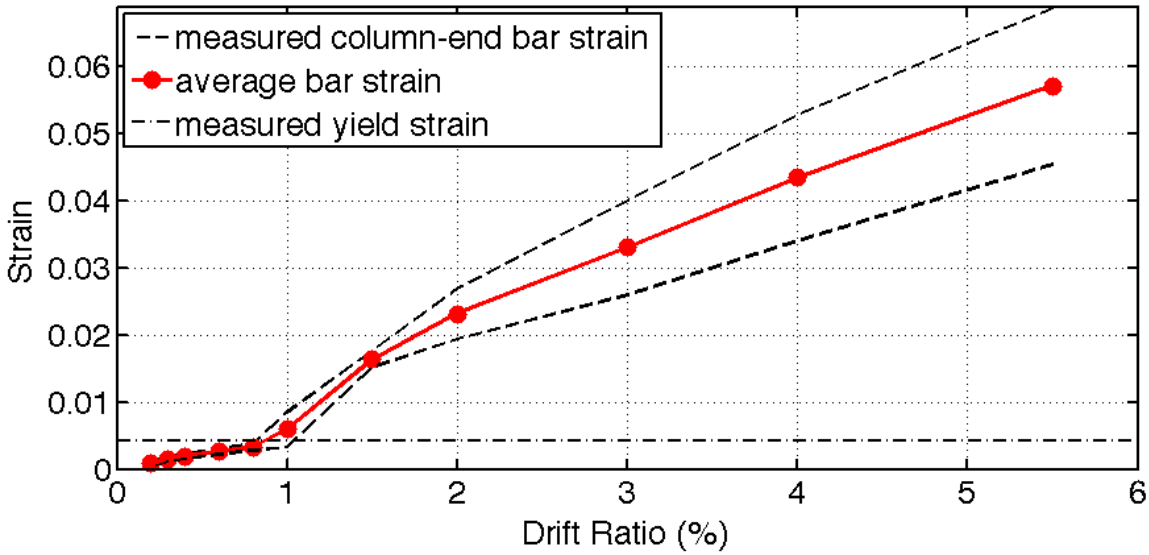

FIGURE 7-29: CL100 –COLUMN-END BAR STRAIN GAUGE RECORDINGS AT EACH DRIFT TARGET AND CALCULATED AVERAGE

7.3.4 Strain Profile

Strain readings over the height of the bottom south-western longitudinal bar are given in Figure 7-30. As it can be seen in Figure 7-30, once flexural yielding occurs, strains tended to concentrate at column ends. However, as the column was pushed past first yield to higher drift targets, inelastic strains were able to spread to 18 inches from the end of the column.

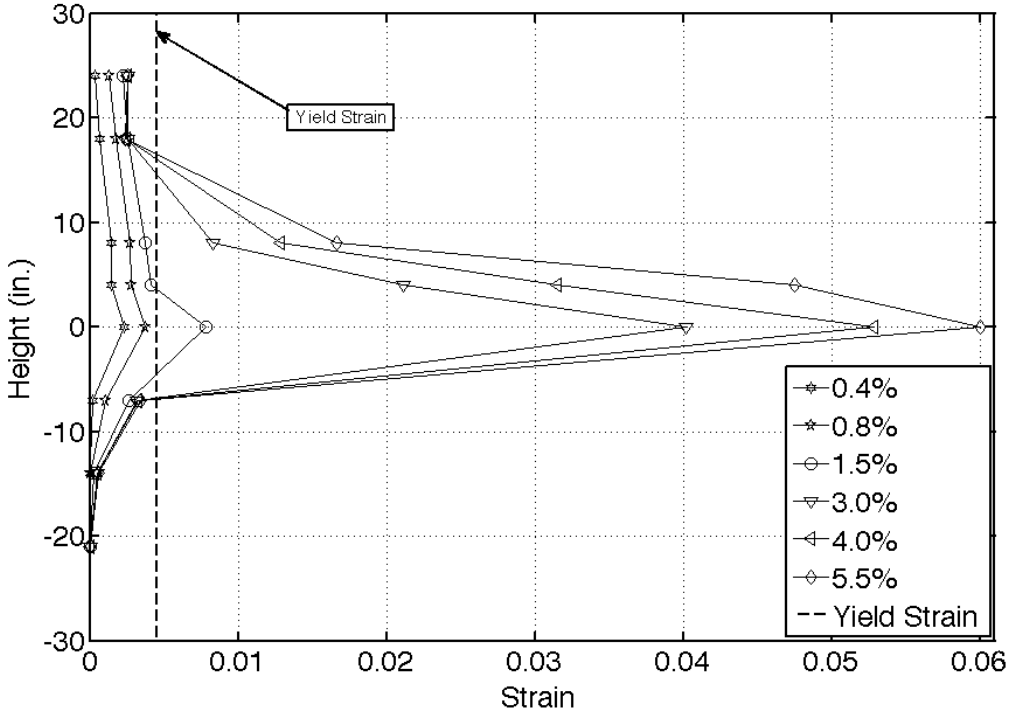

FIGURE 7-30: CL100 – LONGITUDINAL REINFORCEMENT STRAIN DEMANDS OVER HEIGHT AT DRIFT TARGETS

7.3.5 Crack Widths

Data from the GVIS was used to monitor the widths of the major flexural cracks at first yield were monitored. Considering that ACI 318-14 intends to limit crack widths to 0.016 inches during service loading, half of this value was used conservatively as a threshold at first yield for cracks of concern. Cracks within nine quadrilateral target elements were identified as satisfying the above-mentioned criteria, for each drift direction; three at the bottom half of the member, and four in the upper part (Figure 7-23). Six cracks formed when the column was pushed to a negative drift (column being pushed north, i.e. left in the pictures), 3 at each end of the member. During the first half cycle to a positive drift (column being pushed south, i.e. right in the pictures), flexural crack widths were measured in the bottom-south and top-north sides of the member. Strain readings between the second elements in from the column vertical surfaces were used to calculate the reported cracks width values. This was done as the outermost targets in the plastic-hinge region were lost at high demands due to cover crushing. The average of these cracks is plotted in Figure 7-31 and identified as cracks occurring during "Half Cycle 1". The same procedure was followed for other positive and negative drift half cycles for each drift target. At first yield, the average of all cracks was 0.014 inches. These cracks opened wider as the member was pushed passed yield. No significant difference in crack width was noticed between the successive half cycles in which the column was being pushed in the same direction. These critical cracks were all located within 18 inches from the ends of the member. As the column was pushed to higher drifts (past 2.0% drift ratio) two large

flexural cracks formed at each end of the member, 9 inches from its ends. Figure 7-38 plots the width of one of these cracks as measured throughout the test.

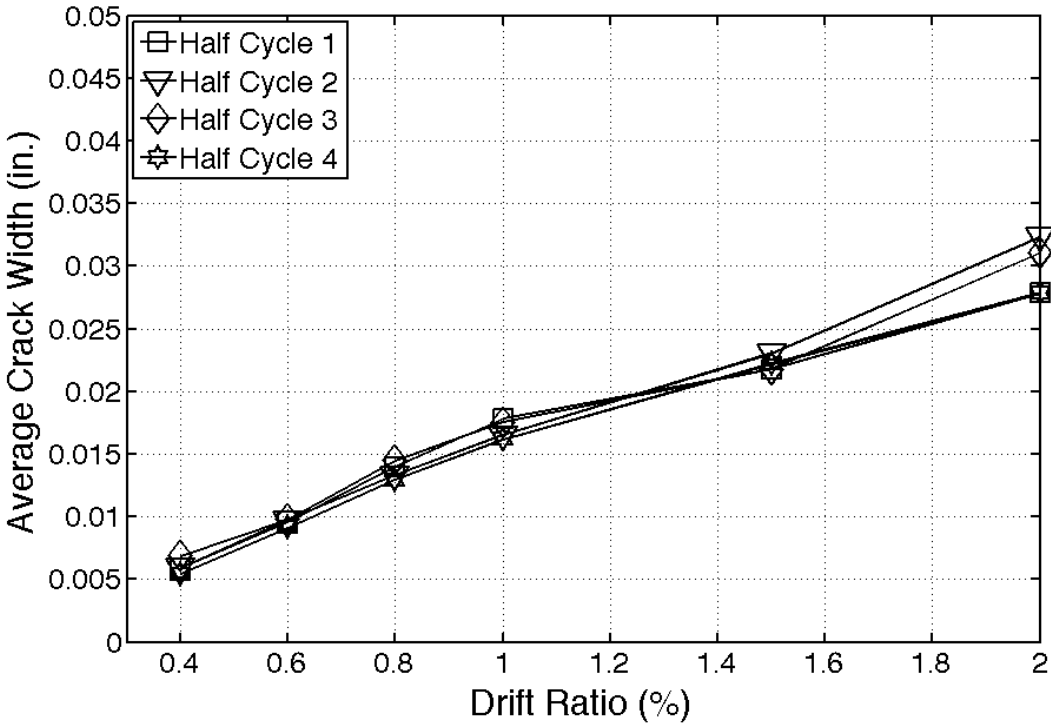

FIGURE 7-31: CL100 - AVERAGE VALUES OF LARGEST FLEXURAL CRACK WIDTHS AT DRIFT TARGETS

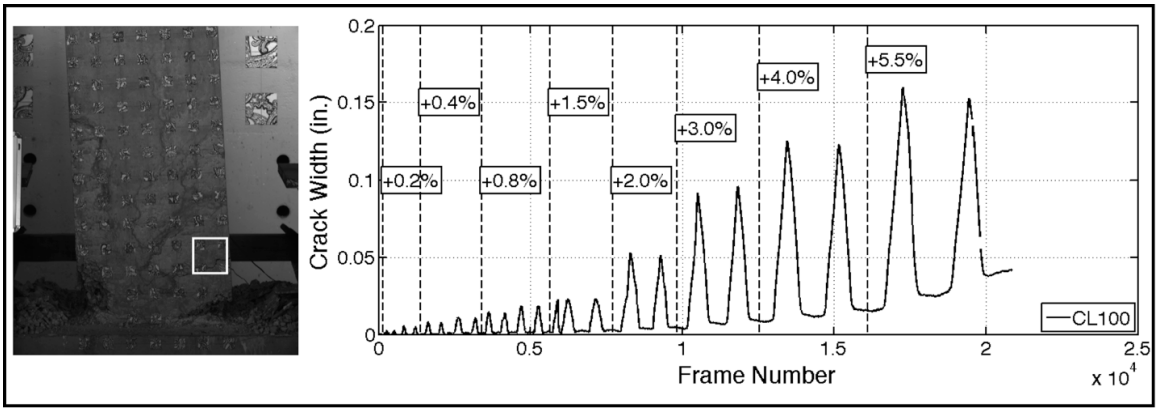

FIGURE 7-32: CL100 – WIDTH OF ONE OF THE TWO LARGEST FLEXURAL CRACKS

7.3.6 Buckling History

Buckling of the longitudinal reinforcement in CL100 was identified through the images taken at the end of each loading half-cycle. Buckling of the first longitudinal bars was observed at the second cycle to a drift ratio of +5.5% (Figure 7-33). The first bars to buckle were the middle bars that were restrained by the 90-degree hook of cross-ties, which opened up allowing the buckling. At this point, the moment strength of the member had dropped by 29% as compared to the peak applied moment at the base. As the column was pushed back to a drift ratio of -5.5%, significant buckling took place, which lead to the lateral strength of the member having decreased by 34% at the onset of the first bar fracture. The rotation of the row of targets located 9 inches over the base, or the 4^{th} target row from the end of the column is plotted in Figure 7-34. The location of this row of targets corresponds to the to the first row of targets above the observed buckling location. The rotation at this location seems to not have captured the progression of buckling.

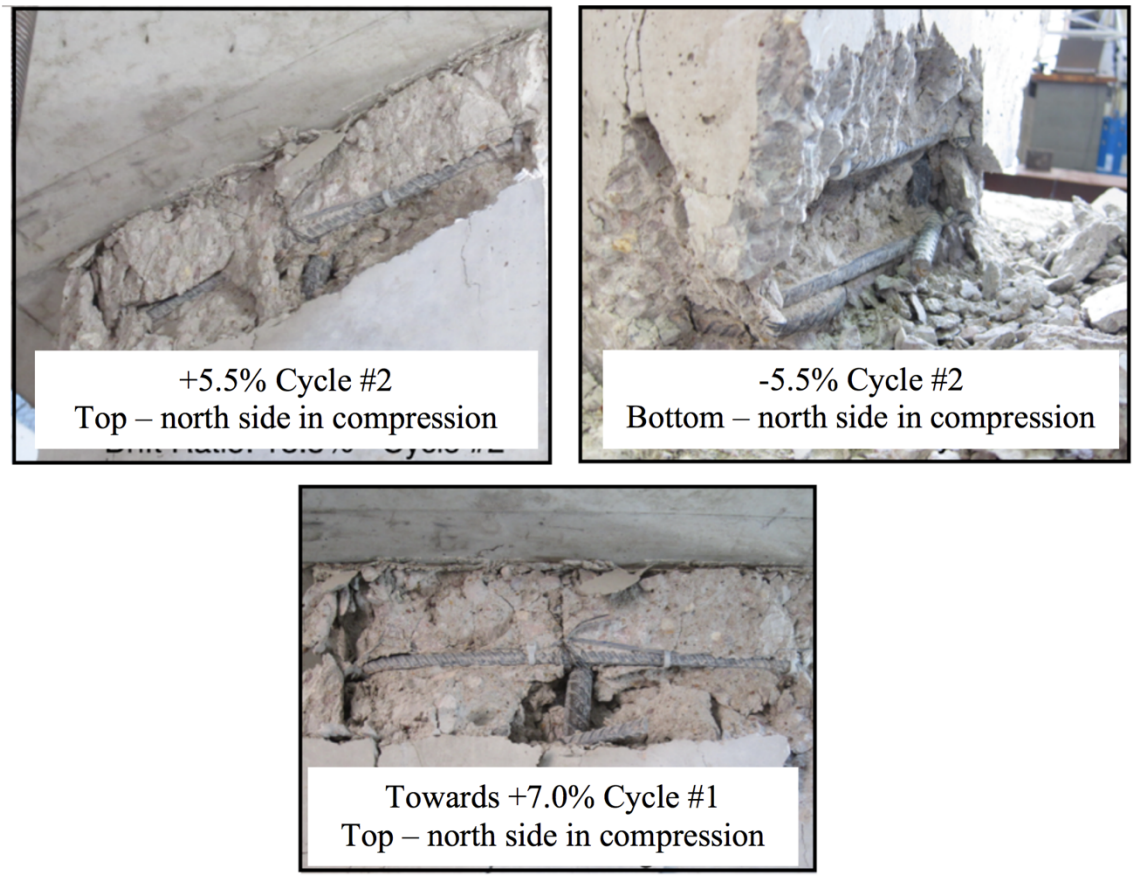

FIGURE 7-33: CL100 – LONGITUDINAL BAR BUCKLING

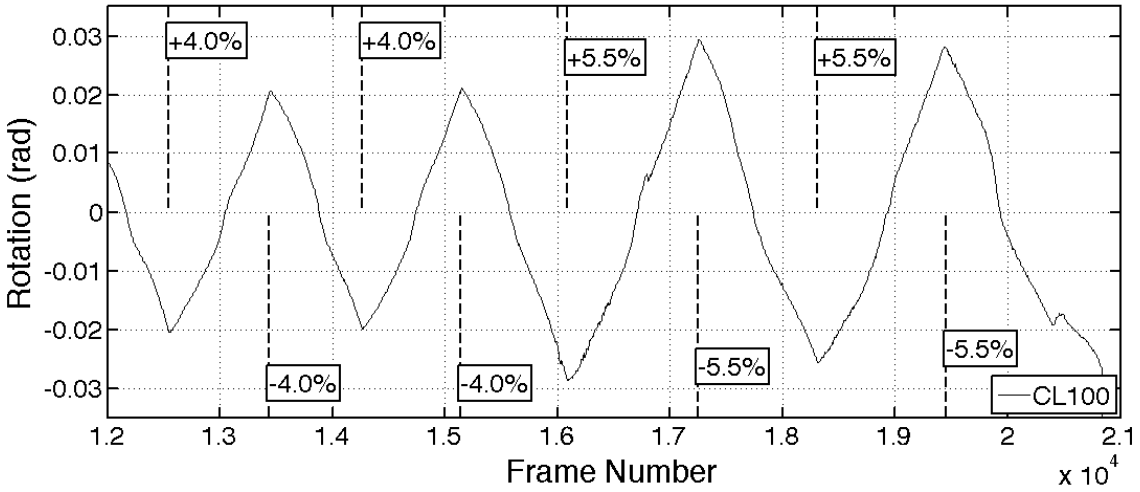

FIGURE 7-34: CL100 – ROTATION AT A DISTANCE 9 INCHES FROM THE BASE

7.3.7 Energy Dissipation

The dissipated energy, defined as the area under the average top and bottom moment versus lateral drift relation, is plotted in Figure 7-35 for each cycle. The average top and bottom moment was used to compute the dissipated energy as moment strength is more representative of column sectional strength, as opposed to lateral-load strength that is influenced by second order deformation effects. Prior to first yielding (drift ratio targets up to 0.8%) the amount of dissipated energy was similar between the two cycles at each target drift. As the column was pushed to higher drifts and damage accumulated, the difference in energy dissipation between the cycles increased. The difference in cumulative dissipated energy between cycles at the end of the 4% drift ratio cycles was 15.2%.

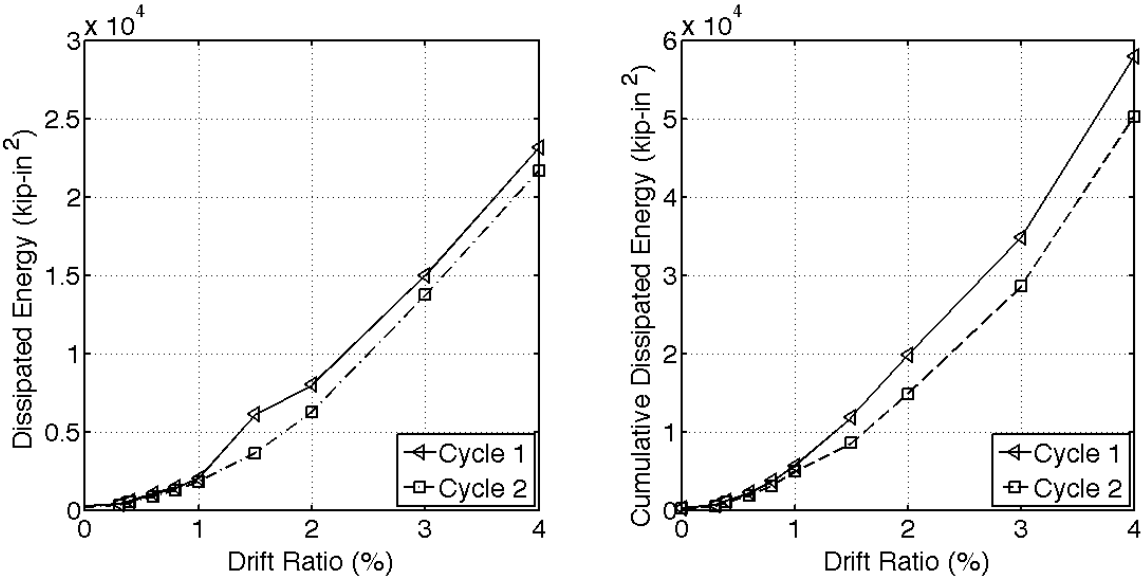

FIGURE 7-35: CL100 – DISSIPATED ENERGY AT DRIFT TARGETS FOR EACH CYCLE

7.4 TEST RESULTS FOR CM100

Test results for column CM100 are reported in this section. Specimen CM100 was reinforced with grade 100 A1035 longitudinal and transverse bars. These bars were produced using the MMFX (M) proprietary process (2012). As for all specimens, CM100 was tested under displacement-controlled quasi-static cyclic lateral loading. The recorded lateral displacement history is shown in Figure 7-36. An axial load of 253 kips was applied by the vertical actuators which together with the 10-kips self–weight of the top footing and test frame resulted in an effective axial load of $15.0\%\ A_g f_c'$ (Figure 7-37). CM100 was loaded at $14.3\%\ A_g f_c'$ up to the first cycle to a drift ratio of 0.3% due to an input error (Figure 7-37). It is believed that this did not affect the overall performance of the test.

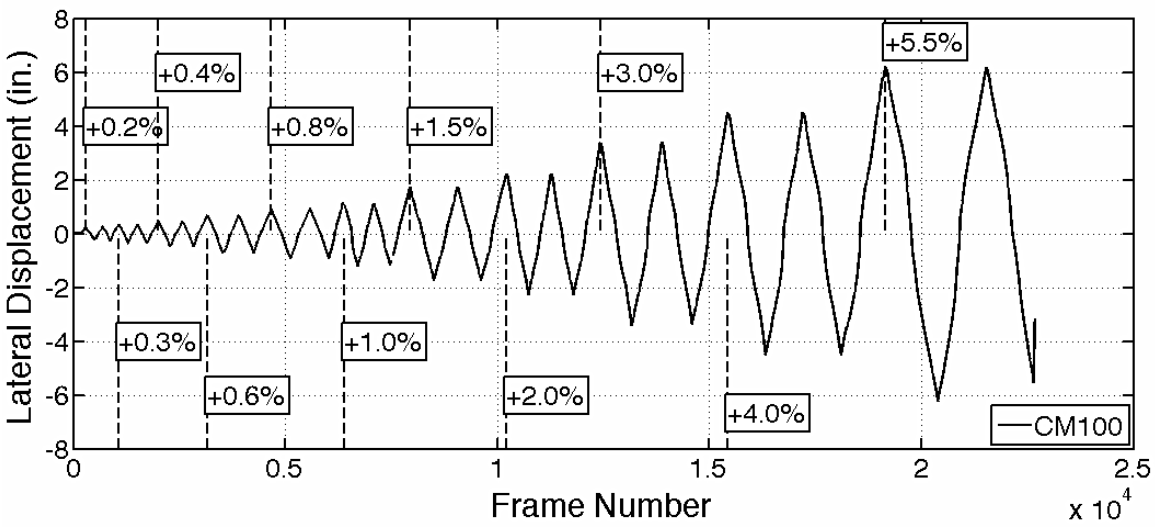

FIGURE 7-36: CM100 – MEASURED LATERAL DISPLACEMENT AT EVERY CAPTURED FRAME

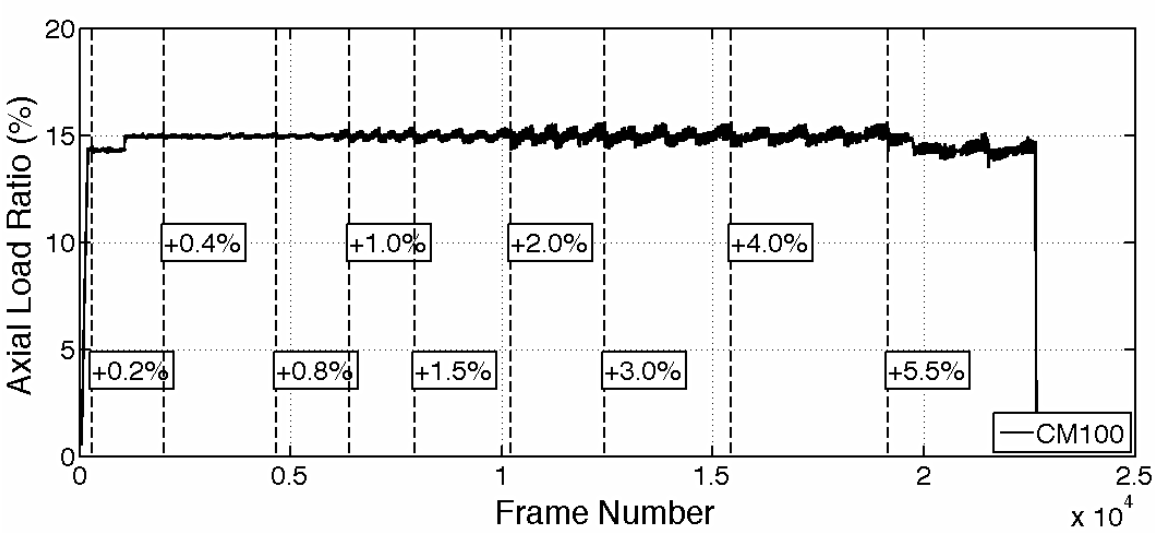

FIGURE 7-37: CM100 – APPLIED AXIAL LOAD RATIO AT EVERY CAPTURED FRAME

7.4.1 General Behavior

Prior to testing, no cracks were noticed on the specimen surface. The recorded lateral force versus drift ratio response of specimen CM100 is plotted in Figure 7-38. Table 7-5 summarizes the lateral force and drift values for all milestones for column CM100. The first flexural cracks in column CM100 were visible at the end of the first cycle to +0.2% drift-ratio excursion (Figure 7-38). These cracks corresponded to surface principal strains at the order of 0.002 (Figure 7-39). The initial flexural cracks propagated inside the centerline of the column leading to the formation of first inclined cracks (Figure 7-39 - 0.6%).

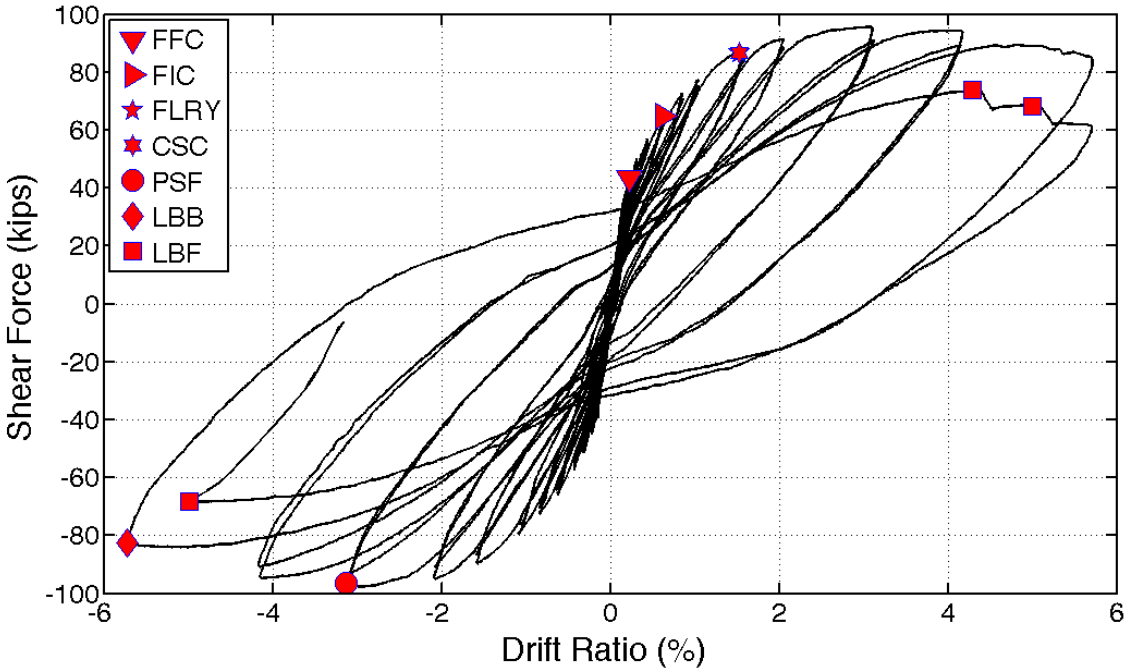

FIGURE 7-38: CM100 – LATERAL RESPONSE

TABLE 7-5: CM100 - BEHAVIORAL MILESTONES

Milestone	Drift Ratio (%)	Lateral Load (kips)
First Flexural Crack	+0.2	+42.6
First Inclined Crack	+0.6	+65.2
First Long. Reinf. Yield	+1.5	+87.5
Cover Splitting Crack	+1.5	+87.5
Peak Shear Force	-2.9	-97.5
Long. Bar Buckling	-5.5	-80.6
Long. Bar Fracture	+4.3	-74.1

First yield in the longitudinal reinforcement was identified at a drift ratio of +1.5%, from strain gauge readings. The relatively high drift at first yield was attributed to the high yield strain of 0.0063 obtained from the 0.2% offset. The maximum applied shear-force of 97.5 kips was recorded at the end of first cycle to a drift ratio of -3.0%. Beyond that drift cycle, the lateral load diminished slightly, driven by second order axial load effects and the accumulation of damage such as concrete spalling.

Top and base moments versus lateral drift ratio are plotted in Figure 7-40. As can be seen, peak moment strength occurred at a drift ratio of 3.0% for the base moment, and 4.0% at the top moment. Gradual degradation of moment strength occurred beyond that drift due to accumulation of damage in concrete. During the first cycle to a drift ratio of -5.5%, initiation of longitudinal bar buckling was observed and was associated with a gradual loss in the moment capacity during that half cycle (Figure 7-41).

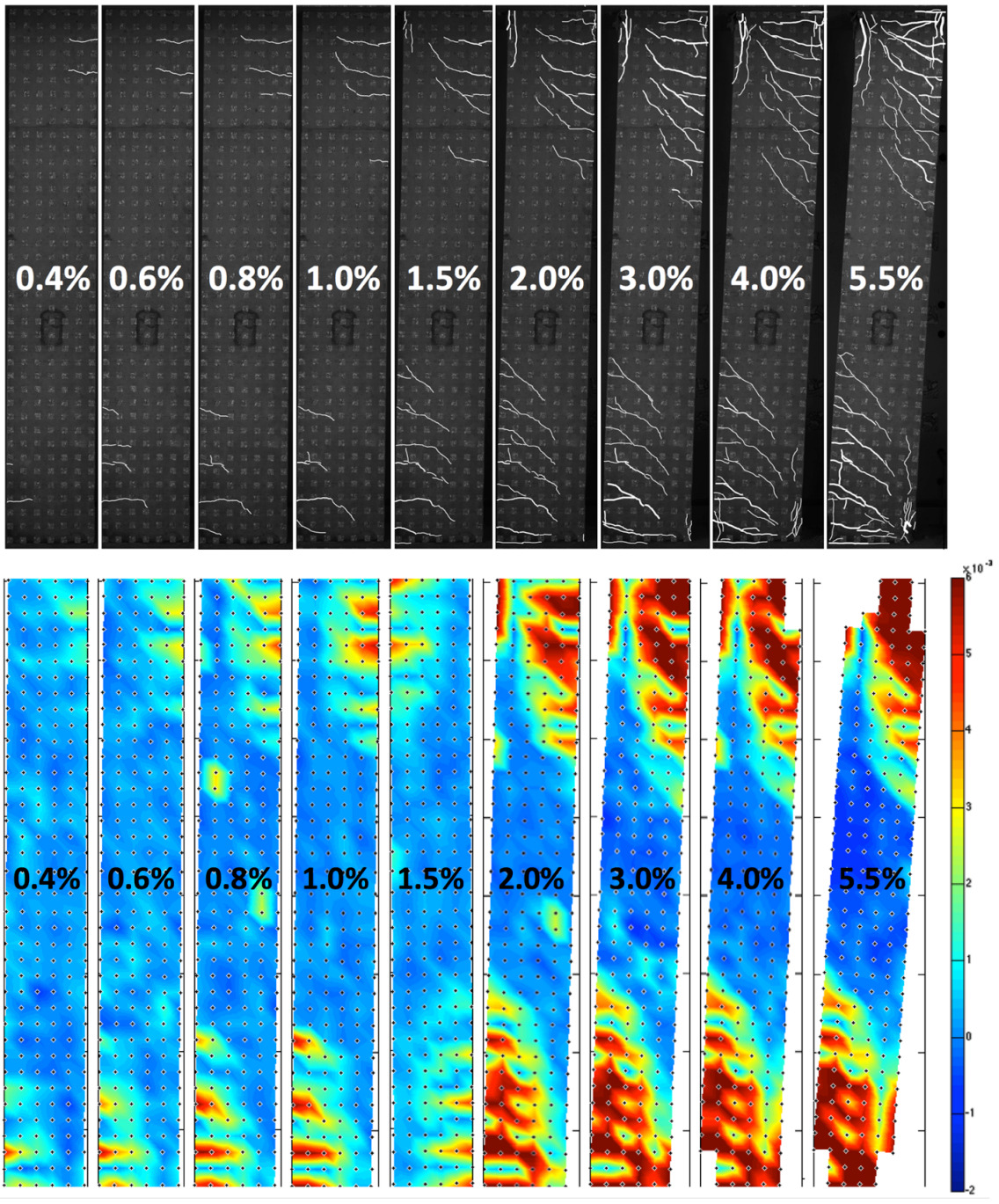

FIGURE 7-39: CM100 - CRACKING PATTERN (UP) AND MEASURED PRINCIPAL STRAINS (DOWN) AT DRIFT TARGETS

As the column was pushed to drift ratios of 4.0%, and 5.5%, increasing crushing and spalling of the concrete cover was observed. In contrast to specimens CH100 and CL100, specimen CM100 had smaller flexural cracks which spread over a larger height, up to 40 inches from its ends. Specimen CM100 formed more cracks with smaller widths when compared to the other specimens reinforced with grade 100 steel. Only one flexural crack had a width on the order of 0.15 inches at the end of the test, while other cracks were narrower than 0.1 inches. At the same drift ratio, vertical cracks at the location of the longitudinal reinforcement propagated up to 24 in. from column ends, indicating some de-bonding between the longitudinal bars and the surrounding concrete. These cracks initiated at a drift ratio of 1.5% drift ratio, which corresponded to a curbing of the rate of increase in longitudinal bars strains with increasing drift ratios. This behavior is discussed in more details in Section 4.4.3.

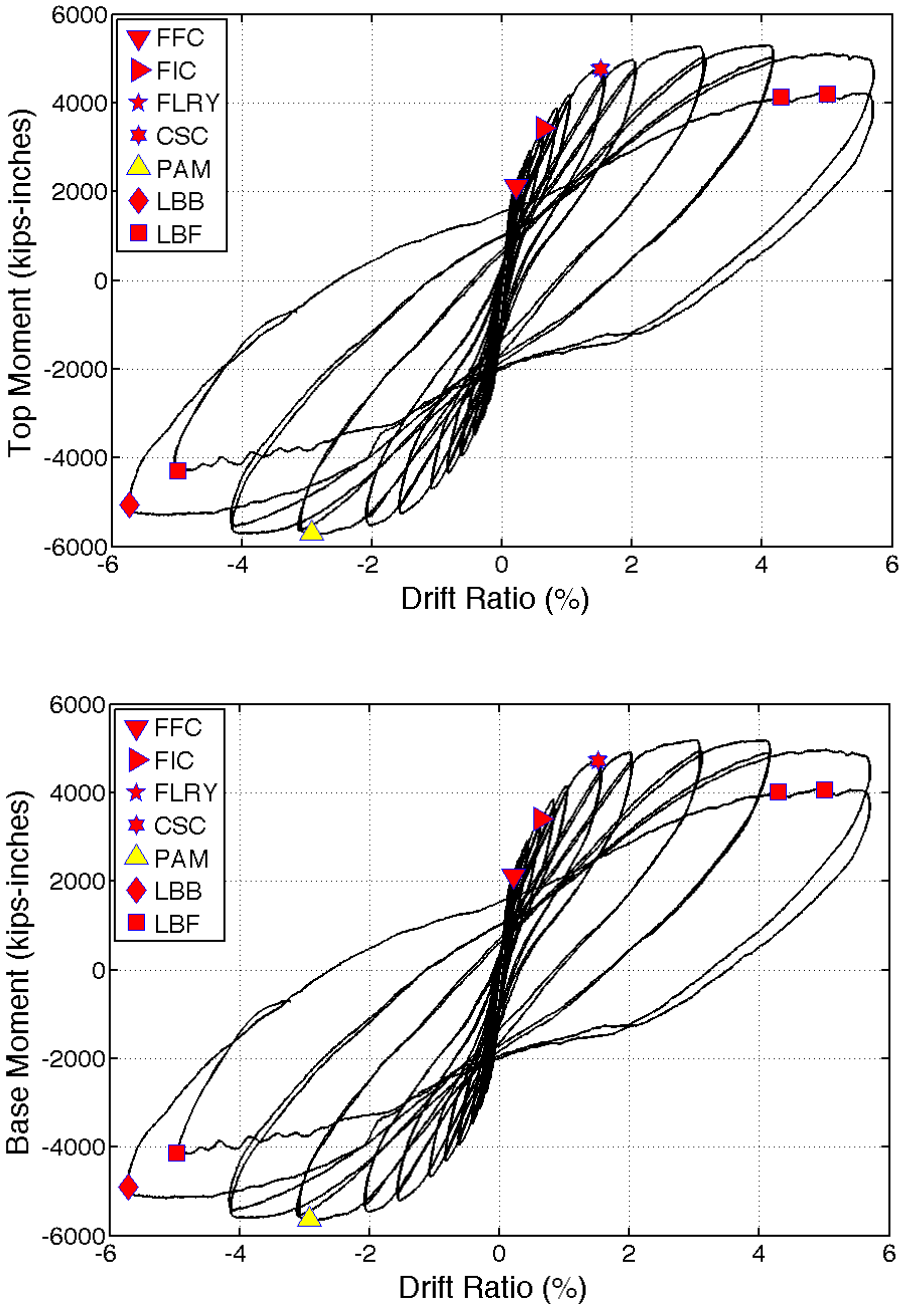

FIGURE 7-40: CM100 - BASE AND TOP MOMENT VS. DRIFT RATIO

The lateral load resistance of the column remained stable and the column maintained axial load capacity past the first cycle to a drift ratio of +5.5% (Figure 7-41). During the first cycle to a drift ratio of -5.5%, the column experienced only a 14% loss in moment strength as compared to the measured peak lateral moment resistance. By then, the cover concrete in the top and bottom plastic hinge regions had spalled to a distance of about 6 in. from column ends. On its way to the second cycle to +5.5% drift cycles, one of the corner longitudinal bars fractured at the base of the column at a drift ratio of 4.3% (Figure 7-41; Figure 7-42). Just prior to first bar fracture, the column had lost 29% of its measured peak moment resistance. The first bar fracture contributed to additional loss in lateral strength and a second bar fracture occurred shortly after, at a drift ratio of 5.0%. A third bar fractured at a drift ratio of -5.0% as the column was being pushed towards the completion of the second cycle to a drift ratio of 5.5%. The column was able to carry the prescribed axial load throughout the test without showing signs of significant axial deformation even after longitudinal reinforcement fracture.

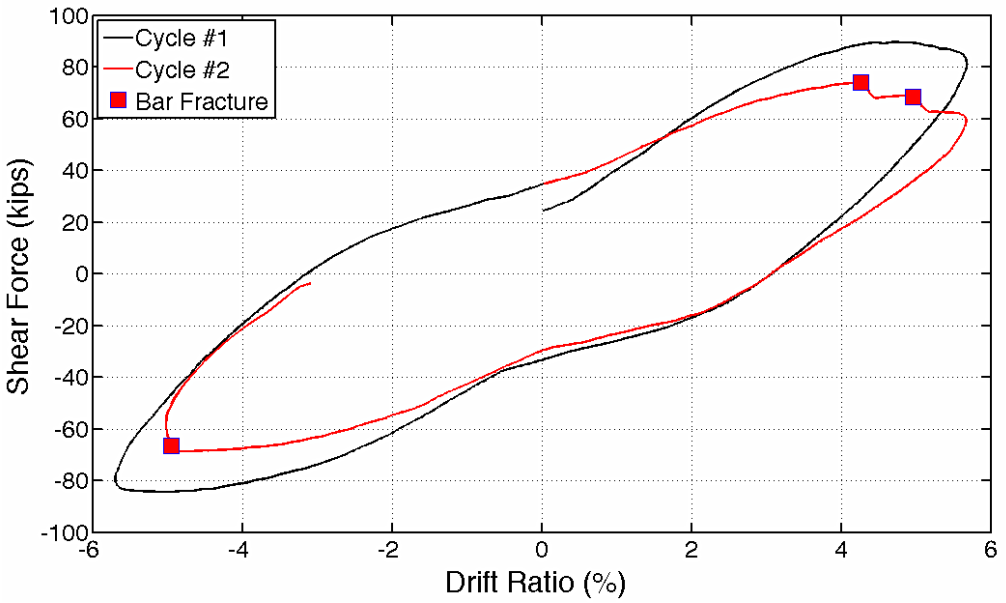

FIGURE 7-41: CM100 – LAST CYCLES RESPONSE

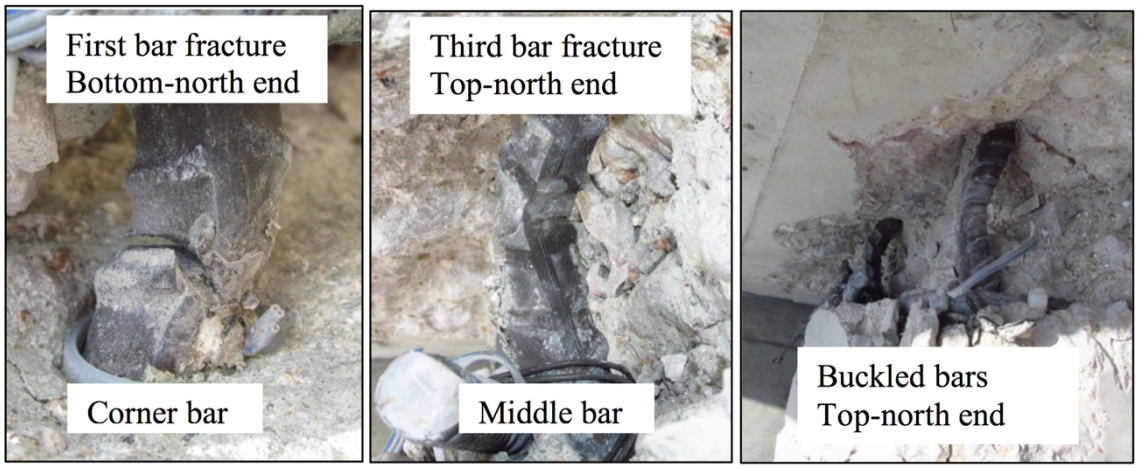

FIGURE 7-42: CM100 – PICTURES OF FRACTURED AND BUCKLED BARS AT THE END OF THE TEST

7.4.2 Deformation Components

Flexural deformations contributed most to the column lateral drift throughout the test (Table 7-6; Figure 7-43). At higher drifts, the relative weight of flexural deformations lowered as the bar-slip component increased from about 25% of the total drift at low drift levels, to about 30% in the post-yield cycles. Possibly, debonding of the longitudinal reinforcement from the surrounding concrete at larger levels of concrete damage resulted in this observed increase in recorded bar-slip contribution. This debonding of longitudinal bars due to concrete damage could have decoupled the bar deformations from measured concrete surface movements, from which bar-slip deformations were extracted. Shear deformations increased in absolute value, but remained relatively low at around 7% of total drift throughout the test. The shear deformations were higher for specimen CM100, as compared to other specimens reinforced with grade 100. The higher shear deformations are attributed to the higher sectional strength due to the high yield strength of the #6 bars used in this specimen. Results for deformation components were not reliable after cycles to a drift ratio of 4.0%.

TABLE 7-6: CM100 - DEFORMATION COMPONENTS AS PERCENTAGE OF TOTAL

Total	Flexure	Bar-slip	Shear
0.2%	72.6%	24.4%	3.9%
0.3%	72.4%	23.6%	4.0%
0.4%	71.4%	23.6%	5.0%
0.6%	69.4%	25.6%	5.1%
0.8%	67.0%	26.8%	6.2%
1.0%	65.9%	27.2%	6.9%
1.5%	63.6%	29.0%	7.5%
2.0%	62.4%	30.5%	7.2%
3.0%	63.2%	29.9%	6.9%
4.0%	60.7%	33.0%	6.2%

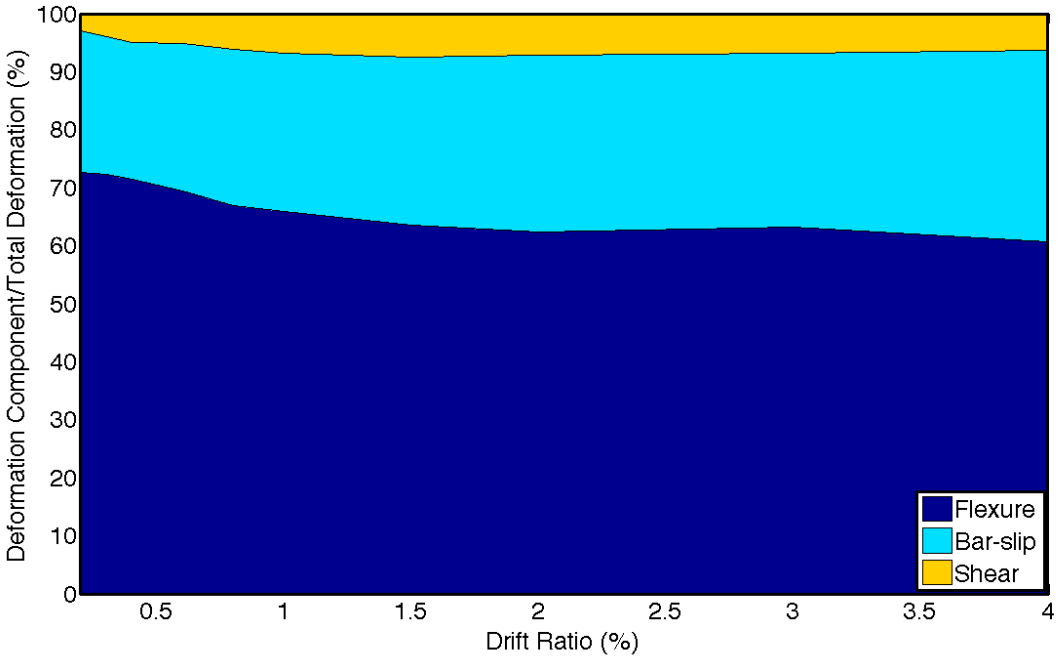

FIGURE 7-43: CM100 – DEFORMATION COMPONENTS

7.4.3 Strain History

Maximum strain demands were recorded at the interfaces between the column and footings. Figure 7-44 shows a typical strain versus lateral load response recorded on longitudinal bars at column ends. Figure 7-45 plots longitudinal bar tension strains at the end of each positive drift cycle target, measured at the top and bottom column interfaces with footings. The #6 bars used as longitudinal reinforcement in CM100 had a yield strain of 0.0063 as obtained from material testing. This strain was first reached at a drift ratio of 1.5% (Figure 7-44; Figure 7-45). After reaching a yield strain as computed with the 0.2% offset rule, the strain demands increased without significant increase in the lateral load. In general, strain demands on longitudinal bars were not much higher in the second cycle to the same drift target, and started to get noticed only at a drift ratio of 4.0%. This difference was however relatively small, and on the order of 5% of the strain value.

Three of the strain gauges showed in Figure 7-45 stopped recording right before the column was pushed to the first cycle to a drift ratio of 5.5%. The strain value at 5.5% drift ratio presented below was linearly interpolated.

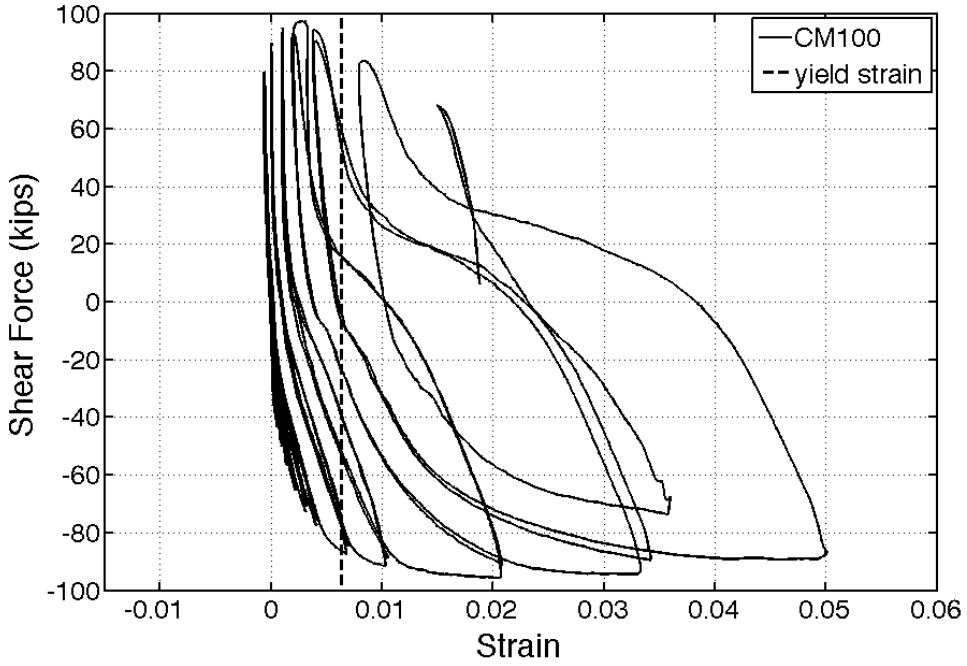

FIGURE 7-44: CM100 – STRAIN GAUGE L4SW (TOP SOUTH-WESTERN CORNER) RECORDING AT THE INTERFACE BETWEEN THE COLUMN AND TOP FOOTING

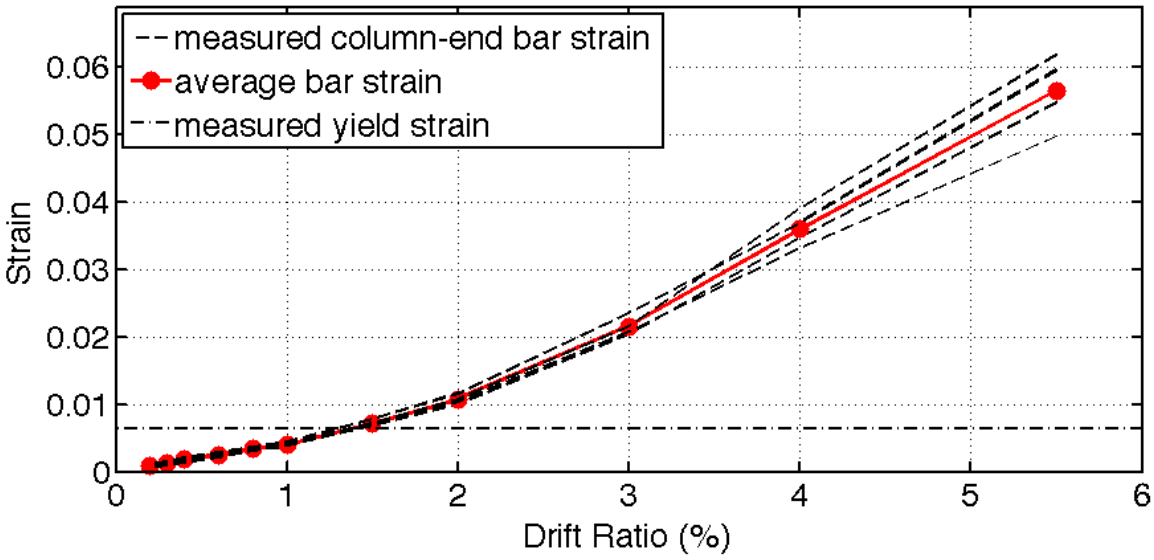

FIGURE 7-45: CM100 – COLUMN-END BAR STRAIN GAUGE RECORDINGS AT EACH DRIFT TARGET AND CALCULATED AVERAGE

7.4.4 Strain Profile

Strain readings over the height of north-eastern longitudinal bar are given in Figure 7-46. As it can be seen in Figure 7-46, as the column was pushed past the first yield to higher drift targets, the yielded length of the bar went up to 20 inches from the base of the column, as compared to 23 inches in specimen CH100. The strain demands between the first cycle to 4.0% drift and first cycle to 5.5% drift ratio were less than 3% (Figure 7-46).

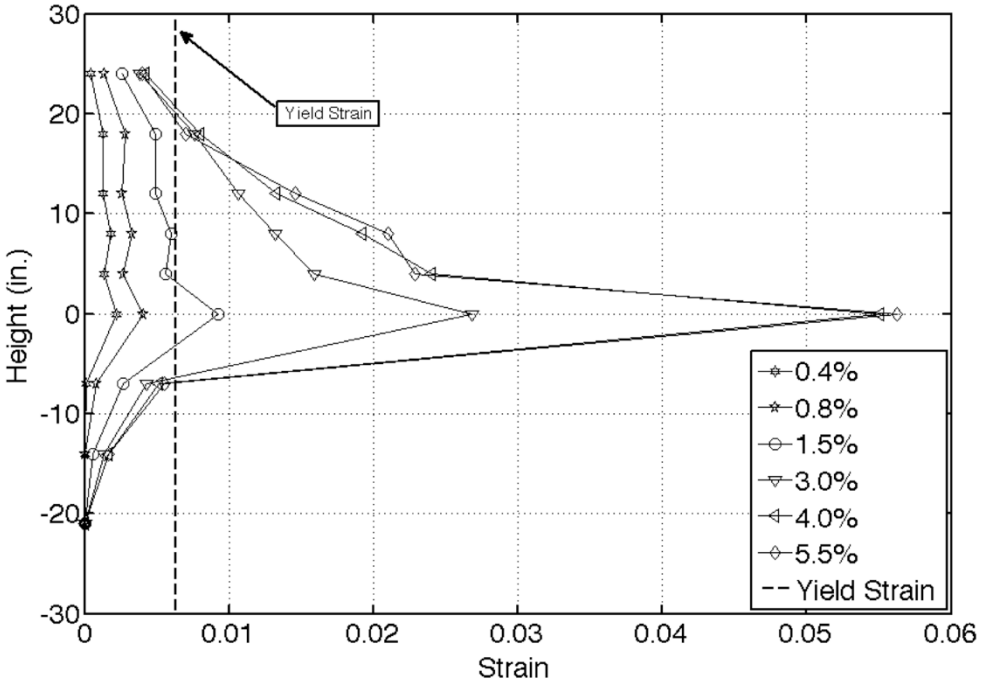

FIGURE 7-46: CM100 – LONGITUDINAL REINFORCEMENT STRAIN DEMANDS OVER HEIGHT AT DRIFT TARGETS

Data from the GVIS was used to monitor the widths of the major flexural cracks at first yield were monitored. These cracks were identified as having a width of 0.008 inches or larger at first yield. Considering that ACI-318-14 intends to limit crack widths to 0.016

inches during service loading, half of this value was used conservatively as a threshold at first yield for cracks of concern. Cracks within nine quadrilateral target elements were identified as satisfying the above- mentioned criteria, for each drift direction; four at the bottom half of the member, and five in the upper part (Figure 7-39). Eight cracks formed when the column was pushed to a negative drift (column being pushed north, i.e. left in the pictures), four in each end of the member. During the first half cycle to a positive drift (column being pushed south, i.e. right in the pictures), flexural crack widths were measured in the bottom-south and top-north sides of the member. The average of these cracks is plotted in Figure 7-47 and identified as occurring during "Half Cycle 1". The same procedure was followed for other positive and negative drift half cycles for each drift target. At 0.8% drift ratio, the average of all cracks was 0.015 inches, as compared to 0.012 inches in CH100 and 0.014 inches in CL100. The slightly larger measured width in CM100 is attributed to one of the cracks which contributed to the increased average crack width in one direction. This crack could have been considered an outlier, but no physical evidence was found to support such a determination. No significant difference in crack width was noticed between the successive half cycles in which the column was being pushed in the same direction. Figure 7-48 plots the width of one of the largest cracks as measured throughout the test. The width of this crack measured at one of the outermost strain-elements of the column, was 0.15 inches by the end of the first cycle to a drift ratio of 5.5%. The largest crack-widths in CH100 and CL100 were measured one strain-element in from the column surface and were in the same range (i.e. 0.15 inches).

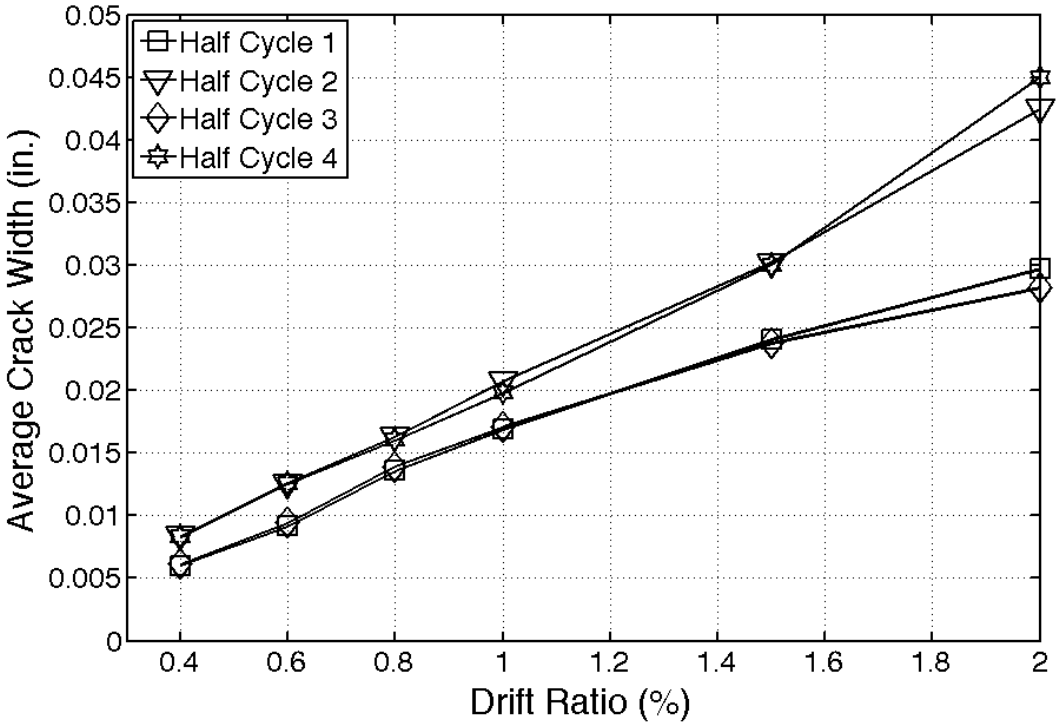

FIGURE 7-47: CM100 - AVERAGE VALUES OF LARGEST FLEXURAL CRACK WIDTHS AT DRIFT TARGETS

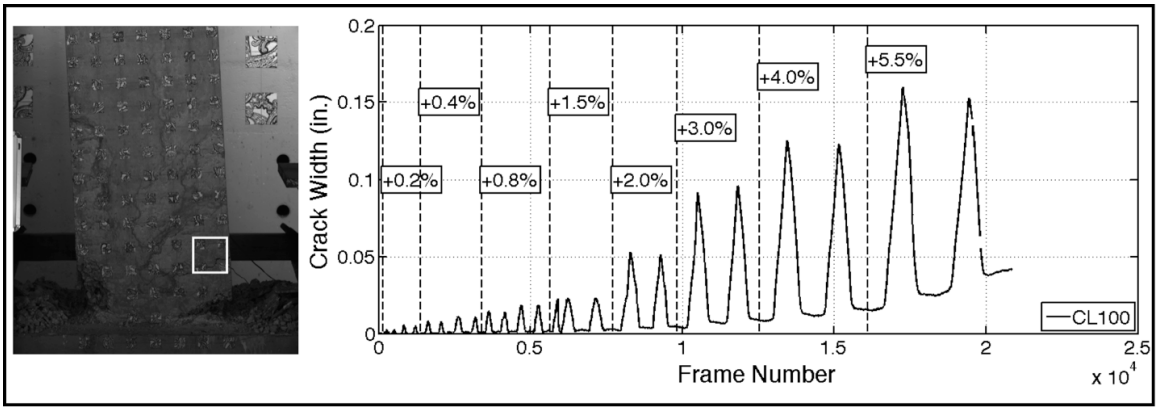

FIGURE 7-48: CM100 – WIDTH OF ONE OF THE TWO LARGEST FLEXURAL CRACKS

7.4.5 Buckling History

Buckling of the longitudinal reinforcement in CM100 was identified through the images taken at the end of each loading half-cycle. Buckling of the first longitudinal bars was observed at the first cycle to a drift ratio of -5.5% (Figure 7-49). At this point, the moment strength of the member had dropped by 14% as compared to the peak applied moment at the base. As the column was pushed back to a drift ratio of +5.5%, significant buckling took place, which lead to the lateral strength of the member having decreased from peak by 29% at the onset of the first bar fracture. Contrary to other columns tested in this study, bends in the crossties in CM100 did not open up and buckling in the longitudinal bars was limited prior to their fracture.

The rotation of the row of targets located 9 inches over the base, or the 4th target row from the end of the column is plotted in Figure 7-50. The location of this row of targets corresponds to the to the first row of targets above the observed buckling location. The rotation at this location seems to not have captured the progression of buckling as most of the rotation in either direction was concentrated over this height.

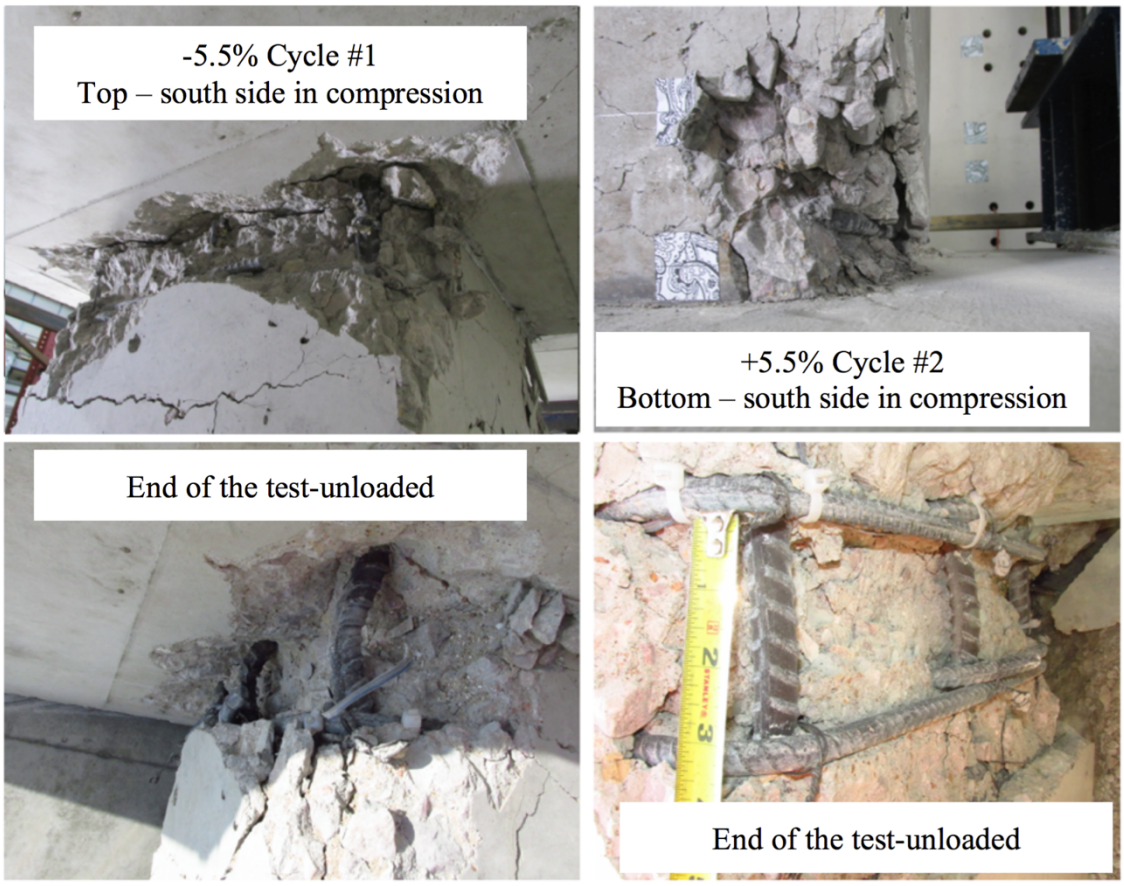

FIGURE 7-49: CM100 – LONGITUDINAL BAR BUCKLING

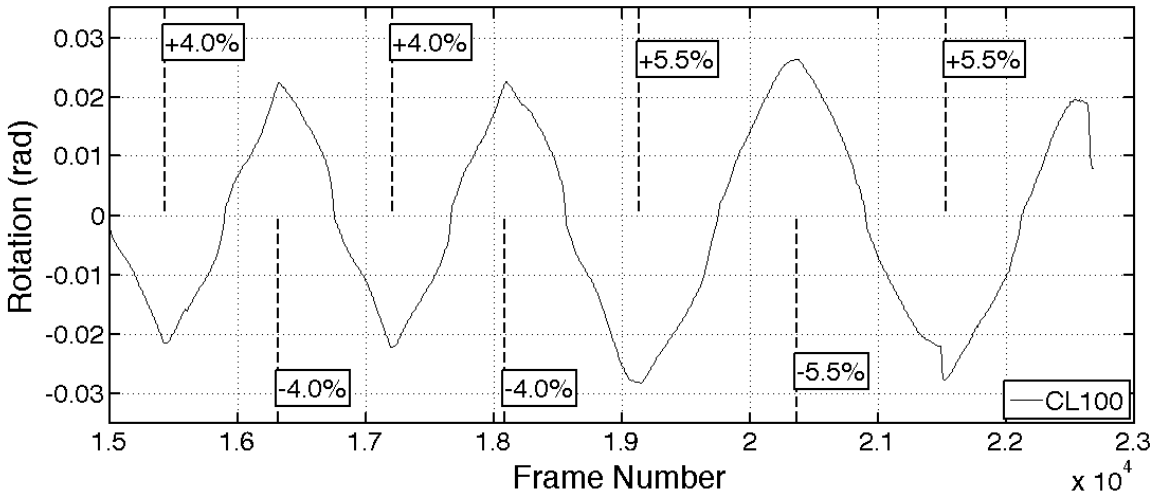

FIGURE 7-50: CM100 – ROTATION AT A DISTANCE 9 INCHES FROM THE BASE

7.4.6 Energy Dissipation

The dissipated energy, defined as the area under the average top and bottom moment versus lateral drift relation, is plotted in Figure 7-52 for each cycle. The average top and bottom moment was used to compute the dissipated energy as moment strength is more representative of column sectional strength, as opposed to lateral-load strength that is influenced by second order deformation effects. Prior to first yielding (drift ratio targets up to 0.8%) the amount of dissipated energy was similar between the two cycles at each target drift. As the column was pushed to higher drifts and damage accumulated, the difference in energy dissipation between the cycles increased. The difference between two consecutive post-yield cycles to the same drift ratio was in the range of 20 to 40%. The difference in cumulative dissipated energy between cycles at the end of the 4% drift ratio cycles was 22.4%.

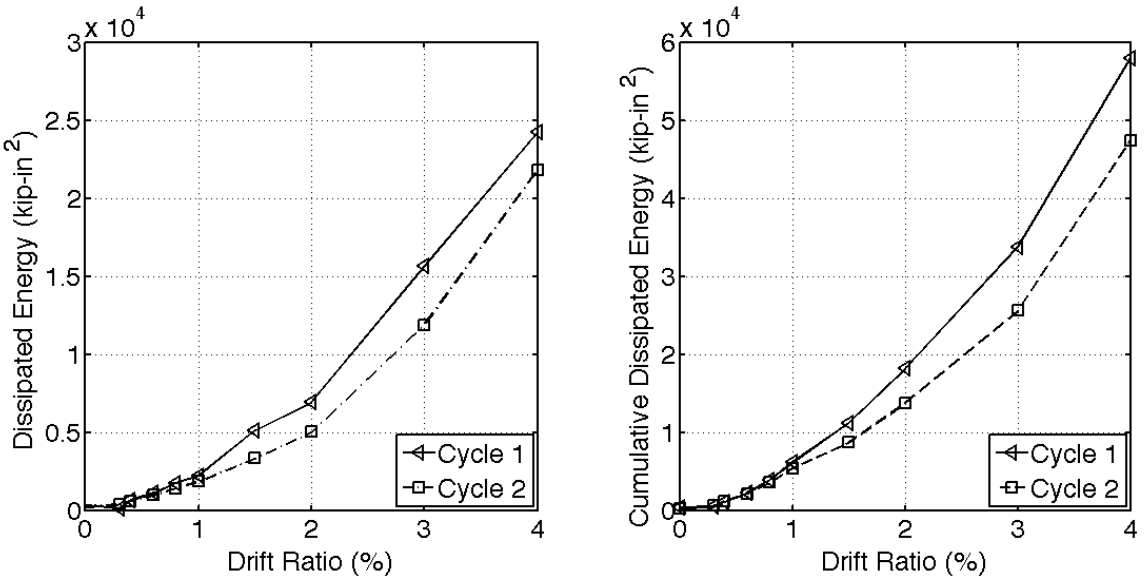

FIGURE 7-51: CM100 – DISSIPATED ENERGY AT DRIFT TARGETS FOR EACH CYCLE

7.5 TEST RESULTS FOR CH60

Results for column CH60 column are reported in this section. Specimen CH60 was reinforced with grade 60 ASTM A706 longitudinal and transverse bars with a high (H) *T*/*Y* ratio of 1.45. This specimen was designed as the benchmark for satisfactory behavior. As for all specimens, CH60 was tested under displacement-controlled quasi-static cyclic lateral loading. The recorded lateral displacement history is shown in Figure 7-52. An axial load of 242 kips was applied by the vertical actuators which together with the 10-kips self–weight of the top footing and testing frame resulted in an effective axial load of 15.2% $A_g f_c'$. The load was kept nearly constant throughout the test as shown in Figure 7-53.

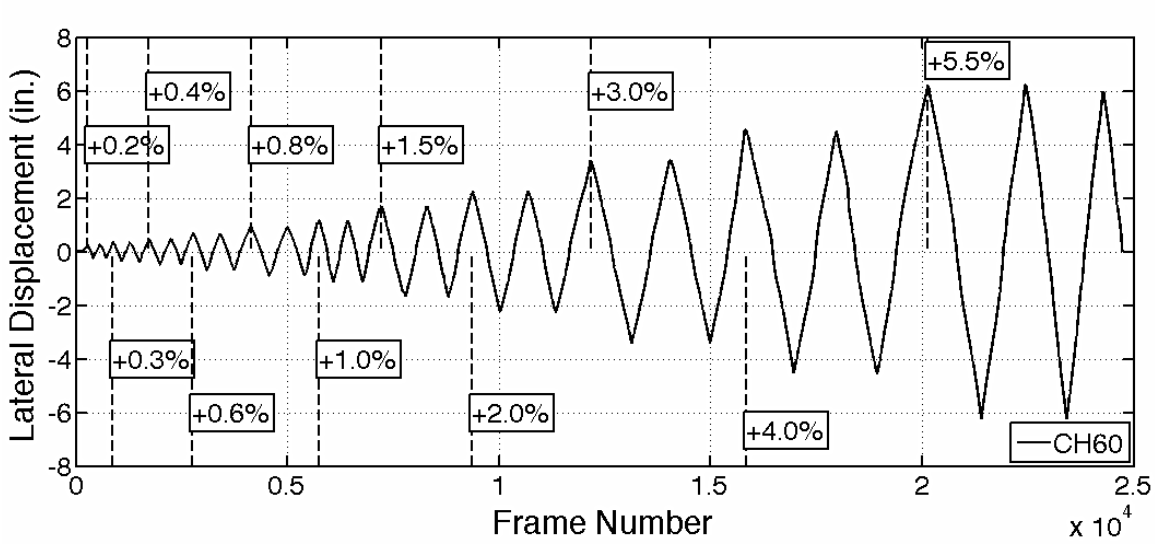

FIGURE 7-52: CH60 – MEASURED LATERAL DISPLACEMENT AT EVERY CAPTURED FRAME

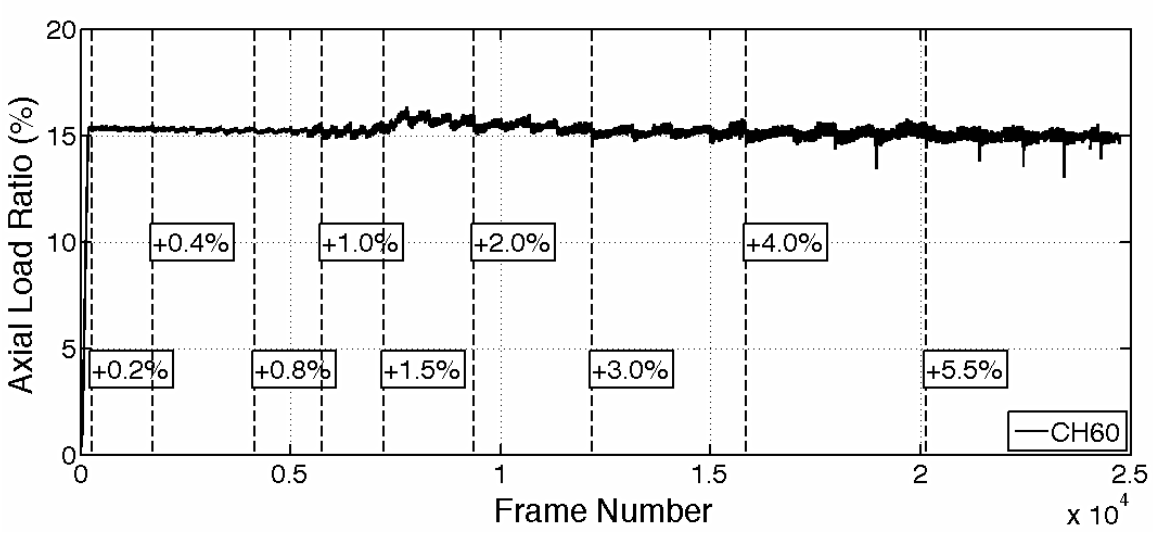

FIGURE 7-53: CH60 – APPLIED AXIAL LOAD RATIO AT EVERY CAPTURED FRAME

7.5.1 General Behavior

Prior to testing, no cracks were noticed on the specimen surface. The recorded lateral force versus drift ratio response of specimen CH60 is plotted in Figure 7-54. Table 7-7 summarizes the lateral force and drift values for all milestones for column CH60. The first flexural cracks were visible at the end of the first cycle to a drift ratio of +0.2% (Figure 7-54). These cracks corresponded to surface principal strains at the order of 0.002 (Figure 7-55). The initial flexural cracks propagated closer to the centerline of the column leading to the formation of first inclined cracks at the end of the first half-cycle to a drift ratio of +0.6% (Figure 7-55).

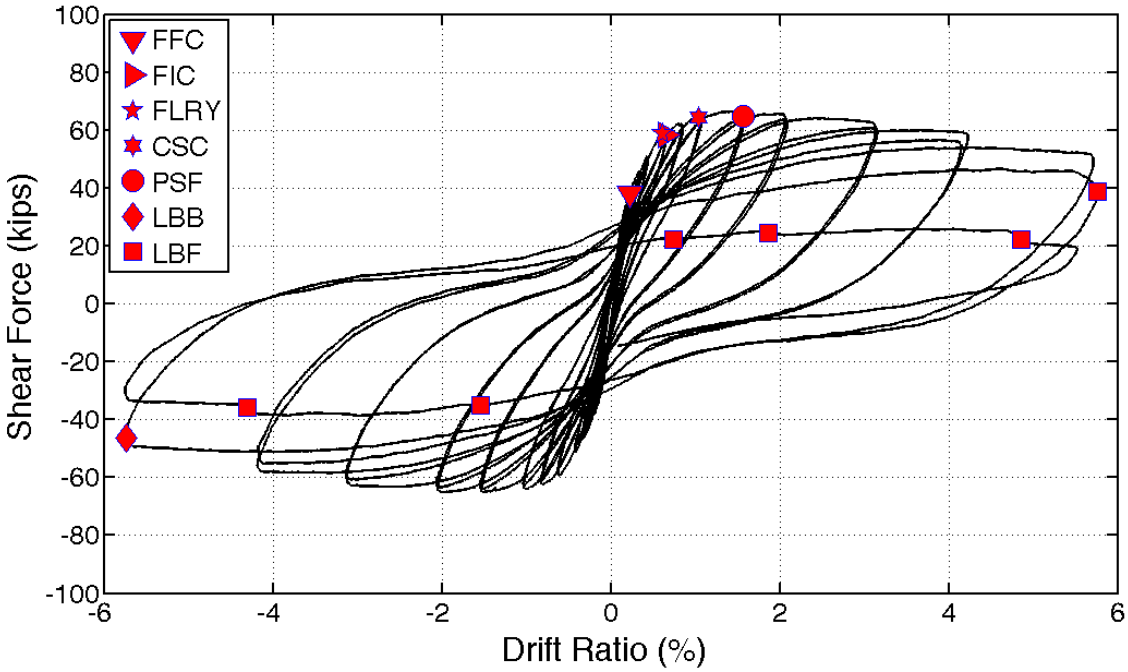

FIGURE 7-54: CH60 – LATERAL RESPONSE

TABLE 7-7: CH60 - BEHAVIORAL MILESTONES

Milestone	Drift Ratio (%)	Lateral Load (kips)
First Flexural Crack	+0.2	+37.9
First Inclined Crack	+0.6	+58.9
First Long. Reinf. Yield	+0.6	+56.3
Cover Splitting Crack	+1.0	+63.7
Peak Shear Force	+1.5	+64.0
Long. Bar Buckling	-5.5	-46.3
Long. Bar Fracture	+5.5	+38.6

First yield in the longitudinal reinforcement was identified from strain gauge readings at the end of the first cycle to a drift ratio of +0.6%. As the column was pushed to the first cycle towards a drift ratio of +1.0%, the initial flexural cracks opened wider and additional cracks formed closer to the column mid-height (Figure 7-55). The maximum applied shear-force of 64.6 kips was recorded at the end of first cycle to a drift ratio of +1.5%. Beyond that drift cycle, the lateral load diminished slightly, driven by second order axial load effects and the accumulation of damage such as concrete spalling. Top and base moments versus lateral drift ratio are plotted in Figure 7-56. As can be seen in the figure, peak moment strength occurred at a drift ratio of 1.5%. Gradual degradation of moment strength occurred beyond that drift due to accumulation of damage in concrete. During the first cycle to a drift ratio of -5.5%, initiation of longitudinal bar buckling was observed and was associated with a gradual loss in the moment capacity during that half cycle (Figure 7-56).

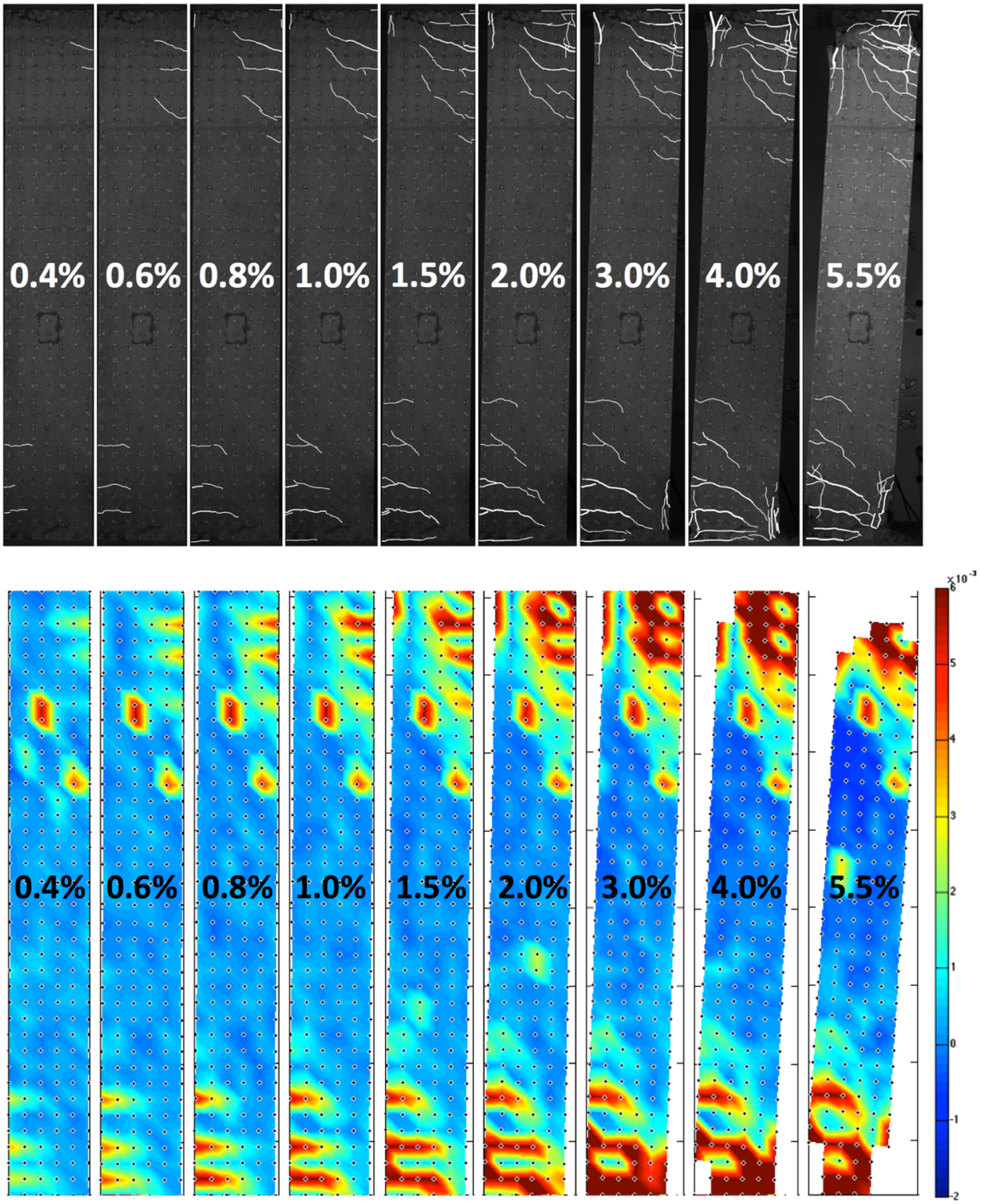

FIGURE 7-55: CH60 - CRACKING PATTERN (UP) AND MEASURED PRINCIPAL STRAINS (DOWN) AT DRIFT TARGETS

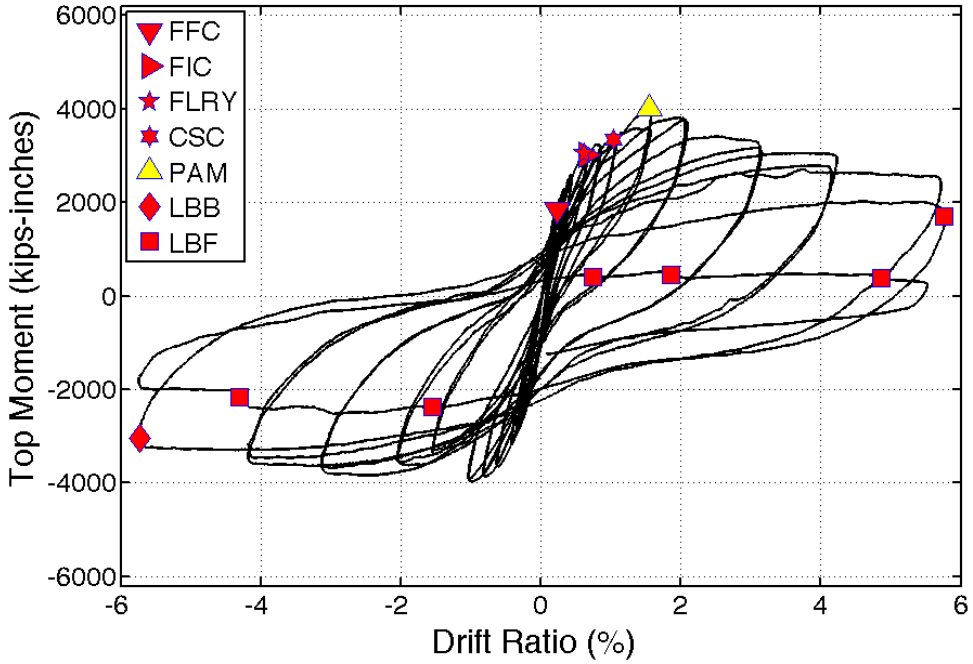

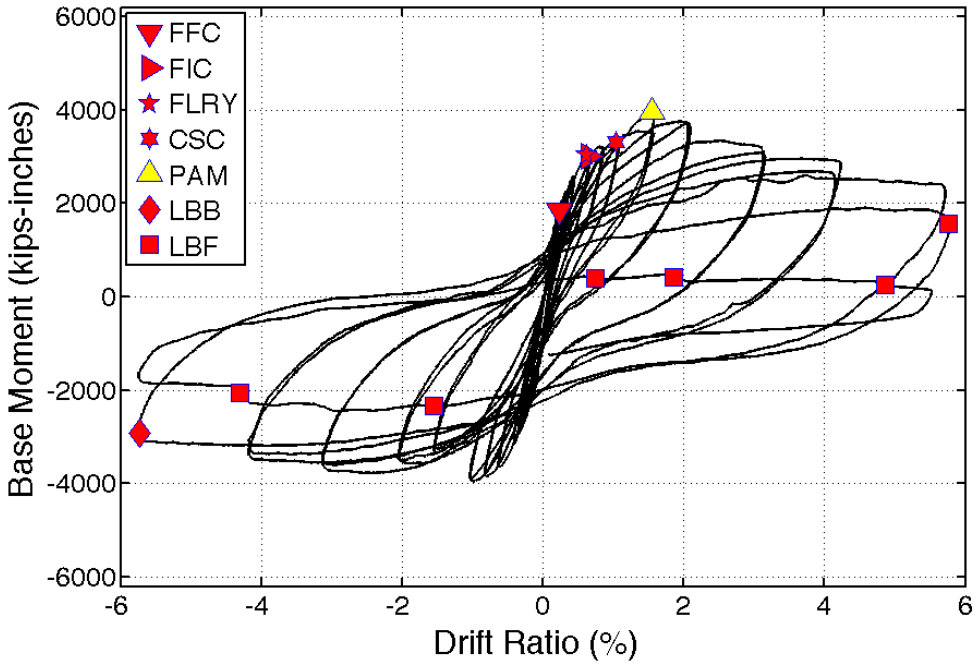

FIGURE 7-56: CH60 - BASE AND TOP MOMENT VS. DRIFT RATIO

As the column was pushed to drift ratios of 3.0%, 4.0%, and 5.5%, increasing crushing and spalling of the concrete cover was observed. The rotation in the plastic hinge region concentrated in four main flexural cracks, two in each column-end. These cracks were 11.5 inches from the ends of the specimen and reached 0.15 in. by the end of the first cycle to a drift ratio of 5.5%. At the same drift ratio, vertical cracks at the location of the longitudinal reinforcement propagated 22 in. from column ends, indicating de-bonding between the longitudinal bars and the surrounding concrete. These cracks initiated a drift ratio of 1.5%, which corresponded to a curbing of the rate of increase in longitudinal bars strains with increasing drift ratios. This behavior is discussed in more details in Section 4.5.3.

The lateral load resistance of the column remained stable and the column maintained axial load capacity past the first cycle to a drift ratio of +5.5% (Figure 7-57). During the second cycle to a drift ratio of +5.5%, the column experienced an 18% loss in peak moment resistance strength as compared to the previous half-cycle, due to significant buckling of longitudinal bars. By then, the cover concrete in the top and bottom plastic hinge regions had spalled to a distance of about 11.5 in. from column ends. As a result, on its way to completing two 5.5% drift cycles, one of the longitudinal bars fractured at the base of the column at a drift ratio of 3.6% (Figure 7-57; Figure 7-58). Just prior to first bar fracture, the column had lost more than 50% of its measured peak lateral moment resistance. The first bar fracture contributed to additional loss in lateral strength. The column was able to carry the prescribed axial load throughout the test without showing

signs of significant axial deformation even after longitudinal reinforcement fracture. It is noteworthy that the middle bar fractured first. This bar was retrained by the 90-degree bend of a cross-tie, which had opened up significantly allowing the bar to buckle (Figure 7-58).

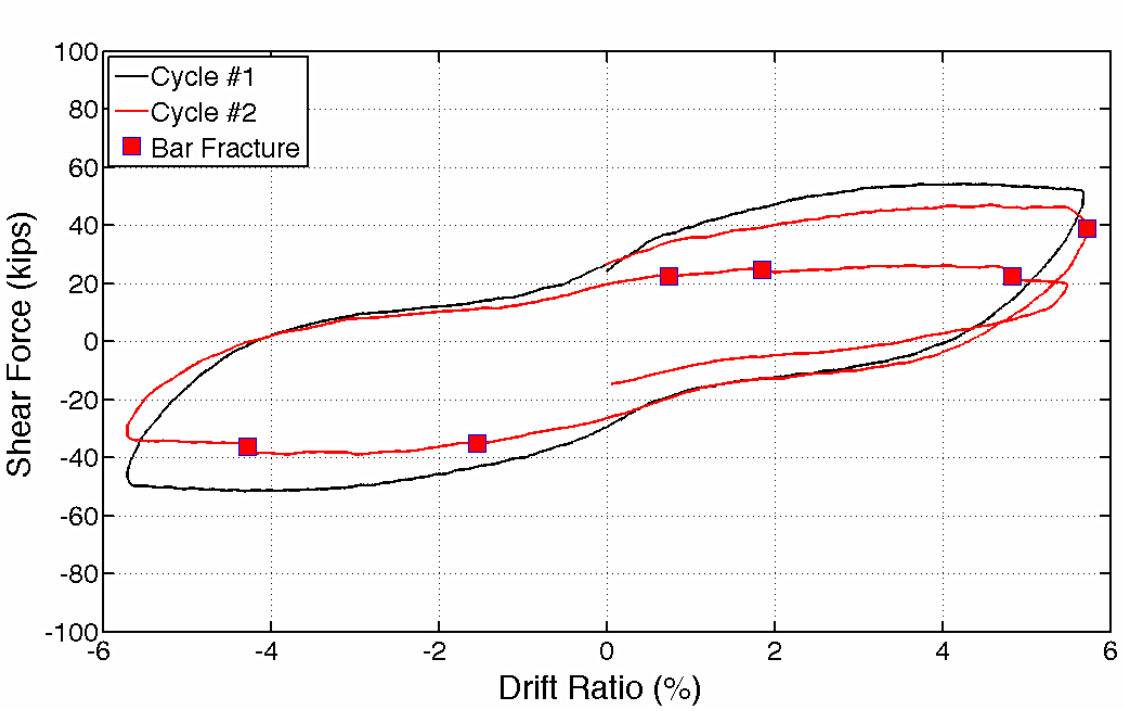

FIGURE 7-57: CH60 – LAST CYCLES RESPONSE

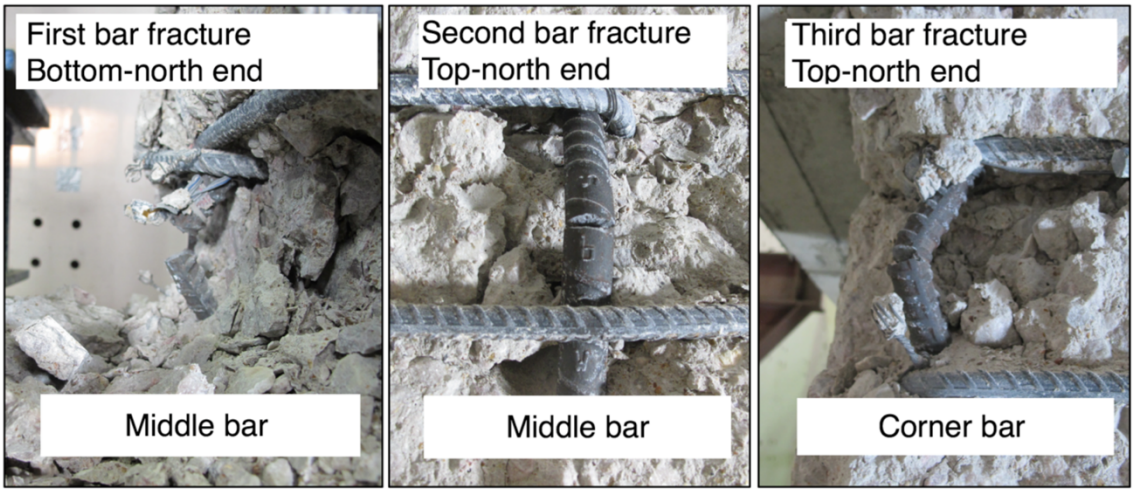

FIGURE 7-58: CH60 – PICTURE OF FRACTURED AND BUCKLED BARS

7.5.2 Deformation Components

Flexural deformations contributed most to the column lateral drift throughout the test (Table 7-8; Figure 7-59). At higher drifts, the relative weight of flexural deformations lowered as the bar-slip component increased from about 25% of the total drift at low drift levels, to about 35% in the post-yield cycles. Possibly, debonding of the longitudinal reinforcement from the surrounding concrete at larger levels of concrete damage resulted in this observed increase in recorded bar-slip contribution. This debonding of longitudinal bars due to concrete damage could have decoupled the bar deformations from measured concrete surface movements, from which bar-slip deformations were extracted. Shear deformations increased in absolute value, but remained relatively low at around 4% of total drift throughout the test. The low amount of shear deformations was due to the applied shear stresses being relatively low. Results for deformation components were not reliable after cycles to a drift ratio of 4.0%.

TABLE 7-8: CH60 - DEFORMATION COMPONENTS AS PERCENTAGE OF TOTAL

Total	Flexure	Bar-slip	Shear
0.2%	72.8%	24.1%	3.1%
0.3%	72.2%	23.9%	3.8%
0.4%	71.4%	24.9%	3.7%
0.6%	65.2%	30.4%	4.4%
0.8%	60.4%	35.1%	4.5%
1.0%	59.7%	35.9%	4.4%
1.5%	60.7%	34.8%	4.5%
2.0%	62.1%	33.4%	4.5%
3.0%	63.2%	32.1%	4.6%
4.0%	63.2%	33.4%	4.3%

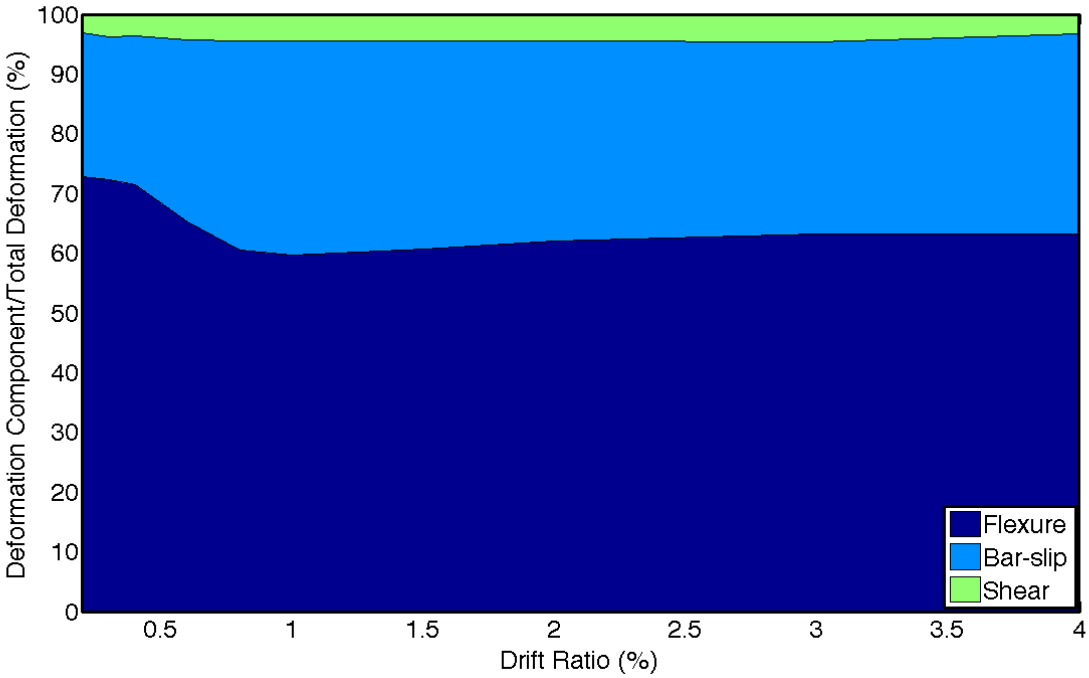

FIGURE 7-59: CH60 – DEFORMATION COMPONENTS

7.5.3 Strain History

Maximum strain demands were recorded at the interfaces between the column and footings. Figure 7-60 shows a typical strain versus lateral load response recorded on longitudinal bars at column ends. Figure 7-61 plots longitudinal bar tension strains at the end of each positive drift cycle target, measured at the top and bottom column interfaces with footings. The #6 bars used as longitudinal reinforcement in CH100 had a yield strain of 0.0024 as obtained from material testing. This strain was first reached at a drift ratio of 0.4% (Figure 7-61). However, the drift ratio of 0.6% was reported as the first yield, as an average between the available strain gauge recordings. After yield, the strain demands increased without significant increase in the lateral load. In general, strain demands on longitudinal bars were higher in the second cycle to the same drift target, with the difference increasing at higher drifts. This difference was however relatively small, and on the order of 5% of the strain value.

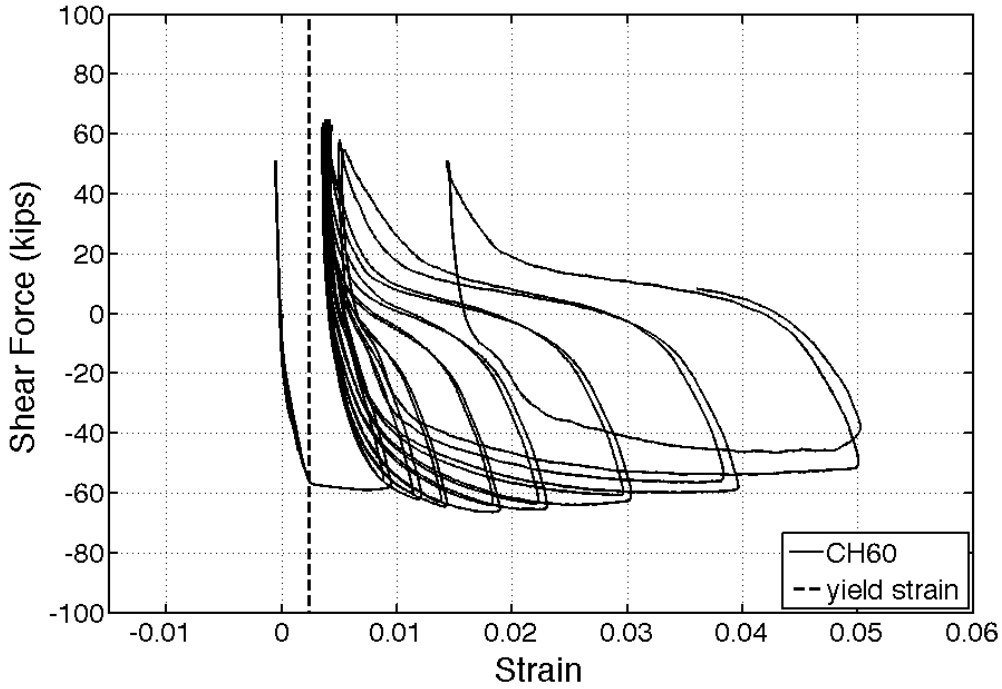

FIGURE 7-60: CH60 – STRAIN GAUGE L4NW (BOTTOM NORTH-WESTERN CORNER) RECORDING AT THE INTERFACE BETWEEN THE COLUMN AND TOP FOOTING

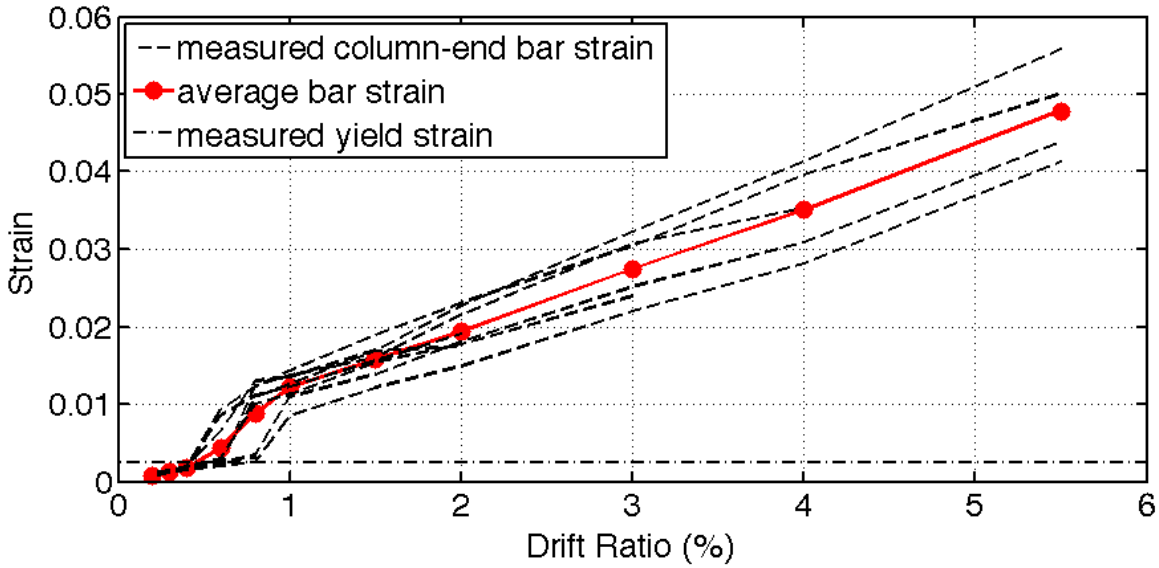

FIGURE 7-61: CH60 – COLUMN-END BAR STRAIN GAUGE RECORDINGS AND CALCULATED AVERAGE

7.5.4 Strain Profile

Strain readings over the height of south-western longitudinal bar are given in Figure 7-62. As the column was pushed past the first yield to higher drift targets, the yielded length of the bar went up to 12 inches from the base of the column, as compared to 23 inches in specimen CH100.

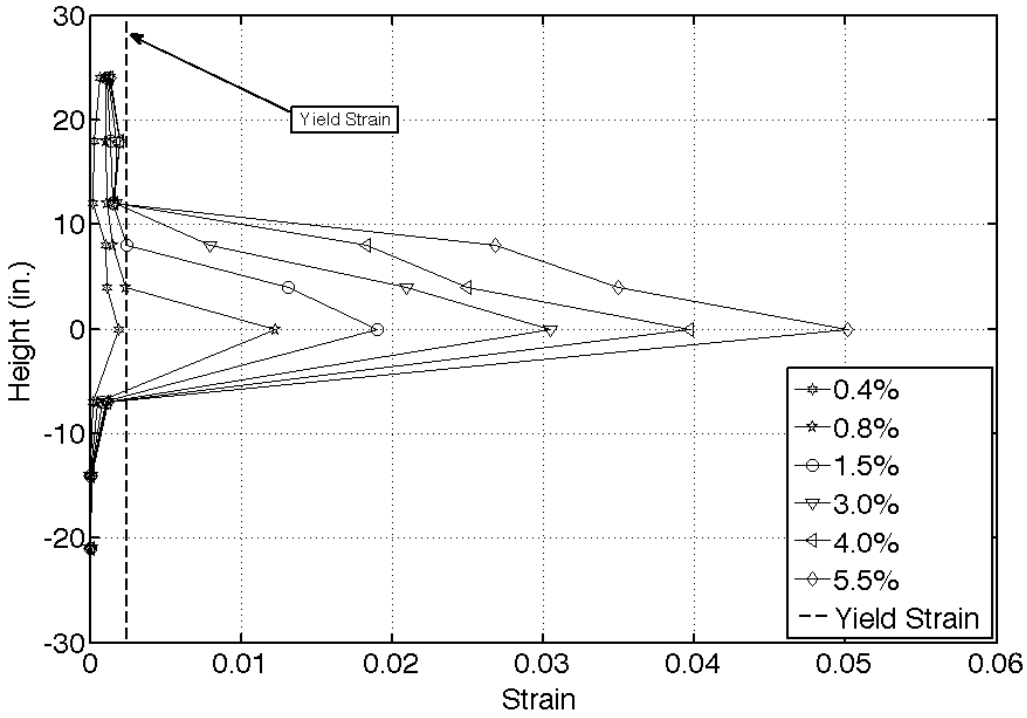

FIGURE 7-62: CH60 – LONGITUDINAL REINFORCEMENT STRAIN DEMANDS OVER HEIGHT AT DRIFT TARGETS

7.5.5Crack Widths

Data from the GVIS was used to monitor the widths of the major flexural cracks at first yield were monitored. These cracks were identified as having a width of 0.008 inches or larger at first yield. Considering that ACI 318-14 intends to limit crack widths to 0.016

inches during service loading, half of this value was used conservatively as a threshold at first yield for cracks of concern. Cracks within seven quadrilateral target elements were identified as satisfying the above- mentioned criteria, for each drift direction; three at the bottom half of the member, and four in the upper part (Figure 7-55). The number of cracks was the same for both directions of loading. During the first half cycle to a positive drift (column being pushed south, i.e. right in the pictures), flexural crack widths were measured in the bottom-south and top-north side of the member. Strain readings between the second elements in from the column vertical surfaces were used to calculate the reported cracks width values. This was done as the outermost targets in the plastic-hinge region were lost at high demands due to cover crushing. The average of these cracks is plotted in Figure 7-63 and identified as cracks occurring "Half Cycle 1". The same procedure was followed for other positive and negative drift half cycles for each drift target. At first yield, at a drift ratio of 0.6%, the average of all cracks was 0.012 inches. These cracks opened wider as the member was pushed passed yield. At a drift ratio of 0.8% the average of these cracks was 0.015 inches which is similar to the average of the cracks measured in other columns at the same drift ratio. No significant difference in crack width was noticed between the successive half cycles in which the column was being pushed in the same direction. These critical cracks were all located within 16 inches from the ends of the member. As the column was pushed to higher drifts (past 1.0% drift ratio) two large flexural cracks formed at each end of the member, 12 inches from its ends. Figure 7-64 plots the width of one of these cracks as measured throughout the test. This crack reached a maximum width of 0.2

inches by the end of the first cycle to a drift ratio of 5.5%, as compared to 0.15 inches for the other columns.

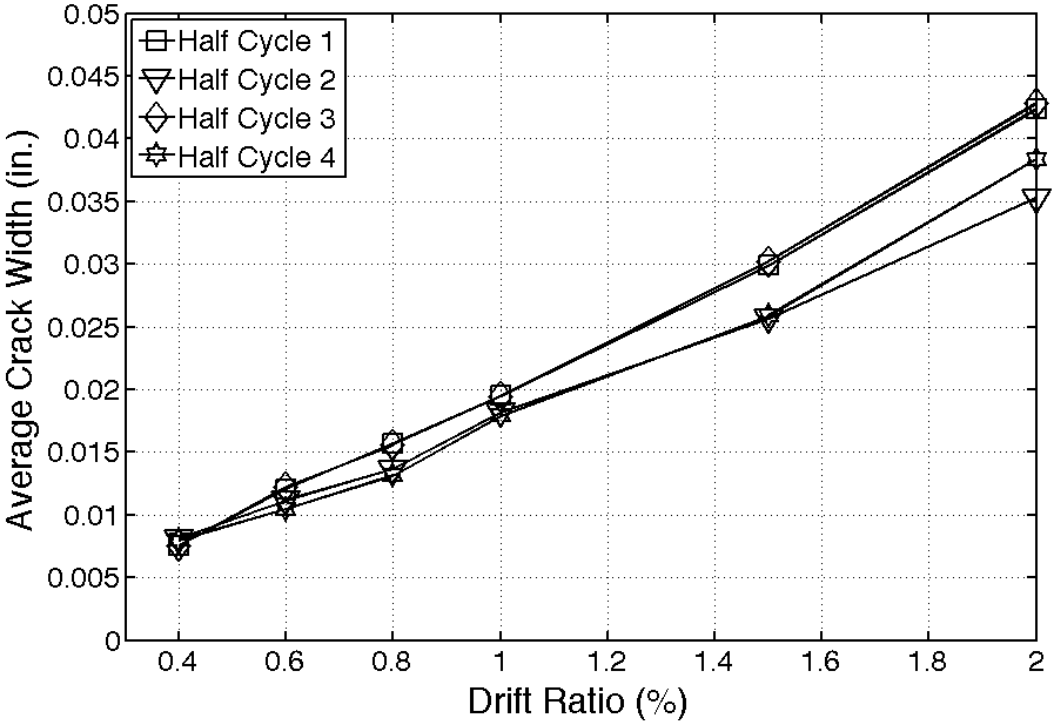

FIGURE 7-63: CH60 – AVERAGE VALUES OF LARGEST FLEXURAL CRACK WIDTHS AT DRIFT TARGETS

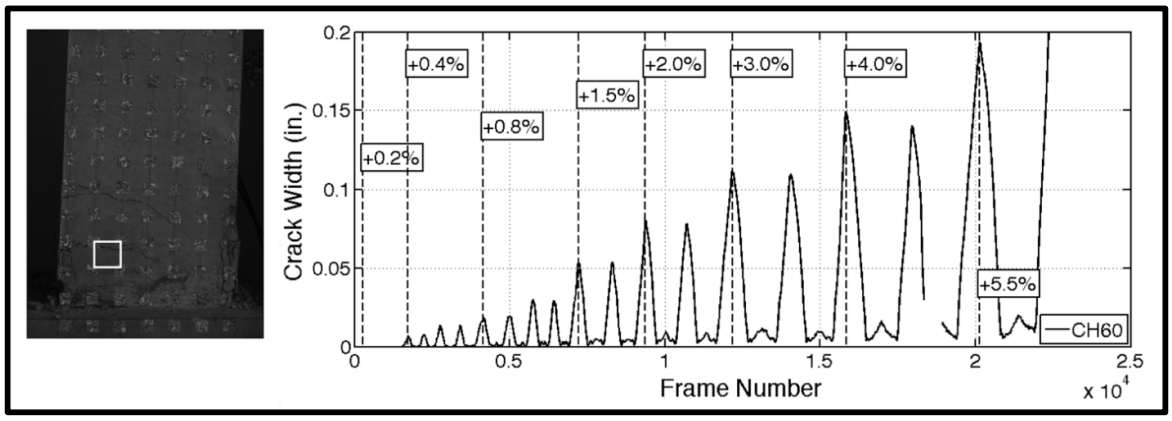

FIGURE 7-64: CH60 – WIDTH OF ONE OF THE TWO LARGEST FLEXURAL CRACKS

7.5.6 Buckling History

Buckling of the longitudinal reinforcement in CH60 was identified through the rotation measured from a row of targets at a distance of 9 inches from the ends of the column (Figure 7-65). These target rows were selected as they corresponded to the end location of the buckled bars. The rotation increased progressively with the increase in lateral drift ratio, indicating an increase in the concentration of rotations at column ends. No difference in rotation was noticed in consecutive cycles to the same drift ratio until after the member completed two full cycles to a drift ratio of 4.0%. An increase in curvature demand was recorded at the first cycle to a drift ratio of +5.5%, as compared to the cycles to 4.0% drift ratio. This was due to the increase in deformation demand, as well as slight buckling, as observed in Figure 7-66. The moment resistance was 22% lower at this point, as compared to the peak measured moment resistance. More significant buckling was observed in the following cycles (Figure 7-65; Figure 7-66). The first bar fracture was noted at the second cycle at a drift ratio of +5.5%. At the onset of the first bar fracture, moment resistance was 33% lower than the peak measured moment resistance.

Transverse reinforcement in column CH60 was spaced at 6 longitudinal bar diameters on center, as compared to 4.7 bar diameters in columns reinforced with grade 100 bars, which may explain why buckling initiated at a lower drift demands in CH60 than in members reinforced with grade 100 steel. Also, the damage in the cover concrete, which lead to the softening of the response was higher in CH60 as compared to other tested specimens.

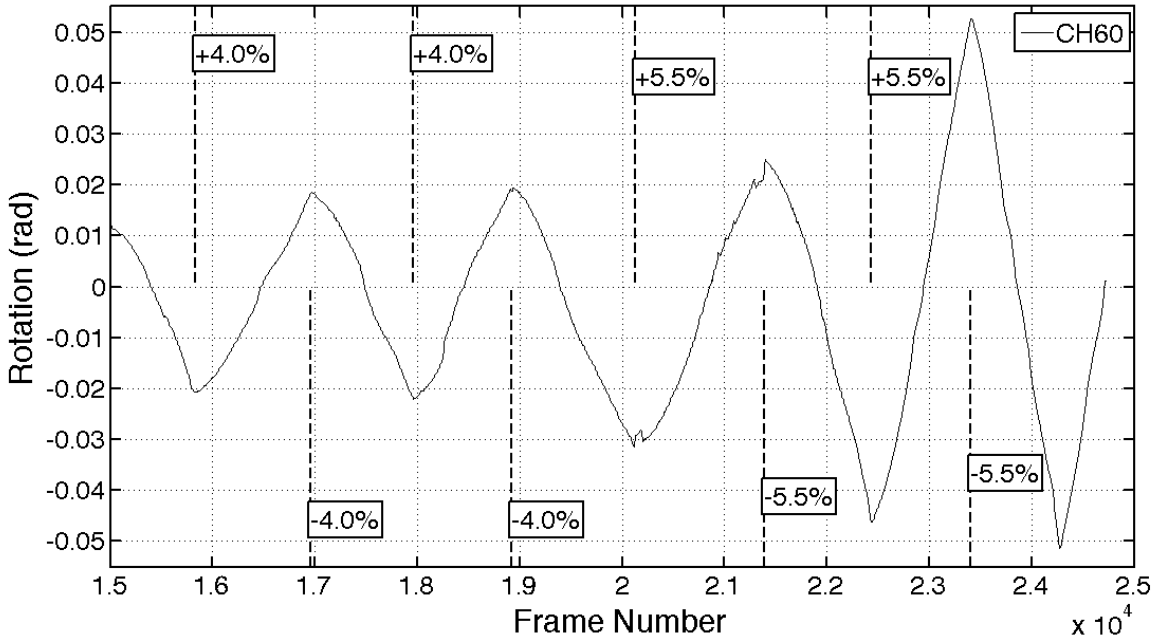

FIGURE 7-65: CH60 – ROTATION AT A DISTANCE 9 INCHES FROM THE BASE

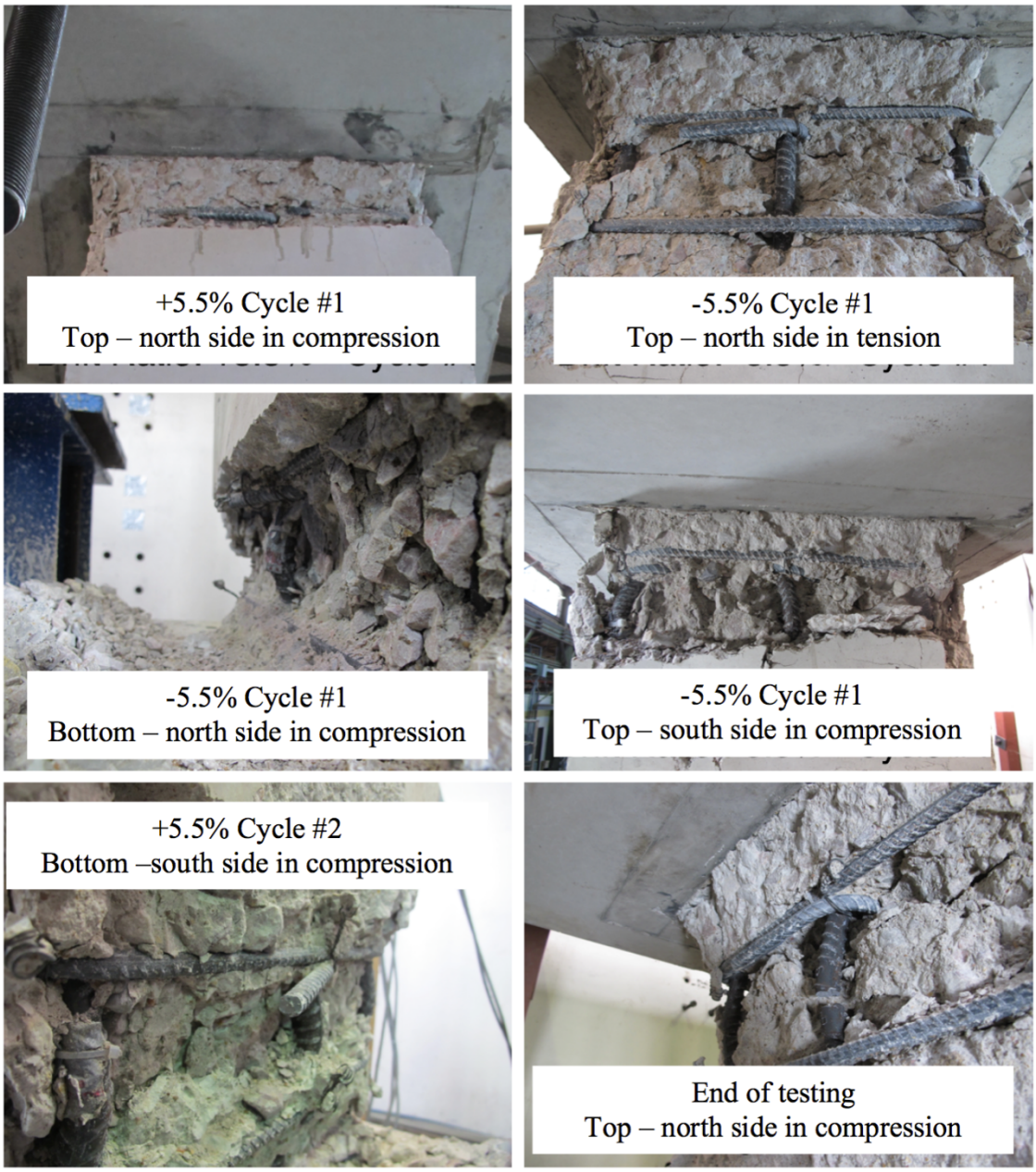

FIGURE 7-66: CH60 – LONGITUDINAL BAR BUCKLING

7.5.7 Energy Dissipation

The dissipated energy, defined as the area under the average top and bottom moment versus lateral drift relation, is plotted in Figure 7-67 for each cycle as moment strength is more representative of column sectional strength, as opposed to lateral-load strength that is influenced by second order deformation effects. The average top and bottom moment was used to compute the dissipated energy. Prior to first yielding (drift ratio targets up to 0.8%) the amount of dissipated energy was similar between the two cycles at each target drift. As the column was pushed to higher drifts and damage accumulated, the difference in energy dissipation between the cycles increased. The difference between two consecutive post-yield cycles to the same drift ratio was in the range of 3 to 20%. The difference in cumulative dissipated energy between cycles at the end of the 4% drift ratio cycles was 8.3%.

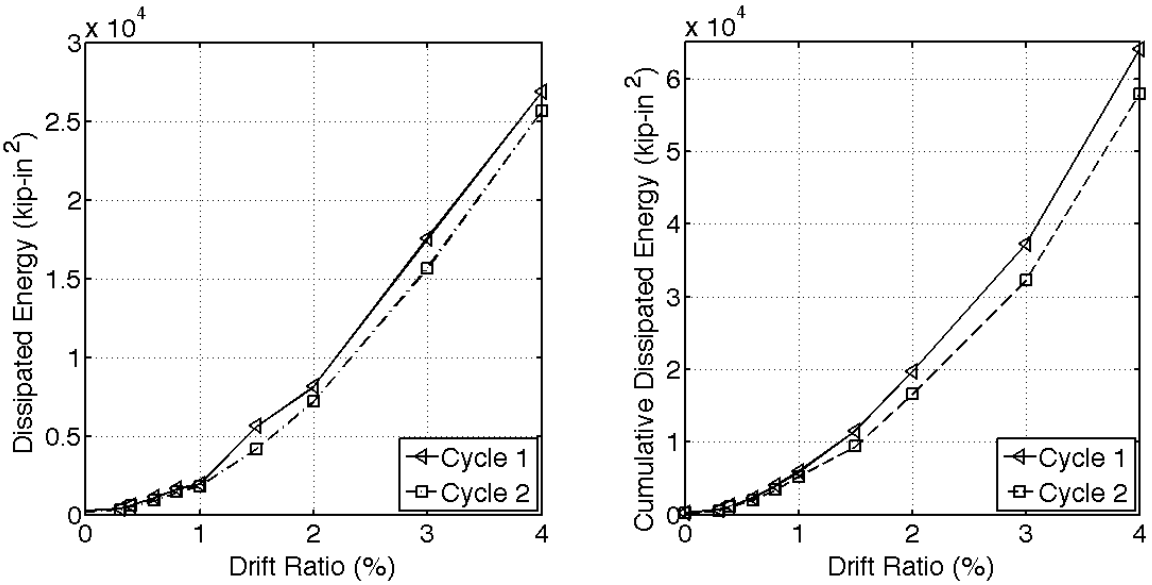

FIGURE 7-67: CH60 – DISSIPATED ENERGY AT DRIFT TARGETS FOR EACH CYCLE

8. APPENDIX C: SUPPORTING INFORMATION FOR CHAPTER 3

8.1 EXPERIMENTAL TESTS

The experimental data upon which this work builds was extracted from four series of tests carried on thirteen concrete frame members:

- Series 1 tests were reported by LeBorgne (2012) and focused on understanding the fundamental changes in column behavior that accompany post-yield shear and axial failure. The columns in Series 1 were identical in design. Both were reinforced with grade 60 ASTM A615 bars. Columns were loaded under the same lateral cyclic protocol but different axial load was applied to each. The column with lower axial load level (2L06) was designed to have longitudinal reinforcement bar yielding at flexural capacity (tension controlled) and the column with high axial load (2H06) was designed to have concrete crushing at flexural capacity (compression controlled).
- Series 2 tests were reported by Sokoli (2014) and Sokoli and Ghannoum (2016) and focused on investigating the ability of high strength-steel transverse reinforcement in maintaining the shear strength of concrete columns at inelastic demands. Three columns were designed to impart large demands on the transverse reinforcement while having similar flexural strengths. These columns were constructed using different grades of reinforcement. Column CS60 was reinforced with grade 60 ASTM A706

bars, column CS80 was reinforced with grade 80 ASTM A706 bars and column CS100 was reinforced with grade 100 bars that did not have ASTM specifications at the time of testing. The same grade of reinforcement was used for both longitudinal and transverse bars in each respective column. Column CS100 sustained a bond failure mechanism, which is not beneficial for the purpose of evaluating strain demands on longitudinal bars. This member was not used to calibrate the proposed Pre-buckling Model, but strain demands prior to de-bonding were used to check the validity of the model.

- Series 3 tests were reported by Sokoli, Limantono, and Ghannoum (2017). Four columns were tested with the main objective to investigate the effects of the different T/Y ratios and ultimate elongations of the longitudinal bars on the plasticity spread and deformation capacity of concrete columns. All columns were geometrically identical, and had the same concrete mix design and the same longitudinal and transverse bar sizes. Three of these columns were reinforced with grade 100 steel that were sourced from different steel manufacturing processes, which led to different post-yield stress-strain curves for these bars. Columns reinforced with grade 100 bars had tighter hoop spacing that the one with grade 60 bars to offset the increased buckling propensity of higher strength bars. Column (C) CH100 was reinforced with grade 100 bars with a relatively high (H) T/Y ratio, and

was produced using the micro-alloying process. Column CL100 was reinforced with grade 100 bars with a relatively low (L) T/Y ratio, and was produced using the quenching and tempering process. Column CM100 was reinforced with grade 100 A1035 bars and was produced using the MMFX (M) proprietary process. Column CH60 was reinforced with grade 60 A706 bars with a relatively high (H) T/Y ratio.

- Series 4 tests were reported by To and Moehle (2017). The beam test matrix mirrored the one of the column tests described in Series 3. Four beams were tested with the goal to investigate the effects of the different longitudinal reinforcement T/Y ratios and ultimate elongations on the plasticity spread and deformation capacity of concrete beams. The beam had nominally identical geometries and concrete mix design. Three of these beams were reinforced with grade 100 steel that were sourced from different steel manufacturing processes, which led to different post-yield stress-strain curves for these bars. Beam (B) BH100 was reinforced with grade 100 bars with a relatively high (H) T/Y ratio, and was produced using the micro-alloying process. Beam BL100 was reinforced with grade 100 bars with a relatively low (L) T/Y ratio, and was produced using the quenching and tempering process. Beam CM100 was reinforced with grade 100 A1035 bars and was produced using the MMFX (M) proprietary process. Beam CH60 was reinforced with grade 60 A706 bars with a relatively high (H)

T/Y ratio. Unlike the columns tests, the hoop spacing in the beams tests was maintained constant regardless of steel grade.

Details about the specimen design, material properties, and loading protocol are presented below for members in each series.

Specimen Design Details

Cross-sectional drawings and geometric details for all specimens are summarized in Table 8.1. This table includes the shear span of the members, which is defined as the distance between the point of zero moment to the point of maximum moment. All columns were tested under double curvature configuration; therefore, the clear length was equal to twice the reported shear span. Beams were tested in a cantilever configuration. Cross-sectional dimensions of Series 3 were considered to be 2/3rd scale, therefore the clear cover was 1 in.

TABLE 8-1: CROSS-SECTIONAL DETAILS

Series Name	Specimen	Reinforcement Type	Cross-section	Shear span, L (in.)
Series 1	2L06	Grade 60 ASTM A615	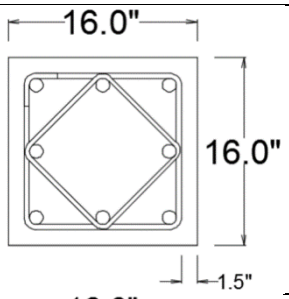	58
	2H06			
Series 2	CS60	Grade 60 ASTM A706	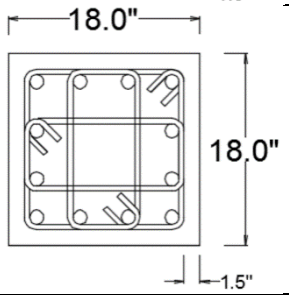	42
	CS80	Grade 80 ASTM A706		
	CS100	Grade 100		
Series 3	CH100	Grade 100	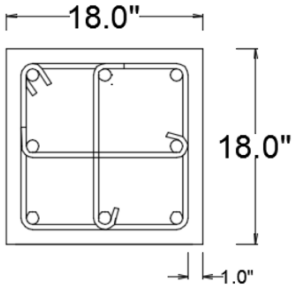	54
	CL100			
	CM100	Grade 100 ASTM A1035		
	CH60	Grade 60 ASTM A706		
Series 4	BH100	Grade 100	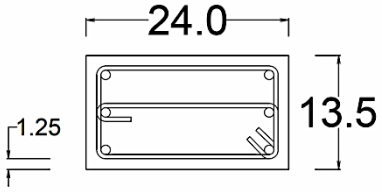	93.75
	BL100			
	BM100			
	BH60	Grade 60 ASTM A706	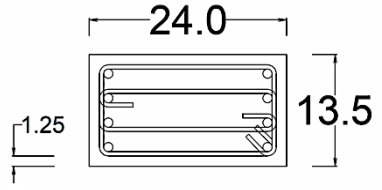	

The reinforcement details for each specimen are summarized in Table 8-2. Longitudinal reinforcement bar size varied from #6 to #10, providing a useful distribution of bar sizes for calibration of the model. For members reinforced with grade 100 steel, the transverse bar center-to-center spacing varied from 4.5 d_b to 5 d_b (where d_b is the nominal bar diameter of longitudinal bars). For members reinforced with grade 60 reinforcement, transverse bar spacing was between 4.4 d_b and 6 d_b.

TABLE 8-2: REINFORCEMENT DETAILS

Series Name	Specimen	Longitudinal Bar Size	Longitudinal Bar Ratio	Transverse Bar Size	Transverse Bar Spacing	
Series 1	2L06	#8	2.5%	#4	6 in.	6 d_b
	2H06					
Series 2	CS60	#10	4.7%	#5	5.5 in.	4.4 d_b
	CS80	#9	3.7%		5.5 in.	4.9 d_b
	CS100	#8	2.9%		4.5 in.	4.5 d_b
Series 3	CH100	#6	1.1%	#4	3.5 in.	4.7 d_b
	CL100					
	CM100					
	CH60				4.5 in.	6 d_b
Series 4	BH100	#8	1.5%	#5	5 in.	5 d_b
	BL100					
	BM100					
	BH60	#9	2.5%		5 in.	4.4 d_b

Material Properties

The average measured concrete compressive strengths at the day of specimen testing are listed in Table 8-3. All values are averages of three tested cylinders. Moderate concrete compressive strength was used in all specimen, varying from 3130 to 5580 psi. High strength concrete was not part of the scope of any of the test series.

TABLE 8-3: CONCRETE COMPRESSIVE STRENGTH

Series Name	Specimen	Concrete Strength (psi)
Series 1	2L06	3130
	2H06	3340
Series 2	CS60	3830
	CS80	4290
	CS100	4650
Series 3	CH100	5210
	CL100	5110
	CM100	5580
	CH60	4570
Series 4	BH100	5000
	BL100	5100
	BM100	5470
	BH60	5340

The measured mechanical properties of the reinforcing bars used in each specimen are listed in Table 8-4. All reported properties are averages of three monotonic tension tests. Yield strength was calculated using the 0.2% offset method. For the longitudinal reinforcing bars, the tensile-to-yield (T/Y) ratio varied from 1.16 to 1.63, and the uniform

elongation from 9.8% to 19.2%. Uniform elongation I the bar elongation at peak stress and was obtained in accordance with ASTM E8.

TABLE 8-4: MECHANICAL PROPERTIES OF REINFORCING BARS

Series Name	Specimen	Bar Size	Yield Strength (ksi)	T/Y Ratio	Uniform Elongation (%)	Fracture Elongation (%)
Series 1	2L06 2H06	#8	65.5	1.63	N/A	14.0
		#3	66.6	1.52	N/A	14.0
Series 2	CS60	#10	67.3	1.41	10.1	18.3
		#5	68.5	1.40	9.9	14.4
	CS80	#9	79.1	1.34	8.8	15.5
		#4	83.7	1.33	8.9	12.1
	CS100	#10	101.5	1.26	8.3	11.6
		#3	118.9	1.18	8.4	10.1
Series 3	CH100	#6	100.0	1.27	7.6	10.4
		#4	101.1	1.21	9.0	12.8
	CL100	#6	106.4	1.16	8.6	12.5
		#4	84.6	1.18	8.0	11.5
	CM100	#6	124.2	1.27	4.9	9.8
		#4	140.5	1.22	4.7	8.6
	CH60	#6	64.4	1.45	11.8	17.6
		#4	68.5	1.40	9.9	12.4
Series 4	BH100	#8	102.1	1.25	9.5	19.2
		#4	N/A	N/A	N/A	N/A
	BL100	#8	105.7	1.17	6.9	10.6
		#4	N/A	N/A	N/A	N/A
	BM100	#8	100.4	1.63	5.6	11.8
		#4	N/A	N/A	N/A	N/A
	BH60	#9	65.1	1.47	11.4	19.2
		#4	N/A	N/A	N/A	N/A

Loading Protocol

The columns in the Series 1 to 3 were tested under double curvature and different levels of axial load ratios (axial load divided by the gross-sectional are multiplied by the compressive concrete strength) as listed in Table 8-5. The axial load ratios varied from 15% to 41% for the columns. The four beams were tested under cantilever configuration, and no axial load was applied to them.

TABLE 8-5: APPLIED AXIAL LOAD RATIO

Series Name	Specimen	Applied Axial Load Ratio
Series 1	2L06	0.19
	2H06	0.41
Series 2	CS60	0.30
	CS80	0.27
	CS100	0.25
Series 3	CH100	0.15
	CL100	0.15
	CM100	0.15
	CH60	0.15
Series 4	BH100	0
	BL100	0
	BM100	0
	BH60	0

The lateral loading protocols for each series of tests are summarized in Table 8-6. Specimens in Series 1, 2 and 3 were tested under displacement controlled quasi-static reversed cyclic loading. The prescribed lateral loading protocols were different between

the series. The Series 1 loading protocol was based on the yield displacement of the high axial load column (2H06). The yield displacement was estimated analytically to be 0.81 inches.

The loading scheme of Series 2 and 3 was based on the drift ratio of the columns as per FEMA 461 recommendations. Tests in Series 4 were run under force control up to first yield (F_y = lateral load applied at the top of the member leading to first longitudinal reinforcement yield). The post-yield lateral loading protocol was carried in displacement control by increments of the measured displacement (Δ_y) at first longitudinal bar yield.

TABLE 8-6: LATERAL LOADING PROTOCOL

Series 1 Displacement Controlled 3-cycles per drift ratios:	Series 2 &3 Displacement Controlled 2-cycles per drift ratios:	Series 4 – BH100; BL100; BM100		Series 4 – BH60	
		Amplitude	# Cycles	Amplitude	# Cycles
0.10%	0.20%	Crack Force	3	Crack Force	3
0.20%	0.30%	0.60 F_y	3	0.60 F_y	3
0.41%	0.40%	0.84 F_y	3	0.84 F_y	3
0.81%	0.60%	1.00 F_y	3	1.00 F_y	3
1.62%	0.80%	1.40 Δ_y	3	1.40 Δ_y	3
3.24%	1.00%	1.96 Δ_y	2	1.96 Δ_y	3
6.48%	1.50%	2.74 Δ_y	2	2.74 Δ_y	3
	2.00%	3.84 Δ_y	2	3.84 Δ_y	2
	3.00%	5.38 Δ_y	2	5.38 Δ_y	2
	4.00%	7.53 Δ_y	2	7.53 Δ_y	2
	5.50%				
	7.00%				

8.2 MATCHED TENSILE STRAINS IN LONGITUDINAL BARS

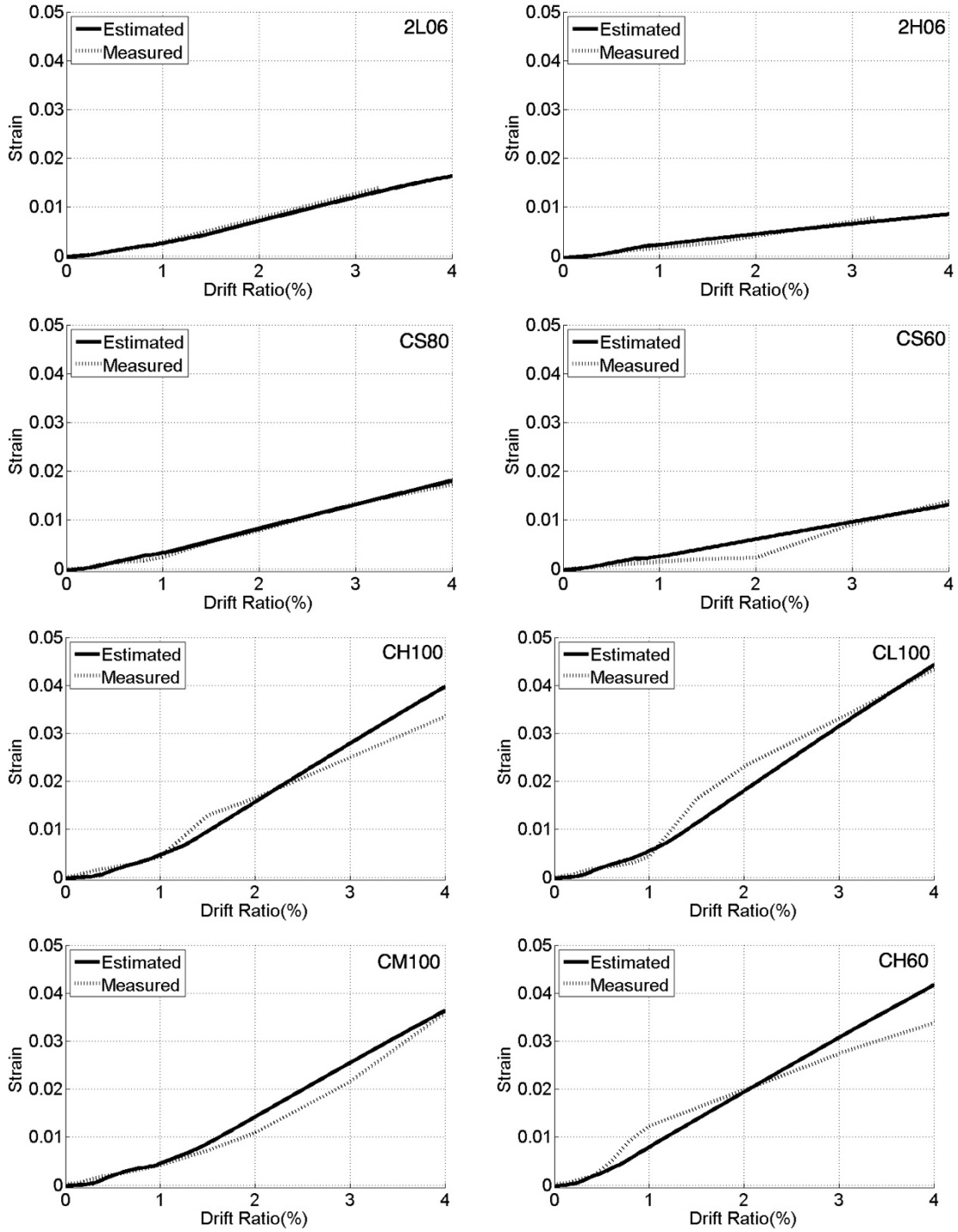

FIGURE 8-1: CONTINUES INTO NEXT PAGE

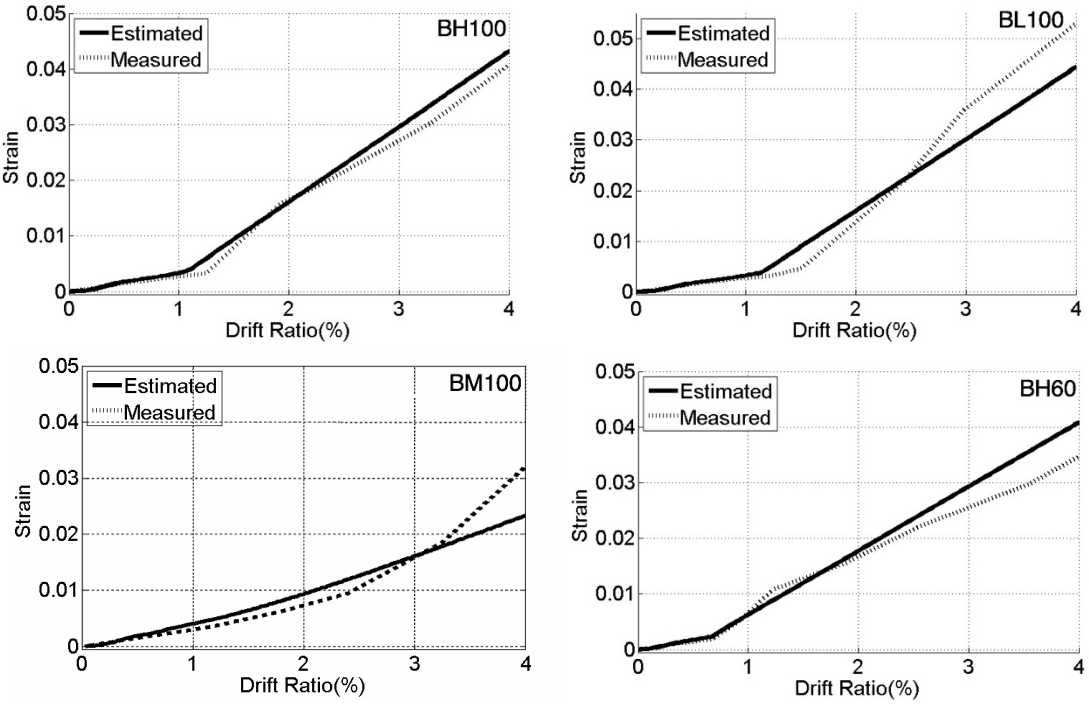

FIGURE 8-1: ESTIMATED VS MEASURED TENSILE STRAINS IN THE BARS

8.3 MATCHED TENSILE STRAINS IN THE CONCRETE SURFACE

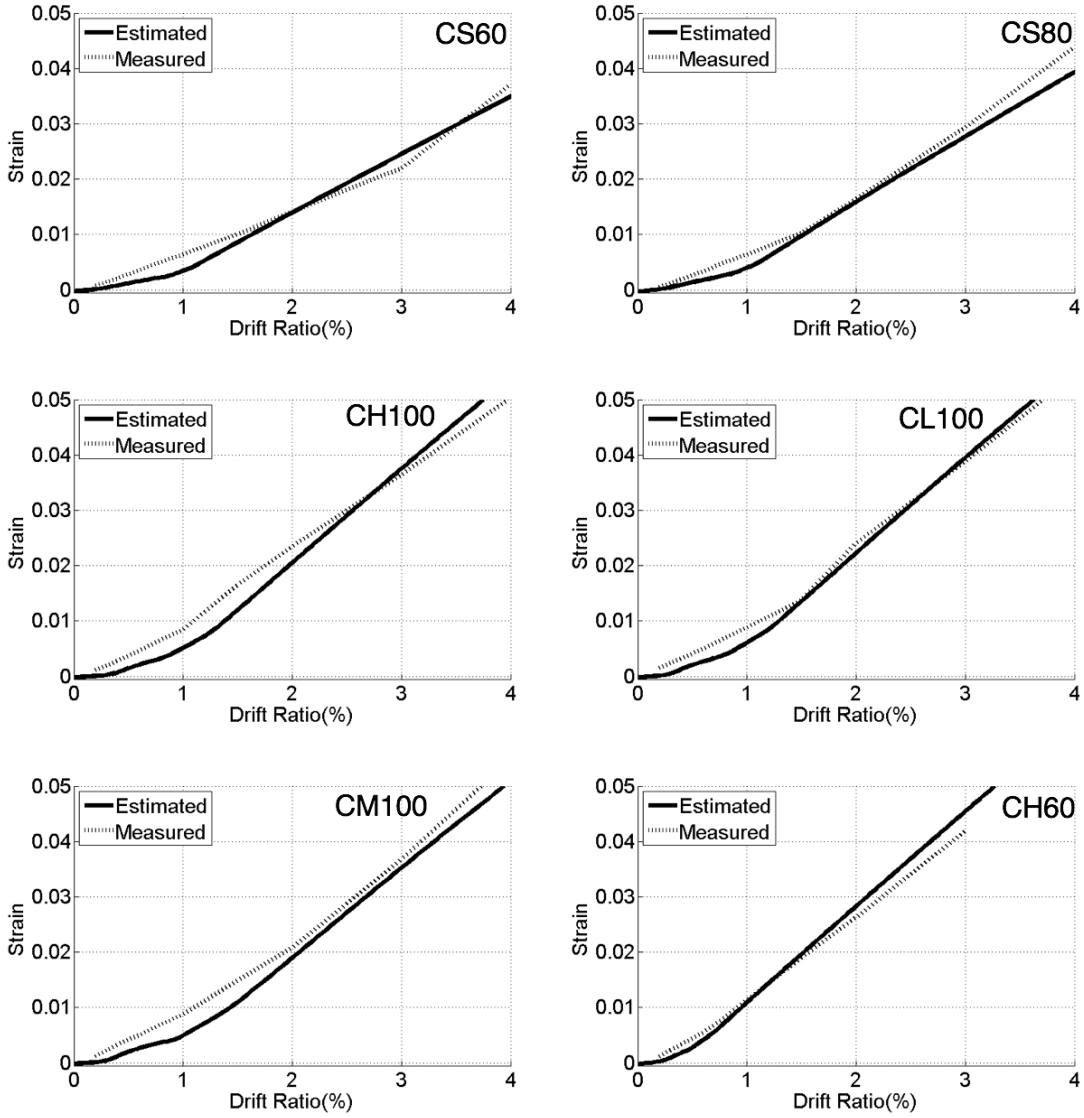

FIGURE 8-2: ESTIMATED VS MEASURED SURFACE TENSILE STRAINS

LIST OF REFERENCES

ACI Committee 318, "Building Code Requirements for Structural Concrete (ACI 318-14) and Commentary (ACI 318R-14)," American Concrete Institute, Farmington Hills, MI, 2014, 519 pp.

ACI Committee 369, "Standard Requirements for Seismic Evaluation and Retrofit of Existing Concrete Buildings (ACI369-17)," American Concrete Institute, Farmington Hills, MI, 2017, 110 pp.

Addessi, D and Ciampi, V., "A regularized force-based beam element with a damage-plastic section constitutive law," *International Journal for Numerical Methods in Engineering,* V. 70, No. 5, 2007, pp. 610–629.

Aoyama, H., 2001, "Design of Modern Highrise Reinforced Concrete Structures," Imperial College Press, London, United Kingdom.

ASCE/SEI 41-13, "Seismic Rehabilitation of Existing Buildings," ASCE/SEI Standard 41-13, American Society of Civil Engineering, Reston, VA, 2013.

ASCE/SEI 41-17, "Seismic Rehabilitation of Existing Buildings," ASCE/SEI Standard 41-17, American Society of Civil Engineering, Reston, VA, 2017.

ASTM A1035 / A1035M-16b, Standard Specification for Deformed and Plain, Low-Carbon, Chromium, Steel Bars for Concrete Reinforcement, ASTM International, West Conshohocken, PA, 2016, www.astm.org.

ASTM A370-17a, "Standard Test Methods and Definitions for Mechanical Testing of Steel Products," ASTM International, West Conshohocken, PA, 2017, 50 pp.

ASTM A706 / A706M-16, Standard Specification for Deformed and Plain Low-Alloy Steel Bars for Concrete Reinforcement, ASTM International, West Conshohocken, PA, 2016, www.astm.org.

ASTM C39/C39M-18, "Standard Test Method for Compressive Strength of Cylindrical Concrete Specimens," ASTM International, West Conshohocken, PA, 2018, 8 pp., www.astm.org.

ASTM E8 / E8M-16a, Standard Test Methods for Tension Testing of Metallic Materials, ASTM International, West Conshohocken, PA, 2016, www.astm.org.

ATC-115 "Roadmap for the Use of High-Strength Reinforcement in Reinforced Concrete Design,", Applied Technology Council, 2015, 197 pp.

Benzoni, G.; Ohtaki, T.; Priestley, M. J. N.; and Seible, F., "Seismic Performance of Circular Reinforced Concrete Columns under Varying Axial Load," SSRP 96/04, Structural Systems Research, University of California-San Diego, La Jolla, CA, 1996.

Berry, M. P., and Eberhard, M. O., "Practical Performance Model for Bar Buckling," *Journal of Structural Engineering, ASCE*, V. 131, No. 7, 2005, pp. 1060–1970.

Berry, M. P., and Eberhard, M. O., "Performance Modeling Strategies for Modern Reinforced Concrete Bridge Columns," PEER-2007/07, Pacific Earthquake Engineering Research Center, University of California-Berkeley, Berkeley, CA, 2007, 213 pp.

Brown, W. A., Lehman, D. E., and Stanton, J. F., "Bar Buckling in Reinforced Concrete Bridge Columns," PEER-2007/11, Pacific Earthquake Engineering Research Center, University of California-Berkeley, Berkeley, CA, 2007, 138 pp.

Bresler, B., and Gilbert, P. H., “Tie Requirements for Reinforced Concrete Columns,” *ACI Structural Journal*, V. 58, No. 5, 555–570.

Coleman, J., and Spacone, E., “Localization Issues in Force-Based Frame Elements,” *ASCE Journal of Structural Engineering*, V. 127, No. 11, 2001, pp. 1257–1265.

Dhakal, R., and Maekawa, K., “Reinforcement Stability and Fracture of Cover Concrete in Reinforced Concrete Members,” *Journal of Structural Engineering,* ASCE, V. 128, No. 10, 2002, 1253–1262.

Elwood, K. J. and Eberhard, M.O., “Effective Stiffness of Reinforced Concrete Columns,” *ACI Structural Journal*, V. 106, No. 4, 2009.

Federal Emergency Management Agency (FEMA), "Interim Testing Protocols for Determining the Seismic Performance Characteristics of Structural and Nonstructural Components." FEMA-461, Federal Emergency Management Agency, Washington, DC, 2007, 138 pp.

Feng, Y., Kowalsky M. J., Nau, J. M., “Finite-Element Method to Predict Reinforcing Bar Buckling in RC Structures,” *Journal of Structural Engineering*, ASCE, V. 141, No. 5, 2015.

Ghannoum, W. M., and Moehle, J. P., “Shake-Table Tests of a Concrete Frame Sustaining Column Axial Failures,” *ACI Structural Journal*, V. 109, No. 3, May-June 2012, pp. 393-402.

Ghannoum, W.M. and Slavin, C.M., "Low-Cycle Fatigue Performance of High-Strength Steel Reinforcing Bars,” *ACI Material Journal*, 113 (6), 2016.

Hoggsett, G. S., “Defining Structurally Acceptable Properties of High-Strength Reinforcing Bars through Low-Cycle Fatigue Testing,” master’s thesis, University of Texas at Austin, Austin, TX, 2017, 118 pp.

Huq, M. S., Weber-Kamin, A. S., Ameen, S., Lequesne D. R., and Lepage, A., “High-Strength Steel Bars in Reinforced Concrete Walls: Influence of Steel Mechanical Properties on Deformation Capacity,” (04-14), Charles Pankow Foundation, 2017, pp. 311. http://www.pankowfoundation.org/download.cfm?ID=319

Karsan, I. D., and Jirsa, J. O. (1969). "Behavior of Concrete Under Compressive Loading," *Journal of Structural Division,* ASCE, V. 95, No. 12, 2543-2563.

Kent, D. C., and Park, R., “Flexural Members with Confined Concrete,” *Journal of Structural Division,* ASCE, V. 97, No. 7, 1971, pp. 1969–1990.

Kwon, Jinhan, “Strength, Stiffness, and Damage of Reinforced Concrete Buildings Subjected to Seismic Motions,” Ph.D. Dissertation, The University of Texas at Austin, Austin, Texas, May 2016.

LeBorgne, M.R., “Modeling the Post Shear Failure Behavior of Reinforced Concrete Columns,” Ph.D. Dissertation, The University of Texas at Austin, Austin, Texas, May 2012.

Limantono, A. A., “Modeling Strain Demands in Longitudinal Steel Bars of Concrete Columns,” master’s thesis, University of Texas at Austin, Austin, TX, 2016, pp. 178.

Macchi, G., Pinto, P.E. and Sanpaolesi, L., "Ductility Requirements for Reinforcement Under Eurocodes," *Structural Engineering International*, 6.4, 1996, pp. 249-54.

Mander. J. B., Priestley, M. J. N., Park, R., "Theoretical Stress-Strain Model for Confined Concrete," *Journal of Structural Engineering*, Vol. 114, No. 8, 1988, pp. 1804-1826.

McKenna, F., Fenves, G.L., Scott, M.H., and Jeremie, B., 2000, *Open System for Earthquake Engineering Simulation*, Open System for Earthquake Engineering Simulation (OpenSEES), University of California, Berkeley.

Menegotto M., Pinto P.E., "Method of Analysis for Cyclically Loaded R.C. Frames Including Changes in Geometry and Non-Elastic Behavior of Elements Under Combined Normal Force and Bending," Istituto di Scienza e Tecnica delle Costruzioni, University of Rome, Report 32, October 1972.

MMFX Technologies Corporation, "Material Properties and Design Considerations MMFX2 (ASTM A1035/AASHTO MP18)," MMFX Product Information, December 2012, 36 pp.

Moyer, M. J., and Kowalsky, G., "Influence of Tension Strain on Buckling of Reinforcement in Concrete Columns," *ACI Structural Journal*, V. 100, No. 1, Jan.-Feb. 2003, pp. 78-85.

Neuenhofer, A., and Filippou, F. C., "Evaluation of Nonlinear Frame Finite-Element Models," *Journal of Structural Engineering*, ASCE, V. 123 No. 7, 1997, pp. 958–966.

NIST, "Use of High-Strength Reinforcement in Earthquake-Resistant Concrete Structures (GCR 14-917-30)," NEHRP Consultants Joint Venture, National Institute of Standards and Technology, Gaithersburg, MD, 2014, 231 pp.

OpenSees, Version 2.4.5, http://opensees.berkeley.edu, accessed May. 13, 2015.

Pantazopoulou, S. J., "Detailing for Reinforcement Stability in Reinforced Concrete Members," *Journal of Structural Engineering,* ASCE, V. 124, No. 6, 1998, 623–632.

Papia, M.; Russo, G.; and Zingone, G., "Instability of Longitudinal Bars in RC Columns," *Journal of Structural Engineering*, ASCE, V. 114, No. 2, 1988, pp. 445-461.

Papia, M., and Russo, G., "Compressive Concrete Strain at Buckling of Longitudinal Reinforcement," *Journal of Structural Engineering*, V. 115, No. 2, 1989, 382–397.

Park, R. and Paulay, T., Reinforced Concrete Structures, Wiley, 1975.

Puranam, A. and Pujol, S., "Minimum Flexural Reinforcement in Reinforced Concrete Walls," 16th World Conference on Earthquake Engineering, 16WCEE, Chile, 2017.

Qi, X. and Moehle, J. P. "Displacement Design Approach for Reinforced Concrete Structures Subjected to Earthquakes," Earthquake Engineering Research Center, University of California, Berkeley, CA, UCB/EERC-91/02, January 1991, 186 pp.

Rodriguez, M., Botero, J., and Villa, J. 1999. "Cyclic Stress-Strain Behavior of Reinforcing Steel Including Effect of Buckling," *Journal of Structural Engineering,* ASCE, V. 125, No. 6, 605–612.

Scott, M. H., and Fenves G. L., "Plastic Hinge Integration Methods for Force-Based Beam–Column Elements," *Journal of Structural Engineering*, ASCE, V. 132, No. 2, 2006, pp. 244-252.

Scribner, C. F. "Reinforcement Buckling in Reinforced Concrete Flexural Members" *ACI Structural Journal*, V. 83 No. 6, 1986, pp. 966–973.

Slavin, C. M., "Defining Structurally Acceptable Properties of High-Strength Steel Bars through Material Testing," master's thesis, University of Texas at Austin, Austin, TX, 2015, 136 pp.

Slavin, C.M. and Ghannoum, W.M., "Defining Structurally Acceptable Properties of High- Strength Steel Bars through Material and Column Testing, PART I: MATERIAL TESTING REPORT," (05-14), Charles Pankow Foundation, August 2015, pp. 135. http://www.pankowfoundation.org/download.cfm?ID=282

Sokoli, D., Shekarchi, W., Buenrostro, E. and Ghannoum, W. M., "Advancing Behavioral Understanding and Damage Evaluation of Concrete Members Using High-

Resolution Digital Image Correlation Data," Earthquakes and Structures, V. 7, No. 5, 2014, pp. 609-626. doi: 10.12989/eas.2014.7.5.609

Sokoli, D., "Seismic Performance of Concrete Columns Reinforced with High Strength Steel," master's thesis, University of Texas at Austin, Austin, TX, 2014, 166 pp.

Sokoli, D. and Ghannoum, W.M., "High-strength Reinforcement in Columns under High Shear Stresses," *ACI Structural Journal*, V. 113, No. 3, 2016.

Sokoli, D. Limantono, and A., Ghannoum, W. M., "Defining Structurally Acceptable Properties of High- Strength Steel Bars through Material and Column Testing, PART II: COLUMN TESTING REPORT," (05-14), Charles Pankow Foundation, August 2017, pp. 219. http://www.pankowfoundation.org/grants.cfm?prodonly=1

Spacone, E., Filippou, F. C., and Taucer, F. F. ''Fibre beam-column model for nonlinear analysis of R/C frames. I: Formulation,'' *Earthquake Engineering and Structural Dynamics*, V. 25, No. 7, 1996, pp. 711–725.

To, D. V. and Moehle, J. P., "Seismic Performance Characterization of Beams with High-Strength Reinforcement," (06-14), Charles Pankow Foundation, 2017, pp. 140.

Wang, Y. C., and Restrepo, J. I., "Strength Enhancement of Concentrically Loaded Reinforced Concrete Columns Using TYFO S Fiber-Wrap Jackets." Res. Rep. 96-12, Dept. of Civil Engineering, Univ. of Canterbury, Christchurch, New Zealand, 1996.

Zhao, D.S. and Ghannoum, W.M., "Setting Bar-Bending Requirements for High-Strength Steel Bars," (01-15), Charles Pankow Foundation, 2016, pp. 92. http://www.pankowfoundation.org/download.cfm?ID=297